Spatiotemporal Models and Simulations Reveal the Physical Mechanisms That Migrating Cells Sense and Self-adapt to Heterogeneous Extracellular Microenvironments

by

Xindong Chen

Thesis submitted for the degree of Doctor of Philosophy

School of Engineering

Cardiff University

2020

I dedicate this to my family, my tutor and my friends who have always lovingly supported me

Acknowledgements

I gratefully thank my supervisor, Dr. Hanxing Zhu, for his invaluable guidance, help and encouragements on my research, and care on my personal life. During this research, I am always encouraged by his enthusiasm, devotion and curiosity to keep working hard. I enjoy doing research with him very much. Every Christmas, he and his family prepare a lot of delicious foods for our lab members. I feel very lucky to be a member of his lab! I also thank my second and third supervisors, Prof. Yacine Rezgui and Prof. Stephane Bordas, for their help and support, and Dr. Peter Theobald for being the internal examiner of my annual reviews during my PhD study.

I gratefully thank Prof. Xiqiao Feng (Tsinghua University) for his invaluable discussions, help and encouragements during my PhD period. I also thank Prof. Ovijit Chaudhuri (Stanford University), Prof. Thomas D. Pollard (Yale University) and Prof. Laurent Blanchoin (Biosciences & Biotechnology Institute of Grenoble) for providing their expert and helpful knowledge over emails. Their and Prof. Fletcher's cutting-edge fundamental experimental researches provide significant backgrounds for this study and also inspire me to work hard.

During the last three and a half years, I got a lot of help from many previous and current lab members. I thank Prof. Guoyang Guan, Xiude Lin, Yang Jiao, Xiaobo Wang, Zhengyang Zhang, Qi Luo, Jishen Yang and Yanhui Ma for being excellent colleagues. It was a great pleasure working with them and I learned a lot from them. I also thank our lab members and Bin Guo, Min Chen, Ping Huang, Xiuyuan Lu, Peng Yang, Quanquan Han, Peng Yu, Chong Chen, Hao Yu, Shangkun Li, Zheyuan Chen and Xiaoyang Liu for their company and the time we joyfully spent together in Cardiff. I thank all the staff in the Research Office for their kind help and thank

the financial support from the China Scholarship Council and Cardiff School of Engineering, which have ensured the accomplishment of the research.

I thank my family and a lot of my friends for always caring, supporting and encouraging me.

Abstract

Cell migration plays essential roles in many normal physiological and pathological processes, such as embryonic morphogenesis, wound healing, tissue renewal, nervous system development, cancer metastasis and autoimmune disorders. Both single cell migration and collective cell migration are powered by the actin-based lamellipodia, filopodia or invadopodia protrusions at their leading edges to migrate through extremely heterogeneous extracellular microenvironments. Although extensive experimental studies about cell migration have been conducted, it is unknown of the intracellular physical mechanisms of how migrating cells sense and adapt to the highly varying extracellular mechanical microenvironments.

To address this, we construct the predictive spatiotemporal model of the lamellipodial branched actin network through simulating its realistic self-assembling process by encompassing key proteins and their highly dynamic interactions. Then, using finite element simulations, we quantitatively demonstrate the mechanical roles of individual intracellular proteins in regulating the elastic properties of the self-assembling network during cell migration. More importantly, we reveal a resistance-adaptive intracellular physical mechanism of cell migration: the lamellipodial branched actin network can sense the variations of immediate extracellular resistance through the bending deformations of actin filaments, and then adapt to the resistance by self-regulating its elastic properties sensitively through Arp2/3 nucleating, remodelling with F-actin, filamin-A and α-actinin and altering the filament orientations. Such resistance-adaptive behaviours are versatile and essential in driving cells to over-come the highly varying extracellular confinements. Additionally, it is deciphered that the actin filament bending deformation and anisotropic Poisson's ratio effect of the branched actin network and Arp2/3 branching preference jointly determine why lamellipodium grows into a sheet-like structure and protrudes against resistance persistently. Our predictions

are confirmed by published pioneering experiments. The revealed mechanism also can be applied to endocytosis and intracellular pathogens motion.

The propulsive force of cell migration is based on actin filament polymerization. We propose a theoretical 'bending-straightening elastic ratchet' (BSER) model, which is based on geometrical nonlinearity deformation of continuum solid mechanics. Then, we develop the self-assembling spatiotemporal mathematical model of the polymerizing lamellipodial branched actin filaments propelling the leading edge protrusion under heterogeneous extracellular microenvironment, and perform large-scale spatial and temporal simulations by applying the BSER theoretical model. Our simulation realistically encompasses the stochastic actin filament polymerization, Arp2/3 complex branching, capping proteins inhibiting actin polymerization, curved LE membrane, rupture of molecular linkers and varying extracellular mechanical microenvironment. Strikingly, our model for the first time systematically predicts all important leading-edge behaviours of a migrating cell. More importantly, we reveal two very fundamental biophysical mechanisms that migrating cells sense and adapt their protruding force to varying immediate extracellular physical constraints, and that how migrating cells navigate their migratory path to in highly heterogeneous and complex extracellular microenvironments. Additionally, our BSER theoretical model and the underlying physical mechanism revealed here are also applicable to the propulsion systems of endocytosis, intracellular pathogen transport and dendritic spine formation in cortical neurons, which are powered by polymerization of branched actin filaments as well.

Filopodia and invadopodia protrusions are the other two types of cell migration behaviours at their leading edges. Through three-dimensional assembling model of filopodial/invadopodial F-actin bundles and finite element simulations, we quantitatively identify how the highly dynamic assembling and disassembling actin filaments and binding and unbinding of crosslinking proteins, i.e., α-actinin and fascin, regulate Young's modulus and buckling behaviours of

filopodia/invadopodia, respectively and combinedly. In addition, thermal induced undulation of actin filaments has an important influence on the buckling behaviours of filopodia/invadopodia. Compared with sheet-like lamellipodia, the finger-like filopodia/invadopodia have a much larger stiffness to protrude in extracellular microenvironment. Thus, they can cooperate with lamellipodia to complementarily split a channel in extracellular microenvironment and drive cell migration through the channel.

Contents

List of Figures

List of Tables

List of Abbreviations

ECM	Extracellular Matrix
FEM	Finite Element Method
LE	Leading Edge
F-actin	Filamentous Actin
RVE	Representative Volume Element
BSER	Bending-straightening elastic racket

Nomenclature

L_c	Contour length
L_p	Persistent length
V_f	Polymerization velocity of actin filaments
δ	Size of an actin monomer
M	Molar concentration of actin monomers
k_{on}	Polymerization rate of actin filaments
k_{off}	Depolymerization rate of actin filaments
L	Total length of actin filaments
C_A	Concentration of F-actin
w	In-plane side length of lamellipodial RVE
h	Thickness of lamellipodia
N_A	Avogadro constant
d_{actin}	Diameter of actin monomer
x_i^p, y_i^p, z_i^p	Pointed end coordinates of actin filament
x_i^b, y_i^b, z_i^b	Barbed end coordinates of actin filament
d	Diameter of actin filament
d^{arp}	Space between to adjacent Arp2/3 along an actin filament
$x_i^{as}, y_i^{as}, z_i^{as}$	Start coordinates of Arp2/3
$x_i^{ae}, y_i^{ae}, z_i^{ae}$	End coordinates of Arp2/3

$r_{ij}^{arp}, \varphi_{ij}^{arp}, \theta_{ij}^{arp}$	Sphere coordinates of Arp2/3 end
α	Arp2/3 branching angle
$d_{\min}^{fls}$	Shortest spatial distance between the two actin filaments
V_f	Actin filament density (or Actin filament volume fraction)
u	Displacement in x direction
v	Displacement in y direction
w	Displacement in z direction
E_s	Young's modulus of solid material
G_s	Shear modulus of solid material
ν_s	Poisson's ratio of solid material
A	Area of cross-section
I	Second moment of cross-section
J	Polar second moment of cross-section
Π_p	True total energy of deformation system
Π_p^*	Possible total energy of deformation system
E_i	Young's modulus in i direction of model
G_{ij}	Shear modulus in the ij-plane of model
E_f	Young's modulus of actin filament
E_c	Young's modulus of crosslinking proteins
K	Successive branching generation number from a mother actin filament
σ	Stress

ε	Strain
f_p	Polymerization force of an actin filament n_{arp}
n_{arp}	Density of Arp2/3
N_{arp}	Total number of Arp2/3
N_m	Total number of mother actin filaments in model
N_c	Total number of crosslinking protein in model
ρ_c	Density of crosslinking proteins
t	Time
l	Length of an actin filament
p	Reconstrait force between a polymerizing actin filament and local LE membrane
ξ	Mean curvature of a bent actin filament
m	The number of mother actin filaments
Π	Total deformation energy of free end actin filaments
F_p	Resultant propulsive force for cell migration
f_r	Resistance from extracellular microenvironment
f_a	Attachment force
f_m	Cell membrane tension
s	Distance of cell migration
$\triangle s$	Step size of LE protrusion
V_m	LE membrane protruding velocity
Φ	Actin filament density pushing against the LE membrane

L_b	Length of filopodia/invadopodia
$N^{actinin}$	Number of α-actinin
N^{fascin}	Number of fascin
p_{cr}	Critical load of F-actin bundle

Chapter 1 Introduction

1.1 Research Background and Objectives

Cells are physical objects, which perform their biological activities, such as migration, endocytosis, growth and mitosis, through interacting with extracellular environments by generating, sensing, transmitting and overcoming forces [1-3]. In vivo, cells are exposed to three-dimensional complex mechanical extracellular microenvironments including hydrostatic pressure, shear stress, compressive stress and tensile stress [3-7]. Cytoskeleton is the dominant player of cell mechanical behaviours [8]. It not only provides mechanical support and regulates morphology of cells, but also generates forces for cell biological functions. In eukaryotic cells, there are mainly three types of cytoskeletal biopolymers, namely, actin filaments, microtubules and intermediate filaments [1, 9, 10]. They are assisted by various binding proteins organizing into different kinds of networks, such as branched actin networks, crosslinked actin networks and parallel actin bundles [9]. These actin networks' mechanical properties and interactions with extracellular matrix determine cell behaviours, regulate cell differentiation, modulate cell fate and function and direct tissue development [1, 5, 7, 9].

Migration is one of the most important fundamental function of cells. It involves in many physiological and pathological processes, such as embryonic morphogenesis, wound healing, cancer metastasis, tissue renewal and autoimmune disorders [2, 9, 11]. There are mainly two kinds of cytoskeletal networks driving cell migration [9]. The first one is the branched actin network, which is a sheet-like structure and exists in lamellipodia. The second one is filopodial/invadopodial filamentous actin (F-actin) bundle, which is a finger-like structure and exist in filopodia and invadopodia. They not only generate propulsive forces by actin

polymerizations but also provide crucial mechanical supports for propelling cells migration through extracellular matrix or adjacent cells [2, 12, 13]. Thus, the elastic properties of these actin filament networks largely determine whether cells can overcome extracellular barriers and split a channel in the confining extracellular microenvironment to migrate through [2, 14, 15]. In addition, when cells migrate in three-dimensional heterogeneous and complex extracellular microenvironments, these actin filament networks also provide significant mechanical sensations and navigate cell migratory paths [16-18]. However, even though extensive experimental studies have been performed, the elastic properties of these actin networks and the underlying fundamental physical mechanism controlling cell migration remain poorly understood [15, 17, 19]. The major challenge for studying them is that, during cell migration, these in vivo actin networks are in highly dynamic and self-assembling stochastic states by remodelling with various intracellular proteins and sensitively interacting with variable extracellular microenvironments. To reveal the physical mechanisms of cell migration, the macroscopic cell migration behaviours and the microscopic elastic properties of these assembling and disassembling actin networks should be probed simultaneously.

Recently, biological scientists jointly appeal for building predictive spatiotemporal cell models to open new dimensions in biological research [20]. Constructing predictive models at the intersection of biology, mathematics, physics and computer science is an important way to perform quantitative analysis and elucidate the underlying mechanisms of complicated biological questions [20-22]. In this research, by constructing the spatial and temporal models of the branched actin network in lamellipodia and the F-actin bundle in filopodia/invadopodia, the underlying biophysical mechanisms of cell migration and how migrating cells sense and adapt to mechanically heterogeneous extracellular microenvironments are studied.

The main objectives and contributions of this research consist of the following five parts, which are demonstrated in five chapters (Chapter 3-7), respectively. They are:

1. Develop codes to construct the continuum mechanics-based three-dimensional self-assembling spatiotemporal model of the lamellipodial branched actin network. In this model, key intracellular proteins and their stochastic assembling reactions are realistically considered. The microscopic geometrical properties of lamellipodial branched actin network regulated by each individual proteins during cell migration can be obtained. The relationships between the self-assembling densities of actin filaments, Arp2/3 complex and crosslinking proteins are also investigated.

2. Study the elastic properties of the lamellipodial branded actin network with finite element method (FEM). Demonstrate the mechanical roles of individual intracellular proteins in regulating the elastic properties of the self-assembling network during cell migration. Reveal the intracellular regulatory physical mechanism of how the lamellipodial branched actin network support cell migration through heterogeneous mechanical extracellular microenvironments.

3. Propose a theoretical ‘bending-straightening elastic ratchet’ (BSER) model based on geometric nonlinear deformation of continuum solid mechanics to explain how migrating cells propel their leading-edge (LE) membranes to protrude in extracellular microenvironments. Develop the self-assembling spatiotemporal mathematical model of the polymerizing lamellipodial branched actin filaments powering the LE protrusion under heterogeneous extracellular microenvironment. This mathematical model systematically encompasses the highly dynamic actin polymerization, capping protein inhabiting filament growth, large-scale deformation of actin filaments, curved LE membrane, deformation dependent Arp2/3 complex branch nucleation, breaking of molecular linkers and varying immediate extracellular resistance.

4. By applying the theoretical BSER model to the spatiotemporal protruding model, perform large-scale numerical simulations to realistically simulate the polymerizing and self-assembling lamellipodial branched actin filaments driving the LEs of migrating cells to protrude in different extracellular mechanical microenvironments, and study LEs' the spatial and temporal protruding behaviours. Predict cell migration behaviours and reveal the underlying fundamental biophysical mechanisms of how migrating cells sense and adapt propulsive force and the migratory path to extracellular microenvironments.
5. Construct the continuum mechanics-based three-dimensional model of F-actin bundle in filopodia and invadopodia. The initial undulated geometries of actin filaments and crosslinking proteins induced by thermal excited bending motions are carefully considered. Investigate the elastic properties of the filopodial/invadopodial F-actin bundles regulated by actin filaments and crosslinking proteins. Explore the why invadopodia and filopodia are important for invasive metastatic cancer cells and why filopodia are required for neurogenesis in cortical neurons. Decipher the significant complementary functions of filopodial/invadopodial F-actin bundles and lamellipodial branched actin networks on cell migration.

1.2 Thesis Organization

This thesis is organized as follows:

Chapter 1 gives brief introductions of the research backgrounds, objectives, methods and organization of this research.

Chapter 2 presents a literature review of intracellular proteins, lamellipodial branched actin network, F-actin bundles in and their mechanical roles in cell migration. The most challenging questions regarding cell migrations at present are also illustrated.

Chapter 3 demonstrates the procedure for developing the three-dimensional self-assembling spatiotemporal model of lamellipodial branched actin network by considering key intercellular proteins and their stochastic binding reactions. It also shows the periodic boundary conditions applied to the representative volume element (RVE) model.

Chapter 4 investigates the elastic properties of the lamellipodial branched actin network with FEM based on the model developed in Chapter 3. The mechanical roles of intracellular proteins in cell migration are analysed and the underlying physical mechanisms of published experimental results are revealed. A physical mechanism that lamellipodial branched actin network adapts to varying external loads for supporting cell migration in heterogeneous extracellular microenvironments is deciphered.

Chapter 5 proposes a theoretical 'bending-straightening elastic ratchet' (BSER) model to explain the LE membrane of migrating cells protruding in extracellular microenvironments. Then, the spatial and temporal lamellipodial protruding model of migrating cells is developed in this chapter.

Chapter 6 performs large-scale simulations of lamellipodium protruding in heterogeneous extracellular mechanical microenvironments with the spatiotemporal model in Chapter 5 by applying the theoretical BSER model. Cell migration behaviours reported by published experimental results are predicted. Two fundamental biophysical mechanisms of how migrating cells sense and adapt their propulsive force to the heterogeneous extracellular microenvironment and how migrating cells navigate their migratory paths in the heterogeneous extracellular microenvironment are revealed, respectively.

Chapter 7 introduces the procedure for constructing the filopodial/invadopodial F-actin bundle model and investigate its elastic properties with FEM. The roles of intracellular proteins in regulating the F-actin bundle stiffness are quantitatively delineated. In addition, the importance of F-actin bundle for invasive behaviours of

cancer cells and neuritogenesis of neurons is analysed. This chapter also demonstrates how filopodial/invadopodial F-actin bundle and lamellipodial actin network complementarily drive cell migration.

Chapter 8 summarizes the main conclusions of the biophysical mechanisms underlying cell migration obtained in this research. Additionally, this chapter also presents research limitations and recommendations for future research work.

Chapter 2 Literature Review

2.1 Biopolymers

Cytoskeleton composed of different kinds of biopolymers provides the mechanical supports, generates forces and regulates morphological features of cells. In eukaryotic cells, as shown in Fig. 2.1, there are mainly three kinds of cytoskeletal biopolymers, which are actin filaments, microtubules and intermediate filaments [1, 9, 10]. They are assisted by various binding proteins organizing into different kinds of cytoskeletal networks, whose mechanical properties and interactions with extracellular matrix determine cell behaviours, modulate cell fate and direct tissue development and postnatal function [3-7, 17, 18].

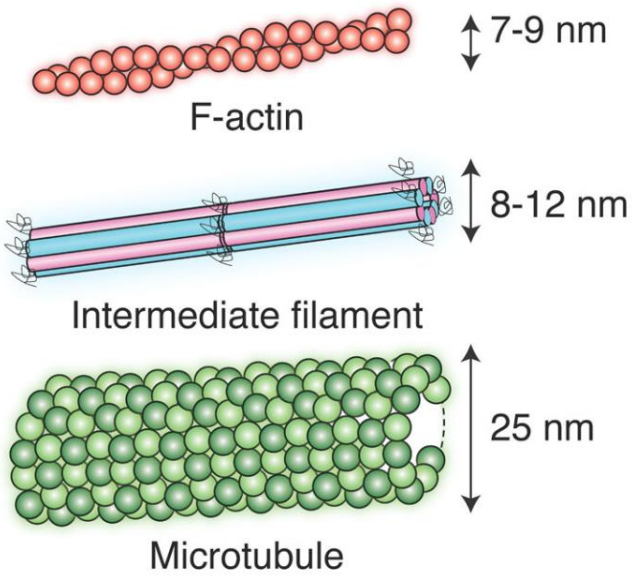

Figure 2.1 Actin filament, intermediate filament and microtubule and their diameters [23].

2.1.1 Actin filament

Actin filaments are double-stranded helical twists with diameters of 7~9 nm [9] , as shown in Fig. 2.1. They grow by adding actin monomers to their ends, i.e., actin polymerization [24]. Actin filaments are polar polymers and have two ends, which are named barbed end and pointed end. The barbed end is much more active in actin polymerization and thus its elongation rate is 10 times faster than that of the pointed end [25]. By connecting with various cross-linkers, actin filaments highly organize into different kinds of networks, such as isotropic crosslinked actin networks, bundled actin networks and branched actin networks, and greatly promote the stiffness of cells. In different kinds of networks, they exhibit different lengths, ranging from several decades nanometres to more than ten micrometres, in order to conduct different biological function. Organized networks of actin filaments determine cell stiffness and transmit force during mechanotransduction, cytokinesis, cell motility and other cellular shape changes [1, 8, 9].

The bending stiffness of actin filaments can be described by the ratio relationship between their contour length L_c and persistence length L_p [26]. The contour length is the length of completely extended actin filaments. The persistence length is defined as the length over which actin filament are undulated under thermal fluctuations and it reflects the flexibility of a material [23, 26]. When the contour length is much larger than the persistence length, actin filaments are flexible and their deformations under forces are mainly due to conformational changes. However, when the contour length is much shorter than the persistence length, actin filaments are very stiff and their deformations are because of the straining of molecular links from equilibrium state [26]. In cells, actin filaments are regarded as semiflexible because their contour length (0.1~10 μm) [27] is comparable to their persistence length (3~17 μm) such that its bending stiffness favors a straight conformation and can just outcompete the entropic tendency of a chain to crumple

up into a random coil [23, 28-30]. The experimental measurements show that Young's modulus of actin filaments is about 1-2 GPa [23, 31] and its viscoelasticity is negligible in millisecond time range [31].

Table 2-1 Dimensions and persistence lengths of cellular biopolymers [23]

Type	Approximate diameter	Persistence length	Contour length
Microtubule	~25 nm	~1-5 mm	10s of μm
Actin filament	7-9 nm	3-17 μm	≤ 20 μm
Intermediate filament	8-12 nm	0.2-1 μm	2-10 μm
DNA	2 nm	50 nm	≤ 1 m

2.1.2 Microtubule

As shown in Fig. 2.1, the diameters of microtubules are about 25 nm [23]. They are stiffest among the three types intracellular biopolymers and their persistence length are about 5 mm [32]. Therefore, microtubules can serve as linear tracks for intracellular traffics [32]. The assembly and disassembly dynamics of microtubules are very complex. They can abruptly switch between periods of growth and shrinkage to meet cell functions [33-35].

2.1.3 Intermediate filament

Intermediate filament derives its name because of its diameter (Fig. 2.1), which is an intermediate size between the diameters of actin filaments and microtubule [36]. It is the most flexible among the three kinds of intracellular biopolymers. In cells, intermediate filaments are much more effective to resist tensile force than compressive force [1]. They can be crosslinked with each other or with actin filaments and microtubules by crosslinking proteins to form networks [37]. Many cell types assemble intermediate filaments in response to mechanical stresses, for

example, airway epithelial cells, in which keratin intermediate filaments form a network that helps cells to resist shear stress [38]. One class of widely expressed intermediate filament, consisting of polymerized nuclear laminas, contributes to the mechanical integrity of the eukaryotic nucleus, and phosphorylation of nuclear laminas by cyclin-dependent kinases helps trigger nuclear-envelope breakdown at the beginning of mitosis [39]. Unlike microtubules and actin filaments, intermediate filaments are not polarized and cannot support directional movement of molecular motors [40].

2.2 Actin binding proteins

There are various types of actin-binding proteins in cells [41]. They bind on actin filaments, intermediate filaments and microtubules to connect them together forming different cytoskeletal networks or regulate their dynamic behaviours. However, in this thesis, only Arp2/3 complex, filamin-A, α-actinin, fascin and capping protein, which participate in building the actin networks for cell migration, are introduced.

2.2.1 Arp2/3 complex

Arp2/3 complex (actin-related proteins) has been discovered for 27 years [42]. As shown in Fig. 2.2 (a), its main function is to initiate a new daughter actin filament by an angle of ~70° from an existing mother actin filament and to form branched filament networks [43, 44], which drives lamellipodia protrusion, vesicle trafficking and pathogen mobility [45]. Malfunction of Arp2/3 complex for generating branched network is closely associated with various kinds of human disease, such as defects in blood-cell function, problems of immunological synapse and cancer cell spreading [46]. The crystal structure of Arp2/3 complex is a flat ellipsoid with a geometrical size of 15nm long, 14nm wide and 7-10 nm thick [47,

48]. The branched junctions created by Arp2/3 complex are relatively rigid under thermal fluctuations [49]. Experimental studies found that Arp2/3 complexes can be classified into two groups, namely Arp2/3high with high-activity subunits and Arp2/3low with low-activity subunits [45]. Arp2/3high displayed low intrinsic stability of branches in vitro, while Arp2/3low generated branches were more stable [45]. Arp2/3 complex is an important actin nucleating molecular machine in eukaryotes [44]. It generates branched actin networks, which play essential roles in cell migrations and bacterium motility (Fig. 2.3 (b) and (c)).

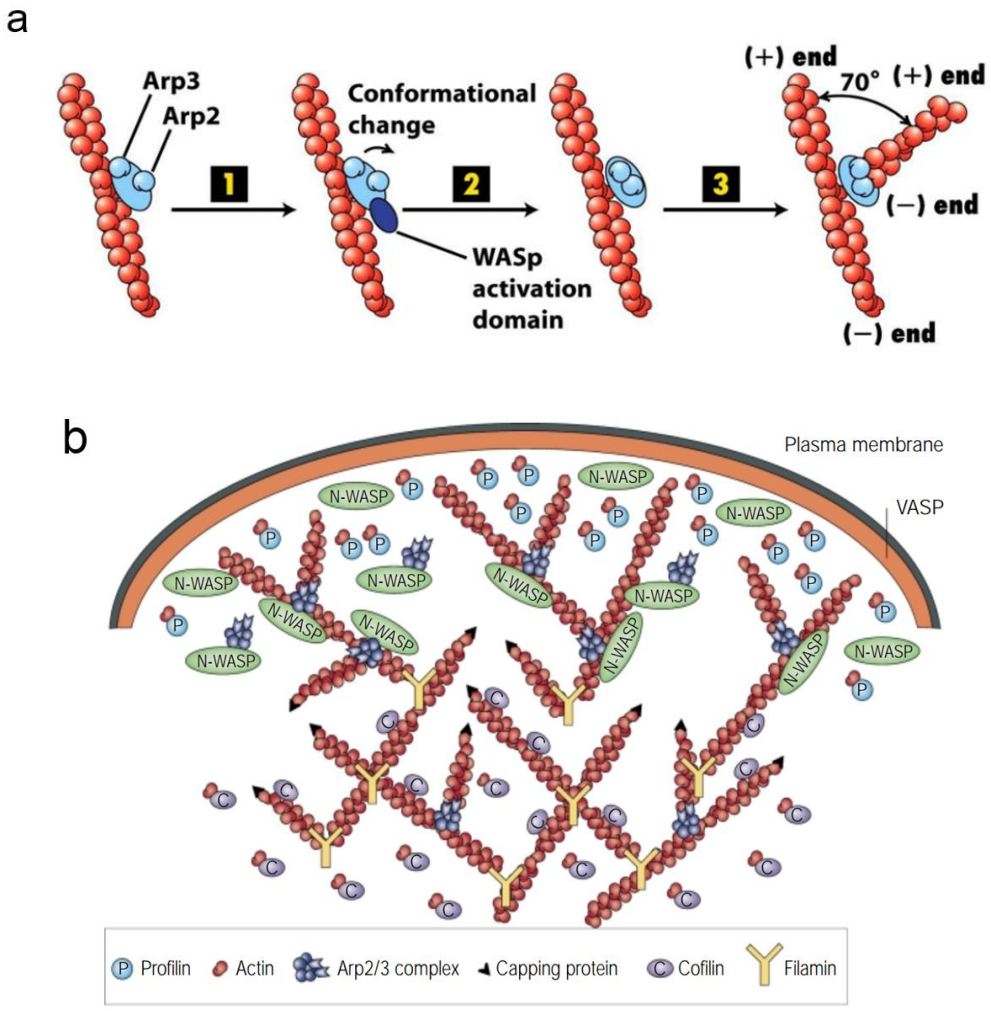

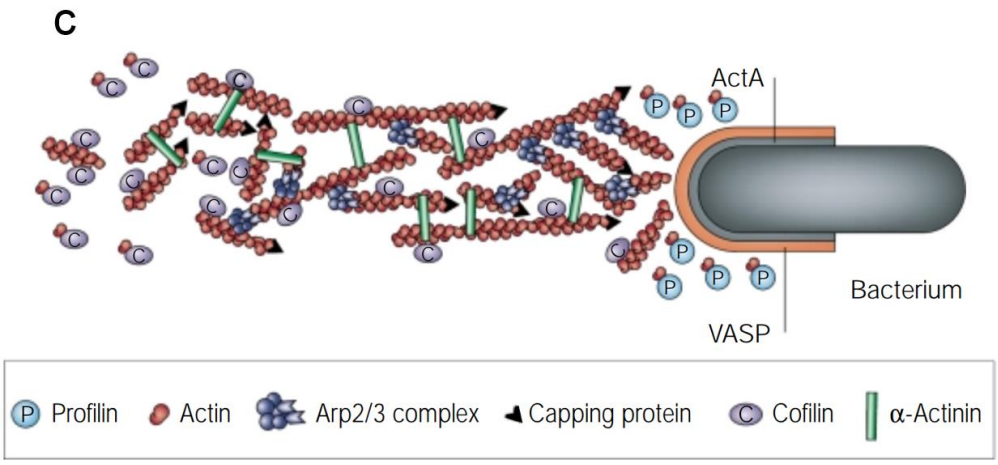

Figure 2.2 Arp2/3 complex generates branched actin filaments. (a) Arp2/3 initiates a new actin filament from an existing one. (b) Lamellipodial branched actin network formed by Arp2/3 complex for cell motility [50]. (c) Branched actin network generated by Arp2/3 complex for bacterium movement [50].

2.2.2 Filamin-A

Filamin was purified in 1975 as the first non-muscle actin-binding protein and it plays a significant role in cytoskeleton by crosslinking actin filaments into networks [51-53]. As shown in Fig. 2.2b, filamin-A cooperates with Arp2/3 complex and α-actinin to form the branched network and stabilize it in lamellipodia. As presented in Fig. 2.3 a-c, filamin-A comprises of two 289kDa subunits that self-associate to form a ~160 nm long semi-flexible strand. Each FLN subunit has an N-terminal spectrin-related actin-binding domain (srABD) followed by 24 repeat β-pleated sheet units. Two intervening calpain-sensitive "hinges" separate the repeats into rod 1 (repeats 1–15), rod 2 (repeats 16–23) and the self-association domain (repeat 24) [54, 55]. The angle between the two FLN subunit is 80°~90° and the shortest distance between the two N-terminal srABDs is ~50 nm [51]. The distance between the two rod 2 ends is ~30 nm [52]. Filamin-A crosslinks two nearly orthogonal actin filaments (Fig. 2.3d and e) [51-54, 56, 57]. Rod 1 is flexible and it has two binding domains, namely, ABD and repeat 9-15 (Fig 2.3 b-e). Rod 2 is shorter and more

compact than road 1 and can still bind partners when FLNa attaches to F-actin. Rod 2 domain may be able to unfold and is likely to contribute to the increased elasticity upon large strain [51]. A bending 'hot-spot' is present between rod 1 and rod 2 (hinge 1, H1 in Fig. 2.3b), which contributes to the high elasticity of pre-stressed FLNa/F-actin networks [51, 57]. Flexible rod 1 domains may increase the likelihood of locating filaments to a crosslink [52]. The C-T accounts for rigid crosslinks [51].

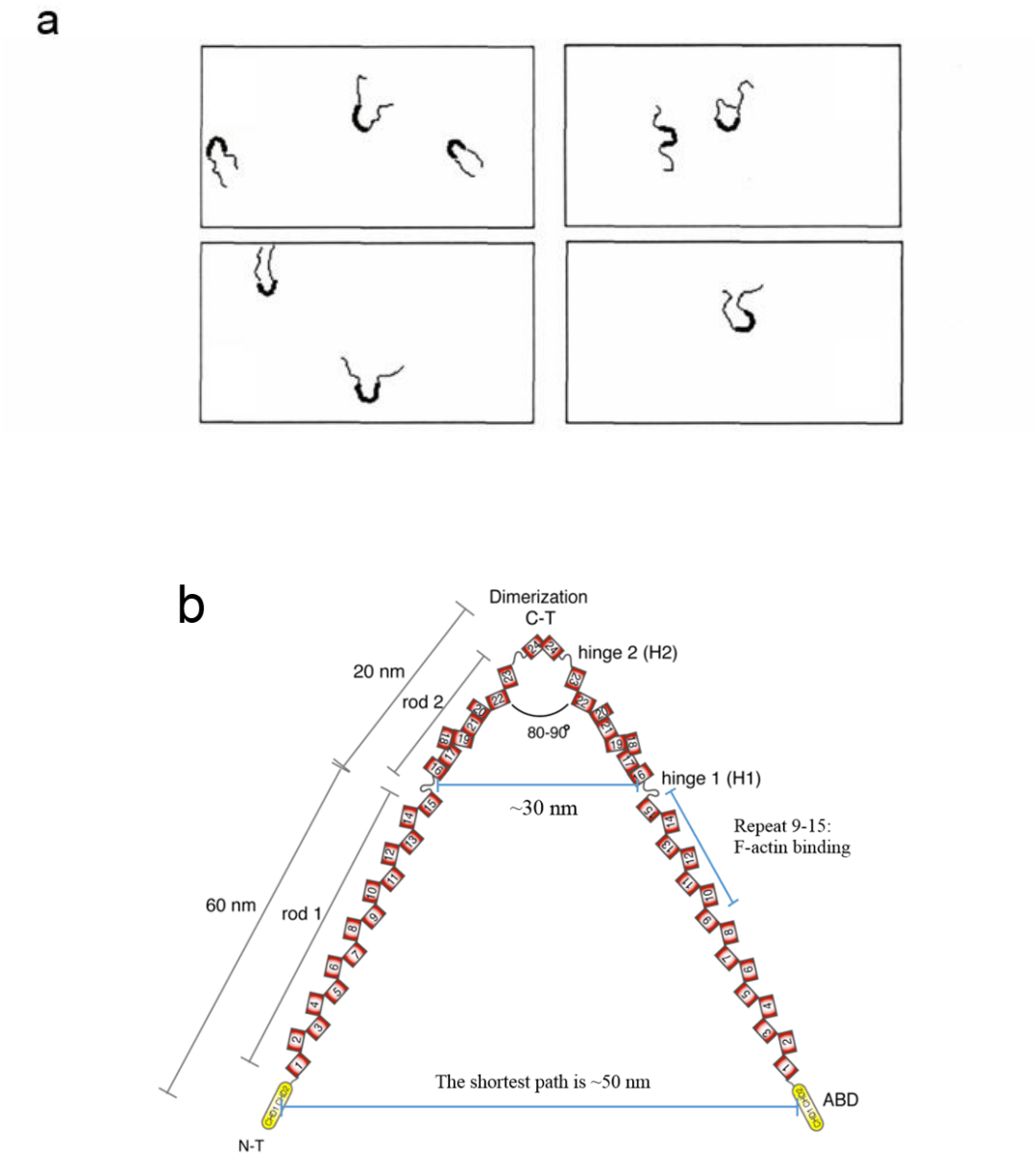

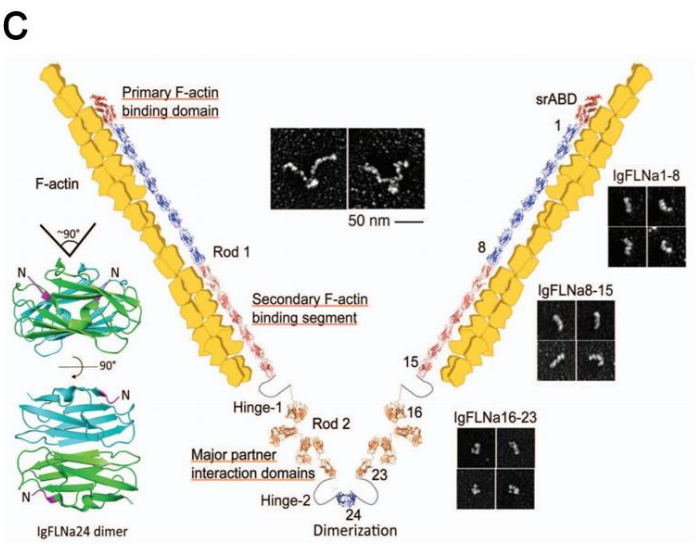
c
Primary F-actin binding domain
srABD
1
F-actin
50 nm
IgFLNa1-8
~90°
Rod 1
8
Secondary F-actin binding segment
IgFLNa8-15
15
Hinge-1
16
Rod 2
IgFLNa16-23
Major partner interaction domains
23
Hinge-2
24
Dimerization
90°
N
N
N
N
IgFLNa24 dimer

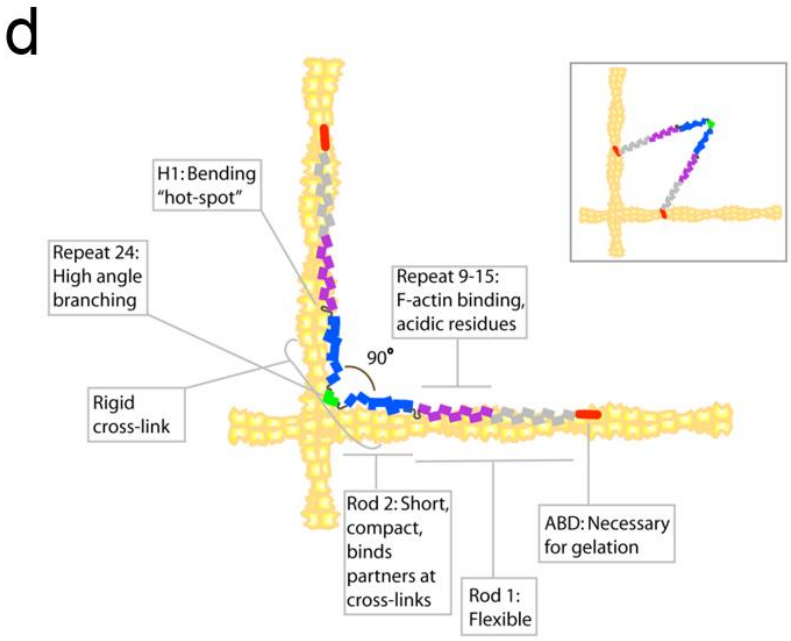
d
H1: Bending "hot-spot"
Repeat 24: High angle branching
Repeat 9-15: F-actin binding, acidic residues
90°
Rigid cross-link
Rod 2: Short, compact, binds partners at cross-links
ABD: Necessary for gelation
Rod 1: Flexible

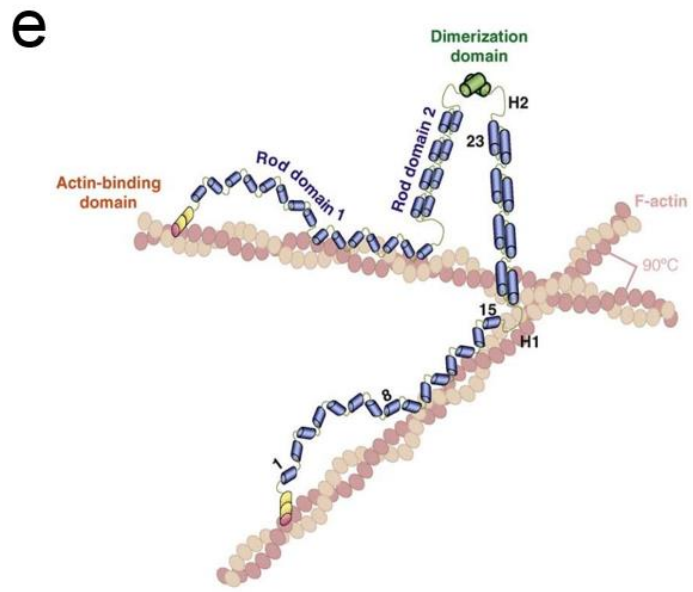

Figure 2.3 Structure of filamin-A and its crosslinking property. (a) Micrographs of filamin-A molecules show a U-shaped self-association region [51, 52]. (b) and (c) Structure of filamin-A and its crosslinking distance [51, 56]. (d) and (e) Filamin-A crosslinking two orthogonal actin filaments [51, 56].

2.2.3 α-actinin

Alpha -actinin is a ubiquitously conserved protein that crosslinks actin filaments and it has 4 isoforms. As shown in Fig.2.4, α-actinin isoforms 1 and 4 in non-muscle and smooth muscle cell connect diverse orientational actin filaments, while isoforms 2 and 3 in skeletal and cardiac muscle cross-link two anti-parallel actin filaments [58-62]. In branched actin filament network, α-actinin connects two parallel branched actin filaments [2, 27, 63]. The total length and diameter of α-actinin rod are 30~35nm and 3~5nm respectively [55, 58-62, 64-66]. α-actinin crosslinkers preferentially oriented at 0°, 60°, 90°, 120°, or 180° and when α-actinin bounds to actin, its length can vary by more than 5.5 nm [62]. Therefore, the connecting distance of actinin is about 24 to 40 nm. Experimental measurements showed that the minimal longitudinal spacing between two adjacent α-actinin along

actin filaments is 31 nm [67]. In addition, the unbinding force between a single actin filament and an α-actinin is in a range of 1.4–97 pN [55, 68]. In experiments, Ehrlicher et al. investigated the effect of binding affinity of α-actinin with actin filament on cellular mechanics and their results showed that increased binding affinity of α-actinin increased the cellular average contractile stress from 1.8 ± 0.7 to 4.7 ± 0.5 kPa [69].

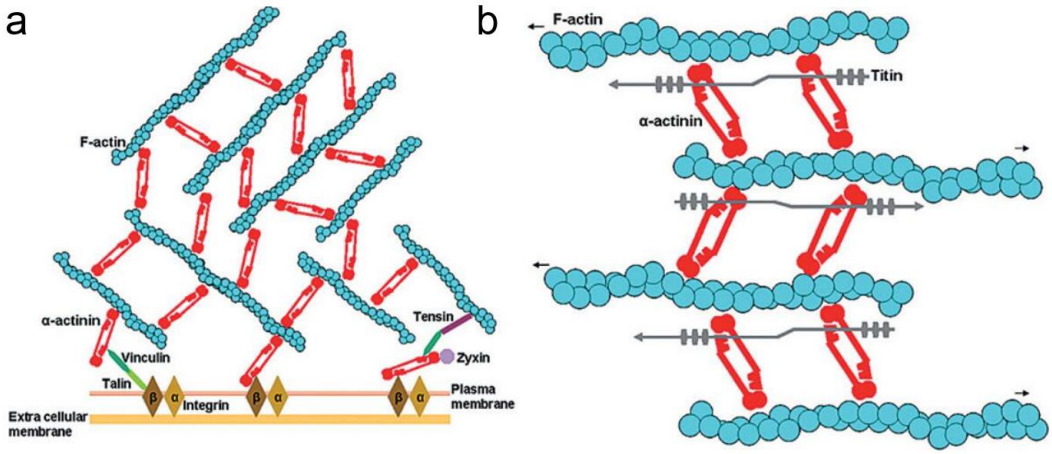

Figure 2.4 α-actinin interactions in focal adhesions and in striated muscle [58]. (a) α-actinin isoforms 1 and 4. (b) α-actinin isoforms 2 and 3.

2.2.4 Fascin

Unlike filamin-A and α-actinin, whose F-actin binding domains are separated by a molecular rod, fascin is a globular protein and has a diameter of 5-8 nm [64]. It uses four tandem β-trefoil domains to bind F-actin [64]. Fascin mainly crosslinks two parallel actin filaments to form F-actin bundles. It localizes in filopodia and invadopodia to facilitate cell migrations and has a similar stiffness of actin filaments [70]. The crosslinking distance of fascin only has 5-15 nm and is much shorter than that of α-actinin [64, 70]. Therefore, in filopodial/invadopodial F-actin bundles, fascin cooperates with α-actinin to generate and strengthen these F-actin bundles [64, 70]. Moreover, fascin also interacts with nuclear envelope protein Nesprin-2 to

promote cell nucleus invading through confined spaces [71, 72]. Collectively, fascin plays a key role in cell migration.

2.2.5 Capping proteins

Capping proteins bind to the growing ends, i.e., barbed ends, of actin filaments to terminate their elongations. In vivo experiments showed that the concentration of capping protein significantly affects cell motility through controlling actin assembling [73]. Thus, capping protein is an important component in the various dynamic actin structures [74]. Capping proteins keep branched actin filaments shorter and denser so that they can provide sufficient mechanical support and propulsive force for pushing cellular membrane forward [9].

2.3 Cytoskeletal actin networks for cell migration

2.3.1 lamellipodial branched actin network

2.3.1.1 Formation of branched actin network and its related biological activities

Branched actin network is created by Arp2/3 complex. Arp2/3 complex binds to an existing actin filament, and then a new filament grows and polymerizes from it [16]. However, this process is extremely complicated, and a great number of proteins participate in it. Pollard et al. proposed a dendritic-nucleation model, which is shown in Fig. 2.5, to illustrate the formation process of the branched network in lamellipodia [10]. In this model, the process of protrusion of lamellipodia generated by the branched network is divided into eleven steps [10]. The above branched actin filament networks activated by the Arp2/3 complex are some independent subnetworks, which are seeded by different primers [9]. Tatyana M. Svitkina et al. found that, even though Arp2/3 complex was the primary binding protein, other

cross-linking proteins, namely α-actinin and filamin-A, also presented in the branched network in lamellipodia [27, 75]. Filamin-A and α- actinin connect these independent subnetworks together and organize them into a highly integrated branched network [2, 76, 77]. Peter Bieling et al. recently studied the stabilization effects of filamin-A and α-actinin on branched actin filament network respectively, and they found both of the crosslinking proteins stiffen the branched actin network [50].

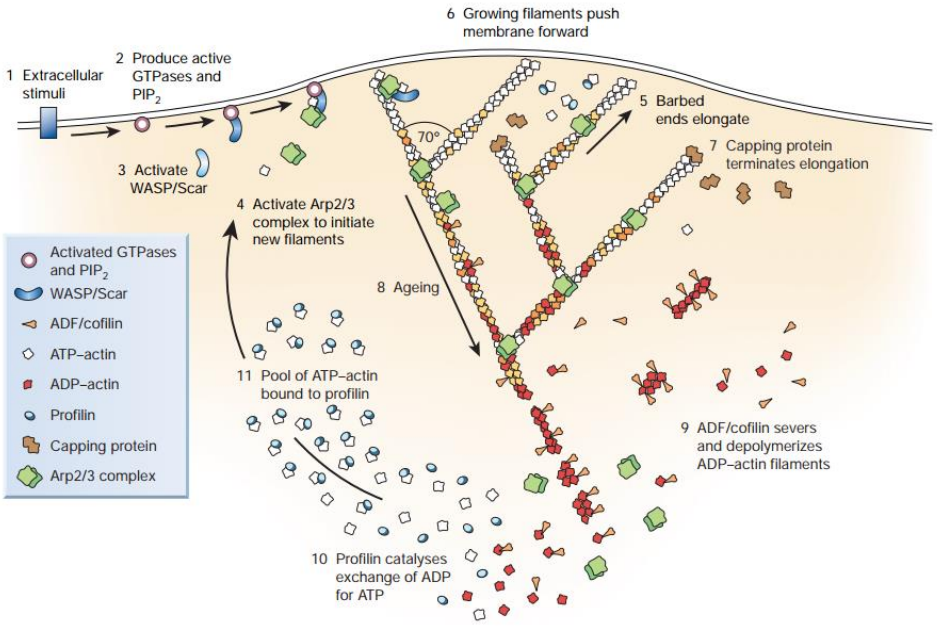

Figure 2.5 The dendritic-nucleation model for protrusion of lamellipodia [10]. The dendritic-nucleation model for protrusion of lamellipodia. External cues (step 1) activate signalling pathways that lead to GTPases (2). These then activate Wiskott–Aldrich syndrome protein (WASP) and related proteins (3), which in turn activate Arp2/3 complex. Arp2/3 complex initiates a new filament as a branch on the side of an existing filament (4). Each new filament grows rapidly (5), fed by a high concentration of profilin-bound actin stored in the cytoplasm, and this pushes the plasma membrane forward (6). Capping protein binds to the growing ends, terminating elongation (7). Actin-depolymerizing factor (ADF)/cofilin then severs and depolymerizes the ADP filaments, mainly in the ‘older regions of the filaments

(8, 9). Profilin re-enters the cycle at this point, promoting dissociation of ADP and binding of ATP to dissociated subunits (10). ATP–actin binds to profilin, refilling the pool of subunits available for assembly (11).

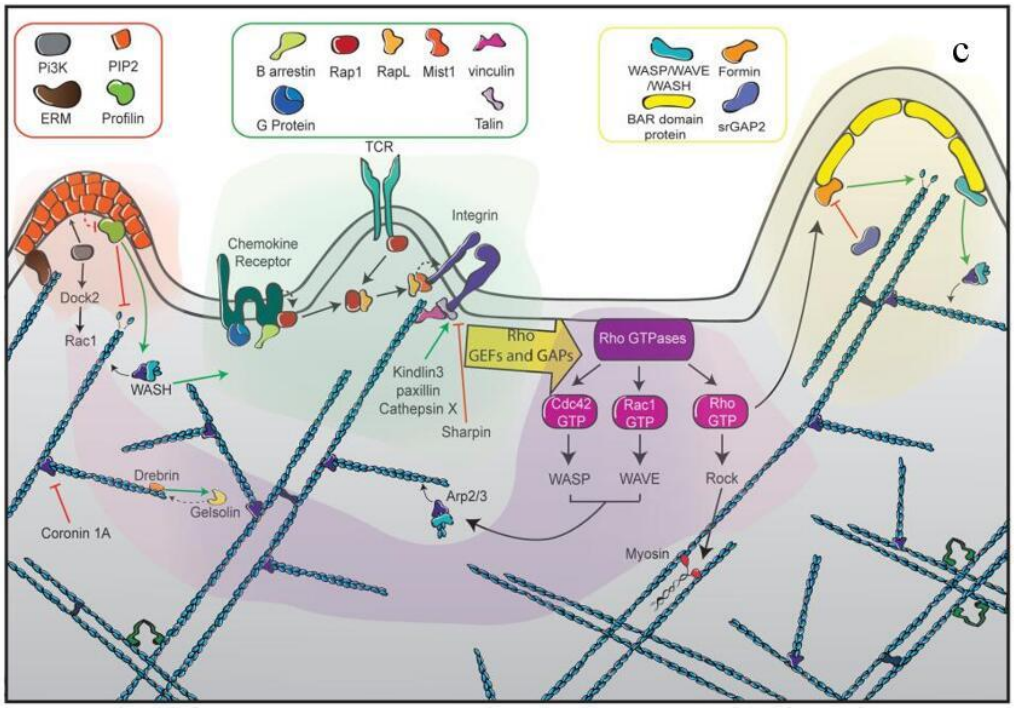

Figure 2.6 Lamellipodial branched actin networks formed by actin filaments, Arp2/3 complex, Filamin-A and α-actinin [63].

The branched actin networks, as shown in Fig. 2.6, are not isotropic, but with most of barbed ends toward one direction. This effect is closely related to the biological functions of branched actin networks in cells. Except for providing mechanical supports, branched actin networks also generate pushing forces by the polymerizations and elongations of their barbed ends. Therefore, they play key roles in cell migrations, endocytosis and propulsions of bacteria through cytoplasm (Fig. 2.7) [8]. The branched actin network forms lamellipodia in cells and its mechanical behaviours determine cellular mobility (Fig. 2.7a), which involves various significant biological processes. For example, immune cells move to capture and destroy pathogens or pathological cell. Cells of animal embryos crawl from one

location in the body to another. Cancer cells spread through the body. Nerve cells grow processes up to 1 m long to find their targets and the formation of spine synapses [8, 78]. When bacteria invade cells, they use cellular proteins to assemble a comet tail (Fig. 2.7b), which is composed of branched filament networks. The polymerizations of actin filaments in the branched network provide propulsion forces for bacteria swimming in cytoplasm. In addition, in the process of endocytosis, the branched network generates force to deform membrane to facilitate substances to enter cells (Fig. 2.7c) [79].

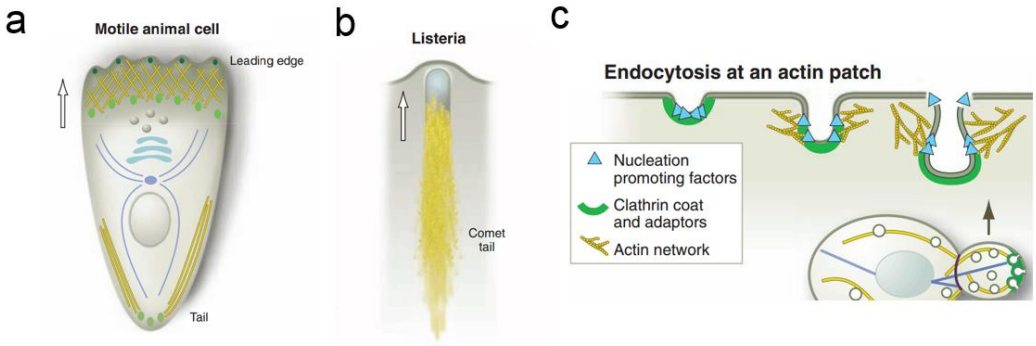

Figure 2.7 Biological functions of branched actin filament network [8]. (a) Cell migration. (b) Motility of bacteria. (c) Endocytosis.

2.3.1.2 Architectures of lamellipodial branched actin network

Lamellipodia is a sheet-like protrusion structure of cells (Fig. 2.8a) and regulates directional cell migration [16, 80]. It is formed by highly branched actin filament network, which is mainly generated by Arp2/3 complex with angles of approximately 70°. The thickness of lamellipodia is normally 0.2 μm [12, 81-87]. The length of lamellipodia, which is in the direction of from leading edge to the nuclear region of cells, is commonly in the range of 7 μm and 18 μm [83]. However, the branched actin filament network exists in the first about 4 μm region from the lamellipodia tip [27, 88]. The width of lamellipodia along the leading edge is in the range of 20~50 μm [85]. Branched actin filament network in lamellipodia provides

significant mechanical support and propulsive force for the movement of cells. Therefore, actin filament length is an important parameter for studying the mechanical properties of the branched network. For example, Mackintosh and Dvid using bulk rheology presented that linear modulus of filament network increased proportional to the square of the actin filaments length [89]. Laurent Blanchoin, et al studied the correlation between filament lengths and the concentrations of proteins for branching and they found filament length was inversely proportional to branch density, namely, with different concentrations of Arp2/3 complex, capping protein and profilin, the lengths of branched actin filament ranged from 0.7μm to 25 μm [49]. Recently, Julien Pernier, et al. investigated the lengths of mother filaments and daughter branches respectively. Most of mother filaments were about 0.8 μm while daughter branches were 2.5 μm [90]. However, these experimental researches about branched filament lengths are all performed in vitro, which has a big disparity in concentrations of proteins with the condition in vivo. Within cells, the typical lengths of filaments range from 100 nm to a few microns while lengths in vitro can be up to 50 μm [91-93]. Consequently, the values of length obtained in vitro can not present the lengths of branched actin filaments in lamellipodia of cells.

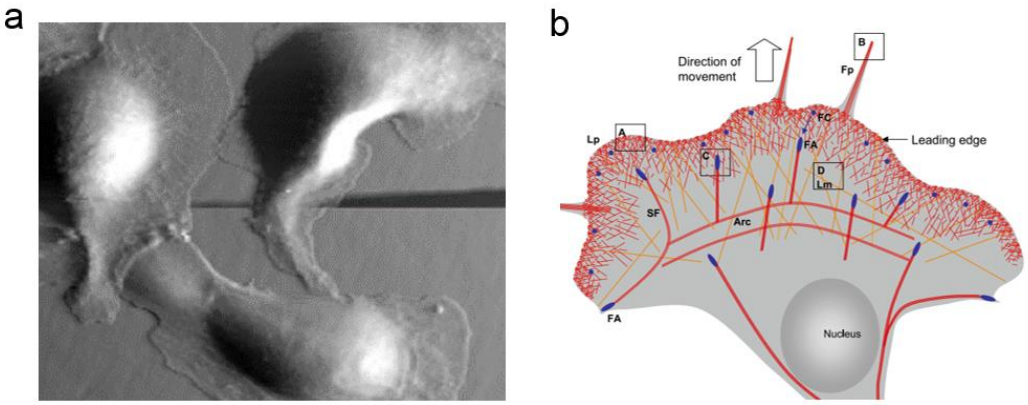

Figure 2.8 Lamellipodia and branched actin network in it for cellular mobility. (a) Sheet-like Lamellipodia of migrating cancer cells [82]. (b) Branched actin network structure in the front part of lamellipodia [94].

In lamellipodia of migrating cells, the lengths of branched actin filaments are influenced by many factors, such as capping proteins, profilins and concentrations of Arp2/3 complex and globular actin in cytoplasm [2]. Thomas D. Pollard and John A. Cooper pointed out that most of the branched filaments are capped by capping proteins before growing longer than 0.5 μm because longer filaments would presumably buckle under force [8]. James E. Bear, et al. investigated the length of branched actin filament in lamellipodia of rat fibroblasts and the values are 50~160 nm (Fig. 2.9a) [95]. Maryse Bailly et al. proposed that filament length at the leading edge ranged from 30 nm to <300 nm (Fig. 2.9b) on the basis of Epidermal Growth Factor Stimulation [96]. Based on theoretical analysis, two simple predictions were made: to grow against membrane resistance, the filaments should be neither too short (filaments shorter than ~70 nm are too rigid to bend enough), nor too long (filaments longer than 500 nm are too soft, so the load would simply buckle them) [97].

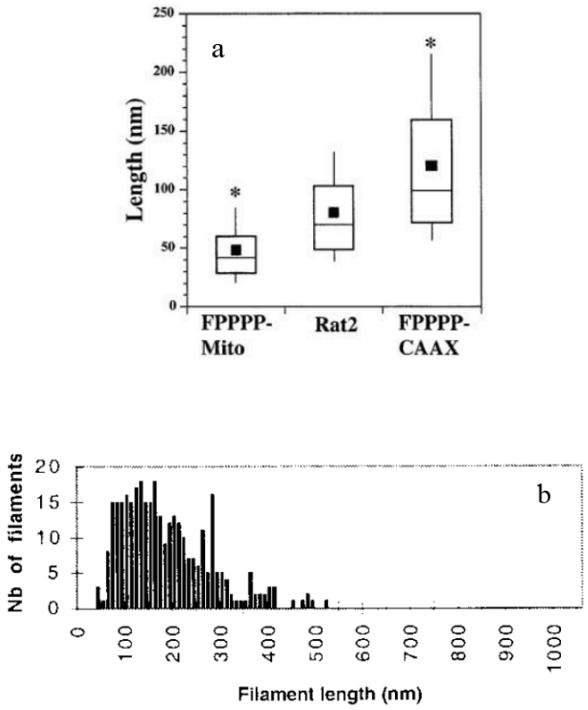

Figure 2.9 Filament length distributions in branched actin network in lamellipodia of migrating cell [95, 96].

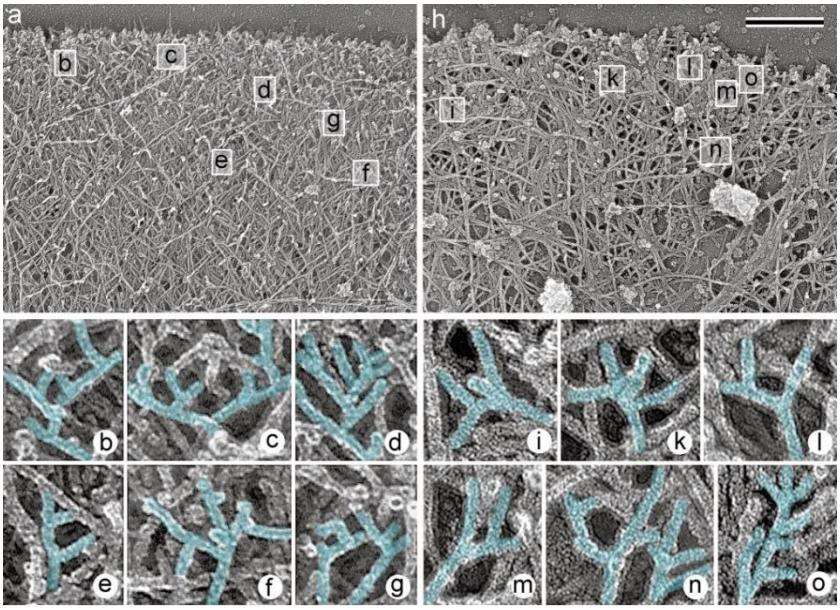

Figure 2.10 Multiple branching of actin filaments in lamellipodia; scale bar: 0.5 μm [27].

On the basis of experiments, Thomas Pujol et al. pointed out that the characteristic length, L, can be chosen as the distance between branching points in the case of branched network and raising the concentration of Arp2/3 in experiments is expected to increase the number of branches and thus decrease length L [98]. The distance between adjacent branching junctions is variable. But most of the branching junctions occurred about 100 nm of each other, which indicated a high probability for branching near the leading edge [12, 27]. The branched angle of actin filaments is determined by Arp2/3 complex, which has an average angle of 67 ± 12º [27, 49, 77, 99, 100]. Tatyana M. Svitkina et al. found that almost all of actin filaments were with barbed end (the fast-growing end) forward in lamellipodia [91]. Using live-cell imaging and electron microscopy, Stefan A. Koestler et al. shown that the angles of actin filaments relative to the leading edge in moving lamellipodia are 15°~90° and that angular shift from protrusion to pause was associated with a proportional increase in filaments oriented more parallel to the leading edge. They proposed the angular transitions of branched actin filaments in lamellipodia serve in adapting to slower protrusion rates

while maintaining the filament densities required for structural support [101]. Branched actin filament density is another fundamental parameter for the mechanical performance of lamellipodia. Using image-based photometry, Vivek C. Abraham et al, obtained F-actin density of 1580 ± 613 μm of F-actin/μm^3, which corresponded to a volume fraction of 5%~10%, in lamellipodia of fibroblasts. They also computed the density of growing actin filament ends at the lamellipodium margin (241 ± 100/μm) and the polymerizing force (1.86 ± 0.83 nN/μm) obtainable via actin assembly [89]. Stefan A. Koestler et al. measured the number of actin filaments along the leading edge of B16 melanoma cells lamellipodia, which was averaged 90 ± 10/μm [102], which is very similar obtained by other researchers [103].

2.3.1.3 Elastic properties of lamellipodial branched actin network and cell migration

Cells are physical objects, which interact with extracellular microenvironments by generating, sensing, transmitting and overcoming forces [2, 9, 104]. Cell migration based on lamellipodium protrusion is a fundamental function in many physiological and pathological processes, e.g., cancer metastasis, embryonic morphogenesis, wound healing, tissue renewal and autoimmune disorders [2, 9, 11]. Although extensive experimental studies have been conducted, cancer cell metastasis until now is still the leading cause of deaths worldwide [18, 105, 106]. The central reason is that a comprehensive and clear description of cell migration mechanism, which can be exploited therapeutically to prevent cancer cell from invading into other tissues or circulating systems, is still lacking [13, 107, 108]. Lamellipodial branched actin network is a sheet-like structure. It not only generates a pushing force by actin polymerization but also provides crucial mechanical support for driving cell migration through extracellular matrix or adjacent cells [2, 12, 13]. Arp2/3 complex nucleates new filaments by an angle of ~70° from pre-existing filaments and creates dendritic subnetworks [49]. These dendritic subnetworks are crosslinked together

by filamin-A and α-actinin forming an interconnected branched actin network (Fig. 2.11) [2, 76, 109, 110]. Cell migrations are largely determined by the mechanical interactions between the lamellipodial branched actin networks and the confining extracellular microenvironments [2, 13, 15]. Previously, much effort has been focused primarily on the mechanical properties of extracellular matrix [15, 104, 111]. However, cell migration is more like an active cellular self-adaptive behaviour [2, 13, 112]. Migrating cells almost never experience mechanically isotropic microenvironments [13, 17, 108]. The underlying intracellular physical mechanisms of how cell self-regulates the elastic properties of the branched actin network to overcome and migrate through the varying 3D extracellular confinement are still unclear.

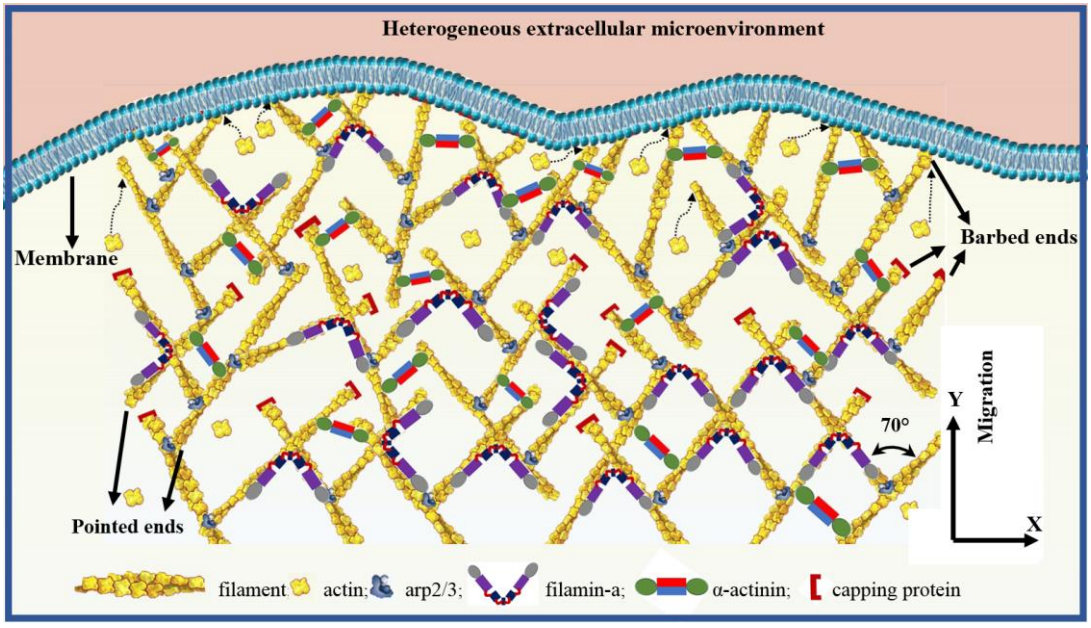

Figure 2.11 Structure of the lamellipodial branched actin network near the leading edge of migrating cells.

The architecture and mechanical properties of branched actin networks are influenced by many factors in cells [113]. Specifically, the concentration of Arp2/3 complex enhances the polymerization rate of actin filaments and concentration of capping protein promotes more frequent filament nucleation by Arp2/3 complex

[114]. The average filament length is determined by the ratio of polymerization rate to the rate of nucleation or capping [2]. Low concentration of capping protein would result in very long filaments and reduce the network stiffness to overcome resisting forces from extracellular environments for cell movements [9, 26, 95, 114]. High concentration of actin monomers improves the volume fraction of branched actin network in lamellipodium and thus may empower cells to have excessive mobility because more filament would produce more resultant propulsion force and support more loads [2, 115, 116]. Experiments also demonstrate that inhibition and flourish of Arp2/3 complex, as well as crosslinking proteins filamin-A and α-actinin [2], can regulate cell migration and result in different trajectories [117-119]. However, the major challenge to investigate the elastic properties of the sheet-like branched actin network is that it is in a highly dynamic and stochastic remodelling state, which involves with various mechano-chemical interactions between different intracellular proteins, such as nucleating, actin polymerizing and depolymerizing, Arp2/3 complex branching, capping protein inhibiting polymerization, crosslinking proteins binding and unbinding [12, 120, 121]. Thus, the network's complexity, stochasticity and highly dynamic biological process hinder one from performing a large number of biological experiments to capture the quantitative relationships between its macroscopic elastic properties and the microscopic structures [122]. To establish such relationships, probing the kinetic architecture of the network assembled or disassembled by different intracellular proteins and measuring its corresponding mechanical properties should be done simultaneously. However, such work is also still lacking.

In addition, experiments revealed that the orientation distribution of actin filaments in the branched actin network is regulated by different magnitudes of extracellular resistance [13, 107]. Maly and Borisy [123] analysed their angles in a keratocyte lamellipodium with platinum replica electron micrograph and showed that most filaments have angles of ±35° to the normal direction of the leading edge. Atilgan et al. [124] and Schaus et al. [125] studied self-organization of filament

orientations in the network with three- and two-dimensional models, respectively. Weichsel and Schwarz [99] modelled the branching of filaments in lamellipodium through stochastic network simulation and deterministic rate equations. They demonstrated that the changes in the growth velocity of the network resulted in a transition between two kinds of filament orientation patterns, with ±35° and ±70°/0° orientation, respectively. Recently, Mueller et al. [13] experimentally studied the relation between the structure of branched actin network and the resisting load. Their results show that higher loads induce a broad angle distribution while lower loads make most filaments growing perpendicularly to the leading edge. Therefore, the orientation pattern of filaments plays a key role in the mechanical behaviours of branched actin networks and in cell motility [107]. Given that the branched actin network provides essential mechanical support for cell migration, such mechanosensitive orientation changes may be related to the mechanical adaptability for cell migration. However, the underlying physical mechanism of the architecture transitions induced by different extracellular resistances remains an open question.

Some researchers studied the mechanical properties of lamellipodia. Valerie M. et al. investigated the elastic property of lamellipodia of migrating keratocytes by atomic force microscopy (AFM) and estimated the apparent stiffness of the leading edge at 10-55 kPa [85]. Christian Rotschth, et al. also found this phenomenon and elastic modulus decreased from ~12 kPa to ~5 kPa from the leading edge to the region of 5μm from the leading edge in their experiments [87]. This gradient of rigidity in lamellipodia from the leading edge to back region is closely related with the distribution of the density and structure of actin filament in lamellipodia [87, 91, 126, 127]. The big difference in the values of elastic modulus obtained by Valerie M. and Christian Rotschth using the same method AFM may be resulted from the different actin filament densities between different types of cells. Mahaffy et al. experimentally determined Poisson ratio of ~0.4 to 0.5 in a very thin regions relatively near the edge of lamellipodia of NIH 3T3 fibroblasts [128].

Branched actin filament networks of lamellipodia provides crucial mechanical supports for cell motility to overcome the stall forces from extracellular environments [2, 26, 98]. Therefore, their mechanical properties are strongly associated with many physiological and pathological processes, such as embryonic development and tissue renewal, metastatic cancer and autoimmune disorders [16, 117, 119, 129, 130]. Laurent et al. [49] experimentally discovered that branches created by Arp2/3 complex are relatively rigid. Chaudhuri et al. [26], Pujol et al. [98] and Kawska et al. [131] studied the mechanical behaviours of branched actin network in vitro experiments. Bieling et al. [2] also experimentally investigated the mechanical response of branched actin networks, in which the crosslinking proteins, filamin-A and α-actinin were taken into account. They consistently concluded that the branched actin network, compared with crosslinked actin networks, has much larger elastic modulus and can bear much higher compressive loads. Recently, Boujemaa-Paterski et al. [113] demonstrated that cells can regulate the rate and direction of their migration by tuning the concentration of actin filaments and the architecture of the network in lamellipodia. Whereas several in vitro experiments measured Young's modulus in the growing direction of the branched actin networks [2, 26, 98, 131], the architectures of their in vitro networks and their boundary conditions might be very different from those of the sheet-like lamellipodia in live migrating cells. More importantly, the elastic properties of the 3D branched actin network contain several independent elastic parameters, i.e., its Young's moduli and Poission's ratios are different in different directions. Cell migration is in a complex 3D highly heterogeneous microenvironment in living tissues [19]. Measuring only one Young's modulus in experiments is far from understanding the elastic properties of the network, let alone studying their interplays with the microenvironment. To decipher the mechanical mechanism of how migrating cells overcome 3D extracellular confinements, it is essential to obtain sufficient mechanical parameters of the branched actin networks and then to analyse their impacts on cell migration.

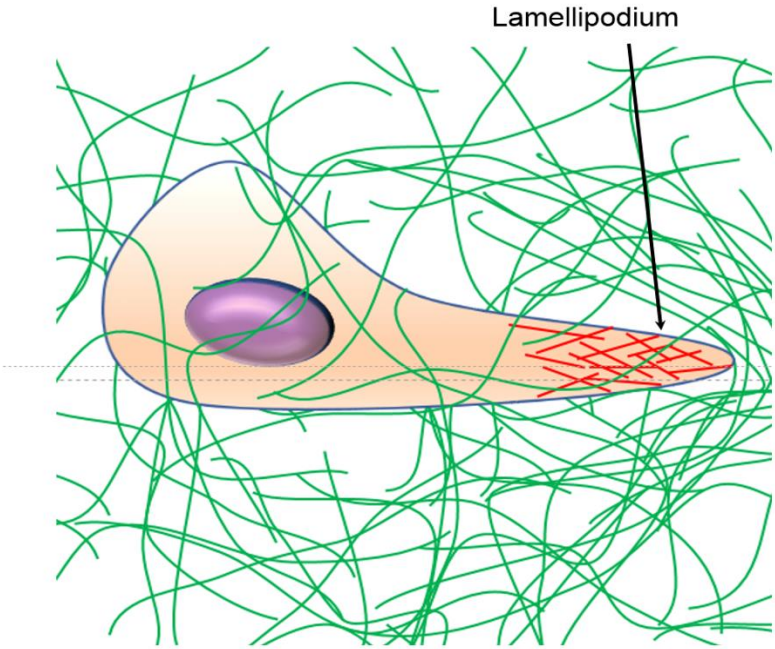

Figure 2.13 Lamellipodium drives cell migration through confining extracellular microenvironments.

2.3.2 Actin-based cell migration model at the leading edge

The actin-based lamellipodial sheet-like protrusion is the most common powering system of cell migration [2, 132]. When cells migrate, lamellipodia protrude into extracellular matrix to sense the mechanical environments and split a sufficient wide channel for the cell to migrate through [15]. In lamellipodia, self-assembling branched actin filaments polymerize and thus generate intracellular force pushing leading edge (LE) membrane to move forward [12, 133]. At the same time, Arp2/3 complexes bind on pre-existing filaments and nucleate new filaments [12, 13], which will generate new propulsive forces propelling the LE membrane [12]. With the LE membrane protruding forward, the earlier formed branched filaments leave the LE membrane and organize into branched actin networks with crosslinking proteins. The network will provide significant mechanical supports for the front polymerizing free actin filament ends pushing the LE membrane [2, 13, 26]. For

both the normal and invasive cell migrations, the LE protrusion is essentially determined by the physical interaction between the polymerizing branched actin filaments and the confining extracellular microenvironment they encountered [11, 19, 104, 133-136]. Only when the three-dimensional lamellipodial LE protrudes into extracellular microenvironment and squeezes a sufficient wide channel, can cell successfully migrate in vivo [15, 134]. However, the LE protrusion is an extremely complicated coordinating process involving with highly dynamic interplays between polymerizing filaments, curved LE membrane, Arp2/3 complex branch nucleation, breaking of molecular linkers and high varying extracellular resistance [19, 137, 138].

Actin polymerization pushing cell membrane forward in lamellipodia has received intense theoretical and numerical analysis. Peskin and his colleagues firstly formulated a Brownian ratchet (BR) model, in which an infinitely stiff actin filament could rectify the Brownian motions of actin monomers and add them to its growing tip producing axial force[139]. On the basis of this BR model, Mogilner and Oster proposed an elastic Brownian ratchet model (EBR) by including the elasticity of actin filaments, which is realized by transforming an inclined actin filament to a spring with an effective spring constant [140]. Maly and Borisy developed a two-dimensional population-kinetics model incorporating branching and capping events based on actin filament orientations [123]. Schaus and his colleagues further developed this model by taking account of the elastic properties of membrane and actin filaments, which were regarded as straight rods[125]. Weichsel and Schwarz adopted two-dimensional stochastic network simulation and deterministic rate equations to describe the growing of branched actin network, in which branching reaction was independent of other factors and the side of mother filament from which the new filament grows was randomly selected [99]. Schreiber and his colleagues constructed a three-dimensional model, where orientations of actin filaments and branching reaction were randomly generated, to describe the actin-based cell motility by considering excluded volume effect [141]. However,

despite existing 2D or 3D models, such as the well-known 'elastic Brownian racket' model [140] and the 'tethered ratchet' model [142], were proposed to study the force-velocity relationships of the growing branched actin filaments pushing LE membrane or the self-organization of branched actin network [99, 125, 140-143], they fail to predict the important protruding behaviours [14]. For example, branched actin filament density in lamellipodia is regulated by varying magnitude of immediate extracellular resistance [2, 13]. In addition, the protruding velocity of polymerizing branched actin filaments is loading history-dependent, namely, when the resisting load increases to a high value and then abruptly decreases to a low value, the protruding velocity will be suddenly improved and much larger than the previous velocity [144]. The central reason is that they either treat actin filaments as rigid rods or are based on small deformation theory of continuum mechanics and ignore the 3D mechanical interactions between the polymerizing free barbed ends of actin filaments and the bent LE membrane. Experiments demonstrate that polymerizing branched actin filaments are subjected to large deformations and even buckle under stall force (Fig. 2.13) [2, 26, 145]. Moreover, the LE membrane is also bent by the polymerizing propulsive force [132]. The 3D mechanical interaction between the bent actin filaments and curved LE membrane largely determines the underlying physical mechanism of actin-based LE protrusion of migrating cells. Furthermore, pioneering experiments revealed that Arp2/3 complex prefers to bind on the convex sides of bent filaments and the branching density is closely related with the curvature of actin filaments [146]. Without considering this mechano-chemical reaction triggered by filament deformation, even though existing models in refs. [99, 125, 140, 142, 143] showed the self-organized orientation of actin filaments, they realized this by pre-constraining Arp2/3 complex branching orientation with referring to cell migration direction. Thus, they cannot present the realistic self-organizing biological process of branched actin filament network during cell migration. Consequently, an adequate theoretical model both revealing the exact underlying biophysical mechanism of filaments pushing membrane

forward from a molecular level and demonstrating the realistic self-assembling process of the lamellipodial branched actin network is still missing.

Table 2-2 Published models and their predictions about the actin-based protrusion behaviours.

Model	Assumption or theory	outcomes	Actin-based protrusion behaviours				
			Filament density is regulated by resistance [2, 13]	Protrusion velocity depends on loading history [144]	Adapt propulsive force and bypass obstacles [134]	Saltatory motion [147]	Assembly of branched actin network [2]
Brownian ratchet model [139]	Filaments were stiff	Generate protrusive forces	×	×	×	×	×
Elastic Brownian ratchet model [140]	Small deformation theory of mechanics	Generate protrusive forces	×	×	×	×	√ (but not self-assembly)
Tethered ratchet model [142, 143]	Small deformation theory of mechanics; considers attachment force	Generate protrusive forces; saltatory protrusion	×	×	×	√	√ (but not self-assembly)
Dendritic-nucleation/array-treadmilling model [99, 125]	Filaments were straight; branching randomly happens	Self-organization of filament orientation patterns	×	×	×	×	√ (but not self-assembly)
Stochastic simulation of actin polymerization [141]	Filaments were rigid rod; excluded volume effects	swelling of cytoskeleton contributes to lamellipod protrusion	×	×	×	×	×

√ denotes successfully predicts the behaviour. × denotes that the model can not predict the behaviour.

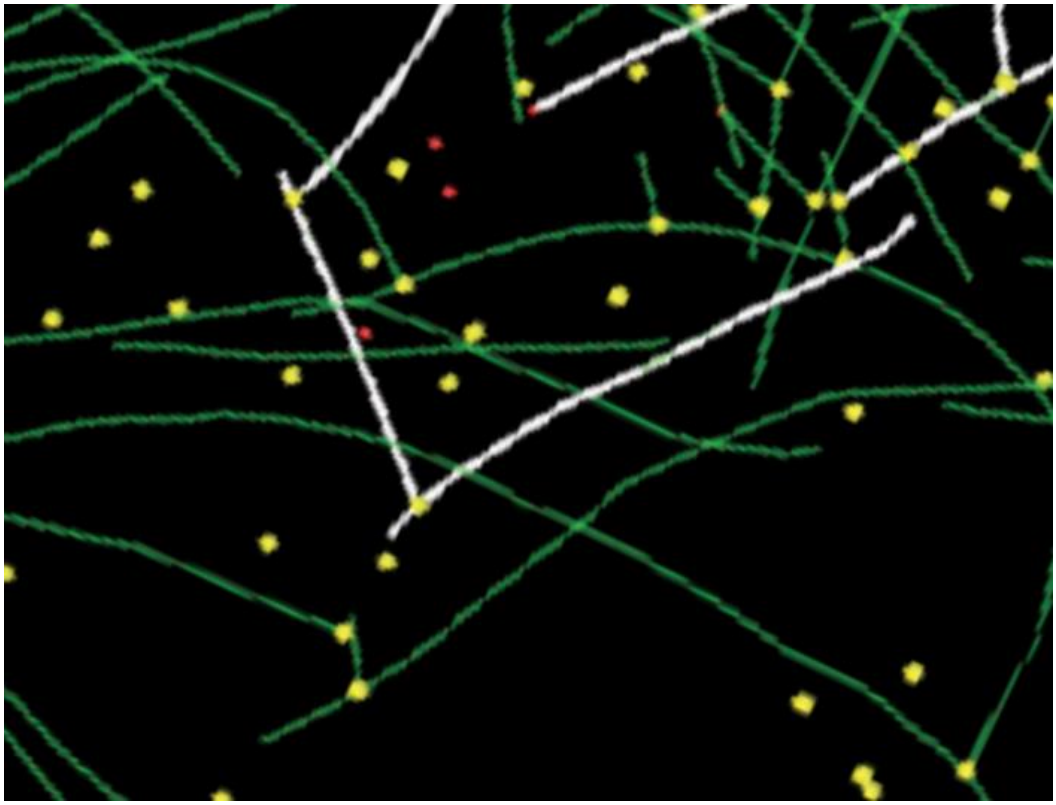

Figure 2.13 Large bending deformation of branched actin filaments at the leading edge of lamellipodium from published experimental tomogram [145].

More importantly, extracellular microenvironments are usually extremely heterogeneous and in highly dynamic states [17]. Recently, experimental study shows that cell predominantly migrates along the path of least resistance [134]. Thus, at the LEs, migrating cells have to be able to mechanically sense the extracellular microenvironments and then accordingly adapt their propulsive forces to overcome the resistances or even steer their migratory paths to circumnavigate high resistance areas in the extracellular microenvironments [2, 13, 113, 134]. However, the physical mechanisms underlying these versatile migrating behaviours are still poorly understood. And a theoretical model, which can predict migrating cells sensing, adapting propulsive force and steering migratory paths in highly varying extracellular mechanical environments, remains an outstanding challenge.

2.3.3 Filopodial/invadopodial F-actin bundle and cell migration

Filopodia and invadopodia protrusions are another two types of actin-based cell migration [66]. Filopodia are transient and extend out from the protruding lamellipodia of migrating cells, while invadopodia are more stable, localize beneath the cell body and possess extracellular matrix-degrading proteases [148-150]. Although they are different in localizations of a cell body and substrate degradation, their molecular machinery, which are responsible for generating filopodia and invadopodia, are very similar [151]. Both filopodia and invadopodia are long, thin and finger-like F-actin bundles (Fig. 2.14), which comprise of parallel actin filaments and crosslinking proteins, such as fascin and α-actinin [64, 151, 152]. Experiments show that filopodia and invadopodia are actively generated in invasive cancer cells [104, 152] and abundant them is regarded as an important feature of metastatic cancer cell [153]. They protrude into extracellular microenvironment from 1 um to more than 10 μm [70, 154]. Thus, they play a critical role in cellular mechanosensing the stiffness of extracellular microenvironment and greatly influence cancer cells invading or metastasizing into surrounding tissues or circulating systems. In addition, neurite extension from the central cell body is important for nervous system development [155, 156]. In this process, filopodia protrusions steer the growths of nervous cells in tissues [157-159]. For example, when filopodia are deprived, nerve growth cones are highly disorientated [160].

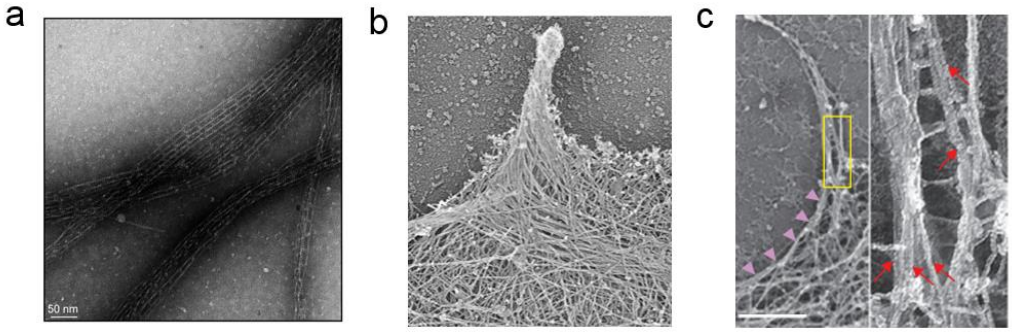

Figure 2.14 Filopodia and F-actin bundles. (a) F-actin bundles in cell [161]. (b) Electron microscopy image of filopodia in a migrating cell [162].(c) Electron microscopy image of filopodia extensions of neurons [158].

The structures of filopodial/invapodial F-actin bundles have been well recognized. The diameters of filopodia/invadopodia are in the range of 60 to 200nm [66, 70]. There are about 10 to over 30 parallel actin filaments in these filopodial/invapodial spaces [66, 70]. These actin filaments can grow to a length from 1μm to more than 10μm [154] and they are crosslinked by α-actinin and fascin to form bundles. The minimal space between two adjacent crosslinking points along an actin filament is about 36 nm [161]. Filopodial/invapodial F-actin bundles penetrating the extracellular microenvironments serve as mechanical sensors to navigate cell migration or growth behaviours. Previously, both experimental and modelling studies have studied the mechanical behaviours of F-actin bundles. For example, in vitro experiments showed that the stiffness of F-actin bundles can be sensitively regulated by crosslinking proteins [59, 66]. Two-dimensional modelling demonstrated that the optimal number of actin filaments in a bundle for supporting a filopodium growing to a length of several microns is about 30 [70]. However, the mechanical properties of F-actin bundles are determined by various factors, such as filament undulations induced by the thermal factor, filament density and the densities of different types of crosslinking proteins, which have different stiffnesses and crosslinking distances. The quantitative relationship between the macroscopic elastic properties and the microscopic structures of F-actin bundles modulated by these factors remains poorly understood. Moreover, when the rigidity of extracellular microenvironment confining filopodia/invadopodia protrusion is very high, the polymerizing F-actin bundles will experience large deformations. However, until now, the mechanical response of nonlinear geometrical deformation of F-actin bundles has not been investigated.

More importantly, migrating cells rely on filopodia or invadopodia to probe the stiffness of extracellular microenvironment [104]. The stiffness of the extracellular

matrix highly and temporally varies. Experiments suggested that the stiffness of extracellular matrix ranges from 0.1 kPa to 1 GPa scale [163-166]. The mechanism of how the filopodial/invadopodial F-actin bundles sense and adapt to the widely varying extracellular microenvironments to open a channel for cell migrating through remains unclear. In addition, filopodial F-actin bundles grow out from lamellipodia and they steer the orientations of lamellipodia [167]. However, it is unknow how the filopodia and lamellipodia work together to drive cell migration in complex extracellular microenvironment.

Chapter 3 Modelling of Assembling Lamellipodial Branched Actin Network

3.1 Introduction

For the study of the micromechanical properties of cytoskeleton comprised of biopolymer network, finite element method (FEM) analysis based on a representative volume element (RVE) model with periodic boundary conditions is an effective method [168-176]. The branched actin network in lamellipodium usually extends several micrometers from the leading edge to the rear [13, 88, 177] and 20~50 μm along the leading edge [85], and has a typical thickness of about 200 nm [124, 178]. Therefore, it is suitable to construct RVE models in the migration plane and perform mechanical analysis using FEM.

However, during cell migration, the lamellipodial branched actin network is in a highly dynamic process interacting with various intracellular proteins and the fluctuating extracellular confining microenvironments. To construct continuum mechanics-based spatial periodic models for FEM mechanical analysis, we first need to simulate the dynamic and stochastic self-assembling process of the branched actin filament network in the sheet-like lamellipodial space and build its spatiotemporal mathematical model, which can realistically capture the self-assembling and remodelling behaviours of the branched actin network in driving cell migration. Then, this mathematical model is constructed into a self-assembling spatiotemporal RVE model. In this process, 4600 lines of computer code are developed. By applying the experimentally measured geometric and elastic properties of actin filament, Arp2/3 complex, filamin-A and α-actinin materials, and periodic boundary conditions to the RVE models, the effective elastic properties of the branched filament networks can be obtained by FEM analysis.

Using this self-assembling RVE model, we can capture and study how the microscopic individual intracellular proteins and the extracellular confining resistance regulate the architecture of the branched actin network, respectively or jointly, and then regulate the macroscopic mechanical properties of the branched actin network for driving cell migration through varying extracellular microenvironment.

3.2 Self-assembling spatiotemporal mathematical model simulates the dynamic growth of the branched actin network driving cell migration.

We develop computer codes to simulate the self-assembling and remodelling process of the 3D branched actin network in a sheet-like space by considering five types key proteins, namely, filamentous actin, Arp2/3 complex, capping protein, filamin-A and α-actinin and their mechano-chemical interactions including actin polymerizing, Arp2/3 complex branching, capping protein inhibiting polymerization and crosslinking proteins' binding and unbinding. All these intracellular proteins are assumed to be uniformly distributed in lamellipodia. This assumption is reasonable because they are coordinated by the treadmilling process between the actin polymerization and depolymerization [27, 125]. In lamellipodia, the polymerization and depolymerization rates of actin are in a dynamics steady state [121]. Thus, here we only consider the net polymerization velocity of actin filaments, which is given by [140].

$$V_f = \delta(k_{on}M - k_{off}) \tag{3.1}$$

Where δ is the size of an actin monomer; k_{on} and k_{off} are the polymerization and depolymerization rates of actin filaments, respectively; and M is the molar concentration of actin monomers.

The relationship between the total length of actin filaments and the concentration of filamentous actin (F-actin) in an RVE domain with the size of $w \times w \times h$ is established as [179]

$$L = \frac{C_A N_A w^2 h d_{actin}}{2} \tag{3.2}$$

where L is the total length of actin filaments; C_A is the molar concentration of F-actin; w and h are the in-plane side length of the selected lamellipodial RVE domain and the typical thickness of lamellipodia (200 nm), respectively; N_A is the Avogadro constant (6.02×10^{23} mol^{-1}), and d_{actin} is the diameter of actin monomer (~5 nm).

A lamellipodial RVE domain of 1000nm×1000nm×200nm is selected to generate a certain number of pointed ends of mother actin filaments by referring to the concentration of F-actin based on Eq. (3.2). Note that since actin filaments are in a dynamic polymerization process during cell migration, the domain of the $1000nm\times1000nm$ square is only used to generate the pointed ends of mother filaments but their polymerization is not confined in it. Specifically, both the x_i^p and y_i^p coordinates of the pointed end of the ith mother filament are randomly generated in the range from 0 to 1000. The z_i^p coordinate of the pointed end is randomly generated by a Gaussian distribution function with a mean of 100 and a standard deviation of 50 because it is assumed that F-actin is more likely denser in area nearing the central layer of a lamellipodium. Meanwhile, the value z_i^p should be confined in the range of 0 to 200. To determine the orientation and the coordinates of the corresponding barbed end of every mother filament (Fig. 3.1), a local spherical coordinate system is created by regarding every pointed end as the origin. In our simulation, the growth of actin filament by polymerization is completed in one step and is capped by a capping protein. The spherical coordinates (r,φ,θ) of the barbed end are randomly generated by a normal or a uniform

distribution as defined in Eq. (3.3). The polymerization length of the filaments, r, is generally in the range of 150 to 300 nm in lamellipodia [8, 95, 96] and is determined by a random number from a normal distribution of $N(250,50)$. Because the length of actin filaments is normally larger than the thickness of lamellipodium, the polar angle φ between actin filament and the positive z axis is confined in a narrow range and given by a random number from a uniform distribution of $U(60°,120°)$. Azimuthal angle θ, the orientation of actin filaments relative to the cell moving direction in the xy-plane, is commonly around ±35° for a cell with a medium moving velocity [99, 123] and is determined by a normal distribution of $N(\pm 35°,15°^2)$. The shadow areas in Fig. 3.1 are the preferred range of the distribution of angle θ. The coordinates of the barbed end (x_i^b, y_i^b, z_i^b) for the ith mother actin filament in the 3D space are obtained by Eqs. (3.4) and (3.5).

$$r \sim N(250,50); \varphi \sim U(60°,120°); \theta \sim N(\pm 35°,15°^2) \tag{3.3}$$

$$\begin{pmatrix} x_i^b \\ y_i^b \\ z_i^b \end{pmatrix} = r_i \begin{pmatrix} \sin\varphi\cos\theta \\ \sin\varphi\sin\theta \\ \cos\varphi \end{pmatrix} + \begin{pmatrix} x_i^p \\ y_i^p \\ z_i^p \end{pmatrix} \tag{3.4}$$

$$\left\{ z_i^p \mid 0 \le z_i^p \le 200 \right\} \tag{3.5}$$

The diameter of actin filaments, d, is 7 nm [9]. After the generation of mother filaments, Arp2/3 complex nucleates and binds on them randomly. To be consistent with experimental measurement, if there are two or more Arp2/3 complex binding on the same filament, there should be an interval d^{arp} between the two adjacent Arp2/3 branching points. d^{arp} is randomly generated from a uniform distribution of $U(50,150)$, which is a reasonable distance in lamellipodium [27, 145]. The number of Arp2/3 complex along an actin filament can be specified by the integer

part of r_i / d^{arp}, where r_i is the length of the *i*th actin filament. Therefore, the coordinates of the *j*th starting point along the *i*th filament can be obtained as

$$\begin{pmatrix} x_{ij}^{as} \\ y_{ij}^{as} \\ z_{ij}^{as} \end{pmatrix} = jd^{arp} \begin{pmatrix} \sin\varphi\cos\theta \\ \sin\varphi\sin\theta \\ \cos\varphi \end{pmatrix} + \begin{pmatrix} x_i^p \\ y_i^p \\ z_i^p \end{pmatrix} \tag{3.6}$$

The length r_{ij}^{arp} and diameter of Arp2/3 complex are about 10 nm [47]. It generates a branch from the mother filament by an angle of around 70° [49]. As a result, the possible branching position of Arp2/3 is constrained on a conical surface around the mother filament. In addition, the polar and azimuthal angles φ_{ij}^{arp} and θ_{ij}^{arp} of Arp2/3 complex in the spherical coordinate system should also satisfy the distributions defined by Eq. (3.3) to meet the relative orientation demand with respect to the direction of cell migration. Moreover, the filament length is normally larger than 100nm in migrating lamellipodia [8, 95, 96]. Thus, the orientation of Arp2/3 complex should also allow the forthcoming nucleated daughter filament to polymerize to a minimum length of 100nm in the sheet-like lamellipodial space. If the coordinates of the *j*th ending point of the Arp2/3 complex are $(x_{ij}^{ae}, y_{ij}^{ae}, z_{ij}^{ae})$ in the global Cartesian coordinate system, the following constraint conditions must be satisfied:

$$\sqrt{(x_{ij}^{ae} - x_{ij}^{as})^2 + (y_{ij}^{ae} - y_{ij}^{as})^2 + (z_{ij}^{ae} - z_{ij}^{as})^2} = r_{ij}^{arp} \tag{3.7}$$

$$\cos\alpha = \frac{(x_i^b - x_i^p)(x_{ij}^{ae} - x_{ij}^{as}) + (y_i^b - y_i^p)(y_{ij}^{ae} - y_{ij}^{as}) + (z_i^b - z_i^p)(z_{ij}^{ae} - z_{ij}^{as})}{\sqrt{(x_i^b - x_i^p)^2 + (y_i^b - y_i^p)^2 + (z_i^b - z_i^p)^2}\sqrt{(x_{ij}^{ae} - x_{ij}^{as})^2 + (y_{ij}^{ae} - y_{ij}^{as})^2 + (z_{ij}^{ae} - z_{ij}^{as})^2}} \tag{3.8}$$

$$\left\{\varphi_{ij}^{ae} \mid 0 \le z_{ij}^{ae} + 100\cos\varphi_{ij}^{ae} \le 200\right\} \tag{3.9}$$

where α is the angle between the mother filament and the Arp2/3 complex, and is randomly determined by a Gaussian distribution of $N(70°, 2°^2)$. Based on the above constraint equations, the end point coordinates $(x_{ij}^{ae}, y_{ij}^{ae}, z_{ij}^{ae})$ of Arp2/3 complex are stochastically generated. After that, the daughter filaments begin to polymerize in the directions of Arp2/3 complex from the same spherical coordinate system. Their growth lengths are also determined by the distribution given in Eq. (3.3). If actin filaments exceed the bottom ($z = 0$) or top ($z = 200$) surface of the lamellipodium in the z direction, they will be capped by capping proteins and the polymerization will be stopped at the plane of $z = 0$ or $z = 200$. Using the same method, the next several generations of Arp2/3 complex and daughter filaments are created from the already generated daughter filaments. Thus, the dendritic structure formed by actin filaments and Arp2/3 complex is constructed as shown in Fig. 3.2, which is comparable to the inserted experimental image [180]. The total length of actin filaments is determined by the concentration of F-actin and given by Eq. (3.2)

The crosslinking proteins (filamin-A and α-actinin) are produced to bind on the dendritic actin filaments, to connect them into an integrated branched actin network and to stabilize the lamellipodium. Instead of liking the cortex model in ref. [168] where crosslinking proteins are generated only according to the shortest distance between two filaments and any two filaments can only be bound together by one crosslinking protein, we generate crosslinking proteins according to their connection properties (i.e., connection angle and distance) and the relative orientation and distance of the two filaments in the three-dimensional sheet-like space. Additionally, like the true condition in a migrating cell, two filaments can be crosslinked by several the same or different types of crosslinking proteins with the experimentally measured intervals. Filamin-A has a length of 160nm and crosslinks two nearly orthogonal actin filaments (70°~110°) [181]. The shortest crosslinking distance is about 30 nm [52]. Therefore, the crosslinking distance of filamin-A is in the range of 30 to 160 nm. In order to decide whether to generate

filamin-A to crosslink two filaments, which are not connected by the same Arp2/3 complex, we first need to calculate the relative angle and the shortest distance between the two filaments. For example, for the ith filament with pointed end of (x_i^p, y_i^p, z_i^p) and barbed end of (x_i^b, y_i^b, z_i^b) and the *j*th filament with pointed end (x_j^p, y_j^p, z_j^p) and barbed end (x_j^b, y_j^b, z_j^b), their relative angle can be obtained by Eq. (3.10).

$$\beta == \frac{180°}{\pi} \arccos \frac{(x_i^b - x_i^p)(x_j^b - x_j^p) + (y_i^b - y_i^p)(y_j^b - y_j^p) + (z_i^b - z_i^p)(z_j^b - z_j^p)}{\sqrt{(x_i^b - x_i^p)^2 + (y_i^b - y_i^p)^2 + (z_i^b - z_i^p)^2}\sqrt{(x_j^b - x_j^p)^2 + (y_j^b - y_j^p)^2 + (z_j^b - z_j^p)^2}} \tag{3.10}$$

$$\left\{\beta \,|\, 70° \le \beta \le 110° \bigcup 250° \le \beta \le 290°\right\} \tag{3.11}$$

If they are appropriate for being crosslinked by filamin-A, the relative angle should satisfy Eq. (3.11). In addition, the shortest spatial distance between the two filaments $d_{\min}^{fls}$, which can be identified from Eqs. (3.12-16), should be in the range of crosslinking length of filamin-A as given by Eq. (3.17).

$$\begin{pmatrix} x_i \\ y_i \\ z_i \end{pmatrix} = \begin{pmatrix} x_i^p \\ y_i^p \\ z_i^p \end{pmatrix} + s \begin{pmatrix} x_i^b - x_i^p \\ y_i^b - y_i^p \\ z_i^b - z_i^p \end{pmatrix} \tag{3.12}$$

$$\begin{pmatrix} x_j \\ y_j \\ z_j \end{pmatrix} = \begin{pmatrix} x_j^p \\ y_j^p \\ z_j^p \end{pmatrix} + t \begin{pmatrix} x_j^b - x_j^p \\ y_j^b - y_j^p \\ z_j^b - z_j^p \end{pmatrix} \tag{3.13}$$

$$f(s,t) = (x_i - x_j)^2 + (y_i - y_j)^2 + (z_i - z_j)^2 \tag{3.14}$$

$$\begin{cases} \dfrac{\partial f(s,t)}{\partial s} = 0 \\ \dfrac{\partial f(s,t)}{\partial t} = 0 \end{cases} \tag{3.15}$$

$$d_{\min}^{fls} = \begin{cases} \sqrt{(x_i - x_j)^2 + (y_i - y_j)^2 + (z_i - z_j)^2} & if\ \ 0 \le s \le 1\ and\ \ 0 \le t \le 1 \\ \sqrt{(x_i - x_j^p)^2 + (y_i - y_j^p)^2 + (z_i - z_j^p)^2} & if\ \ 0 < s < 1\ and\ \ t < 0 \\ \sqrt{(x_i - x_j^b)^2 + (y_i - y_j^b)^2 + (z_i - z_j^b)^2} & if\ \ 0 < s < 1\ and\ \ 1 < t \\ \sqrt{(x_i^p - x_j)^2 + (x_i^p - x_j)^2 + (x_i^p - x_j)^2} & if\ \ s < 0\ and\ \ 0 < t < 1 \\ \sqrt{(x_i^b - x_j)^2 + (x_i^b - x_j)^2 + (x_i^b - x_j)^2} & if\ \ s < 0\ and\ \ 0 < t < 1 \\ \sqrt{(x_i^p - x_j^p)^2 + (y_i^p - y_j^p)^2 + (z_i^p - z_j^p)^2} & if\ \ s < 0\ and\ \ t < 0 \\ \sqrt{(x_i^b - x_j^b)^2 + (y_i^b - y_j^b)^2 + (z_i^b - z_j^b)^2} & if\ \ 1 < s\ and\ \ 1 < t \\ \sqrt{(x_i^b - x_j^p)^2 + (y_i^b - y_j^p)^2 + (z_i^b - z_j^p)^2} & if\ \ 1 < s\ and\ \ t < 0 \\ \sqrt{(x_i^p - x_j^b)^2 + (y_i^p - y_j^b)^2 + (z_i^p - z_j^b)^2} & if\ \ s < 0\ and\ \ 1 < t \end{cases} \tag{3.16}$$

$$\left\{ d_{\min}^{fls} \mid 30 \le d_{\min}^{fls} \le 160 \right\} \tag{3.17}$$

On the basis of the above connection distance principles and relative orientation between two actin filaments, filamin-A is generated in the model. Experiments also showed that the shortest spacing between the two adjacent filamin-A binding on an actin filament is about 36 nm, which is the actin helical repeat [181]. Thus, to be consistent with the realistic condition in live cells, several filamin-A can be created

along two filaments with the intervals of an integral multiple of the actin helical repeat in our mathematical model as long as they satisfy Eqs. (3.11 and 3.17). Another type of crosslinking protein existed in lamellipodia is α-actinin. Compared with filamin-A, α-actinin can crosslink two filaments with variable relative angles in lamellipodia [58, 61]. Its linking distance is in the range from 24 nm to 40 nm [67, 182]. The minimal interval between the adjacent α-actinin along an actin filament is about 31 nm [58, 67]. Similarly to filamin-A, α-actinin can be constructed to crosslink actin filaments according to its connection principles. In our mathematical model, both filamin-A and α-actinin are not permitted to crosslink the mother and daughter filaments connected by the same Arp2/3 complex. Additionally, it may be appropriate to generate both filamin-A and α-actinin in some locations in the model. It is assumed that filamin-A has the priority over α-actinin because concentration of filamin-A in lamellipodium is higher than α-actinin [27] and it has 4 binding sites while α-actinin has only 2, which enables filamin-A to have more opportunity to bind actin filaments. Because actin filaments are quite short (100~300nm) [8, 95, 96] and their density is small (3.0%~10.0%) in lamellipodium [89], there are few entanglements (the overlap of cross-sections of two actin filaments) between them in the branched actin network. Moreover, compared with crosslinking proteins, entanglements are usually more fragile-like and easy to break [183]. Therefore, entanglements are deliberately ignored in our simulation.

To construct the self-assembling RVE model, we shift the parts of filaments, Arp2/3 complex, filamin-A and α-actinin outside the square domain 1000nm×1000nm (i.e., the RVE) into the domain by translating 1000nm in the x or y direction (Fig. 3.3) so that the RVE model is periodic in these directions. The diameters of actin filaments, Arp2/3 complex and crosslinking proteins (filamin-A and α-actinin) are about 7 nm [9], 10 nm [47] and 4 nm [182], respectively. They are also assigned to the RVE model. Thus, continuum mechanics-based hybrid biopolymer network models describing the dynamic lamellipodial branched actin

networks are created (Fig. 3.4). Note that, both the microscopic and the macroscopic spatiotemporal reconfiguration of the network, which is induced by the varying extracellular confining resistance in cell migration process, can be realistically simulated by this RVE model through regulating the Arp2/3 complex nucleating, F-actin, filamin-A and α-actinin self-assembling and disassembling and actin filament polymerizing orientations.

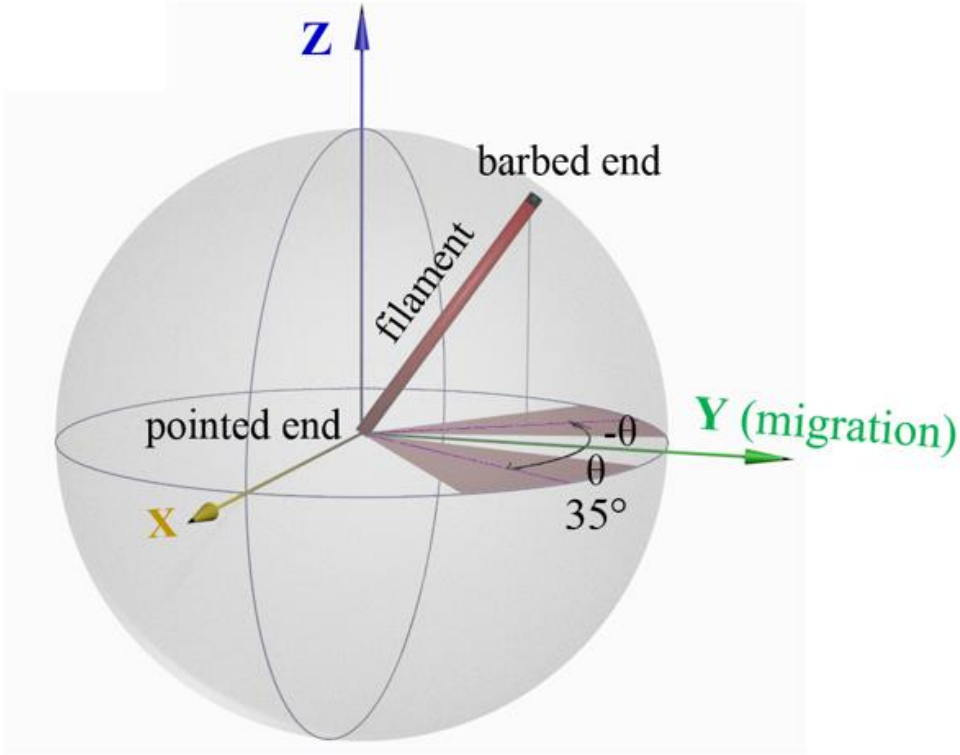

Figure 3.1 Stochastically created actin filaments with barbed end polymerizing forward based on the spherical coordinate system (shadow areas are the preferential angle with respect to the cell moving direction).

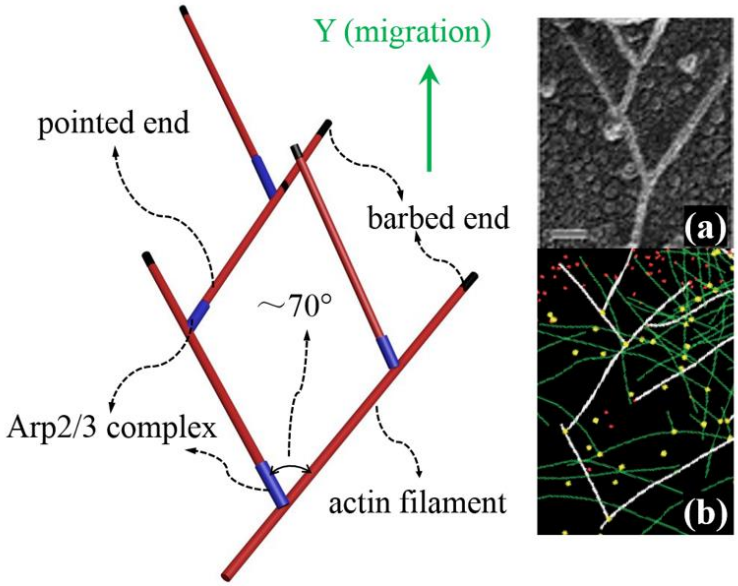

Figure 3.2 The dendritic structure created by Arp2/3 complex nucleating and branching out from existing filaments stochastically in our model; the inserted figures (a) and (b) are experimental images of branched actin filament from ref. [145] and ref. [180], respectively.

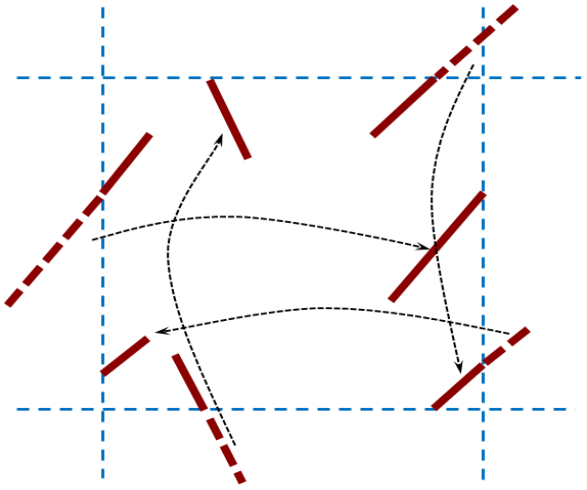

Figure 3.3 Schematic operation of generating actin filaments, Arp2/3 complex and crosslinking proteins (filamin-A and α-actinin) on the boundaries of a periodic RVE model.

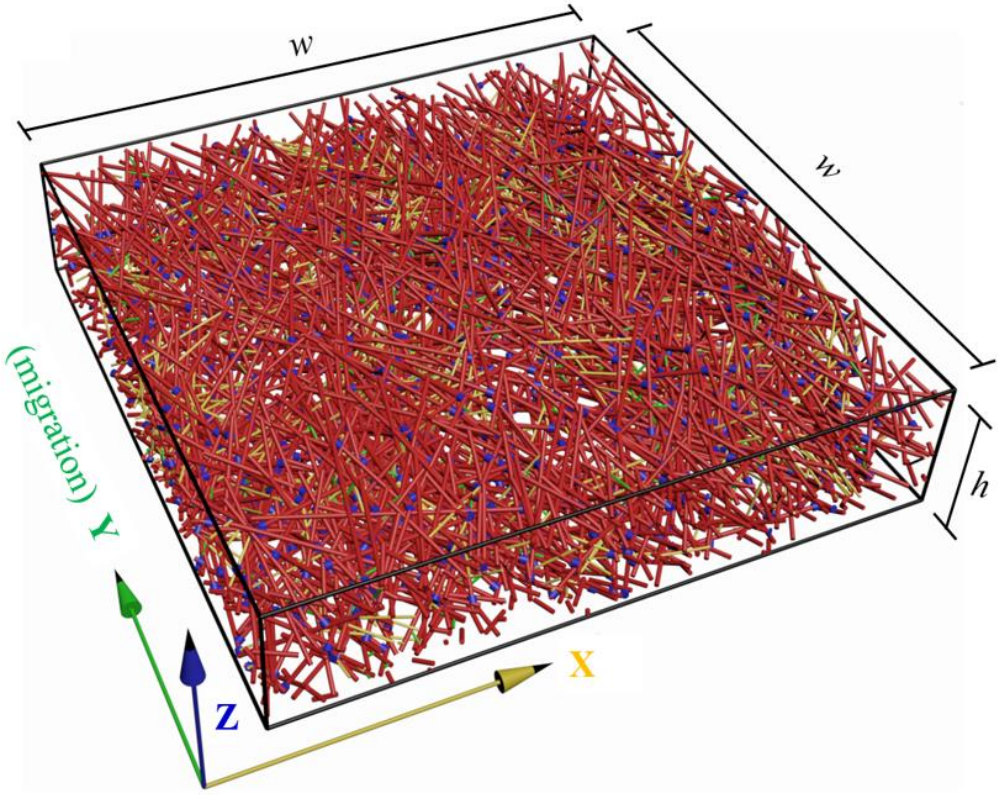

Figure 3.4 A representative volume element (RVE) model of the branched actin network (red: actin filament; blue: Arp2/3 complex; yellow: filamin-A; green: α-actinin). This model is periodic in the *xy*-plane. Its side lengths in both the x and y directions are 1000nm and thickness in the *z* direction is 200nm, which is the typical thickness of lamellipodia. The *x*, *y* and *z* directions are the transverse direction, cell migrating direction and out-of-plane direction, respectively.

3.3 RVE model validation with published experimental data.

As shown in Fig. 3.2, the architecture generated in our RVE model is very similar to the experimental images of the branched actin network in ref. [145] and ref. [180]. In addition, as expected, it can be seen from Fig. 3.5 that with the increase of filament density V_f , both the numbers of filamin-A and α-actinin increase with growing gradients because higher V_f means more appropriate crosslinking positions between filaments. For the usual density range (3.0%~10.0%) of actin filaments [89], the number of Arp2/3 complex in the RVE model is larger than that of filamin-A, which, in turn, is larger than that of α-actinin. This is consistent with the experimental measurements of the relative densities of connection proteins [27]: the density of Arp2/3 complex is larger than that of filamin-A, and the latter, in turn, is larger than that of actinin in the branched actin network in lamellipodium. Because the average interval d^{arp} between two adjacent Arp2/3 complexes along an actin filament in all models is based on experimental measurements [27, 145], the number of Arp2/3 in the RVE model can reflect its realistic density in lamellipodia. Therefore, our model can successfully predict the densities of filamin-A and α-actinin. Moreover, as shown in Table 3-4, our RVE models with an actin filament density of 7.8% have about 290 filaments per micron at the cross-section of $y = 1000$, which agrees well with the experimental data [89] that there are about 300 filaments per micron length of lamellipodium margin in keratinocyte and fibroblast, whose actin filament density of the branched actin network in lamellipodia is also normally 7.8% [179].

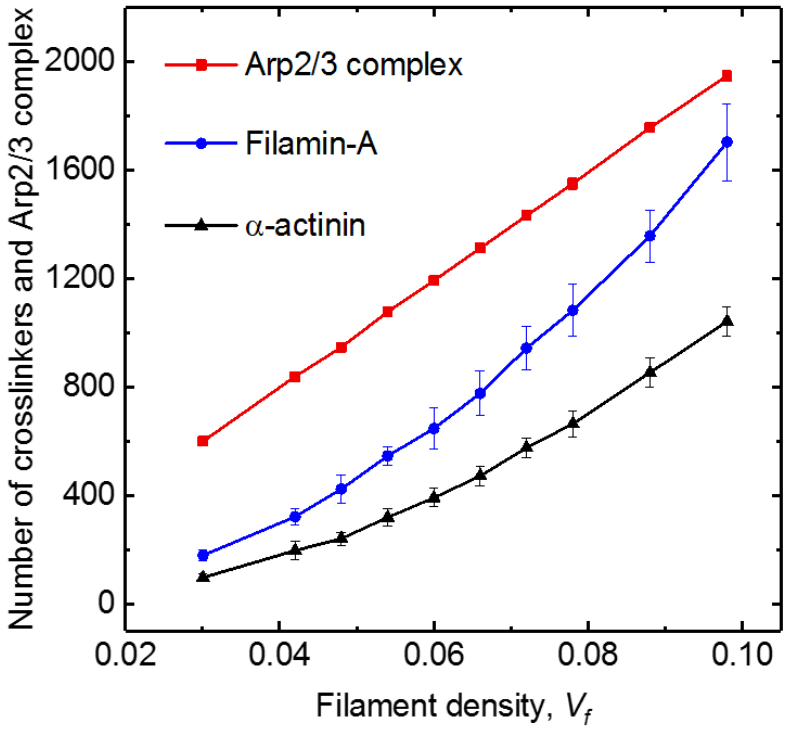

Figure 3.5 Numbers of Arp2/3 complex, filamin-A and α-actinin per um^2 in the xy-plane of the models.

3.4 Mesh and boundary conditions of the RVE model.

The hybrid branched and cross-linked actin filament network in the RVE model (Fig. 3.4) is meshed into quadratic interpolated B32 beam elements with circular cross-sections in ABAQUS simulations. This element type is based on the Timoshenko beam theory allowing for bending, torsion, axial compression/stretching and transverse shear deformation. The solid materials of actin filaments and crosslinking proteins are assumed to be isotropic and linear elastic, whose Young's moduli and Poisson's ratios are obtained from the literature and given in Table 3-1. According to experimental measurements, filamin-A and α-actinin have similar mechanical performances [55], and thus are assumed to have the same mechanical properties. Compared with actin filaments and crosslinkers,

the dimensions of Arp2/3 complex are very small (assumed to be a cylinder with both diameter and length being 10 nm) [47] and the connections formed by it between the mother and daughter actin filaments are relatively rigid [49]. Thus, the elastic properties of Arp2/3 complex are assumed to be the same as those of actin filaments. The diameters and elastic properties of actin filaments and crosslinking proteins are obtained from refs. [23, 31, 184, 185] as shown in Table 3-1. The Young's modulus of actin filaments is measured by in vitro nanomanipulation with microneedles [31].

Table 3-1 Diameters and elastic properties of actin filaments and crosslinking proteins

Types of proteins	Diameter of cross-section	Poisson's ratio	Young's modulus	Refs.
Actin filaments	7 nm	0.3	2 GPa	[23, 31, 184]
Arp2/3 complex	10 nm	0.3	2 GPa	[47]
Crosslinking proteins (filamin-A and α-actinin)	4 nm	0.3	60 MPa	[185]

Periodic boundary conditions are applied to the RVE models (Fig. 3.4) in the x and y directions. Constraint equations of the periodic boundary nodes for meeting the continuity and equilibrium of adjacent RVEs are given by Eqs. (3.18-25).

$$u_i^{x=0} - u_{i'}^{x=1000} = u_j^{x=0} - u_{j'}^{x=1000} \tag{3.18}$$

$$v_i^{x=0} - v_{i'}^{x=1000} = v_j^{x=0} - v_{j'}^{x=1000} \tag{3.19}$$

$$w_i^{x=0} - w_{i'}^{x=1000} = w_j^{x=0} - w_{j'}^{x=1000} \tag{3.20}$$

$$\theta_i^{x=0} = \theta_{i'}^{x=1000} \tag{3.21}$$

$$u_i^{y=0} - u_{i'}^{y=1000} = u_j^{y=0} - u_{j'}^{y=1000} \tag{3.22}$$

$$v_i^{y=0} - v_{i'}^{y=1000} = v_j^{y=0} - v_{j'}^{y=1000} \tag{3.23}$$

$$w_i^{y=0} - w_{i'}^{y=1000} = w_j^{y=0} - w_{j'}^{y=1000} \tag{3.24}$$

$$\theta_i^{y=0} = \theta_{i'}^{y=1000} \tag{3.25}$$

Where u , v and w denote the displacements in the *x*, *y* and *z* directions, respectively. i and j are the nodes on the boundary of $x=0$ or $y=0$ while i' and j' are their corresponding nodes on the opposite boundary (i.e., $x=1000$ or $y=1000$), respectively. θ represents the rotational angles around the *x*, *y* and *z* axes.

On the top and bottom surfaces of a lamellipodium, the branched actin filament network is constrained by the membrane. Therefore, all the nodes on the boundary of $z=0$ are assumed to have zero displacement in the z direction and all the nodes on the boundary of $z=200$ are assumed to have the same displacement in the *z* direction, which can be determined via Eq. (3.28).

$$w_i^{z=0} = 0 \tag{3.26}$$

$$w_{i'}^{z=200} = w_{j'}^{z=200} \tag{3.27}$$

$$\sum_{i'=1}^{n} F_{zi'}^{z=200} = 0 \tag{3.28}$$

Where w denotes the displacement in the *z* direction; i are the nodes on the $z=0$ boundary; i' and j' are the nodes on the $z=200$ boundary; $F_{zi'}$ and n are the force component in the *z* direction of node i' and the total number of nodes on the $z=200$ boundary, respectively.

3.5 Elastic constants of the branched actin filament network.

Under the imposed boundary displacement, the total energy of the RVE model is the sum of the strain energies of bending, axial, shear and torsion deformations of actin filaments, Arp2/3 complex, filamin-A and α-actinin, and can be expressed as

$$U_{total} = \frac{1}{2}\sum_{<ij>}\int (E_s I(\frac{d\theta(s_{ij})}{ds_{ij}})^2 + E_s A(\frac{du(s_{ij})}{ds_{ij}})^2 + \lambda G_s A(\frac{dv(s_{ij})}{ds_{ij}} - \theta(s_{ij}))^2 + G_s J(\frac{d\varphi(s_{ij})}{ds_{ij}})^2) ds_{ij} \tag{3.29}$$

$$G_s = \frac{E_s}{2(1+\nu_s)} \tag{3.30}$$

where i , j and s_{ij} are respectively the two vertices and length of a segment of actin filaments, Arp2/3 complex, filamin-A or actinin in the RVE model; E_s and G_s are their Young's and shear moduli; A, I and J are the area, the second moment and polar second moment of their cross-sections, respectively. $u(s_{ij})$ and $v(s_{ij})$ are axial and transverse displacements. $\theta(s_{ij})$ and $\varphi(s_{ij})$ are the rotation and torsion angles of the centroidal axis of the fiber segment; and $\lambda = 10/9$ is the

transverse shear coefficient of the circular cross-section. Based on the minimum total potential energy principle (Eq. 3.31), the system equilibrium deformation state can be solved.

$$\prod_p^* \geq \prod_p \tag{3.31}$$

where $\prod_p$ and $\prod_p^*$ are the true and possible total energies of system, respectively. The effective elastic modulus of the bulk network can be calculated by

$$E_k = \frac{\sum_i (f_k)_i w}{(wh)d_k} = \frac{\sum_i (f_k)_i}{hd_k} \tag{3.32}$$

where d_k is the imposed displacement in direction *k*. w and h are the side length and thickness of the RVE model (see Fig. 3.2). $(f_k)_i$ is the reaction force in direction k of the *i*th node on the boundary whose normal direction is k. As can be seen from Tables 3-2 and 3-3, the elastic constants of the branched actin network obtained from uniaxial compression or tension tests satisfy the following relation

$$\frac{v_{ij}}{E_j} = \frac{v_{ji}}{E_i} \quad (i, j = 1,2,3 \; and \; i \neq j) \tag{3.33}$$

where Poisson's ratios are defined as $v_{ij} = -\varepsilon_i / \varepsilon_j$ and ε_i is the normal strain in direction *i* when an uniaxial stress is applied in the direction j; E_i is the Young's modulus in the *i* direction; 1, 2 and 3 represent the *x*, *y* and *z* directions, respectively. The branched actin filament network material has three orthogonal planes of elastic symmetry. Thus, normal stresses only generate normal strains and each shear stress only generates the corresponding shear strain independently; and in order to fully describe the elastic mechanical behaviours of this model, nine independent elastic constants (E_1, E_2 , E_3, G_{12}, G_{23} , G_{31}, v_{12}, v_{23}, v_{31}) are required because the

compliance matrix is symmetric. G_{ij} is the shear modulus in the *ij*-plane. The constitutive relationship of the branched actin filament network material is given by

$$\begin{pmatrix} \varepsilon_{11} \\ \varepsilon_{22} \\ \varepsilon_{33} \\ \gamma_{12} \\ \gamma_{23} \\ \gamma_{31} \end{pmatrix} = \begin{pmatrix} \frac{1}{E_1} & -\frac{\nu_{12}}{E_2} & -\frac{\nu_{13}}{E_3} & 0 & 0 & 0 \\ -\frac{\nu_{21}}{E_1} & \frac{1}{E_2} & -\frac{\nu_{23}}{E_3} & 0 & 0 & 0 \\ -\frac{\nu_{31}}{E_1} & -\frac{\nu_{32}}{E_2} & \frac{1}{E_3} & 0 & 0 & 0 \\ 0 & 0 & 0 & \frac{1}{G_{12}} & 0 & 0 \\ 0 & 0 & 0 & 0 & \frac{1}{G_{23}} & 0 \\ 0 & 0 & 0 & 0 & 0 & \frac{1}{G_{31}} \end{pmatrix} \begin{pmatrix} \sigma_{11} \\ \sigma_{22} \\ \sigma_{33} \\ \sigma_{12} \\ \sigma_{23} \\ \sigma_{31} \end{pmatrix} \tag{34}$$

Table 3-2 Elastic properties of the filament network obtained from uniaxial tension, compression and pure shear tests at filament density of 7.8% (Note that Poisson's ratios of fibre-network materials are closely related with their connectivity and can be positive, zero and negative [186]. The actin filaments and crosslinking proteins in our RVE models are generated stochastically and thus some models have negative Poisson's ratios).

NO.	V_f	E_1	v_{21}	v_{31}	E_2	v_{12}	v_{32}	E_3	v_{13}	v_{23}	G_{12}	G_{23}	G_{31}
1	0.0778522	4.2678778	0.0940823	0.0107896	20.614739	0.454437	0.1036847	3.1668505	0.0080062	0.0159281	3.8039541	3.3630058	1.2642774
2	0.0792666	5.0243766	0.0962565	0.0193171	17.63162	0.3377849	0.0496505	2.8521148	0.0109654	0.0080315	4.2306291	2.6399285	1.1847965
3	0.0771606	3.7419244	0.1207253	0.0701783	13.85511	0.4470061	0.1775703	2.017227	0.0378323	0.0258532	3.4785341	2.0618086	0.9480159
4	0.0780412	5.5472525	0.1151662	0.0557327	16.702145	0.3467524	0.1003146	2.3234713	0.0233436	0.013955	3.9214906	2.635923	1.3032033
5	0.0768723	2.9230772	0.0857754	0.0765217	14.16518	0.4156666	0.1461422	2.0510438	0.0536932	0.0211606	3.2755838	2.4807765	1.0088077
6	0.0771209	3.9816797	0.0803671	0.0623932	17.9945	0.3632048	0.1969901	2.4995533	0.0391681	0.0273632	3.2167591	2.7780695	1.1669275
7	0.0785634	4.2849766	0.0796984	0.0359364	20.172541	0.3751989	0.2095834	2.486744	0.0208553	0.0258361	4.6956616	3.1840253	1.145986
8	0.0787042	4.8105972	0.1160545	0.0158504	25.545948	0.61629	0.3894709	2.4860765	0.0081913	0.0379025	6.1795781	3.1765928	1.4013368
9	0.0766642	3.5332456	0.0784434	-0.0012	18.989353	0.4215921	0.155589	2.0047291	-0.000681	0.0164257	2.7375534	2.5943198	0.8740904
10	0.078482	4.5412194	0.0597446	0.0480986	15.679609	0.2062821	0.2550507	2.110767	0.0223565	0.0343398	3.2832644	2.466487	1.0488424
11	0.0782078	4.1816981	0.0890421	0.069263	20.511339	0.436754	0.0533849	2.1503483	0.035617	0.0055967	4.8359572	3.1812485	1.1190167
12	0.0786592	4.6561181	0.1328038	0.0599033	23.108978	0.6591241	0.0605109	3.0369098	0.0390714	0.0079521	5.6760994	3.255354	1.4256858
13	0.0792858	4.3561747	0.1034888	0.0342232	23.564185	0.5598098	0.243775	2.7082838	0.021277	0.0280176	5.4312688	3.6277938	1.3157345
14	0.0765458	4.7955925	0.1442149	0.0586948	17.184436	0.5167769	0.2419162	2.682194	0.0328283	0.0377589	4.6900256	2.909648	1.2631975
15	0.077912	4.8739016	0.0652526	0.05947	19.601748	0.3955753	0.1671987	2.463021	0.0303461	0.0163618	4.3468909	2.6012198	1.2359605
16	0.0779638	3.9286531	0.1066913	0.0424206	19.304405	0.4785685	0.1863177	2.592608	0.0265858	0.023443	3.9924441	3.0921485	1.150878
17	0.0788466	3.8822397	0.1166994	0.0256228	16.775916	0.4644003	0.1779509	2.4915293	0.0177641	0.0212088	4.0073034	2.6035683	1.007417
18	0.0780435	4.0378125	0.1228836	0.0368926	18.167973	0.5529096	0.2442945	1.9488515	0.0178062	0.0262051	4.3874763	2.3978463	1.0167932
19	0.0770202	4.2241363	0.119251	0.0049068	14.608055	0.4123979	0.1730022	2.3752303	0.0027591	0.0281297	3.669225	2.3978763	0.9771235
20	0.0770612	3.5938134	0.112496	0.0279667	18.707518	0.5855956	0.1996629	3.005836	0.0233912	0.0320809	4.0125828	2.9531295	1.1459111
21	0.0765107	4.0981138	0.1194188	0.0802675	20.492428	0.5971482	0.3156111	2.3124925	0.0452935	0.0356155	4.5749059	3.1770935	1.2366593

22	0.0797588	5.642365	0.175075	0.0789544	17.821861	0.5529885	0.1794574	2.6204168	0.0366679	0.0263863	4.5555672	2.777565	1.3265745
23	0.0774463	2.2097366	0.0864393	0.0313045	14.563214	0.5696757	0.1882368	2.1272375	0.0301357	0.0274956	2.7335994	2.5983623	0.6794959
24	0.0778448	4.6102844	0.14059	0.0325993	18.238496	0.5561805	0.1260762	2.648472	0.0187273	0.0183079	5.5051769	2.4909135	1.1921749
25	0.0771923	4.4607059	0.09891	0.0170179	17.60364	0.3903363	0.1160297	2.6349368	0.0100525	0.0173675	3.9358297	2.5376955	1.1978278
26	0.0768698	3.43743	0.0668624	-0.034843	18.568499	0.3611813	0.0935916	2.9745265	-0.030151	0.0149926	3.4933303	2.8012683	1.1250177
27	0.0786199	2.9962525	0.0621988	0.0132914	21.413665	0.4445231	0.163905	2.791442	0.0123829	0.0213663	3.2703084	2.7799155	0.8966991
28	0.0778698	4.0795019	0.1364903	0.0122197	16.09174	0.5383911	0.1762109	2.1576678	0.006463	0.0236273	4.0499259	2.2417545	1.0299721
29	0.0795129	4.3093334	0.0811484	0.0632936	22.014955	0.4145603	0.1662105	2.563016	0.0376445	0.0193505	4.0896959	3.02968	1.1907323
30	0.0790069	4.2832084	0.1043167	0.0556636	16.77212	0.4084816	0.260241	2.7940193	0.0363108	0.0433527	4.0249734	2.7485953	1.4839206
Average	0.0779635	4.17711	0.1036862	0.0387584	18.548864	0.4626531	0.1772543	2.5025872	0.0224901	0.0233804	4.1368532	2.7861204	1.1454359
Std.	0.0009176	0.7135686	0.0267501	0.0270037	2.7861428	0.0992592	0.0739765	0.3291576	0.0164743	0.0090594	0.8167818	0.3525769	0.1728945

Table 3-3 Relationships between the elastic constants of the branched actin filament network with a filament density of 7.8%.

NO.	V_f	v_{21}/E_1	v_{12}/E_2	v_{31}/E_1	v_{13}/E_3	v_{32}/E_2	v_{23}/E_3
1	0.0778522	0.0220443	0.0220443	0.0025281	0.0025281	0.0050296	0.0050296
2	0.0792666	0.0191579	0.0191579	0.0038447	0.0038447	0.002816	0.002816
3	0.0771606	0.0322629	0.0322629	0.0187546	0.0187546	0.0128162	0.0128162
4	0.0780412	0.020761	0.020761	0.0100469	0.0100469	0.0060061	0.0060061
5	0.0768723	0.0293442	0.0293443	0.0261785	0.0261785	0.010317	0.010317
6	0.0771209	0.0201842	0.0201842	0.0156701	0.0156701	0.0109472	0.0109472
7	0.0785634	0.0185995	0.0185995	0.0083866	0.0083866	0.0103895	0.0103895
8	0.0787042	0.0241248	0.0241248	0.0032949	0.0032949	0.0152459	0.0152459
9	0.0766642	0.0222015	0.0222015	-0.00034	-0.00034	0.0081935	0.0081935
10	0.078482	0.0131561	0.0131561	0.0105916	0.0105916	0.0162664	0.0162689
11	0.0782078	0.0212933	0.0212933	0.0165634	0.0165634	0.0026027	0.0026027
12	0.0786592	0.0285224	0.0285224	0.0128655	0.0128655	0.0026185	0.0026185
13	0.0792858	0.0237568	0.0237568	0.0078563	0.0078563	0.0103451	0.0103451
14	0.0765458	0.0300724	0.0300724	0.0122393	0.0122393	0.0140776	0.0140776

15	0.077912	0.0091016	0.0091016	0.0153514	0.0153514	0.0063838	0.0063838
16	0.0779638	0.0271572	0.0271572	0.0107977	0.0107977	0.0082761	0.0082761
17	0.0788466	0.0300598	0.0300598	0.0066013	0.0066012	0.0078798	0.0078798
18	0.0780435	0.0304332	0.0304332	0.0091368	0.0091368	0.0134464	0.0134464
19	0.0770202	0.0282309	0.0282309	0.0011616	0.0011616	0.0118429	0.0118429
20	0.0770612	0.0313027	0.0313027	0.0077819	0.0077819	0.0106729	0.0106729
21	0.0765107	0.0291399	0.0291399	0.0195865	0.0195865	0.0154014	0.0154014
22	0.0797588	0.0310287	0.0310287	0.0139931	0.0139931	0.0100695	0.0100695
23	0.0774463	0.0391174	0.0391174	0.0141666	0.0141666	0.0129255	0.0129255
24	0.0778448	0.0304949	0.0304949	0.007071	0.007071	0.0069126	0.0069126
25	0.0771923	0.0221736	0.0221736	0.0038151	0.0038151	0.0065912	0.0065912
26	0.0768698	0.0194513	0.0194513	-0.010136	-0.010136	0.0050403	0.0050403
27	0.0786199	0.0207589	0.0207589	0.004436	0.004436	0.0076542	0.0076542
28	0.0778698	0.0334576	0.0334576	0.0029954	0.0029954	0.0109504	0.0109504
29	0.0795129	0.0188308	0.0188308	0.0146876	0.0146876	0.0075499	0.0075499
30	0.0790069	0.0243548	0.0243548	0.0129958	0.0129959	0.0155163	0.0155163
Average	0.0779635	0.0250191	0.0250191	0.0094307	0.0094307	0.0094928	0.0094929

Table 3-4 When filament density is 7.8%, the statistic numbers of Arp2/3 complex, filamin-A, α-actinin, crosslinking proteins (filamin-A + α-actinin) and actin filaments at the cross-section of *y=1000*, and the average length of actin filaments, r_a, in the RVE model.

NO.	V_f	Arp2/3	Filamin-A	α-actinin	Crosslinking proteins	Average length of filament, r_a	Number of actin filaments at y=1000
1	0.0778522	1559	1164	771	1935	0.2485194	319
2	0.0792666	1578	1076	670	1746	0.2496607	272
3	0.0771606	1526	941	560	1501	0.2509361	303
4	0.0780412	1553	1120	630	1750	0.2501986	277
5	0.0768723	1532	1146	669	1815	0.2498419	289
6	0.0771209	1541	1150	662	1812	0.2501807	328

7	0.0785634	1565	1157	662	1819	0.2492589	284
8	0.0787042	1563	1043	679	1722	0.2506234	284
9	0.0766642	1514	999	591	1590	0.2520023	291
10	0.078482	1562	1022	635	1657	0.2496101	329
11	0.0782078	1562	1056	682	1738	0.2491956	271
12	0.0786592	1551	1349	712	2061	0.2510958	337
13	0.0792858	1577	1192	729	1921	0.250328	294
14	0.0765458	1538	1121	628	1749	0.2476965	285
15	0.077912	1552	981	688	1669	0.2518485	270
16	0.0779638	1558	1123	662	1785	0.2513505	297
17	0.0788466	1544	1062	677	1739	0.2512433	278
18	0.0780435	1527	1004	682	1686	0.2533318	289
19	0.0770202	1529	904	669	1573	0.2493868	244
20	0.0770612	1545	1030	670	1700	0.248436	290
21	0.0765107	1512	1077	671	1748	0.2511801	299
22	0.0797588	1584	1015	717	1732	0.2501497	255
23	0.0774463	1522	936	576	1512	0.2518649	290
24	0.0778448	1551	1110	655	1765	0.249415	325
25	0.0771923	1541	987	647	1634	0.2474771	322
26	0.0768698	1528	1157	610	1767	0.2495217	283
27	0.0786199	1584	1168	639	1807	0.2477742	259
28	0.0778698	1538	1019	700	1719	0.2510429	243
29	0.0795129	1586	1112	723	1835	0.2495293	319
30	0.0790069	1591	1181	681	1862	0.2489937	362
Average	0.0779635	1550.4333	1080.0667	664.9	1744.9667	0.2500564	292.93333
Std.	0.0009176	21.623573	92.375658	44.242777	116.93374	0.0013584	27.32756

Chapter 4 Elastic Properties of Assembling Lamellipodial Branched Actin Network

4.1 Introduction

FEM analysis is an effective method for studying the micromechanical properties of cytoskeletal networks [104, 168]. Using FEM, we have performed more than 24000 calculations and studied over 4000 stochastic models constructed in Chapter 3 to capture how the highly dynamic branched actin network self-regulates its macroscopic elastic properties through self-assembling with intracellular proteins and altering filament orientations when cell migrates through varying extracellular resistance. Each data point in our results is a mean value calculated from about 30 random models with the same set of parameters (Tables 3-2 to 3-4 in chapter 3). By probing the microscopic self-assembling architecture changes adjusted by intracellular proteins and the macroscopic mechanical responses simultaneously, we quantitatively identify how these intracellular proteins individually or combinedly regulate the elastic properties of the branched actin network. Specifically, F-actin concentration sensitively affects the stiffness of the network with roughly a cubic scale. Both successive Arp2/3 branching and crosslinking proteins (filamin-A and α-actinin) are linearly correlated with the network stiffness. Increased density of Arp2/3 first strengthens and then unexpectedly weakens the network due to that excessive high density of Arp2/3 inevitably induces local heterogeneity. In addition, we find that, under the extracellular resistance load (compressive load in cell migration direction), the in-plane Poisson's ratio ν_{12} is much larger than the out-of-plane value ν_{32}. The deformation mechanism of the branched actin network is dominated by the in-plane backward bending of actin filaments. Because Arp2/3 complex prefers to bind on the negative curvature side

of bent filaments to nucleate new filaments [146, 187], these results reveal the physical mechanism why lamellipodium grows into a sheet-like structure and drives cell migration forward. By investigating the effect of filament orientation distribution changes induced by different magnitudes of extracellular resistances, our results elucidate the underlying mechanical mechanism of the architecture transitions, suggesting that each transition makes the network stiffer to overcome the increasing extracellular load. Importantly, we reveal that, on the basis of the deformation of actin filaments, the network can sensitively sense the varying resistance and adapt to it by self-regulating the elastic properties through Arp2/3 complex nucleating, remodelling with the intracellular proteins and altering the filament orientations. Such resistance-adaptive behaviours are versatile and essential in regulating cell migration through varying extracellular microenvironments. Our predictive spatiotemporal model provides a comprehensive insight into the microscopic mechanism of intracellular proteins for regulating cell migration. Moreover, we find that the lamellipodial branched actin network exhibits unique elastic properties that fundamentally distinct from those of crosslinked actin networks.

4.2 Results

4.2.1 Resistance-adaptive actin filament density improves the network stiffness sensitively.

During cell migration, actin filament assembly and disassembly occur simultaneously in the lamellipodial branched actin network, which makes the network in perturbation states [120]. Experimental results show that when extracellular resistance for cell migration increases, filament density in the branched actin network also increases [2, 13, 113]. Here, we investigate why filament density increases, how it regulates the elastic properties of the

lamellipodial actin network and how the latter, in turn, affects cell protrusion in highly heterogeneous 3D extracellular microenvironments.

According to electron microscopy investigation, the concentration of F-actin C_A in lamellipodia is normally in the range of 0.5 mM to 2 mM [26, 188] and can reach up to 10 mM in some local areas [114, 189]. Using Eq. (3.2) in chapter 3, the total length of actin filaments can be calculated, which agrees well with the experimental measurements, i.e., 180~500μm total length of filaments per μm^2 in the lamellipodia [89]. Based on the dimensions of actin filaments and lamellipodia, the actin filament density of the branched actin filament networks in lamellipodia can be obtained in the range of 3%~10% [26, 89, 114, 188, 189]. In the RVE model, the density (or solid volume fraction) of actin filaments can be derived as

$$V_f = \frac{\sum_{i=1}^{N^{filament}} r_i \pi d^2}{4w^2 h} = \frac{L\pi d^2}{4w^2 h} \tag{4.1}$$

where $N^{filament}$ and L are the total number and total length of actin filaments in the RVE model in chapter 3, respectively; r_i is the length of the *i*th actin filament; d is the diameter of actin filaments; w and h are the side length and thickness of the RVE model (Fig. 3.4 in chapter 3), respectively. Note that, with Eqs. (3.2) and (4.1), F-actin concentration C_A and filament density V_f can be converted to each other.

Our results show that both the Young's and shear moduli of the branched actin network scale with F-actin concentration C_A (or filament density V_f): $E_1 \sim C_A^{3.5}$, $E_2 \sim C_A^{3.2}$, $E_3 \sim C_A^{2.2}$, $G_{12} \sim C_A^{3.6}$, $G_{23} \sim C_A^{3.0}$ and $G_{31} \sim C_A^{3.2}$ (Figs. 4.1 and 4.2). The scaling exponents of the branched actin network are much higher than those of the crosslinked actin network, e.g., $C_A^{2.0}$ [2, 190]. Thus, compared with the crosslinked actin network, the stiffness of the branched actin network is much more sensitive to filament density. When filament density increases from 3.0% to 9.8%, Young's moduli E_1, E_2 and E_3 increase from 0.09 kPa to 8.64 kPa, from 0.56 kPa to 39.37

kPa and from 0.37 kPa to 4.38 kPa, respectively. E_2 is much larger than E_1 and E_3, indicating that the network is highly anisotropic and the stiffness in the cell moving direction is the largest. This is important for cell migration because insufficient stiffness of the branched actin network in this direction is unable to overcome confining resistance and thus causes cells to lose mobility [17]. Since denser filament network has a higher stiffness for overcoming resistance, our prediction well interprets the directional actin-based motility that the overall direction of branched actin network growth is deflected towards denser area [113]. Our numerical results are in good quantitative agreement with both the in vivo and in vitro experimental data (Table 4-1) in refs. [2, 26, 82, 83, 87, 98]. For example, the filament density V_f of the branched actin network in keratocyte lamellipodium is normally around 8% [191] and its in vivo measured Young's modulus E_2 is in the range of 21 kPa to 44 kPa [83], which agrees well with our numerical prediction: 16 kPa to 39 kPa when the filament density is from 7.0% to 9.8%. Even though the exact filament densities in these published experiments are not given, our results are in the same order with these experimental data, especially in contrast with the over 100-fold magnitude difference of the crosslinked actin network between previous studies and in living cells [192].

Among the different shear moduli, the in-plane shear modulus G_{12} is the largest, which rapidly increases from 0.08 kPa to 9.2 kPa with the increase of filament density V_f. A recent experiment showed that heterogeneity in the branched actin network is a dominant factor for steering cell movement [113]. In addition, invadopodia usually grow out from the branched actin network in cancer cells to protrude forward [15]. They both indicate that the branched actin network must be able to bear high shear force in the moving plane as a result of that active moving area or invadopodia growing area undertakes much higher load than other areas.

Thus, the high shear modulus G_{12} is crucially important for maintaining stability of the branched actin network in cell directional migration process.

To explore whether the actin filaments or the crosslinking proteins dominate the stiffness of the branched actin network, we perform some separate finite element numerical simulations/tests by using a Young's modulus 10 times larger or smaller than the actual E_f of actin filaments or the actual E_c of the crosslinking proteins. It is found that the stiffnesses of the branched filament networks with different actin filament densities are all primarily dependent on the stiffness of the actin filaments and less sensitive to the stiffness of the crosslinking proteins (Fig. 4.4). Furthermore, the gradient of the log-log scaling relationship between Young's modulus E_2 of the branched filament network and the actin filament density is larger than 3 (Fig. 4.1), indicating that the bending deformation of actin filaments is the dominant deformation mechanism of the branched filament networks. Additionally, under uniaxial compression tests in the cell migrating direction, both Poisson's ratios ν_{12} and ν_{32} increase with increasing filament density (Fig. 4.3). Strikingly, ν_{12} is always much larger than ν_{32}, which suggests that the network is much easier to deform in the in-plane transverse direction rather than the out-of-plane direction (i.e., the thickness). Collectively, they indicate that when cell migrates under extracellular resistance, the deformation of the branched actin network is predominately the backward bending of actin filaments in the migration plane. Because Arp2/3 complex is preferential to binding on the convex side of a bent mother filament and branching out a daughter filament [146], the results explain why lamellipodium grows into a sheet-like structure and protrudes forward. More importantly, they also reveal the physical mechanism of the recent experimental finding that a high resistance force induces a high filament density in lamellipodia [13]: if the stiffness of the polymerizing branched actin network with a low filament density is not sufficient to overcome the confining extracellular microenvironment, actin filaments will be largely bent in the moving plane, and

thus more Arp2/3 complex will bind on the convex side of the bent filaments to branch out more daughter filaments making the filament density increase, which in turn sensitively strengthen the network to overcome the extracellular resistance and propel cell migration.

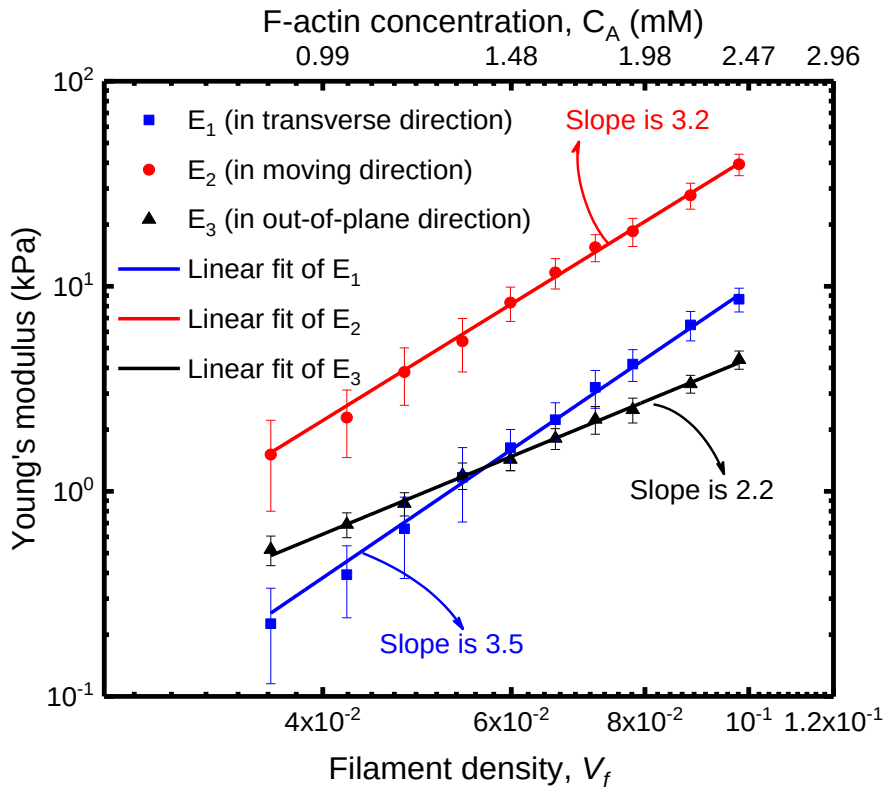

Figure 4.1 The relationship between Young's moduli and actin filament density of the lamellipodial branched actin network. Young's moduli: E_1 in the transverse direction (x direction in Fig. 3.4 in chapter 3), E_2 in cell moving direction (y direction in Fig. 3.4 in chapter 3) and E_3 in the out-of-plane direction (z direction in Fig. 3.4 in chapter 3), respectively.

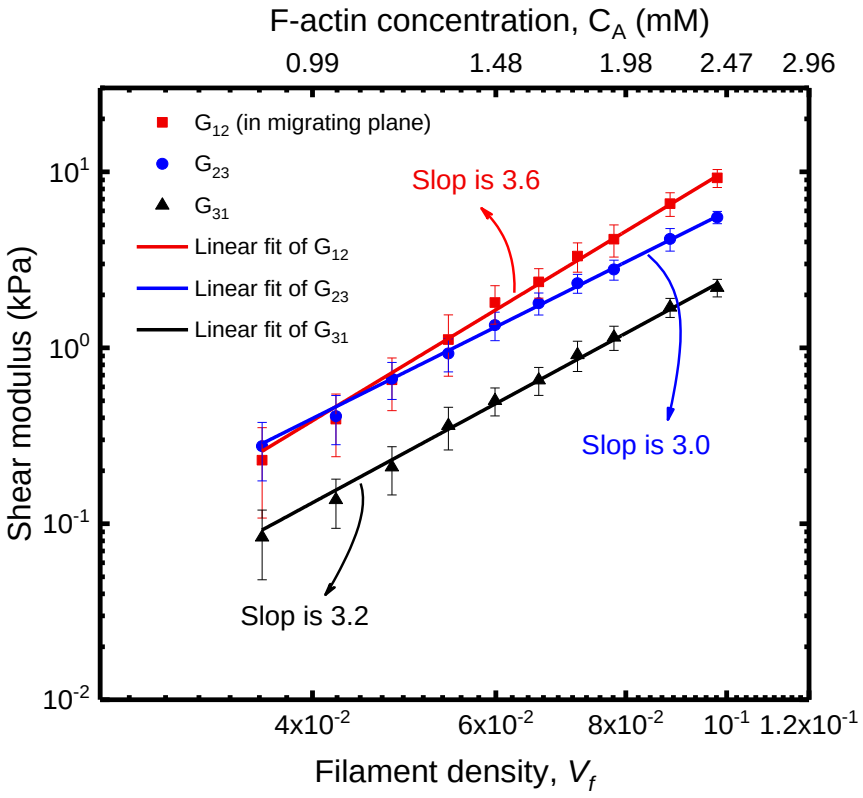

Figure 4.2 The relationship between shear moduli and actin filament density of the lamellipodial branched actin network. Shear moduli: G_{12} in the *xy*-plane, G_{23} in the *yz*-plane and G_{31} in the *xz*-plane in Figure 3.4 in chapter 3.

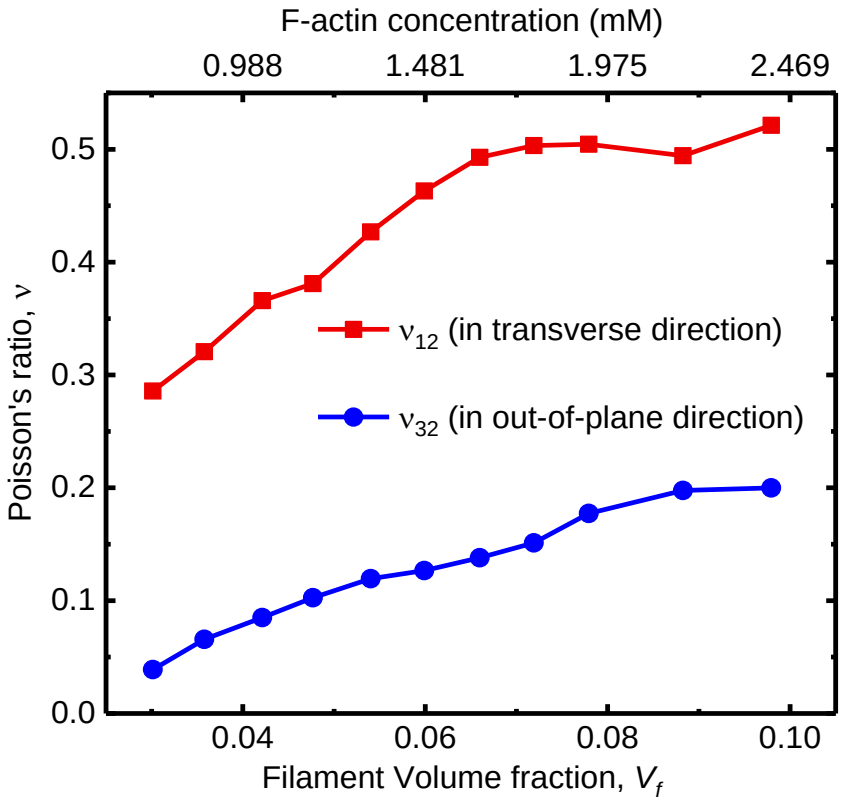

Figure 4.3 Poisson's ratios are defined as $v_{ij} = -\varepsilon_i / \varepsilon_j$ where ε_i is the strain in the i direction when uniaxial stress is applied in the j direction.

Table 4-1 Comparison of Young's modulus E_2 in cell moving direction between our numerical simulation results with V_f from 3.0% to 9.8% and those from the *in vivo* and *in vitro* experiments.

Experiment type	Cell type	E_2 (kPa)	Filament density	Method	Ref.
Our prediction	--	0.6-39	3.0% ~ 9.8%	FEM numerical simulation	-
In vitro	--	1.0-20	--	Atomic force microscope (AFM)	ref.[2]
In vitro	--	0.8-5	--	AFM	ref.[26]
In vitro	--	1.0-10	--	Magnetic dipolar attraction between colloids	ref.[98]
In vivo	Adenocarcinoma cells	2.0-10	--	AFM	ref.[82]

In vivo	Fish epidermal keratocytes	21-44	about 8.0%	AFM	ref.[83]
In vivo	Motile 3T3 fibroblasts	3.0-12	--	AFM	ref.[87]

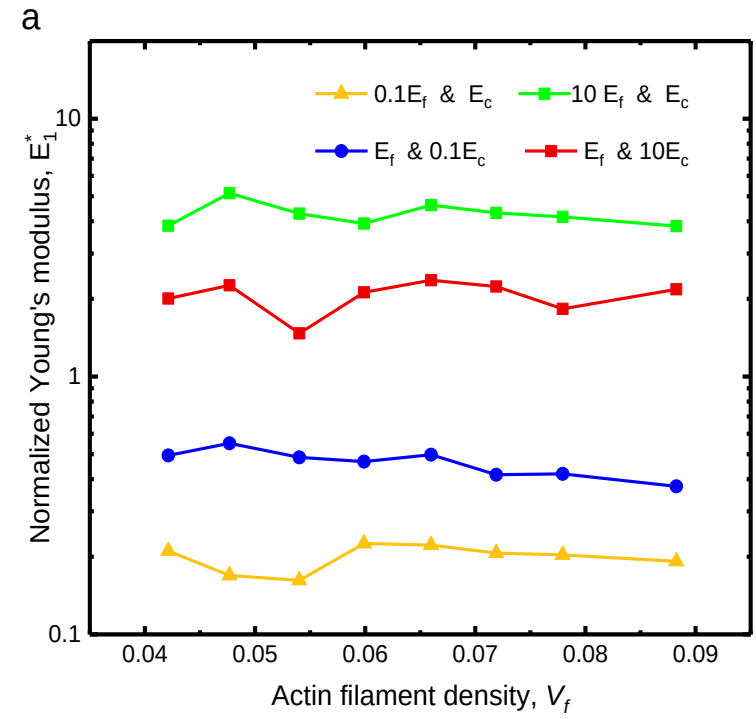

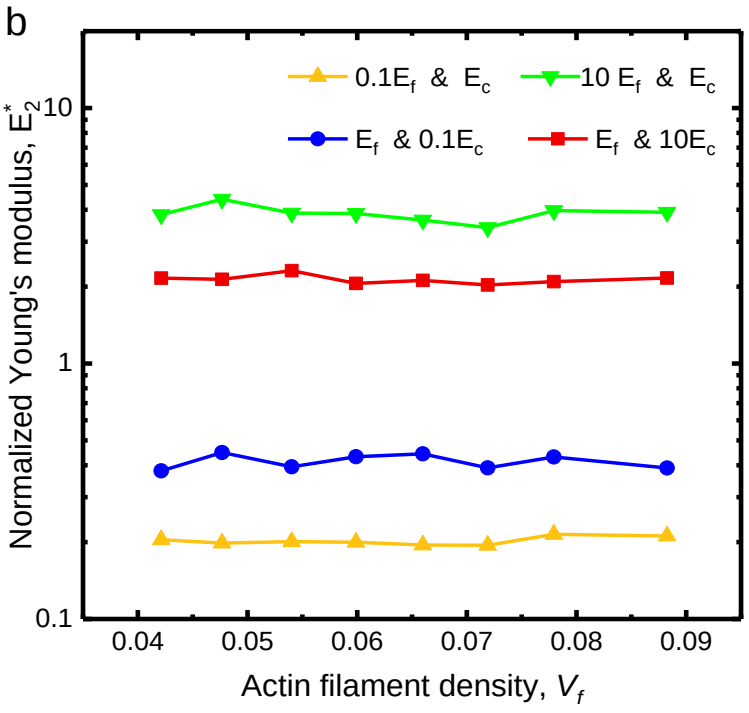

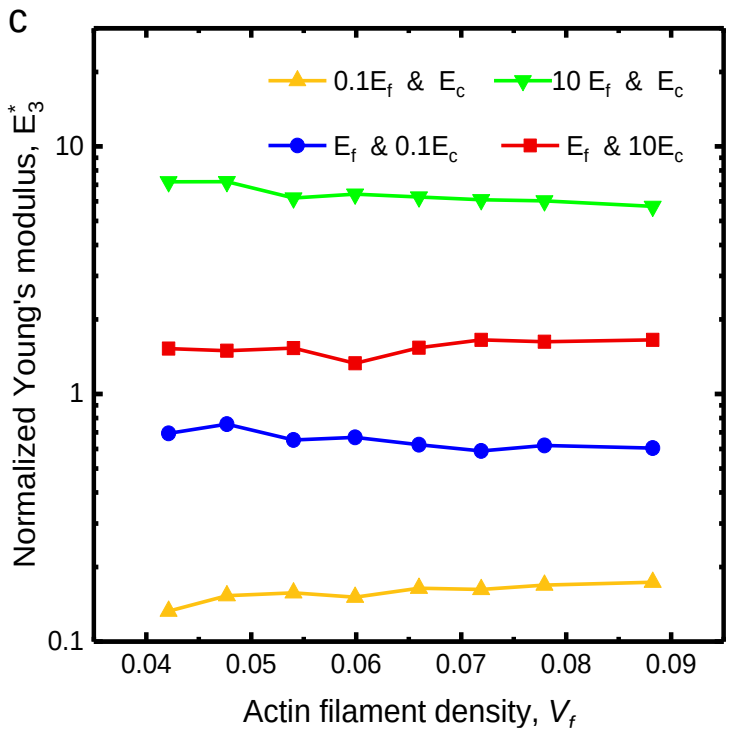
c
0.1E_f & E_c
10 E_f & E_c
E_f & 0.1E_c
E_f & 10E_c
Normalized Young's modulus, E*_3
10
1
0.1
0.04
0.05
0.06
0.07
0.08
0.09
Actin filament density, V_f

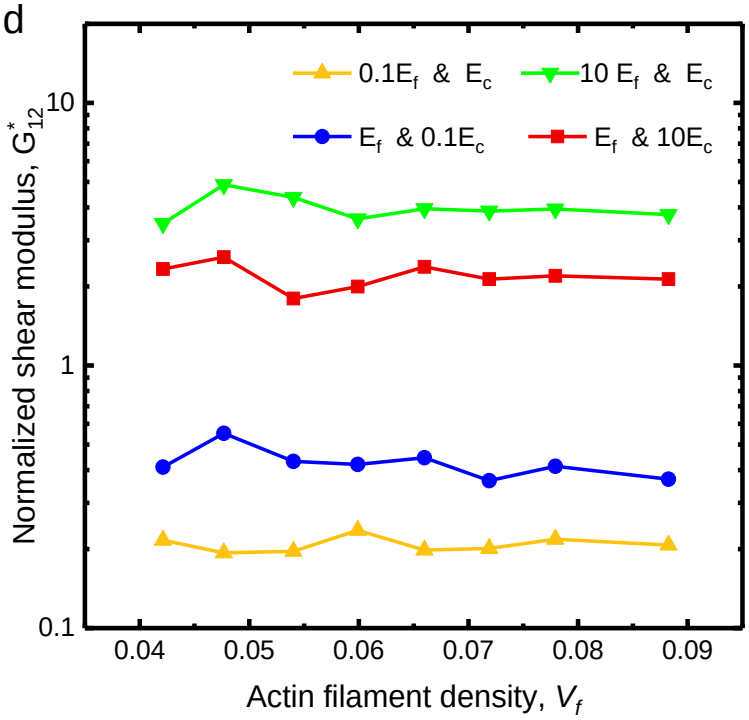
d
0.1E_f & E_c
10 E_f & E_c
E_f & 0.1E_c
E_f & 10E_c
Normalized shear modulus, G*_12
10
1
0.1
0.04
0.05
0.06
0.07
0.08
0.09
Actin filament density, V_f

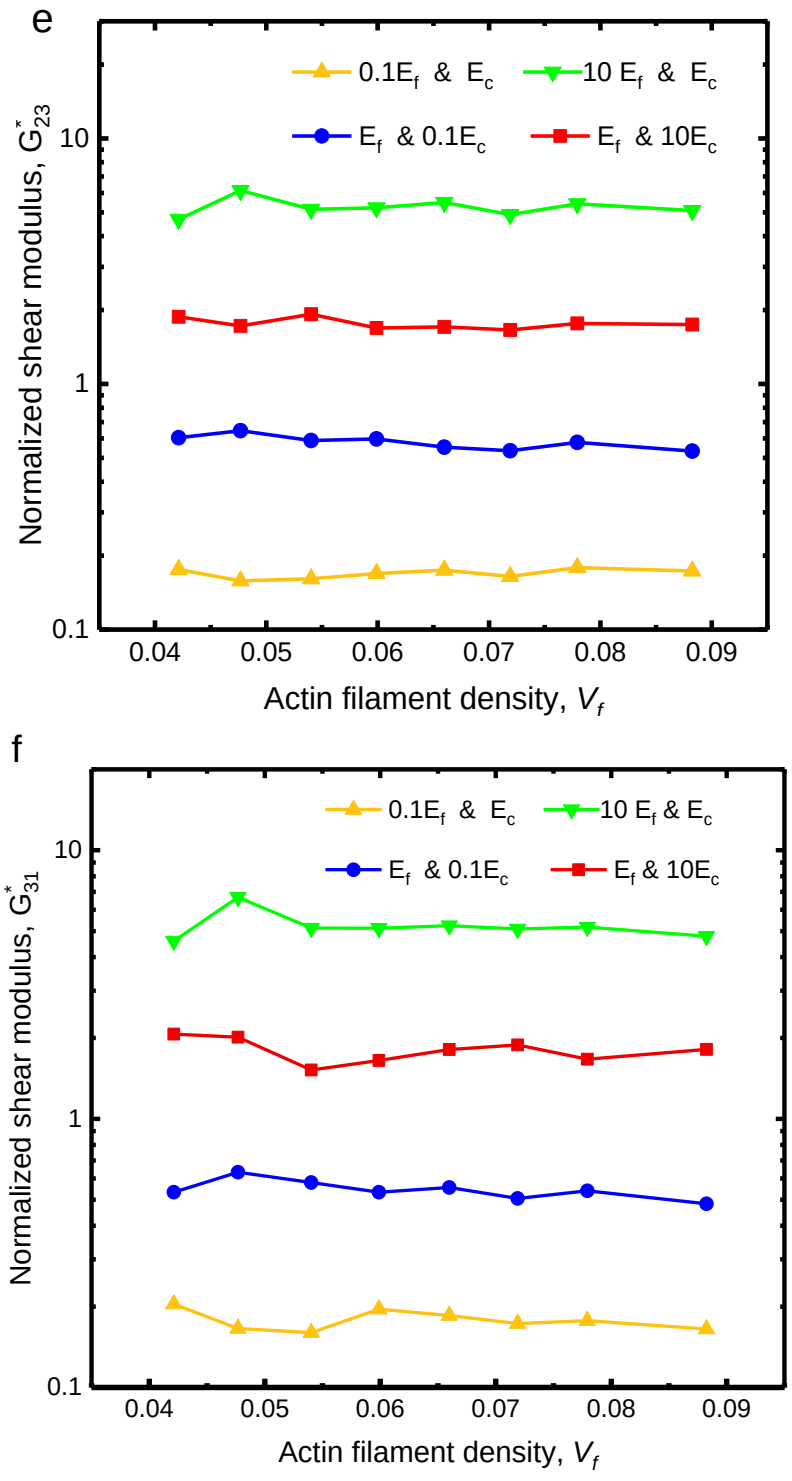

Figure 4.4 The dimensionless Young's and shear moduli of the branched actin network when the Young's modulus of actin filaments is $10E_f$ or $0.1E_f$ and the

Young's modulus of crosslinking proteins is $10E_c$ or $0.1E_c$, respectively. (a) E_1^*; (b) E_2^*; (c) E_3^*; (d) G_{12}^*; (e) G_{23}^*; (f) G_{31}^*. Note that to explore whether the actin filaments or the crosslinking proteins dominate the stiffness of the branched actin network, the results are normalized by the Young's or shear modulus of the branched actin network with the same filament density when the Young's moduli of actin filaments and crosslinking proteins are E_f and E_c. It is found that the normalized values are all more or less constant under the different actin filament densities, which indicates that under all the actin filament densities, the stiffnesses of the branched filament networks are primarily dependent on the stiffness of the actin filaments and less sensitive to the stiffness of the crosslinking proteins.

4.2.2 Successive branches formed by Arp2/3 Complex are essential for cell migration

In this section, we explore the effect of the successive branching generation number K created by Arp2/3 complex from mother filaments (Fig. 4.5) on regulating the elastic properties of the network and investigate its possible value by calculating the network deformation under actin filament propulsive force. In order to exclude the impact of Arp2/3 complex density, the average interval d^{arp} along actin filaments for forming one Arp2/3 complex is generated by using the same uniform distribution ($U(50,150)$) in all models. Here we take the lamellipodium of keratocytes as an example, whose filament density is about 7.8%.

Our results show that the Young's and shear moduli approximately linearly increase with the successive branching generation number K (Figs. 4.6 and 4.7). This sensitive enhancement effect on the network stiffness can be interpreted by the increase of the relatively rigid dendritic size (Fig. 4.5) in the migration direction. When cells move or spread, they use the polymerization force of actin filaments to overcome extracellular microenvironment. We then ask whether the branched actin

network with a small number of successive branching generations K is able to support cell migration. In keratocyte lamellipodium, each filament averagely produces a pushing force of about 2 pN by polymerization [103, 115] and there are about 150 filaments pushing against per um length of the leading membrane [89, 102, 103]. The compressive stress σ and strain ε of the branched actin network in the cell migration direction (i.e. the y direction) can be obtained as

$$\sigma = \frac{nf_p}{wh} \tag{4.2}$$

$$\varepsilon = \frac{\sigma}{E_2} \tag{4.3}$$

where n is the total number of actin filaments that push against the leading edge membrane of lamellipodium; f_p is the average polymerization force (in the cell movement direction) generated by an actin filament. According to (Eq. (4.2)), the stress under the resultant pushing force in this direction can be calculated as 1.5 kPa. With the Young's modulus of the branched actin network obtained from our finite element simulations, this indicates that the compressive strain of the branched actin network with $K = 2$ (Fig. 4.6) is more than 15% (Eq. (4.3)), implying that the network would be too soft [174] and thus can't effectively support the pushing force for cell motility. Therefore, we conclude that most of the subnetworks should have at least 3 successive branching generations in a protruding lamellipodium. Our prediction is supported by the high-resolution experimental images which show that filaments in migrating lamellipodia branch in several successive generations [12, 27, 180]. Because Arp2/3 complex prefers to bind on bent filaments [146, 187] and thus the branched actin network can regulate its successive branches to adapt for cell migration, the low number of successive branching generations in the experiment [145] might be observed from cells that were not in an active migration state.

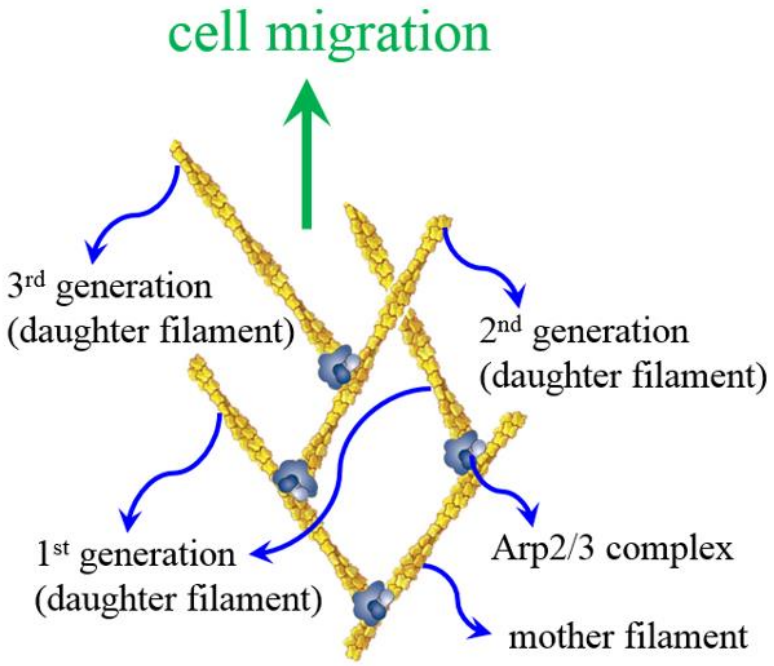

Figure 4.5 Successive branching generations in dendritic structure.

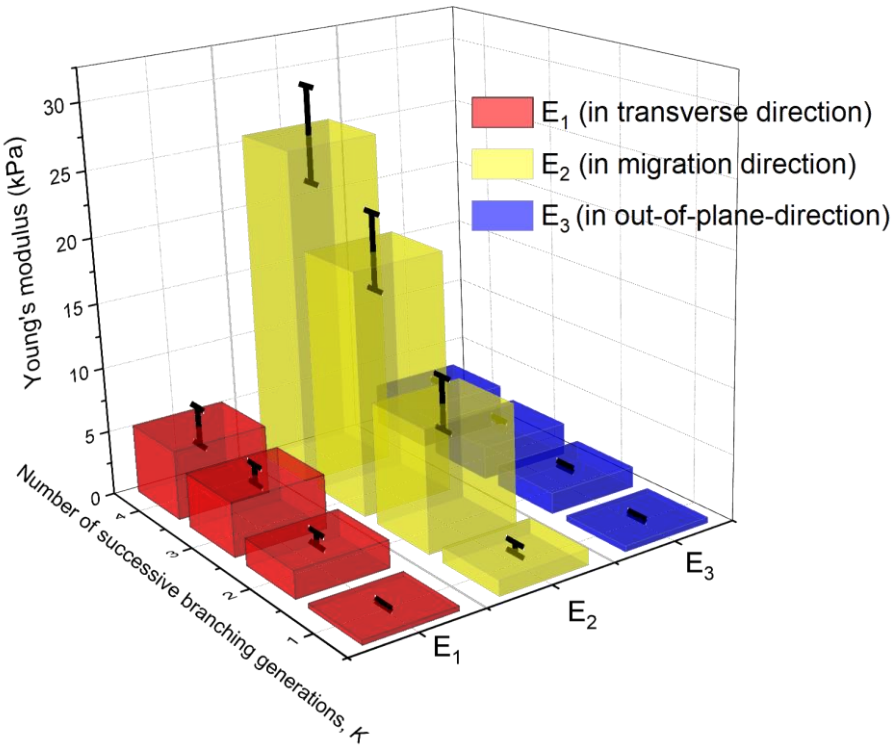

Figure 4.6 The relationship between Young's moduli and the number of successive branching generations from a mother filament of the lamellipodial branched actin network.

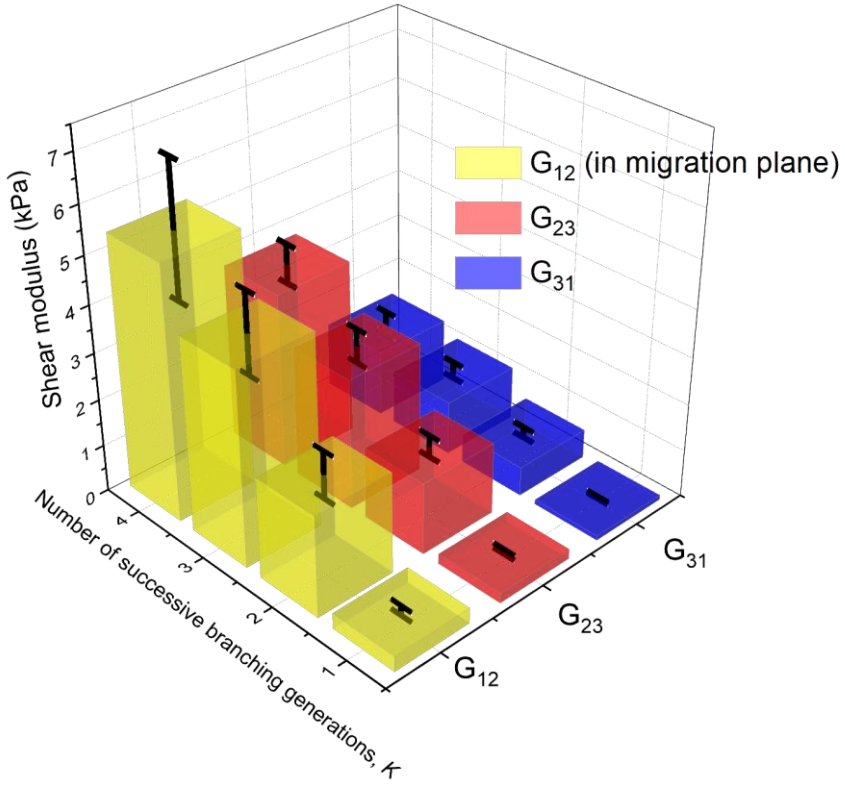

Figure 4.7 The relationship between shear moduli and the number of successive branching generations from a mother filament of the lamellipodial branched actin network.

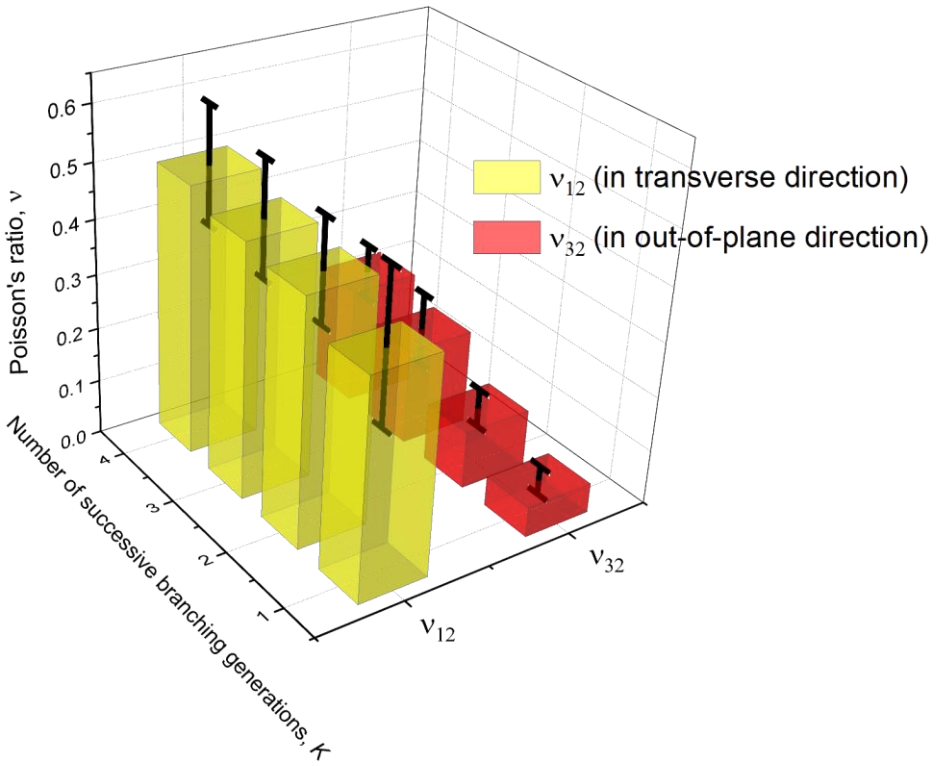

Figure 4.8 Poisson's ratios under the compressive force along the moving direction.

4.2.3 Strengthening and local heterogeneous weakening effects of self-regulated Arp2/3 complex density on the network stiffness

Experiments showed that the concentration of Arp 2/3 complex plays an essential role in cell motility by affecting the branching density in the branched actin network [118, 119]. Here we examine the effects of Arp2/3 complex branching density n_{arp} on the elastic properties of the branched actin network. To avoid the influence of successive branches formed by Arp2/3 complex, we fix the number of successive branching generations at $K = 3$. The density of Arp 2/3 complex n_{arp} is defined as

its average number along the average length of actin filaments, and can be obtained from the following equation

$$N_m(n_{arp}^3 + n_{arp}^2 + n_{arp}) = N_{arp} \tag{4.4}$$

where N_m and N_{arp} are the total number of the mother filaments and the total number of Arp 2/3 complex in the model, respectively. Because the branching connection formed by Arp2/3 complex is relatively rigid [88], the average value of d_{arp}, defined as the distance between two adjacent Arp2/3 complexes along a filament, is also named as characteristic length l_c in the branched actin filament [98].

The simulation results show that the evolution of both the Young's and shear moduli with the increase of branching density can be divided into two stages (Figs. 4.9 and 4.10). When the branching density n_{arp} increases in the normal range from 0.9 to 2.5, it has a noticeable improving effect on the elastic properties of the branched actin network, especially on E_1, E_2 and G_{12} in the cell migration plane (Figs. 4.9 and 4.10). These results explain the experimental findings [118, 119, 193] that inhibition of Arp 2/3 complex for actin nucleation negatively regulates cell migration and invasion. We interpret this sensitive relationship between the macroscopic elastic properties and microscopic branching density formed by Arp2/3 complex as the result of the decrease in the characteristic length l_c. As demonstrated by the stress contour along branched filaments (Fig. 4.11), stress mainly distributes in the filament segments formed by two adjacent Arp2/3 complex branch points. However, when the branching density is over 2.5, its further increase unexpectedly makes the Young's and shear moduli decrease except that only E_3 increases slightly. This indicates that under a certain F-actin concentration, when the branching density is too high, the stiffness of the branched actin network decreases, which is not efficient for supporting cell migrations. Experimental

results also showed that excessive high branch density formed by the Arp 2/3 complex leads to slower cell protrusion [95].

To further investigate the physical mechanisms of why an excessive high branching density induces a lower mechanical stiffness, we check the architectures of these self-assembling models. Strinkingly, the actin network with high Arp2/3 branching density shows severse local heterogeneity (Fig. 4.13). Because the generation of daughter filaments is controlled by Arp2/3 complx branching, excessive branching of Arp2/3 complex inevitably results in local heterogeneity of the global network when the concentration of F-actin is kept constant. We then deliberately regulate the stochastic generation process of Arp2/3 complex to make the distribution of the branches more homogeneous. Our simulation results (highlighted by broken green ellipses in Figs. 4.9 and 4.10) indicate that although the density of Arp2/3 complex n_{arp} increases to 3.62, the Young's and shear moduli are both improved. Consequently, it is the local heterogeneity induced by excessive high branching of Arp2/3 complex that causes the low elastic stiffness. This is also confirmed by the experimental observation that local fractures in the branched actin network occur under the resistance load for cell motility [194]. However, cells have self-regulation mechanisms to optimize their branching density to favor their movements. For example, Profilin, Ena/VASP, Arpin and Gadkin proteins in lamellipodia can negatively regulate the density of Arp2/3 complex branches [44, 95, 120]. Heterogeneity resulted from high branching density of Arp2/3 complex, however, is not always adverse to cell migrations. It is an important way for cells to steer their migrating directions [113].

Our results show that for the branched actin network with the normal filament density of 7.8%, its stiffness reaches the peak value when the branching density is about 2.5, indicating that the optimal spacing between two adjacent branching points along a filament is about 100 nm. In addition, both the Poisson's ratios ν_{12}

and v_{32} noticeably decrease with the increasing branching density and v_{12} is also always larger than v_{32}.

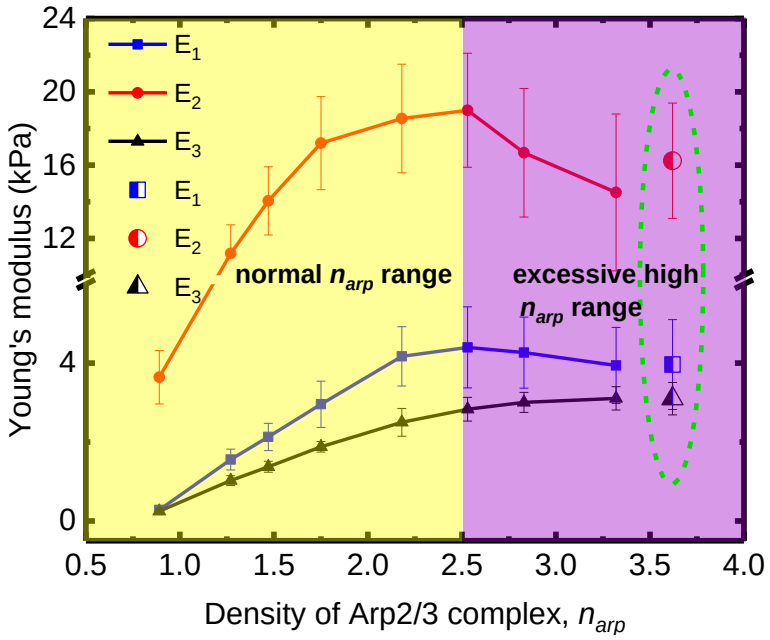

Figure 4.9 Arp2/3 complex density n_{arp} regulates the Young's moduli of the branched actin network.

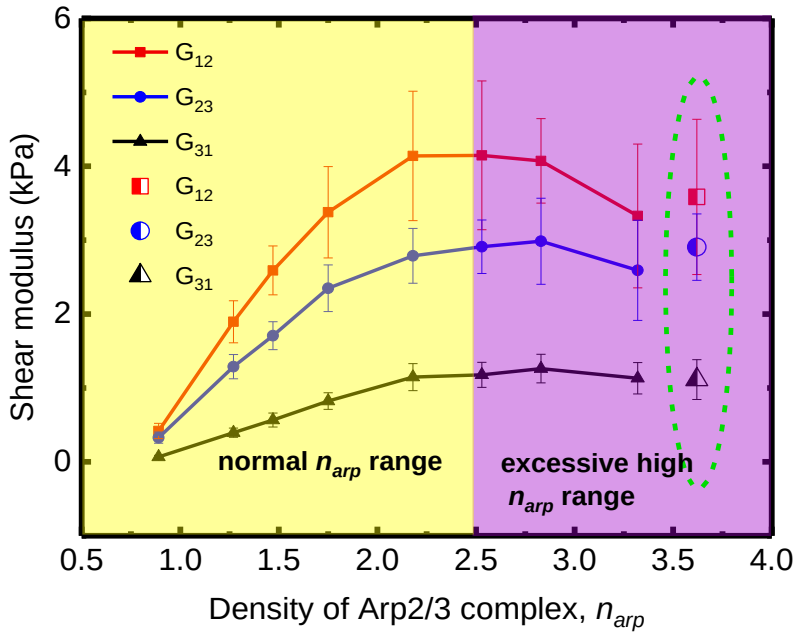

Figure 4.10 Arp2/3 complex density n_{arp} regulates the shear moduli of the branched actin network.

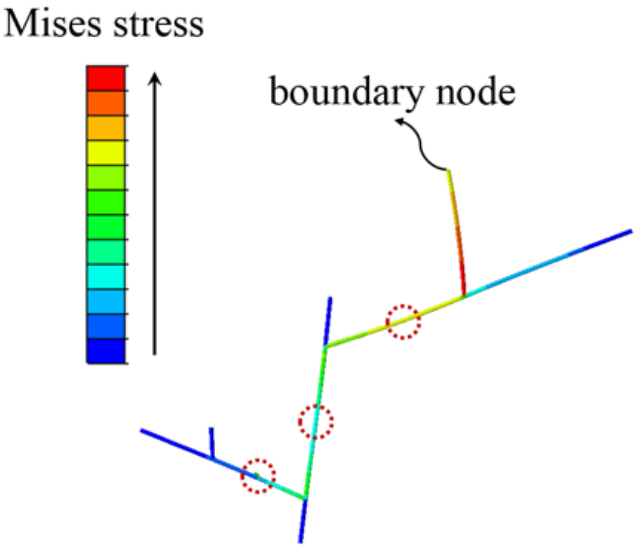

Figure 4.11 Mises stress distribution in the local structure of the network.

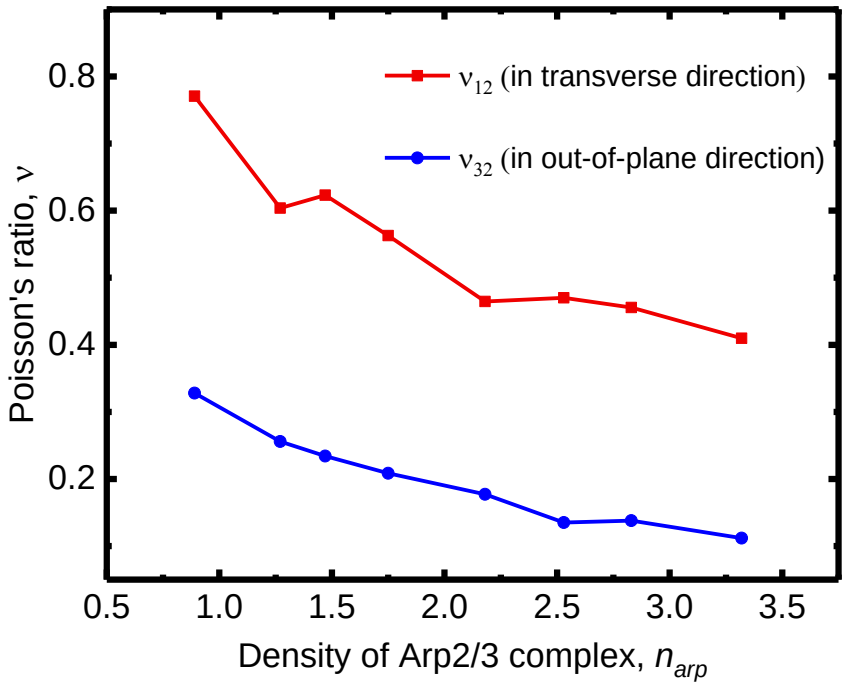

Figure 4.12 Arp2/3 complex density n_{arp} regulates the Poisson's ratios of the branched actin network.

a

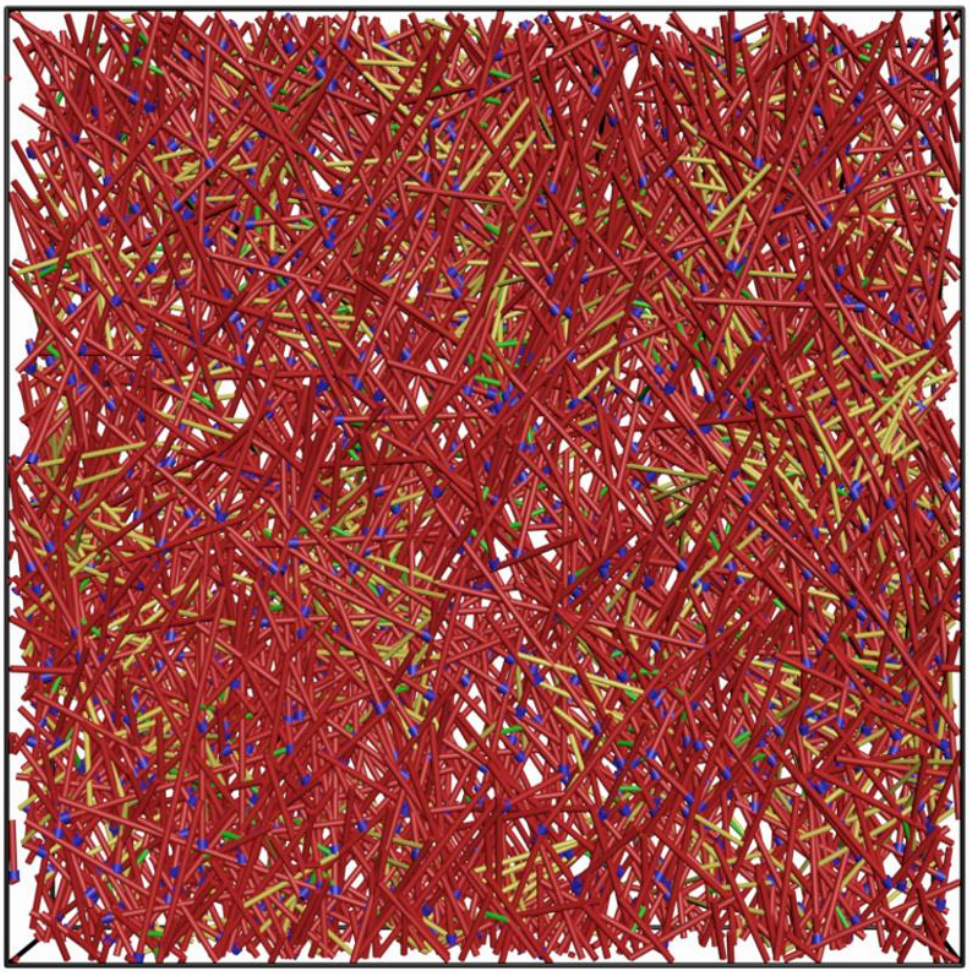

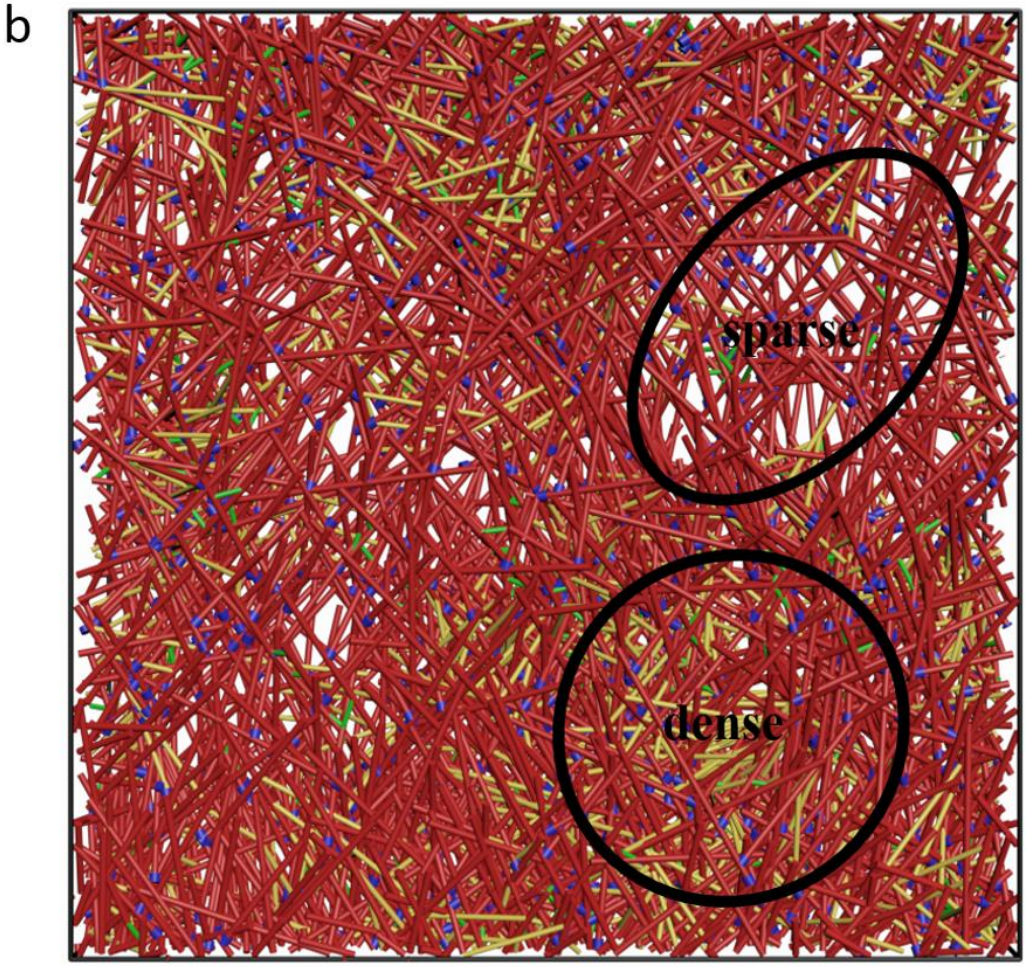

Figure 4.13 Architectures of branched actin networks when actin filament density is 7.8%. (a) Arp2/3 complex density $n_{arp} = 2.5$ (b) Arp2/3 complex density $n_{arp} = 3.3$.

4.2.4 Density of crosslinking proteins regulated by filament density linearly strengthen the network stiffness by increasing connectivity

Crosslinking proteins crosslink and stabilize the dendritic subnetworks into an integrated branched actin network [2, 9, 27, 50, 76, 109, 110]. Theoretical analysis shows that crosslinking connectivity between fibres is a key parameter influencing the mechanical behaviour of fibre networks [170]. Experiments show that mutations

and dysfunction of crosslinking proteins significantly impact the mechanical performance of cytoskeleton [69, 195]. Here, we ask, when they are assembling or disassembling in the branched actin network, how they influence the elastic properties of the lamellipodial branched actin network, and then how they affect cell migration. The density of crosslinking proteins (including both filamin-A and α-actinin) ρ_c is defined as the average number of them along the average length of a filament, and given by

$$\rho_c = r_a N_c / L \tag{4.5}$$

where N_c is the total number of filamin-A and α-actinin, r_a is the average length of actin filaments and L is the total length of actin filaments in the RVE model (Fig.3.4 in chapter 3). To quantitatively assess the impact of crosslinking density on the elastic properties of the branched actin network, we develop the models by giving different possibilities p_c of 1.0, 0.9, 0.8, 0.7, 0.6, 0.5, 0.4 and 0.3 for generating a cross-linker between the two possible points of two filaments to simulate the assembling or disassembling of crosslinking proteins during cell migration. The maximum crosslinking density ρ_c is found to be proportional to the filament density (Fig. 4.14), which suggests the the density of crosslinking proteins can be regulated by filament density. For a given filament density, the crosslinking density has a specific range (Figs. 4.14-17). The larger the filament density of the branched actin network, the broader the range of the crosslinking density ρ_c.

Analogously to the impact of the number of successive branching generations, all the Young's and shear moduli increase linearly with the density of the crosslinking proteins (Figs. 4.15 and 4.16). For the common filament density of 7.8% in keratocytes, as the density of crosslinking proteins increases from 0.33 to 1.08, Young's moduli E_1, E_2 and E_3 and shear moduli G_{12}, G_{23} and G_{31} rise from 0.48 to 4.17 kPa, 2.60 to 18.55 kPa, 0.99 to 2.50 kPa, 0.46 to 4.14 kPa, 0.54 to 2.79 kPa and from 0.18 to 1.15 kPa, respectively. Apparently, the improving effects on E_2,

E_1 and G_{12} in the lamellipodium protrusion plane are very prominent (Figs. 4.15 and 4.16 and 4.18). In addition, the Young's modulus E_2 is improved from 2.60 to 18.55 kPa, which agrees well with the experimental results [2] that crosslinking proteins, i.e., filamin-A and α-actinin, enhance E_2 of the branched actin network from 6 kPa to about 20 kPa. Comparisons of the curve gradients at different filament densities reveal that with the increase in the filament density, the densities of crosslinking proteins exhibit a more obvious influence on the stiffness of the branched actin network (Figs.4.15-4.18). Poisson's ratios v_{12} and v_{23} slightly increase with the increase of the density of crosslinking proteins (Fig. 4.17) as a result of increasing connectivity in the network. Furthermore, in all of these models, Young's modulus E_2 is significantly larger than the other elastic moduli (Fig. 4.18).

Although the crosslinking proteins are very flexible [23, 55, 185], their stabilizing effect by increasing the interpenetrating connectivity in the branched actin network is rather distinct. The branched actin network with a low density of crosslinking proteins is incapable of supporting the propulsion force for cell motility. This reveals the underlying physical mechanism for the experimental finding of human melanoma cells that without crosslinking protein filamin-A, individual Arp2/3 complex is insufficient for maintaining the mechanical stability of the branched actin network at the leading edge [76]. More importantly, here we find that the density of crosslinking proteins has a linear relationship with filament density. Increased extracellular resistance can induce the increase of filament density during cell migration [2, 13]. Consequently, increased resistance intrigues the assembling of crosslinking proteins in the branched actin network, which in turn makes the network stiffer to adapt to the increased resistance for cell migration.

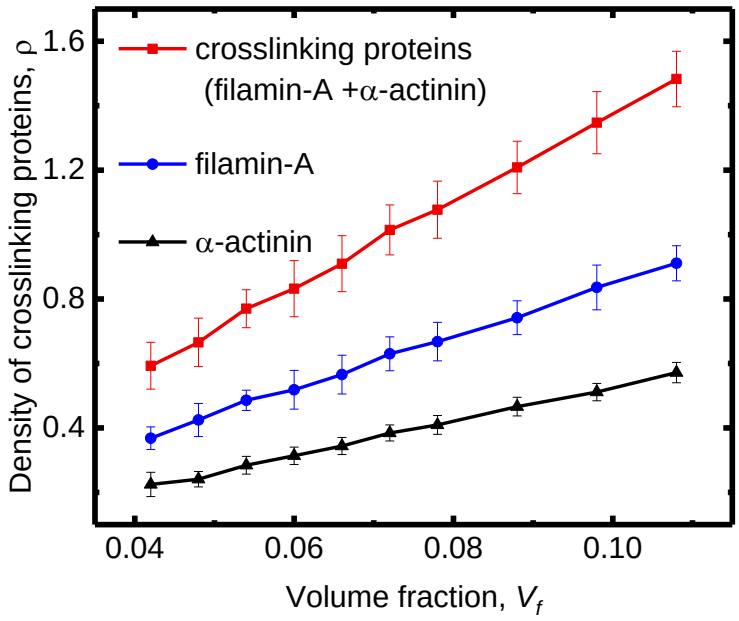

Figure 4.14 Maximum density of crosslinking proteins vs. densities of actin filaments.

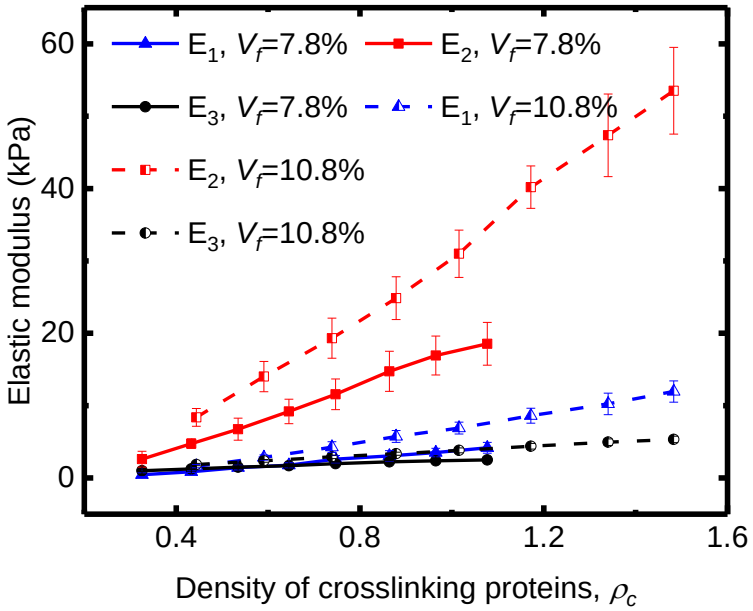

Figure 4.15 Young's modulus vs. the density of crosslinking proteins.

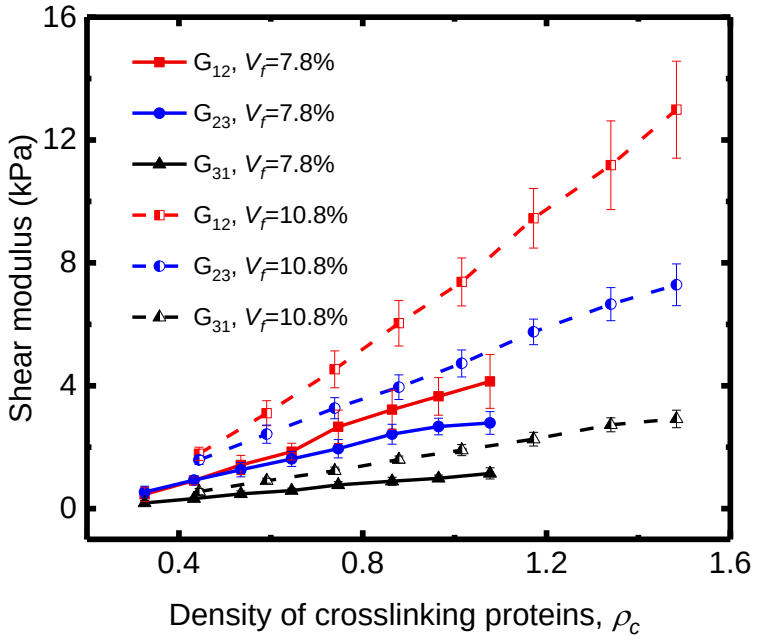

Figure 4.16 Shear moduli vs. the density of crosslinking proteins;

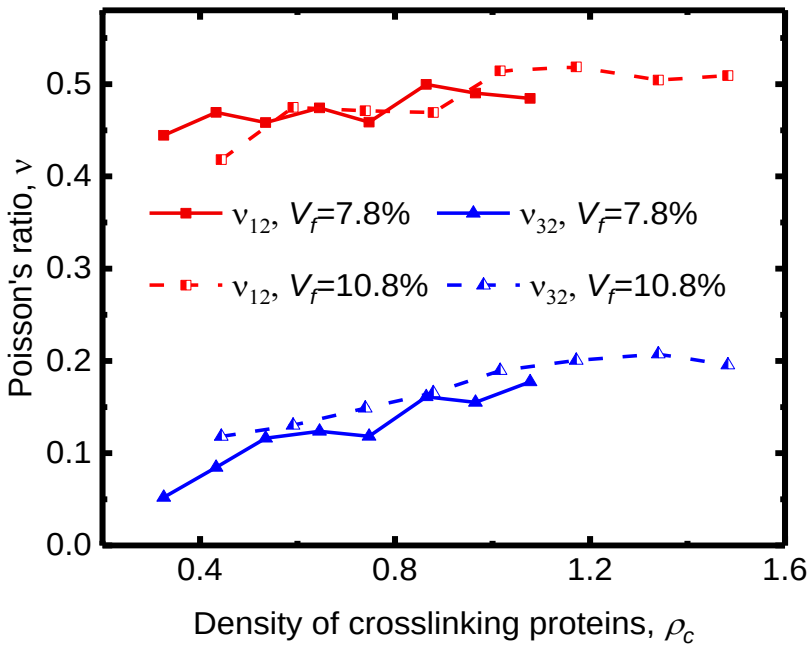

Figure 4.17 Poisson's ratios under uniaxial stress in the y-axis vs. the density of crosslinking proteins;

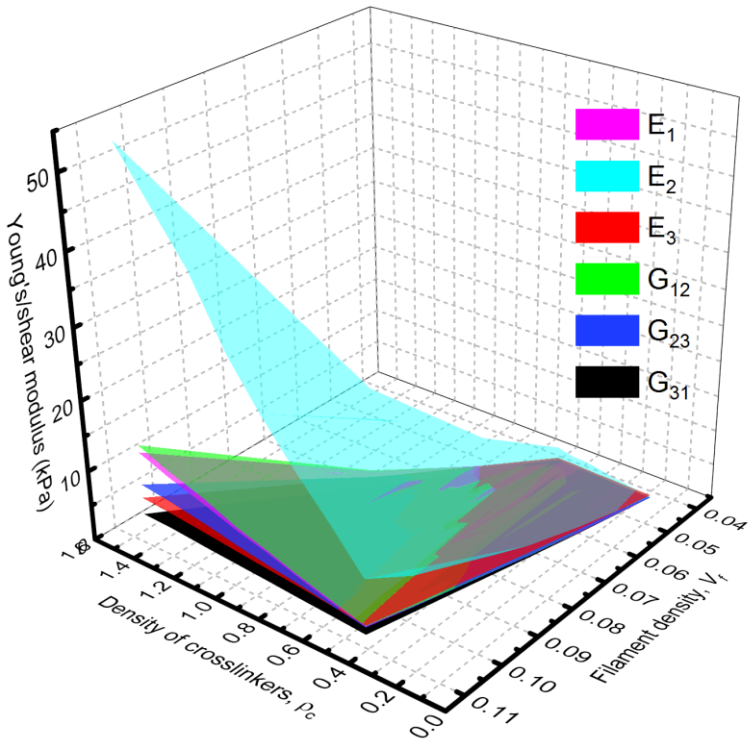

Figure 4.18 Comparison of Young's and shear moduli obtained from 15000 numerical simulations for more than 2400 stochastic models under different combinations of filament densities and crosslinking densities. It shows that Young's modulus E_2 in cell moving direction is much larger than others.

4.2.5 Resistance-adaptive filament orientation transitions are to meet the stiffness demand for cell migration

The orientation of actin filaments in the branched actin network, defined as the angle between an actin filament and cell migration direction, is an important characteristic presented during cell mobility [13, 99, 102, 107, 123, 196, 197]. Both experimental [13] and simulation [99] studies show that actin filaments in the

branched actin network exhibit three types of orientation distribution patterns, i.e., narrow angle pattern (Fig. 4.19a), ±35° angle pattern (Fig. 4.19b) and broad angle pattern (4.19c) [99, 123-125]. When the extracellular resistance load increases from low to high, the orientation distribution of actin filaments in the branched actin network transforms from the narrow angle pattern to the ±35° angle pattern and then to the broad angle pattern, meanwhile, cell migration velocity decreases [13, 99]. Here, we construct the three types of architecture models of the branched actin networks (Figs. 4.19a-c) and explore the underlying physical mechanism of their architecture transformations in response to different magnitudes of extracellular confining resistance.

When the filament density is low (<6.0%), the filament network with the narrow angle pattern has larger Young's modulus E_1 and shear modulus G_{12}, and similar Young's moduli E_2 and E_3 compared to those of the network with the ±35° pattern (Figs. 4.20 and 4.22). This indicates that the narrow angle pattern network with a low filament density is overall stiffer than its counterpart network with the ±35° pattern. However, when filament density increases to intermediate level, Young's modulus E_2 in the cell moving direction of the ±35° pattern network obviously exceeds that of the narrow angle pattern network, suggesting that the ±35° pattern filament network is more stable and effective in supporting cell migration. Since the increase of filament density is induced by increasing extracellular resistance [13], this helps to explain the experimental results that with the increase of extracellular confining resistance, the network architecture transforms from the narrow angle pattern to the ±35° pattern. To be more specific, in the initial stage of cell migration, cell is subject to a low resisting force and most of the filaments grow perpendicularly to the leading membrane, thus an efficient pushing force can be generated to drive cell forward with a rapid velocity. However, with the increase in the resistance force, the filament network with the narrow angle pattern can't support it in the movement direction. Consequently, branched actin filaments rotate and are bent under force (meanwhile, because Arp2/3 complex prefers to bind on

the bent filaments, this also improves the possibility of Arp2/3 complex nucleating more daughter filaments and makes the network's filament density increase from the low level to the intermediate level), changing their orientations into the ±35° pattern to meet the stiffness demand in the cell migration direction.

When the filament density V_f increases to a high level (>9.0%), the Young's modulus E_1 and shear modulus G_{12} of the -70/0/+70° broad angle pattern network are obviously larger than those of the ±35° pattern network, while the Young's moduli E_2 and E_3 of the two patterns are almost the same (Figs. 4.21 and 4.22). In addition, compared to the Poisson's ratio of the ±35° pattern network, the Poisson's ratio ν_{12} of the -70/0/+70° broad angle pattern network is much smaller. These results consistently indicate that the -70/0/+70° broad pattern filament network has stiffer elastic properties. This provides a good explanation for the experimentally observed secondary transformation [13] that when the extracellular confining resistance increases from intermediate range to high range, the filament network architecture transforms from the ±35° pattern into the -70/0/+70° broad pattern. More specifically, with the increase in the resistance force, the stiffness of filament network with the ±35° pattern is incapable of overcoming the extracellular resistance force. Thus, filaments rotate and grow denser, leading to the network architecture transforming from the ±35° pattern into the -70/0/+70° broad angle pattern. We speculate that, under a high extracellular resistance load, the branched actin network needs higher E_1 and G_{12} to prevent large transverse and shear deformations in the migration plane, consequently, adjusting its network architecture to meet the stiffness demand for cell migration.

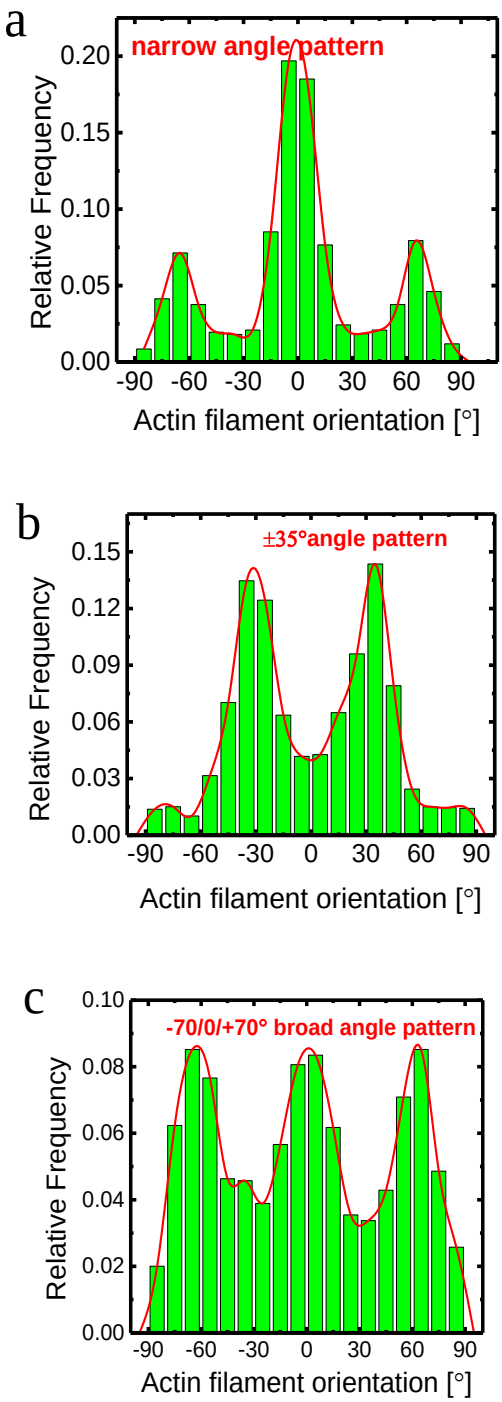

Figure 4.19 Filament orientation distribution. (a) Narrow angle pattern (low actin filament density). (b) ±35° angle pattern (intermediate actin filament density). (c) -70/0/+70° broad angle pattern (high actin filament density).

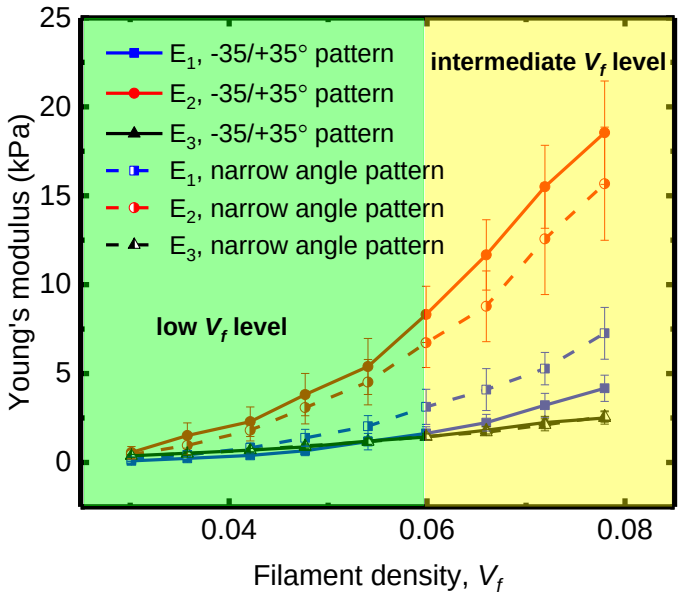

Figure 4.20 Comparison of the Young's moduli between the narrow angle pattern and the ±35° pattern.

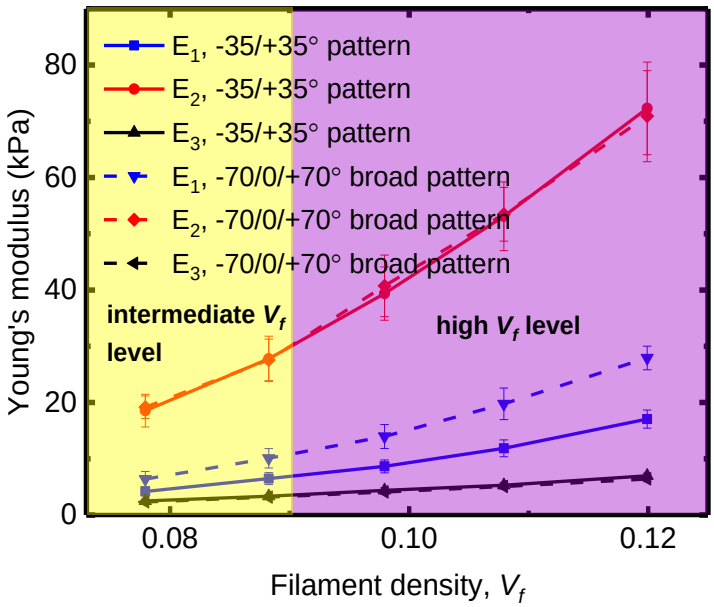

Figure 4.21 Comparison of the Young's moduli between the ±35° pattern and the -70/0/+70° broad angle pattern.

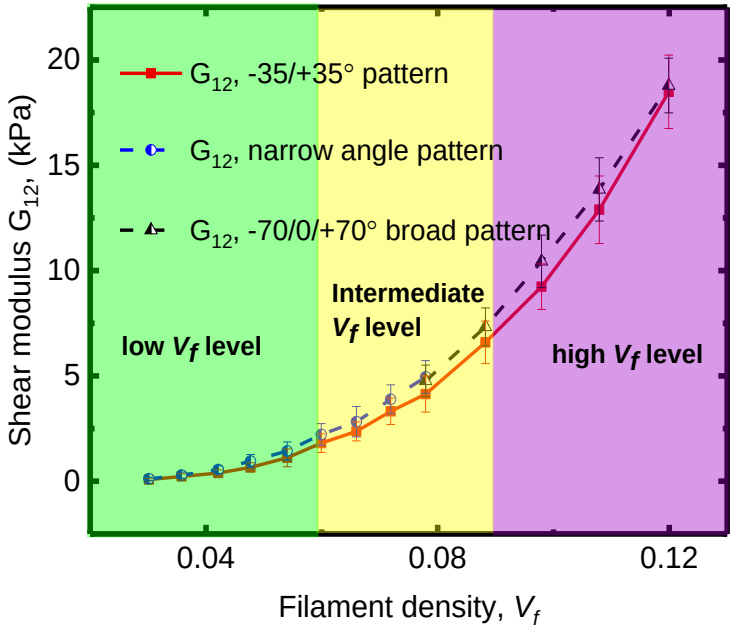

Figure 4.22 Comparison of the shear moduli between the narrow angle pattern, the ±35° pattern and the -70/0/+70° broad angle pattern.

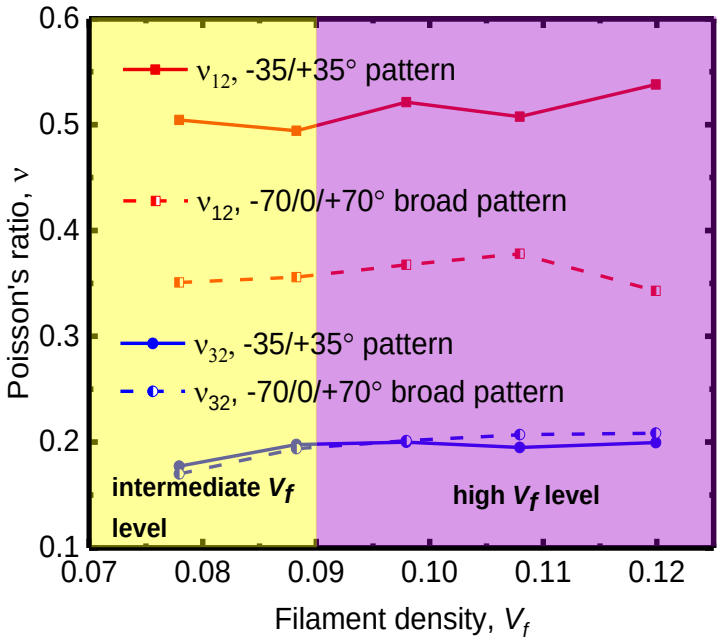

Figure 4.23 Comparison of the Poisson's ratios between the ±35° pattern and the -70/0/+70° broad angle pattern.

4.3 Discussion

4.3.1 Resistance-adaptive elastic properties of branched actin network through remodeling with intracellular proteins and altering geometry.

Three-dimensional extracellular microenvironments are extremely complex and mechanically heterogeneous [2, 13, 17, 108]. When lamellipodial branched actin network drives cells migrating through them, it must experience highly varying immediate resistance [2, 13, 108, 113]. We demonstrate that F-actin concentration (or filament density) improves the stiffness of the branched actin network sensitively. In addition, under the resistance load, the deformation mechanism of the network is mainly dominated by the bending deformation of actin filaments. Because Arp2/3 complex prefers to bind on the convex side of a bent actin filament and nucleates a daughter actin filament [146, 187], it is revealed that, on the basis of actin filament deformations, the polymerizing branched actin network can mechanically sense the varying stiffness of confining microenvironments and accordingly self-regulate its elastic properties by increasing or reducing its filament density through Arp2/3 complex nucleating daughter actin filaments to adapt to the varying load. Specifically, when the resistance impeding cell migration increases, actin filaments in the branched actin network will be bent more severely, and thus more Arp2/3 complexes will bind on them and nucleate more daughter filaments. Hence, the stiffness of the branched actin network becomes larger, which enables the migrating cell to overcome the increased resistance. This resistance-adaptive mechanical mechanism interprets the experimental results [2, 13] that increased resistance load induces high lamellipodial actin network density.

Apart from that, our study unveils the physical mechanism underlying filament orientation transitions under increasing resistance. Each transition makes the branched actin network stiffer, which suggests that the transitions are also mechanical adaptation behaviours for cells to overcome the confining resistance. Moreover, our results demonstrate that the assembling density of crosslinking proteins (filamin-A and α-actinin) improves the network's elastic moduli linearly through increasing its interpenetrating connectivity. Thus, crosslinking proteins provide another important level of stiffness regulation. Since insufficient stiffness of the branched actin network is unable to breach the confinement of extracellular microenvironments, we think that's why the branched actin network with Arp2/3 complex alone and without crosslinking protein filamin-A was unable to drive human melanoma cell migration across porous filters in previous experiments [76]. Notably, we find that the density of crosslinking proteins is proportional to the filament density in the branched actin network. This key feature suggests anthor mechanism regulating cell migration that increased extracellular resistance leads to the increase of filament density, which in turn improves the self-assembling of crosslinking proteins to strengthen the branched actin network for overcoming the increased resistance. Consequently, the assembly of crosslinking proteins in the branched actin network is also a resistance-adaptive behaviour.

In summary, our predictive spatiotemporal model reveals that migrating cells first can sensitively sense the varying extracellular resistance through the bending deformations of actin filaments in the lamellipodial branched actin network. Then, based on the actin filament deformations, cells self-regulate the elastic properties of the branched actin network in a broad range through Arp2/3 nucleating, remodeling with F-actin, filamin-A and α-actinin and altering actin filament orientations to adapt to and to overcome the resistance. Such resistance-adaptive behaviours are versatile and essential in driving cell migration through highly varying and complex 3D confining extracellular microenvironments.

4.3.2 Arp2/3 complex affects the stiffness of branched actin network and cell migration from three aspects.

Arp2/3 complex plays an essential role in determining cell migration behaviours. We find that it can significantly influence the stiffness of the branched actin networks and then affects cell migration from three important aspects, i.e., successive branching generations nucleated by it, its density and distribution uniformity. The number of successive branching generations formed by it linearly enhances the stiffness of the branched actin network. Branched actin network with low successive branching generations is unable to support the driving force for cell migration. In addition, increased branching density of Arp2/3 complex in the normal range significantly improves the network stiffness. Published experiments showed that Arp2/3 complex is dense in metastatic cancer cells [44, 198]. Thus, our results may explain why cancer cells have active migration abilities because a higher density of Arp2/3 complex means a stiffer branched actin network, which can facilitate cancer cells to overcome extracellular resistance more easily and to invade into other tissues and circulatory systems. Furthermore, our results show that, when the Arp2/3 density is in excessive high range, its increase unexpectedly has opposite effect: weakening the network stiffness. Experimental results also showed that excessive high branch density formed by the Arp 2/3 complex leads to slower lamellipodium protrusion [95]. We check the architectures of our self-assembling models and find that when F-actin concentration is kept constant, excessive high density of Arp2/3 complex will inevitably result in severe local inhomogeneities, which is responsible for the poor elastic properties of the global network. This may also explain why branched actin network has local fractures when it protrudes forward under resistance in ref. [194]. However, cells can intelligently regulate the Arp2/3 complex branching density by some regulatory proteins, such as Profilin, Ena/VASP proteins, Arpin and Gadkin, to avoid extreme heterogeneity in the branched actin network [44, 95, 120]. Finally, our results also

indicate that heterogeneity makes some local areas of branched actin network stiffer, which may be related to the mechanisms of branched actin network steering cell migration.

4.3.3 The unique elastic properties of the branched actin network are much different from those of the crosslinked actin network.

Our results show that the Young's and shear moduli of the lamellipodial branched actin network in cell migration direction scale with the filament density to the power of 3.2 and 3.6 ($C_A^{3.2}$ and $C_A^{3.6}$, where C_A is the concentration of F-actin in the network), respectively, which significantly differ from the scaling power of 0.6 reported by the in vitro experiments [2]. Their experimental results showed the scaling power of the branched actin network is much smaller than that ($C_A^{2.0}$) of the crosslinked actin network [190]. Conversely, here our data demonstrate that compared to the crosslinked actin network, the stiffness of the branched actin network is much more sensitive to F-actin concentration. Since crosslinking proteins are much more flexible than actin filaments, the stiffness of the crosslinked actin network is mainly dominated by the weaker crosslinking proteins [199]. In the branched actin network, however, the branching junction nucleated by Arp2/3 complex is relatively rigid [49] and consequently, the stiffness of the branched actin network is more dominated by actin filaments rather than by crosslinking proteins. Such much stronger dependence on F-actin concentration of the branched actin network has significant functional meaning in sensitive regulation of cell migrations through complex microenvironments. We speculate that the published experimental scaling power of 0.6 [2] is mainly due to extremely heterogeneity in the in vitro constructed branched actin network and our results have demonstrated that the uniformity of Arp2/3 complex branching is a key factor impacting the network stiffness. In cells, however, as we previously discussed, there are some Arp2/3 complex regulatory proteins, which can tune the density of Arp2/3 complex

in the branched actin network and improve its efficiency in driving cell migration. More importantly, our study is based on predictive spatiotemporal model, which replicates architectures of the lamellipodial sheet-like branched actin network in migrating cells. Nevertheless, the published experiment [2] is based on the in vitro constructed branched actin network [2], whose structure might be very different from the in vivo sheet-like architecture.

Next, the stiffness of the branched actin network is several orders larger than that of the crosslinked actin network, and the latter is only several Pa to several hundred Pa [192, 199, 200]. In addition, unlike the isotropic crosslinked actin network, the lamellipodial branched actin network is an orthotropic material, of which the Young's modulus in the cell migration direction and the shear modulus in the cell migration plane are notably larger than other moduli. As insufficient stiffness in the cell migration direction of the branched actin network is unable to overcome the extracellular resistance, such superior and special elastic properties have significant consequences for ensuring the mechanical functions of supporting and steering cell migration. Importantly, finger-like filopodia and invadopodia, which are another crucial way of cells mechanically sensing and splitting extracellular matrix, especially for tumor cell invasion and metastasis, [104, 201], usually grow out from the lamellipodial branched actin network. When they protrude in confining extracellular matrix, they will generate high local load on the branched actin network. Therefore, the high elastic and shear moduli of the branched actin network also play an essential role in supporting the activities of filopodia and invadopodia.

4.3.4 Why do lamellipodia grow into sheet-like structures and directionally and persistently drive cell migration against resistances?

Under the resistance load from cell migration direction, the dominant deformation mechanism of the branched actin network is the bending of actin filaments. Because the in-plane Poisson's ratio is much larger than the out-of-plane Poisson's ratio, when cells migrate forward, the actin filaments in the branched actin network mainly undergo backward bending in the lamellipodial migration plane. This feature is crucially important for cell migration. Because Arp2/3 complex prefers to bind on the convex side of a bent actin filament, this feature promotes Arp2/3 complex nucleation and branching a daughter actin filament. Note that, the in-plane backward bending of actin filaments also essentially determines the polymerizing direction of the daughter filament to be in the direction of cell migration. That's why lamellipodia grow into sheet-like structures and persistently grow toward the extracellular confining load. Thus, it is the dominant deformation mechanism and the asymmetric in-plane and out-of-plane Poisson's ratios' effects of the network and Arp2/3 complex branching preference that jointly determine why the lamellipodia grow into sheet-like structures and persistently protrude forward under extracellular confining resistance.

4.3.5 Clinical values

Despite decades of experimental and clinical studies, cancer cell metastasis is still the major cause of mortality in patients [18, 105, 106]. One of the central reasons is that the underlying microscopic intracellular physical mechanism regulating cell migration is unclear [17, 18, 202]. Here, using predictive spatiotemporal model, we identify a resistance-adaptive intracellular mechanical self-regulation mechanism by which the lamellipodial branched actin network senses and adapts to varying

extracellular resistances. Next, this study systematically shows the quantitative relationships between the macroscopic elastic properties of the branched actin network and microscopic intracellular proteins, i.e., F-actin concentration, successive branching generations nucleated by Arp2/3 complexes, density of Arp2/3 complex and density of crosslinking proteins (filamin-A and α-actinin). In addition, the mechanical roles of the individual proteins in the process of lamellipodium driving cell migration are clearly demonstrated. Therefore, our results have important clinical values and applications. For example, while clinical trials show that extracellular protease inhibitors, such as the matrix metalloproteinase inhibitor, have little effect as targets for anticancer therapy [203], our results suggest that creating intracellular inhibitors for Arp2/3 complex might be more effective for reducing cancer cell invasion and metastasis. Except for cancer metastasis, the physical mechanism revealed here also has important clinical values for the pathological problems of embryonic morphogenesis, wound healing, tissue renewal and autoimmune disorders.

Furthermore, Arp2/3 complex also participates in constructing other branched actin networks, which play central mechanical roles in endocytosis, phagocytosis, vesicle trafficking, intracellular pathogen transport and dendritic spine formation [8, 13]. Although here we focus specifically on lamellipodial branched actin network and cell migration, the discovered elastic properties and mechanisms of the highly dynamic network can provide important insights into the underlying physical mechanisms of other physiological and pathological processes.

Chapter 5 Bending-straightening Elastic Racket Theoretical Model and Actin-based Lamellipodial Migration Spatiotemporal Model

5.1 Introduction

To address these fundamentally important questions stated in section 2.3.3, we propose a 'bending-straightening elastic racket' (BSER) model based on geometric nonlinear continuum mechanics theory. In this theoretical BSER model, the spatial and temporal mechanical interactions between the polymerizing free barbed ends of branched actin filaments and the curved LE membrane constrained by extracellular microenvironment are clearly described. Then, we develop the spatiotemporal mathematical model of the three-dimensional self-assembling lamellipodial branched actin filaments pushing the LE membrane forward. This mathematical model systematically encompasses the highly dynamic actin polymerization, capping protein inhabiting filament growth, large-scale deformation of actin filaments, curved LE membrane, deformation dependent Arp2/3 complex branch nucleation, breaking of molecular linkers and varying immediate extracellular resistance.

5.2 Bending-straightening elastic racket (BSER) theoretical model

We first investigate the theoretical mechanical interactions between a polymerizing actin filament and the curved local LE membrane. Near the LE membrane of the

lamellipodium, pointed ends of actin filaments are connected with branched actin network by Arp2/3 complex. The lamellipodial branched actin network establishes integrin-mediated adhesions with extracellular matrix to produce anchor points such that force of actin polymerization can be used for LE membrane protrusion [16, 204]. The network has a high stiffness with Young's modulus about 20 kPa in the migration direction (for the normal actin filament density, see Chapter 4) [2] The binding junction formed by Arp2/3 complex on actin filaments is relatively rigid [49]. Therefore, we hypothesize that the polymerizing actin filaments are fixed at their pointed ends. The LE membrane is bent (Fig. 5.1a) due to the propelling force of growing branched actin filaments beneath it [133]. By referring to differential geometry thought, we simulated this curved LE membrane by dividing it into several continuous inclined planes. Fig.5.1b shows the bottom membrane and the bottom inclined LE membrane. Because the LE membrane is confined by the extracellular microenvironment, we first assume that it is fixed. Even though the force interaction between all polymerizing actin filaments and the bent LE membrane is a three-dimensional problem, the interaction between a single polymerizing actin filament and the local curved membrane can be studied in a 2D deformation plane (Fig. 5.1b). We hypothesize an actin filament and the perpendicular distance of its pointed end to the inclined local LE membrane is h. The polymerizing growth rate of its free barbed end is V_{fil}. If the beginning polymerization time is assumed to be 0. At time t, the length of the actin filament is $l(t)$. Thus,

$$l(t) = V_{fil} t \tag{5.1}$$

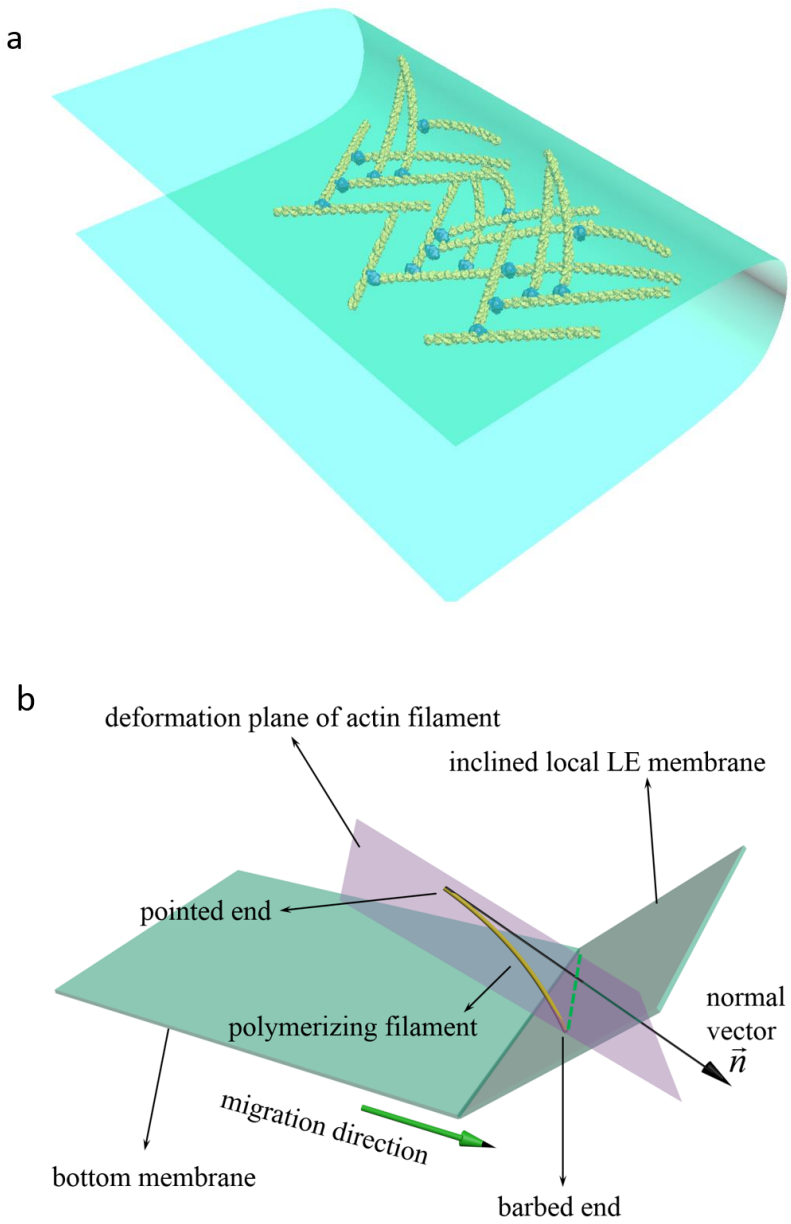

Figure 5.1 Lamellipodial branched actin filaments push the bent LE membrane. (a) Cartoon demonstration of lamellipodial polymerizing branched actin filaments pushing against the curved LE membrane in three dimensions. (b) The interaction between a polymerizing actin filament and the local LE membrane, which is assumed as an inclined plane according to its local curvature and cell migrating direction.

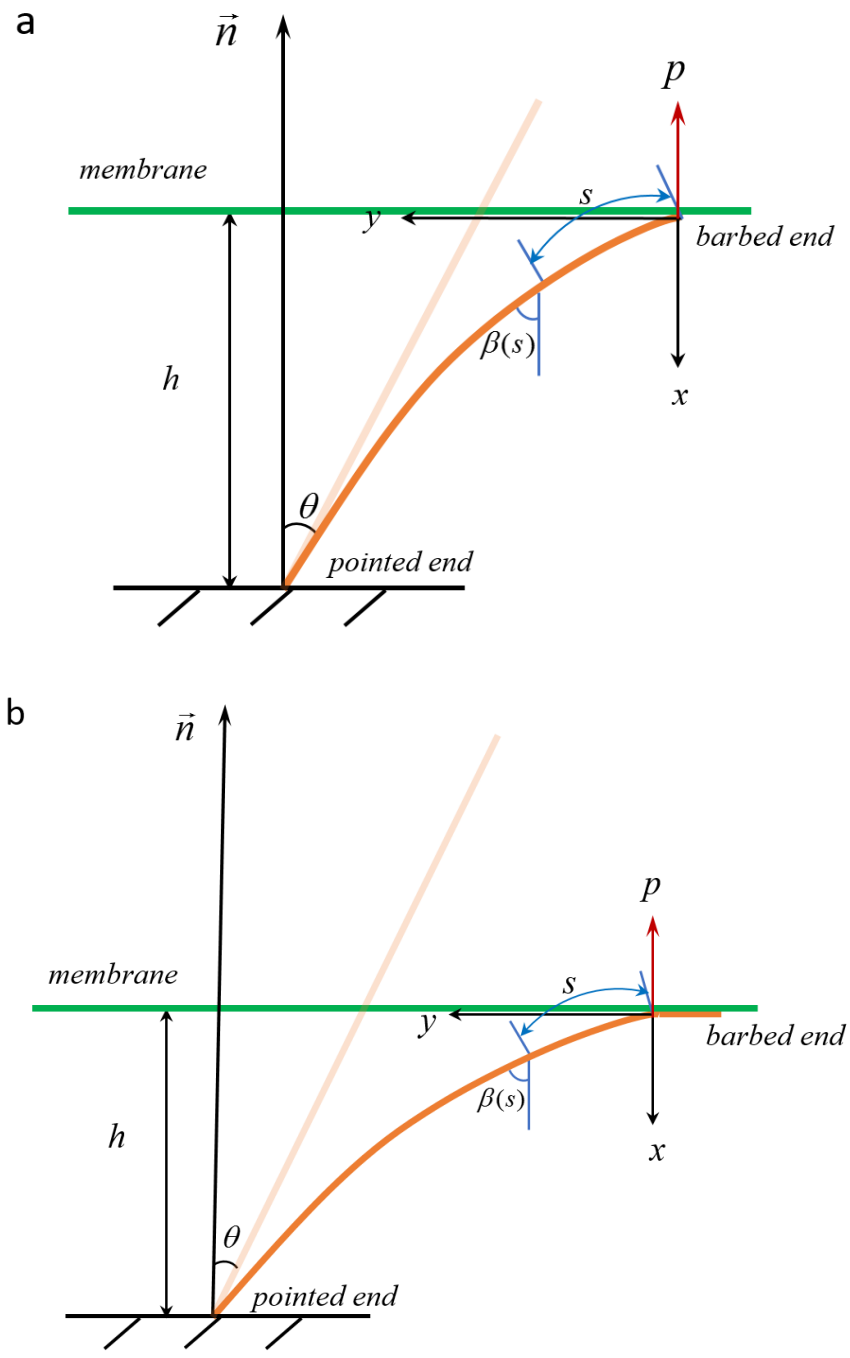

Figure 5.2 Demonstration of the dynamic interaction between the polymerizing actin filament and the local LE membrane in the deformation plane in figure 5.1b.

(a) Actin filament has a point-contact with the local LE membrane. (b) Actin filament has a line-contact with the local LE membrane. Yellow and green represent the actin filament and the local LE membrane, respectively. $\vec{n}$ is the normal direction of the local LE membrane and is parallel with the *x*-axis.

For analysis, the barbed end and pointed end of the polymerizing actin filament are named as $s = 0$ and $s = l(t)$, respectively. When the polymerizing barbed end of the actin filament has not reached the inclined local LE membrane yet, i.e., $l(t)\cos\beta < h$, there is no force interaction between them and thus the actin filament is straight. Therefore, the constraint force p acting on the local LE membrane is 0.

With the polymerizing time increase, the length of the actin filament increase. When the barbed end reaches the membrane, i.e., $l(t)\cos\theta \geq h$, the growing filament is compressed, sheared and bent as the result of the constraint of the local LE membrane. When the angle $\beta(0)$ of the barbed end is less than $\pi/2$, the growing barbed end slides along the local LE membrane in the deformation plane and has a point-contact with it. The deformed configuration of the polymerizing actin filament and the restraint force p acting on the local LE membrane is shown in Fig. 5.2a. The relationship between the bending curvature and the bending moment is expressed as

$$\frac{d\beta_b(t)}{ds} = -\frac{p}{EI}\int_0^{s(t)}(1-\varepsilon)\sin\beta ds \tag{5.2}$$

$$\varepsilon = \frac{p\cos\beta}{EA} \tag{5.3}$$

where E is the Young's modulus of actin filaments and is 2 GPa [23]. A and I are the cross-sectional area and the second moment of the cross-sectional area of actin filaments. They can be calculated with the diameter (7nm) of actin filaments. At the pointed end of the actin filament, i.e., $s = l(t)$, $\beta_b(l(t)) = \theta$. Thus, the angle

$\beta_b(s)$ along the deformed actin filament as a result of combined effects of bending, polymerizing growth and axial compression can be determined as

$$\beta_b(s,t) = \theta + \frac{p}{EI}\int_{s(t)}^{l(t)}[(1-\varepsilon)\int_0^{s(t)}(1-\varepsilon)\sin\beta ds]ds \tag{5.4}$$

The angle induced by transverse shear deformation of the polymerizing actin filament can be expressed as

$$\beta_s(s,t) = \frac{\kappa p \sin\beta}{GA} = \frac{2\kappa(1+\nu)p\sin\beta}{EA} \tag{5.5}$$

where ν is Poisson's ratio of the actin filament material and is about 0.3 [23]; κ is the shape factor and is 10/9 for a circular cross-section. Thus, the total angle of the deformed actin filament is

$$\beta(s,t) = \beta_b(s,t) + \beta_s(s,t) \tag{5.6}$$

For a given value of the polymerizing length ($l = V_{fil}t$) of the actin filament at time t, the nonlinear function $\beta(s)$ can be determined using the iterative method [173, 174] and the deformation compatibility condition is

$$\int_0^{l(t)}(1-\varepsilon)\cos\beta ds = h(t) \tag{5.7}$$

At time t, to solve the nonlinear function $\beta(s,t)$, we reverse the interacting process by using the local LE membrane to compress the actin filament to meet the Eq. (5.7). Specifically, we first assume actin filament to be straight. Then, we divide its length $l(t)$ into 100000 elements and apply load p by very small increments of $\triangle p$ (0.01pN) using iterative method in the normal direction of the local LE membrane to compress the actin filament. The initial strain ε is chosen as $\frac{\triangle p\cos\beta(s)}{EA}$ and initial angle $\beta(s)=\theta$. With the deformation compatibility

equation of $h(t)$ (Eq. (5.7)), the convergent solution of $\beta(s,t)$ and the corresponding restraint force p that the polymerizing actin filament acts on the LE membrane can be obtained through iterations.

The mean curvature ξ of the geometrical nonlinear deformed actin filament is given as

$$\xi(t) = \frac{\beta(0) - \beta(l(t))}{l(t)} \tag{5.8}$$

The total deformation energy of the actin filament $U(t)$ is given as the sum of bending energy $U_b(t)$, the axial compression energy $U_c(t)$ and shearing deformation $U_s(t)$ energies

$$U_b(t) = \frac{1}{2} EI \int_0^{l(t)} (\frac{\beta_b(t)}{ds})^2 ds = \frac{p^2}{2EI} \int_0^{l(t)} [\int_0^{s(t)} (1 - \frac{p\cos\beta}{EA}) \sin\beta ds]^2 ds \tag{5.9}$$

$$U_c(t) = \frac{1}{2} \int_0^{l(t)} \frac{(p\cos\beta)^2}{EA} (1 - \frac{p\cos\beta}{EA}) ds \tag{5.10}$$

$$U_s(t) = \int_0^{l(t)} \frac{\kappa(1+\nu)(p\sin\beta)^2}{EA} (1 - \frac{p\cos\beta}{EA}) ds \tag{5.11}$$

$$U(t) = U_b(t) + U_c(t) + U_s(t) \tag{5.12}$$

When the angle of the barbed end $\beta(0)$ increases to $\pi/2$, the barbed end of the actin filament begins to have line contact with the local LE membrane (Fig. 5.2b). Thus, with the continuing polymerization of the actin filament, its length growth will not result in the changes of restraint force p and deformation energy U because the polymerizing line contact part of the actin filament has no deformation. In the above analysis, the restraint force p is in the normal direction of the local LE membrane rather than in the cell migration direction. If the angle between the

normal direction of local LE membrane and the direction of cell migration is ϕ, the propulsive force f_p (in cell migration direction) acting on the local LE membrane for cell migration by the actin filament can be express by

$$f_p(t) = p(t)\cos\phi \tag{5.13}$$

During cell migration, the polymerizing lamellipodial branched actin filaments experience large scale deformations due to the constraint of the LE membrane and extracellular matrix [2, 26]. Pioneering experiments showed that the bending deformation of actin filaments can intrigue a mechano-chemical reaction that Arp2/3 complexes bind on the convex side of the actin filament and nucleate daughter actin filaments [146]. The number of Arp2/3 complexes n_i^{arp} binding on the actin filament i increases with the increase of the deformation curvature ξ_i [146]. We hypothesize the relationship between the space d^{arp} of two adjacent Arp2/3 complex branches along an actin filament and deformation curvature ξ as Eq. (5.14). If the length of actin filaments is l_i, the number of Arp2/3 complexes binding on it as well as the number of daughter actin filaments nucleated can be expressed by Eq. (5.15).

$$d^{arp} = \begin{cases} 300 & if\ \ 0 \le \xi < 0.3 \\ 150 & if\ \ 0.3 \le \xi < 1 \\ 100 & if\ \ 1 \le \xi < 3 \\ 80 & if\ \ 3 \le \xi < 4 \\ 50 & if\ \ \xi \ge 4 \end{cases} \tag{5.14}$$

$$n_i^{arp} = l_i / d^{arp} \tag{5.15}$$

Thus, the number of actin filaments $N(t)$ at the time t pushing against the LE membrane can be expressed as

$$N(t) = \sum_{i=1}^{m} n_i^{arp}(\xi_i) + m(t) \tag{5.16}$$

where $m(t)$ is the number of mother actin filaments pushing against the LE membrane. With more and more daughter filaments being generated, the resultant propulsive force F_p exerting on the LE membrane increases and its value at a time t can be expressed

$$F_p(t) = \sum_{j=1}^{N(t)} f_{pj}(\theta, t) \tag{5.17}$$

The total elastic energy $\prod$ of all the free ends filaments pushing the leading edge membrane at time t is

$$\Pi(t) = \sum_{j=1}^{N(t)} U_j(\theta, t) \tag{5.18}$$

When the LE membrane continuously moves forward, some of the actin filaments will become straight and finally detach with the LE membrane due to capping proteins stopping their barbed ends polymerizations. Experimental studies showed that some actin filaments are linked to LE membrane surface through N-WASP protein [205, 206], which will generate an adhesion attachment force to pull back the LE membrane [113, 142, 143, 206]. When the detachment happens, the attachment force disappears suddenly. Thus, there are four forces acting on the LE membrane: propulsive force F_p, attachment force f_a, membrane tension f_m and extracellular resistance f_r (Fig. 5.3).

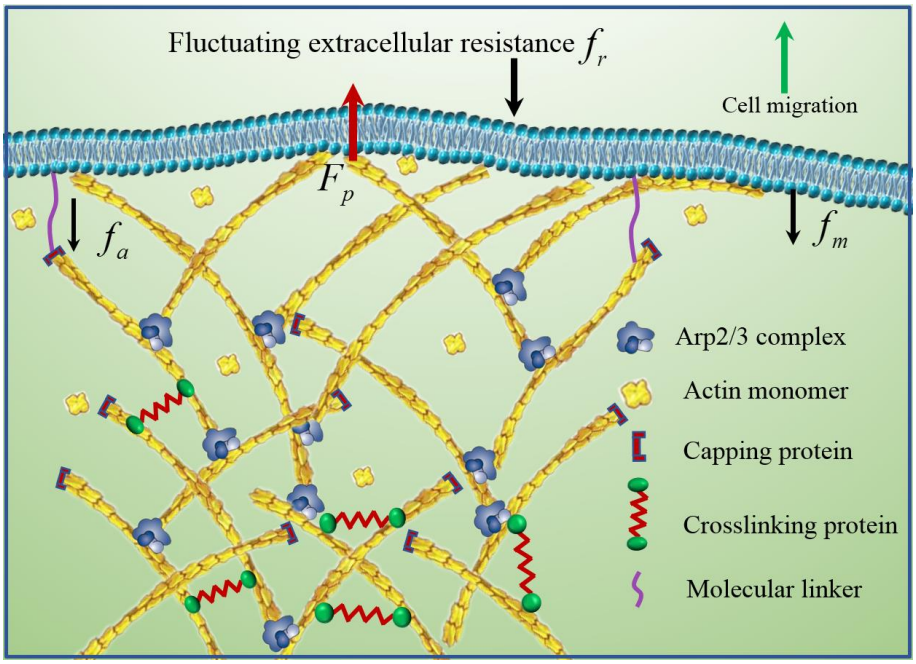

Figure 5.3 Cartoon demonstration of forces acting on the lamellipodial LE membrane during cell migrating in extracellular microenvironment.

The extracellular resistance force f_r for lamellipodia protruding forward is in the range of 0.4 nN/μm and 2 nN/μm [89]. The LE membrane tension force f_m at the leading edge is about 365 pN/μm [207]. The attachment force f_a between the barbed ends of actin filaments and the LE membrane is estimated at 300～1200 pN/μm [142]. In the balanced state, the four forces, i.e., propulsive force, attachment force, LE membrane tension and extracellular resistance force, should satisfy

$$F_p = f_a + f_r + f_m \tag{5.19}$$

The abrupt break of these attachment molecular linkers results in the saltatory motion of branched actin filaments [142, 143]. Experiments showed that the saltatory step size ΔS is about 6 nm [147, 208]. In the realistic condition, cells migrate in extremely complex extracellular microenvironments. There is not only

the break of molecular linkers between barbed ends of actin filaments and LE membrane, but also the ruptures of extracellular crosslinking matrix networks [15, 209] and some of nascent integrin adhesion bonds [210], which fix the LE membrane to extracellular matrix. Thus, for simplifying the model to capture the main characteristics of cell migration at the LE membrane, it is assumed that when the resultant propulsive force is higher than the stall force ($f_a + f_r + f_m$), some of these molecular linkers break and the LE membrane protrudes forward with a step size $\triangle s$. Therefore, at the time $t+1$, the position $s(t+1)$ of the LE membrane in cell migration direction can be expressed by

$$s(t+1)=\begin{cases} s(t) & if\ F_p \le f_a + f_r + f_m \\ s(t)+\triangle s & if\ F_p > f_a + f_r + f_m \end{cases} \tag{5.19}$$

When the LE membrane protrudes one step, the bent actin filaments extend simultaneously. Both the propulsive force and the deformation energy of them are released partially. Therefore, we name our model as 'bending-straightening elastic racket' (BSER) model. As the LE membrane protrudes forward step by step, some of the actin filaments fall behind and lose contact with the LE membrane. They will form the branched actin network with crosslinking proteins, such as filamin-A and α-actinin, to support cell protrusion [27]. If the interval time between the two adjacent protruding steps is $\triangle t$, the LE membrane protruding velocity V_m in each saltatory step is calculated by

$$V_m = \frac{\triangle s}{\triangle t} \tag{5.20}$$

5.3 Self-assembling spatiotemporal mathematical model

We develop a framework to simulate the three-dimensional self-assembling branched actin filaments driving the LE membrane forward both spatially and

temporally. In this framework, the mechanical interactions between the growing branched actin filaments and the curved LE membrane, which is confined by the varying immediate extracellular microenvironment, are described by our proposed BSER model. The complicated stochastic mechanochemical reactions, such as the highly dynamic actin polymerization, capping protein inhabiting filament growth, Arp2/3 complex nucleation and molecular linker rapture between the filament barbed end and curved LE membrane, are systematically incorporated. The LE lamellipodium usually has a thickness of about 150 nm and a width of about 20~50 μm [85]. Thus, in our spatiotemporal model, we use periodic boundaries in the horizontal direction, which is perpendicular to the direction of cell migration.

Under the propulsive force of the actin filaments, the LE membrane is bent [133]. By referring to the differential geometry thought, we divide the LE membrane into four inclined planes to represent it (Fig. 1a and b). The equation of the *k*th membrane plane can be expressed by a point $(x_{mpk}, y_{mpk}, z_{mpk})$ on it and its normal vector $(0, \sin\theta_{mpk}, \cos\theta_{mpk})$ as follow

$$\sin\theta_{mpk}(y - y_{mpk}) - \cos\theta_{mpk}(z - z_{mpk}) = 0 \tag{5.21}$$

where θ_{mpk} is the inclined angle of the *k*th membrane plane with respect to the cell migration plane. Then, actin monomers stochastically nucleate into a certain number of short actin filaments in the three-dimensional lamellipodial space. Specifically, the pointed end coordinates (x_i^p, y_i^p, z_i^p) of the *i*th filament are randomly generated in the rectangular domain of $1000nm \times 50nm \times 150nm$, respectively. To make actin filament grow in the lamellipodial sheet-like space, a local spherical coordinate system is created by regarding every pointed end as the origin. This local spherical coordinate system is used to determine the orientation and the final barbed end coordinates $(r_i, \varphi_i, \theta_i)$ of each actin filament. Actin filaments normally grow to a length of about 200 nm in lamellipodia [12, 95]. They are confined in the lamellipodium. The orientation of actin filaments relative to the

cell migrating direction is generally about ±35° [99]. Thus, the final spherical coordinates $(r_i, \varphi_i, \theta_i)$ of the barbed end are randomly generated by a normal or a uniform distribution defined as

$$r_i \sim N(200, 30);\ \varphi \sim U(70°, 110°);\ \theta \sim N(\pm 35°, 15°) \tag{5.22}$$

The final coordinates (x_i^b, y_i^b, z_i^b) of the barbed end of the ith actin filament in the global Cartesian coordinate system are expressed by Eq. (5.23). To grow in the lamellipodial sheet-like space, it should satisfy Eq. (5.24).

$$\begin{pmatrix} x_i^b \\ y_i^b \\ z_i^b \end{pmatrix} = r_i \begin{pmatrix} \sin\varphi\cos\theta \\ \sin\varphi\sin\theta \\ \cos\varphi \end{pmatrix} + \begin{pmatrix} x_i^p \\ y_i^p \\ z_i^p \end{pmatrix} \tag{5.23}$$

$$\left\{ z_i^p \mid 0 \le z_i^p \le 150 \right\} \tag{5.24}$$

The polymerizations of actin filaments are realistically simulated by adding actin monomers to the barbed ends. The final coordinates of the barbed end mean the coordinates after the barbed end being capped by a capping protein and also losing contact with the LE membrane. Before this stage, however, the barbed end is in a very dynamic state. The growth rate V_{fil} of the polymerizing free barbed ends of actin filaments is expressed by

$$V_{fil} = \delta(C_a k_{on} - k_{off}) \tag{5.25}$$

where $\delta \approx 2.5$ nm is the half size of an actin monomer; C_a is the local actin monomer concentration; $k_{on} \approx 10\ \mu M^{-1}s^{-1}$ is the polymerizing rate constant and $k_{off} \approx 1\ s^{-1}$ is the depolymerizing rate constant [25]. Thus, before the barbed end attaching the LE membrane, the coordinates of it at the time t is

$$\begin{pmatrix} x_i^b(t) \\ y_i^b(t) \\ z_i^b(t) \end{pmatrix} = V_{fil}(t - t_i^{begin}) \begin{pmatrix} \sin\varphi\cos\theta \\ \sin\varphi\sin\theta \\ \cos\varphi \end{pmatrix} + \begin{pmatrix} x_i^p \\ x_i^p \\ x_i^p \end{pmatrix} \tag{5.26}$$

where t_i^{begin} is the time that actin filament begins to polymerize. After the barbed end attaching the LE membrane, the continuous polymerizing actin filament is bent due to the confinement of the LE membrane and extracellular resistance. When the bending curvature reaches a certain value, Arp2/3 complexes will nucleate and stochastically bind onto the convex side of the actin filament with an interval d^{arp}. The mechanical interaction between the polymerizing actin filament and the protruding curved LE membrane is described by our BSER model. The whole process of lamellipodia protrusion is in a very high dynamic state. In order to identify the coordinates of the Arp2/3 complex during this dynamic process, we create a local Cartesian coordinate system $O'x'y'z'$ by regarding the pointed end of the actin filament as the origin O'. Plane $O'x'y'$ is the deformation plane of actin filament due to its mechanical interaction with inclined LE membrane plane. Axis $O'x'$ is the normal vector of the inclined LE membrane plane. For the jth Arp2/3 complex on the *i*th actin filament, the deflection vector $(\triangle x'_{ijk}(t), \triangle y'_{ijk}(t), \triangle z'_{ijk}(t))$ of the Arp2/3 complex by interacting with the inclined LE membrane plane k in the local coordinate system at the time t can be calculated according to the nonlinear geometrical deformation of actin filament with the BSER model. Then, with Jacobian determinant, the dynamic coordinates $(x_{ij}^{as}(t), y_{ij}^{as}(t), z_{ij}^{as}(t))$ of the Arp2/3 complex attaching the actin filament in the global Cartesian coordinate system at the time t can be obtained by

$$\begin{pmatrix} x_{ij}^{as}(t) \\ y_{ij}^{as}(t) \\ z_{ij}^{as}(t)\_ \end{pmatrix} = \begin{bmatrix} \frac{\partial x}{\partial x'} & \frac{\partial x}{\partial y'} & \frac{\partial x}{\partial z'} \\ \frac{\partial y}{\partial x'} & \frac{\partial y}{\partial y'} & \frac{\partial y}{\partial z'} \\ \frac{\partial z}{\partial x'} & \frac{\partial z}{\partial y'} & \frac{\partial z}{\partial z'} \end{bmatrix} \begin{pmatrix} \triangle x'_{ijk}(t) \\ \triangle y'_{ijk}(t) \\ \triangle z'_{ijk}(t) \end{pmatrix} + V_{fil}(t_{ijk}^{arp} - t_i^{begin}) \begin{pmatrix} \sin\varphi\cos\theta \\ \sin\varphi\sin\theta \\ \cos\varphi \end{pmatrix} + \begin{pmatrix} x_i^p \\ y_i^p \\ z_i^p \end{pmatrix} \quad (5.27)$$

where t_{ijk}^{arp} is the time that the *j*th Arp2/3 complex attaches the *i*th actin filament as a result of mechanical interaction with the inclined LE membrane plane k. The Jacobian determinant can be calculated from the transformation relationship between the local and global Cartesian coordinate system. When an actin filament grows to its final length, capping protein will cap it and stop it from polymerization. Thus, the final length of the *i*th actin filament also can be expressed by

$$r_i = V_{fil}(t_i^{cap} - t_i^{begin}) \quad (5.28)$$

where t_i^{cap} is the time that a capping protein binds on the barbed end of the actin filament.

The length r_{ij}^{arp} of Arp2/3 complex is normally about 10 nm [47]. It binds on the convex side of a bent actin filament [146] with an angle of about 70° [49]. Thus, the possible branching position of Arp2/3 complex is constrained on a half conical surface around the actin filament. The azimuthal angle φ_{ij}^{arp} of Arp2/3 complex in its local spherical system is generated by the distribution defined by Eq. (5.22). Daughter actin filament will nucleate and grow out from the Arp2/3 complex with a final length of about 200nm in lamellipodia. Therefore, the azimuthal angle φ_{ij}^{arp} should allow the forthcoming nucleated daughter filament to polymerize to a length, which is produced by the distribution $N(200,30)$. Collectively, the azimuthal angle

φ_{ij}^{arp} and the end point coordinates $(x_{ij}^{ae}(t), y_{ij}^{ae}(t), z_{ij}^{ae}(t))$ of the *j*th Arp2/3 complex on the ith actin filament at time t should satisfy Eqs. (5.29-31)

$$\left\{\varphi_{ij}^{arp} \mid 0 \le z_{ij}^{ae}(t) + 200\cos\varphi_{ij}^{arp} \le 150\right\} \tag{5.29}$$

$$\sqrt{(x_{ij}^{ae}(t) - x_{ij}^{as}(t))^2 + (y_{ij}^{ae}(t) - y_{ij}^{as}(t))^2 + (z_{ij}^{ae}(t) - z_{ij}^{as}(t))^2} = r_{ij}^{arp} \tag{5.30}$$

$$\cos\alpha = \frac{\triangle x_{ijk}^{local}(t)(x_{ij}^{ae}(t) - x_{ij}^{as}(t)) + \triangle y_{ijk}^{local}(t)(y_{ij}^{ae}(t) - y_{ij}^{as}(t)) + \triangle z_{ijk}^{local}(t)(z_{ij}^{ae}(t) - z_{ij}^{as}(t))}{\sqrt{\triangle x_{ijk}^{local}(t)^2 + \triangle y_{ijk}^{local}(t)^2 + \triangle z_{ijk}^{local}(t)^2}\sqrt{(x_{ij}^{ae}(t) - x_{ij}^{as}(t))^2 + (y_{ij}^{ae}(t) - y_{ij}^{as}(t))^2 + (z_{ij}^{ae}(t) - z_{ij}^{as}(t))^2}} \tag{5.31}$$

where $(\triangle x_{ijk}^{local}(t), \triangle y_{ijk}^{local}(t), \triangle z_{ijk}^{local}(t))$ is the local vector of the bent actin filament segment, where Arp2/3 complex binds on. This vector updates with time as a result of actin filament polymerization, LE membrane protrusion and the mechanical interaction between them. It can be calculated with the BSER theoretical model. α is the angle between the mother filament and the Arp2/3 complex, and is generated by a Gaussian distribution of $N(70°, 2°)$.

After the binding of Arp2/3 complex, a daughter actin filament begins to nucleate from it with the barbed end in its branching orientation. Then, the daughter filament polymerizes by adding actin monomers onto the barbed end. The position of the daughter filament is also in a dynamic state with Arp2/3 complex, whose position is determined by the deflection equation of the mother filament. Similar to the mother actin filament, the polymerizing daughter filament will also mechanically interact with the LE membrane and be bent. New Arp2/3 complexes will bind on it and branch next generation daughter actin filaments. With more and more actin filaments pushing against the LE membrane, the propulsive force F_p increases. When the propulsive force is larger than the resultant force of membrane tension force f_m, extracellular resistance f_r and attachment force f_a of molecular linker, the molecular linker will rupture and the LE membrane will protrude one step. Thus, these bent actin filaments pushing against the LE membrane will either

extend partially or straighten as a result of falling behind the LE membrane. Meanwhile, the mechanochemical reactions, such as actin filament polymerizing, Arp2/3 complex binding, capping protein capping and new actin filament nucleating, are consistently happening. Collectively, using our BSER model, we construct here the self-assembling spatial and temporal evolution of positions, protrusions and mechanical interactions of lamellipodial branched actin filaments and curved LE membrane in three dimensions.

Chapter 6 Migrating Cells Sense and Adapt to Extracellular Microenvironment

6.1 Introduction

By applying our theoretical BSER model to the spatiotemporal model constructed in Chapter 5, we perform large-scale numerical simulations to realistically simulate the polymerizing and self-assembling lamellipodial branched actin filaments driving the LEs of migrating cells to protrude in different extracellular mechanical microenvironments, and study the spatial and temporal LE protruding behaviours of migration cells. Strikingly, unlike previous models [99, 125, 140-143], which can only predict one or two cell migration features, our BESR model very systematically and consistently predicts all the aforementioned important cell migration behaviours in section 2.3.2 in chapter 2. Our spatial and temporal simulation results are validated by a series of advanced experimental results in refs. [2, 13, 95, 113, 115, 123, 134, 144, 147]. The self-assembling evolution process of the sheet-like architecture of the lamellipodial branched actin network during driving cell migration is also exhibited. More importantly, we reveal the very fundamental microscopic physical mechanisms underlying these macroscopic actin-based cell migration behaviours in highly varying extracellular microenvironments. It is fundamentally important to elucidate these physical mechanisms for the ultimate goal of finding effective therapies, which can improve the beneficial migration of normal cells, such as for embryonic morphogenesis, wound healing and autoimmune disorders, and block the invasion of harmful cells, such as cancer cells metastasis.

6.2 Results

6.2.1 Propulsive force acting on local LE membrane, deformation energy and mean curvature of a growing filament

To gain insight into the evolutions of the propulsive force, deformation energy and mean curvature of a polymerizing actin filament pushing against the curved LE membrane, we first assume that the LE membrane is unmovable due to confinement of an extremely high extracellular resistance f_r. The local LE membrane plane is assumed to have an inclined angle of $60°$ relative to cell migrating plane. In order to fully present the mechanical interaction between the polymerizing actin filaments and the LE membrane, actin filaments here are allowed to polymerize to a longer length of 300nm and then are capped by capping proteins and stop growing. The Young's modulus of actin filaments is about 2 GPa [23]. Experimental measurements showed that most of the lamellipodial branched actin filaments at the LE membrane have an angle θ around $\pm 35°$ with respect to cell migrating direction in the migrating plane [123]. Thus, here we demonstrate three kinds of spatial conditions of actin filaments, which have in-plane angles $\theta = 25°,\ 35°$ and $45°$, respectively. Their out-of-plane angles are all kept being $5°$ in the lamellipodial sheet-like space. Actin monomer concentration at the LE membrane is normally 10-50 μM [140]. We assume that it is 40 μM. Thus, according to Eq. (5.25), an actin monomer is added to the barbed end of an actin filament every 2.5 ms and hence the growing rate of actin filaments is 1 nm/ms [99].

As shown in Fig. 6.1a, the propulsive force for cell migration produced by the actin filament with the common in-plane angle $\theta = 35°$ is in the range of 0-8 pN, which agrees well with the published experimental data 0-9 pN [115]. With the nucleating of actin monomers at the barbed end of the actin filament, the evolution of the force interaction between an actin filament and the local LE membrane is

complicated (Fig. 6.1a). Specifically, at the initial stage when actin filament has not reached the LE membrane yet, the propulsive force acting on the membrane, deformation energy and mean curvature of the actin filament are all zero. After the barbed end reaching the LE membrane, actin filament begins to have a point contact with the membrane. Both the propulsive force and the mean bending curvature rapidly increase to maximum values and afterward decrease gradually with the continuing polymerization of the actin filament. The deformation energy of actin filament shows a consistent increase with a declining gradient. Importantly, the propulsive force, deformation energy and bending curvature of the actin filament with a small in-plane angle θ are much larger than those of the actin filament with a large angle, which highlights that the actin filament with a small in-plane angle is much more effective for propelling cell migration. For the condition of $\theta = 25°$, when the actin filament polymerizes to 262.5 nm, the point-contact with the LE membrane becomes a line-contact, which indicates that the polymerizing barbed end of the actin filament is paralleled with the local inclined LE membrane from this time. Thus, even though actin monomers continuously nucleate at the barbed end, the actin filament has no more deformation. As a result, the protruding force, deformation energy and mean curvature of the actin filament keep constant (Fig. 6.1a-c). However, for the actin filaments with $\theta = 35°$ and $45°$, before they are capped by capping proteins at the length of 300 nm, they have not reached their critical lengths at which they have line contacts with the inclined local LE membrane. The critical length of an actin filament is affected by its spatial orientation and relative position to the local LE membrane.

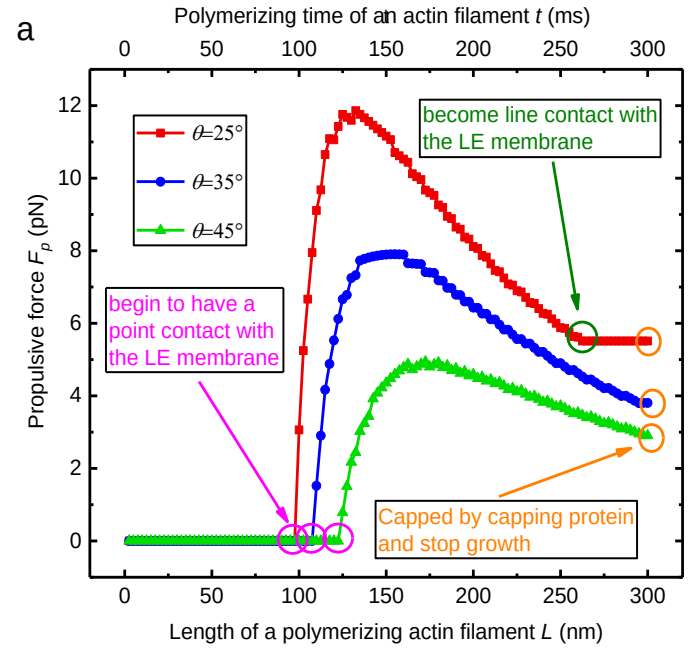
a
Polymerizing time of an actin filament t (ms)
0
50
100
150
200
250
300
Propulsive force F_p (pN)
0
2
4
6
8
10
12
θ=25°
θ=35°
θ=45°
become line contact with the LE membrane
begin to have a point contact with the LE membrane
Capped by capping protein and stop growth
Length of a polymerizing actin filament L (nm)

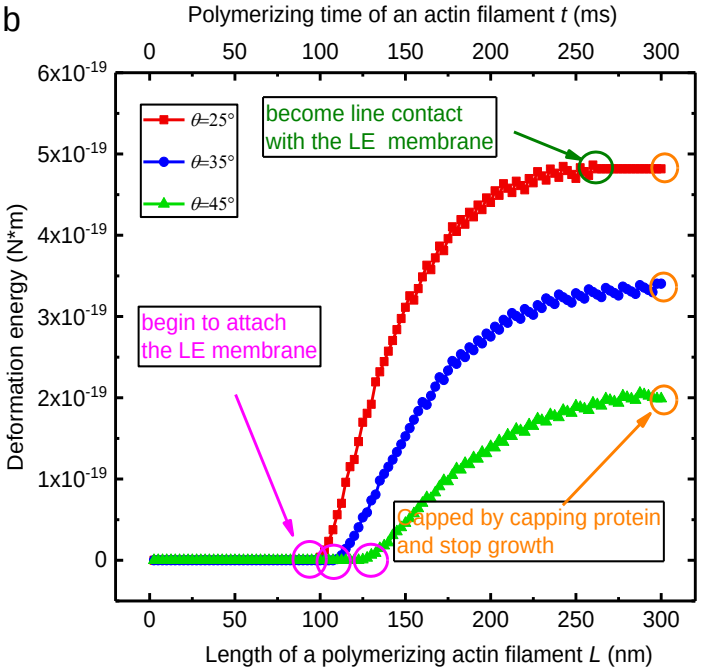
b
Polymerizing time of an actin filament t (ms)
0
50
100
150
200
250
300
Deformation energy (N*m)
0
1x10-19
2x10-19
3x10-19
4x10-19
5x10-19
6x10-19
θ=25°
θ=35°
θ=45°
become line contact with the LE membrane
begin to attach the LE membrane
Capped by capping protein and stop growth
Length of a polymerizing actin filament L (nm)

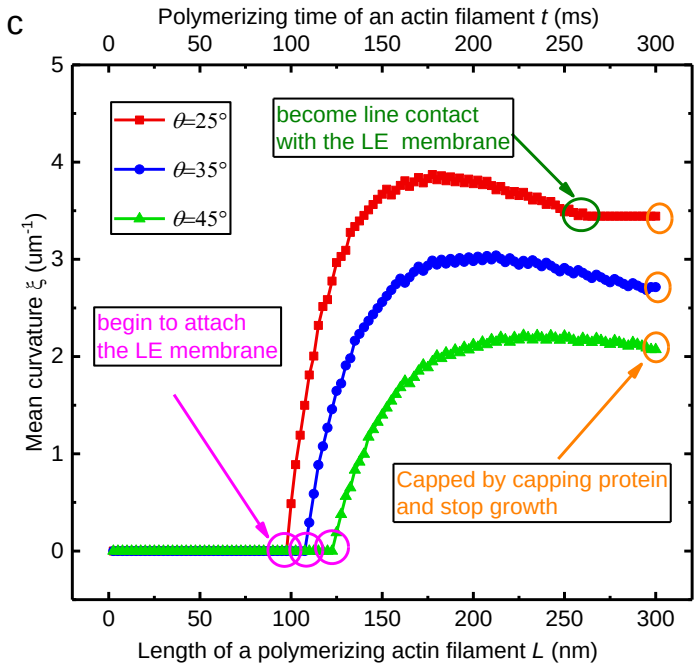

Figure 6.1 Evolution of the force interaction between polymerizing actin filaments and the local LE membrane. Here the local LE membrane is assumed unmovable due to the constraint of extracellular confining microenvironment. (a) Propulsive force for cell migration acting on the local membrane under the polymerizations of actin filaments with time. (b) Deformation energy of polymerizing actin filaments. (c) Mean bending curvature of polymerizing actin filaments.

Next, we assume that the polymerization of actin filament has finished to explore the mechanical interaction between the actin filament and the protruding LE membrane. With the movement of the LE membrane step by step, the propulsive force actin on local LE membrane, deformation energy and mean curvature of actin filaments significantly changes (Fig. 6.2a-c). Interestingly, even though the three actin filaments have different in-plane angles, when they contact the local LE membrane by a point, both the propulsive forces F_p and the mean bending curvatures of them reduce with similar gradients. In addition, the mean curvature of actin filaments approximately has a linear relationship with the moving distance of the LE membrane. For the actin filament with $\theta = 20°$, when it has a line contact

with the LE membrane, the propulsive force and the bending curvature are more sensitive to the LE protruding distance than those of the point contact stage. Moreover, while the LE membrane protrudes forward, the deformation energy stored in actin filaments releases with a descending gradient. Reducing the in-plane angle of actin filaments leads to an increased sensitivity of deformation energy to the LE migration distance. Finally, with the persistently moving forward of the LE membrane, actin filaments capped by capping proteins leave and fall behind the local LE membrane. Thus, the propulsive force actin on LE membrane, deformation energy and mean curvature of them all reduce to 0.

Note that, in our following spatial and temporal simulations, the polymerization and assembly of branched actin filaments and the protrusion of the LE membrane governed by Eq. (5.19) happen simultaneously as the realistic condition in migrating cells.

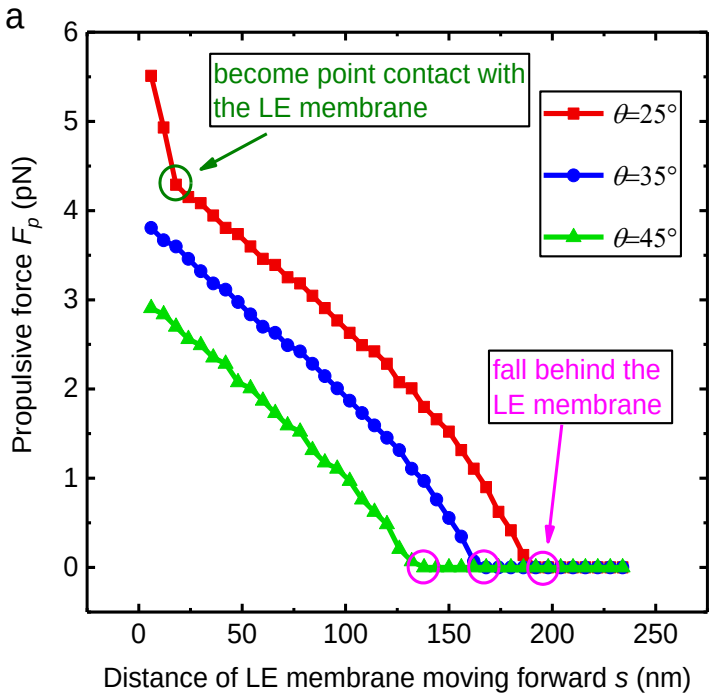

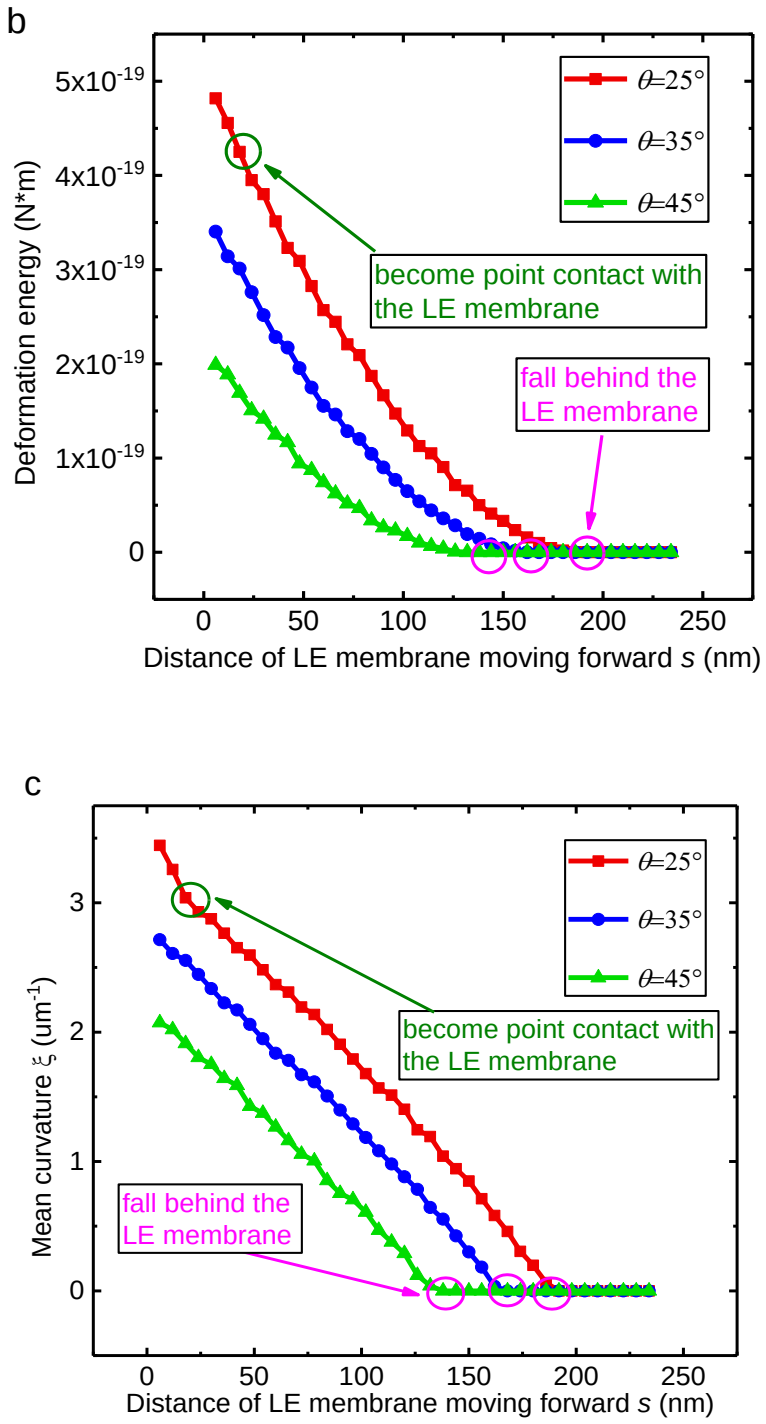

Figure 6.2 Evolution of the force interaction between actin filaments and the local LE membrane during the LE membrane moving forward with step by step. (a) The

propulsive force of actin filaments when the LE membrane moves forward. (b) Deformation energy of actin filaments when the LE membrane moves forward. (c) Mean curvature of actin filaments when the LE membrane moves forward.

6.2.2 BSER model predicts that filament density is regulated by extracellular resistance and reveals the physical mechanism that migrating cells sense and adapt to extracellular load.

Published experimental results show that lamellipodial filament density adapts to varying extracellular load during cell migration [2, 13]. Here we ask whether the proposed ESBR model can predict this significant feature and thus reveal the underlying physical mechanism of it. We first keep the extracellular resistance as a constant $f_r = 1$ nN/μm along the LE membrane, which is in the general range $0.4 - 2$ nN/um for keratocytes and fibroblasts [89]. When the polymerizing actin filaments drive the LE membrane protrudes forward, the density of actin filaments Φ pushing the LE membrane stably fluctuates in a very narrow range 150-190/μm (red line in Fig. 6.3a) , which agrees well with the experimentally measured data 100-300/μm in ref. [89]. Then, we regulate the resistance f_r by improving it to 3 nN/μm in the time frame 500-625 ms (blue line in green shadow area in Fig. 6.3a-d) and also assume that the available actin monomers for assembling actin filaments are sufficient. Before the increase of the extracellular resistance ($t < 500$ ms and $f_r = 1$ nN/um), as the constant load condition, branched actin filament density fluctuates in the range of 150-190/μm. However, when the extracellular resistance f_r suddenly increases to 3 nN/μm at the time $t = 500$ ms, the increased resistance sensitively induces a significant increase of filament density from 150/μm to 250/μm (Fig. 6.3a). Then, at the time of $t = 625$ ms, we reduce the resistance from 3 nN/μm to the previous magnitude 1 nN/μm, filament density also gradually decreases to its previous level with the LE protrusion. Strikingly, Our model well predicts the most recent experimental result that increased extracellular mechanical

resistance induces denser branched actin filaments in refs. [2, 13]. Moreover, our results also show that both the deformation energy stored in the free barbed ends of actin filaments (Fig. 6.3d) and the propulsive force (Fig. 6.3c) for cell migration simultaneously fluctuates with the actin filament density. We further identify that the variation of filament density is to meet the force and energy demand of cell migration for overcoming the extracellular resistance.

More importantly, since filament density is regulated by the nucleation of Arp2/3 complex, whose density, in turn, is determined by the bending curvatures of actin filaments, our results quantitatively reveal the underlying physical mechanism of the load adaption of lamellipodial actin filament density. Specifically, even though the polymerizing velocity of the free barbed ends of branched actin filaments is constant $V_{fil} = 1$ nm/ms , when the extracellular resistance f_r of cell migration increases from 1 nN/μm to 3 nN/μm, the protrusion velocity V_m decreases (pink circle in Fig. 6.3b). This suggests that the bending curvatures of polymerizing actin filaments increase, which sensitively improves the binding of Arp2/3 complex on the convex sides of actin filaments. As a result, more daughter actin filaments are branched out from the increased density of Arp2/3 complex. Unlike previous models [99, 123, 125, 141] where Arp2/3 complex branching direction is controlled deliberately, Arp2/3 complex branching out new actin filaments in our spatiotemporal model is based on the bending deformation of mother actin filaments under the extracellular resistance load. Thus, this also explains why the branched actin filaments persistently self-assemble towards the LE membrane and push it against extracellular resistance. Our predictions are also validated by the experimental results [118] that when the nucleation activity of Arp2/3 complex is reduced by Arpin, the persistence and frequency of the LE membrane protrusion of migrating cells significantly decrease. The architecture of the branched actin network generated by our self-assembling spatiotemporal model (Fig. 6.4a) is consistent with the experimental data (Fig. 6.4b) in ref. [123]. Furthermore, our results also reveal that varying extracellular resistances that a migrating cell

experiences induce the density heterogeneity of its global lamellipodial branched actin filament network, and clearly demonstrate this self-assembling evolution process.

Together, our ESBR model also deciphers the intracellular physical mechanism of migrating cells sensing and adapting to extracellular resistance on molecular level at their LE: migrating cells can sensitively sense the immediate variations of extracellular resistance through the bending deformation of lamellipodial actin filaments under the LE membrane; then, they adapt the density of actin filaments pushing against the LE membrane through modulating Arp2/3 complex binding activity intrigued by the bending curvature of actin filaments to further regulate the propulsive forces and energy, which are needed for overcoming the increased extracellular resistance. Strikingly, through this mechanism, cells can most efficiently use their intracellular proteins according to their demands to propel their migration in complex and high dynamic mechanical extracellular environments.

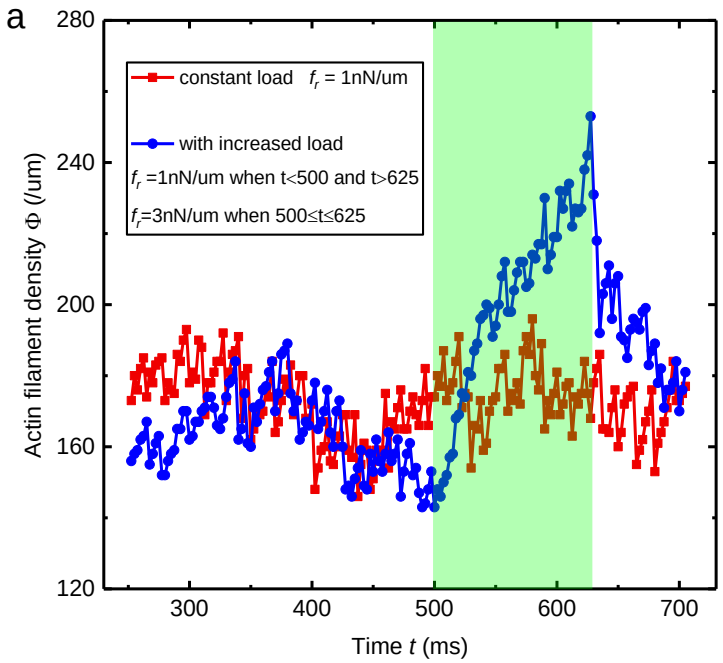

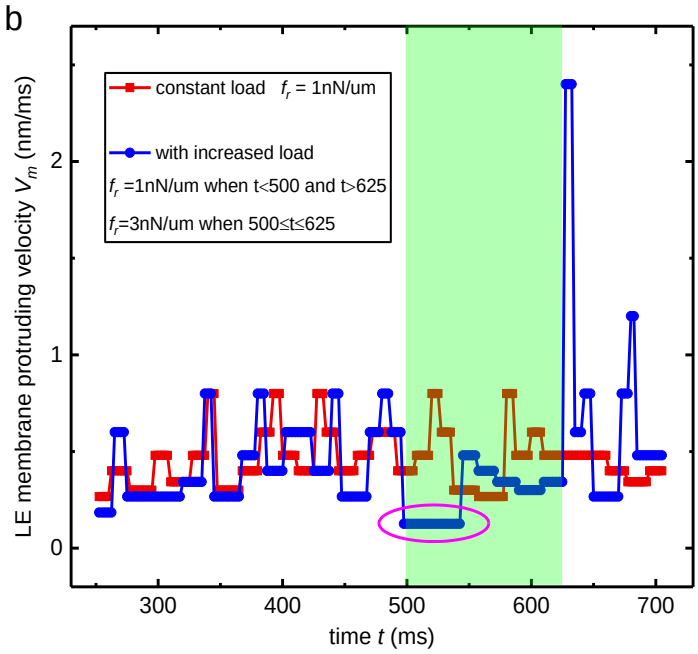
b
constant load f_r = 1nN/um
with increased load
f_r =1nN/um when t<500 and t>625
f_r=3nN/um when 500≤t≤625
LE membrane protruding velocity V_m (nm/ms)
0
1
2
300
400
500
600
700
time t (ms)

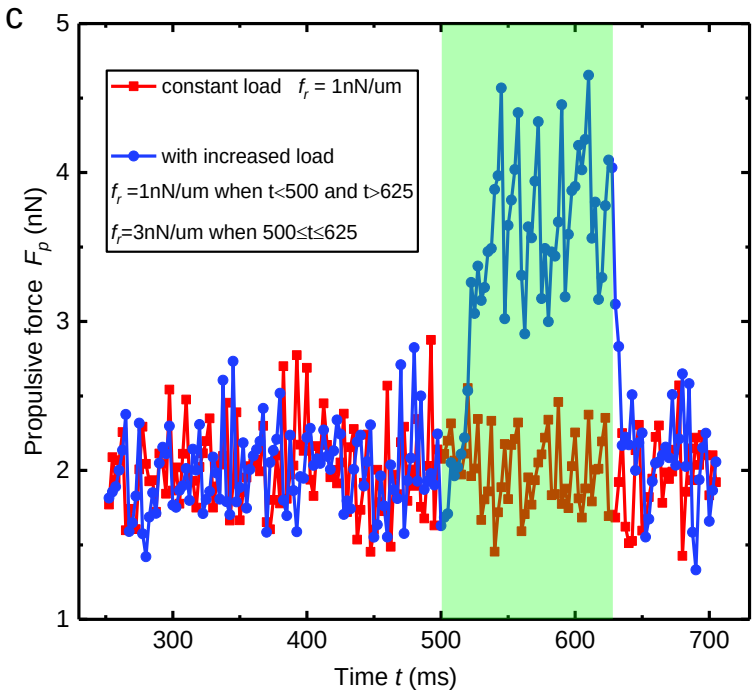
c
constant load f_r = 1nN/um
with increased load
f_r =1nN/um when t<500 and t>625
f_r=3nN/um when 500≤t≤625
Propulsive force F_p (nN)
1
2
3
4
5
300
400
500
600
700
Time t (ms)

d

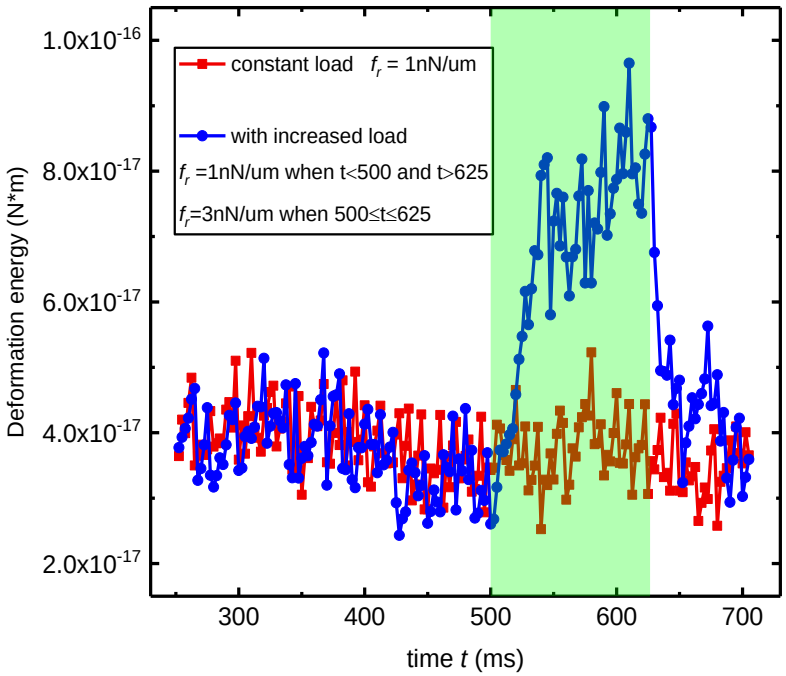
constant load f_r = 1nN/um
with increased load
f_r =1nN/um when t<500 and t>625
f_r=3nN/um when 500≤t≤625
Deformation energy (N*m)
1.0x10-16
8.0x10-17
6.0x10-17
4.0x10-17
2.0x10-17
300
400
500
600
700
time t (ms)

e

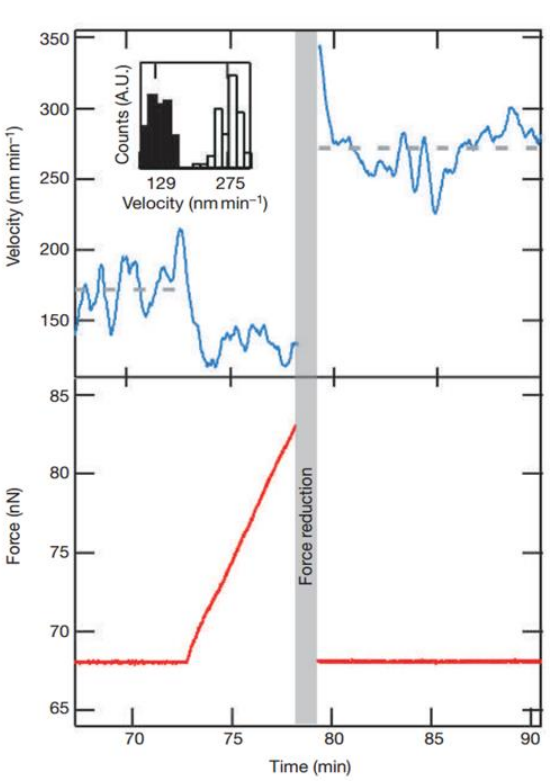
Counts (A.U.)
129
275
Velocity (nm min⁻¹)
Velocity (nm min⁻¹)
350
300
250
200
150
85
80
75
70
65
Force (nN)
Force reduction
70
75
80
85
90
Time (min)

Figure 6.3 Spatial and temporal interaction evolutions while polymerizing lamellipodial branched actin filaments of a migrating cell drive the LE membrane protrusion under constant and fluctuating extracellular resistances. Here we select a time frame $250-700$ ms for comparison. (a) Comparison of polymerizing actin filament densities under constant and fluctuating extracellular resistances. (b) Comparison of the LE membrane protruding velocities of a migrating cell under constant and fluctuating extracellular resistances. (c) Comparison of the propulsive forces of a migrating cell under constant and fluctuating extracellular resistances. (d) Comparison of the deformation energies stored in polymerizing branched actin filaments of a migrating cell under constant and fluctuating extracellular resistances. (e) Experimental result of LE protruding velocity reactions of the polymerizing branched actin filament under fluctuating external load in ref. [144]. Note that, the different time scales in (b) and (e) are due to different polymerization rates of actin filaments because our simulation is *in vivo* context while the experimental result is based on an *in vitro* constructed branched actin network. The polymerization rate of actin filaments can be influenced by various factors, such as concentration of actin monomers [113]. Thus, the different time scales do not interfere with the comparisons of the corresponding results.

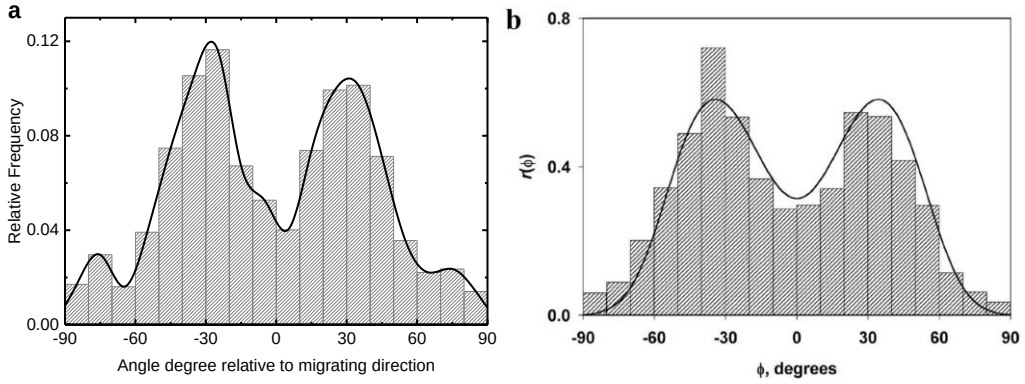

Figure 6.4 The architecture of lamellipodial branched actin network generated from our spatiotemporal model simulation is very similar to that of experimental measurement. (a) Histogram of migrating-plane angle between actin filaments and the migrating direction obtained from our spatiotemporal simulation model. (b)

Histogram of migrating-plane angle between actin filaments and the migrating direction experimentally measured from Xenopus keratocyte lamellipodium in ref. [123].

6.2.3 Protruding velocity loading history dependant is induced by actin filament density loading history dependant

Extracellular microenvironments are highly varying and mechanically heterogeneous [2, 17, 108]. Thus, we ask an important question that how the protruding LE membrane of migrating cells responds to fluctuating immediate extracellular resistance f_r, and explore whether our ESBR model can predict the experimentally discovered behaviour [144] that branched actin filaments protruding velocity depends on external loading history (Fig. 6.3e).

Our predictions show that when the extracellular resistance force f_r increases at the time of $t = 500$ ms, the moving velocity V_m of the LE membrane suddenly decrease from 0.6 nm/ms to 0.12 nm/ms (pink circle area of the blue line in Fig. 6.3b), which is smaller than the normal velocity range $0.26 \sim 0.8$ nm/ms under the constant resistance $f_r = 1$ nN/μm (red line in Fig. 6.3b). Our results well predict the experimental finding that an increased extracellular resistance leads to an abrupt decrease of protruding velocity of branched actin filament network [144]. Moreover, our results also show that with the continuing polymerizations of actin filaments, the decreased protruding velocity will return to the common velocity range (blue line in shadow area in Fig. 6.3b) due to the increasing density of actin filaments induced by the increased extracellular resistance. Then, we reduce the extracellular resistance from 3 nN/μm to its previous value 1 nN/μm at the time of $t = 650$ ms. Strikingly, the protruding velocity of the LE membrane abruptly increases to a very high value 2.4 nm/ms (blue line in Fig. 6.3b). This high velocity sustains only 7.5 ms and then fluctuates around 0.8 nm/ms (Fig. 6.3b). Compared with the

velocity under the constant extracellular load condition (red line in Fig. 6.3b), our results strongly indicate that the protruding velocity of the LE membrane is strongly loading history dependent. Again, our prediction is consistent with and is confirmed by the experiment results [144] that branched actin filament network protruding velocity under a given load depends on its loading history, and a single $f_r - V_m$ relationship is inadequate to descript actin-based motility behaviours. In addition, an interesting thing is that the transient high protruding velocity of the LE membrane is even larger than the polymerizing rate V_{fil} of actin filaments. This is because although the extracellular load reduced, the density of bending actin filaments is still very high (Fig. 6.3a). Their bending curvatures, propulsive forces and deformation energies are also very high (Figs. 6.3c and d). Thus, they can easily overcome the reduced extracellular load and instantly propel the LE membrane to protrude with a transient high velocity. After that, the density of actin filaments pushing against the LE membrane reduces in a gradual process (Fig. 6.3a). Thus, the subsequent protruding velocity still fluctuates in relatively high values around 0.8 nm/ms. Collectively, our spatiotemporal simulation results (Fig. 6.3b) agree strikingly well with the published experimental results (Fig. 6.3e). It is revealed that the nature of the protruding velocity depending on loading history is that the actin filament density depends on loading history.

Interestingly, even though branched actin filaments polymerize with a constant rate $V_{fil} = 1$ nN/μm and extracellular resistance is kept constant $f_r = 1$ nN/μm in our spatiotemporal model (red line in Fig. 6.3a-d), the protruding velocity V_m of the LE membrane under the propulsive force is not stable. Our results show that the LE membrane of migrating cells protrudes with periodic high and low velocity alternations, which is consistent with the experimental measurements in refs. [144, 147]. The predicted fluctuating velocity is in the range of $0.26 \sim 0.8$ nm/ms. It is similar to the experimental data $0.05 \sim 0.5$ nm/ms [147, 211, 212]. Then, we further investigate why the LE membrane protrudes with high and low velocity alternations.

It is found that the density of polymerizing actin filaments also shows high and low value alternations (Fig. 6.3a), which induce the co-fluctuations of the LE protruding velocity.

6.2.4 Migrating cell LE circumnavigates obstacles and migrates along the low resistance path

In living tissue, the LEs of migrating cells must be able to respond to multiple obstacles they encounter, ranging from stiff, narrow ECM pores, lateral compression and confinement to physically impenetrable barriers [19]. Recent experimental studies show that cells circumnavigate high resistance region and migrate predominantly through the low resistance microenvironment [134]. We examine whether our BSER can predict this behaviour and explore the underlying physical mechanism of migrating cells adapting their migratory paths. We generate two stages of the extracellular microenvironment in front of the lamellipodial LE membrane to simulate a cell migrating in heterogeneous extracellular microenvironments. Initially, the extracellular microenvironment is homogeneous and the resistance is 1 nN/μm. However, at the position of 162 nm in front of the LE membrane, the extracellular microenvironment becomes heterogeneous. Specifically, the central region is a weak extracellular barrier and has a resistance of 2 nN/μm while both the right and left sides are strong barriers and their resistances are 20nN/um. Interestingly, our simulation results show that, in the first homogeneous mechanical environment, the left, central and the right parts of the LE membrane protrude with similar velocities and they move forward synchronously (Fig. 6.5a). The actin filament densities of the two sides are also almost the same (Fig. 6.5b). However, when they encounter different mechanical extracellular confining microenvironments at the position of 162nm (shadow area in Fig. 6.5a and b), the LE membrane stops moving forward on both the left and right sides due to the strong extracellular resistances, but protrudes from the central region where the extracellular resistance is weak and circumnavigates the strong

barriers on the two sides (Figs. 6.5a and c). Thus, our model demonstrates how the LEs lead the migrating cells to circumnavigate obstacles or rigid extracellular microenvironment to migrate along the low resistance path in the published experimental findings in ref. [134].

In order to reveal the underlying physical mechanism of these behaviours, we further examine what is the microscopic reaction of the self-assembling branched actin filaments when the LE membrane encounters high resistances or obstacles. It shows that actin filaments massively deformed with the polymerization of actin monomers at their barbed ends and a large number of Arp2/3 complexes abruptly bind on these bending actin filaments and nucleate daughter actin filaments to generate more propulsive forces for pushing the LE membrane against the extracellular confinement (shadow area of red and blue lines Fig. 6.5b). However, the maximum density of actin filaments in migrating cells is constrained by the number of available actin monomers [113] and is about 340/μm [89]. Thus, when the density of branched actin filaments reaches its threshold value, if the increased resultant propulsive force is still unable to overcome the resistance, the LE membrane will stop protruding from this side and select a weak mechanical region to protrude into and to open a wide channel to migration through. This physical mechanism significantly facilitates the rapid navigation of cell migration in complex extracellular microenvironments.

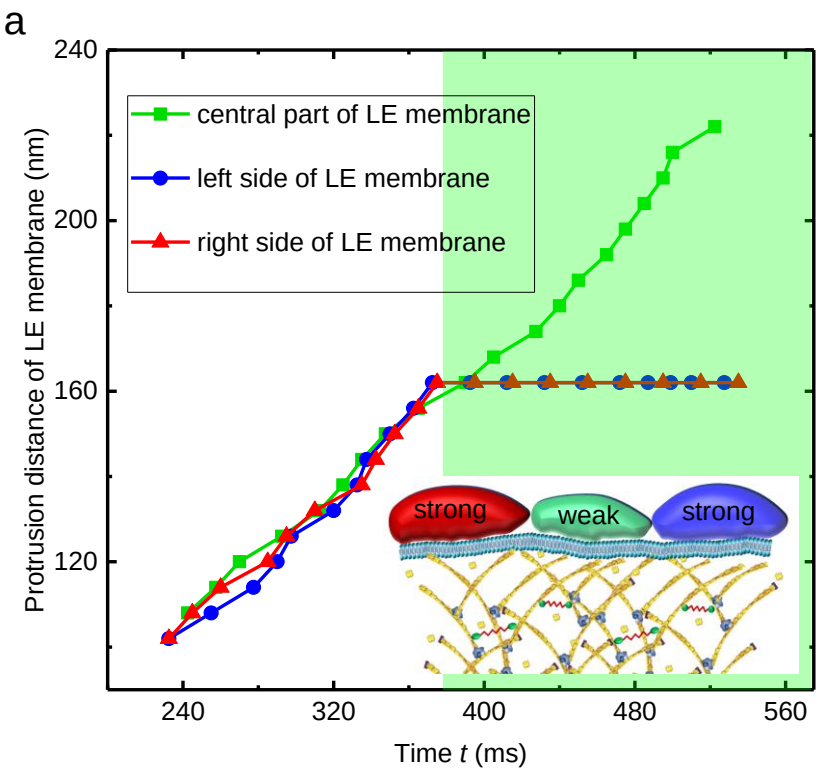
a
central part of LE membrane
left side of LE membrane
right side of LE membrane
strong
weak
strong
Protrusion distance of LE membrane (nm)
240
200
160
120
240
320
400
480
560
Time t (ms)

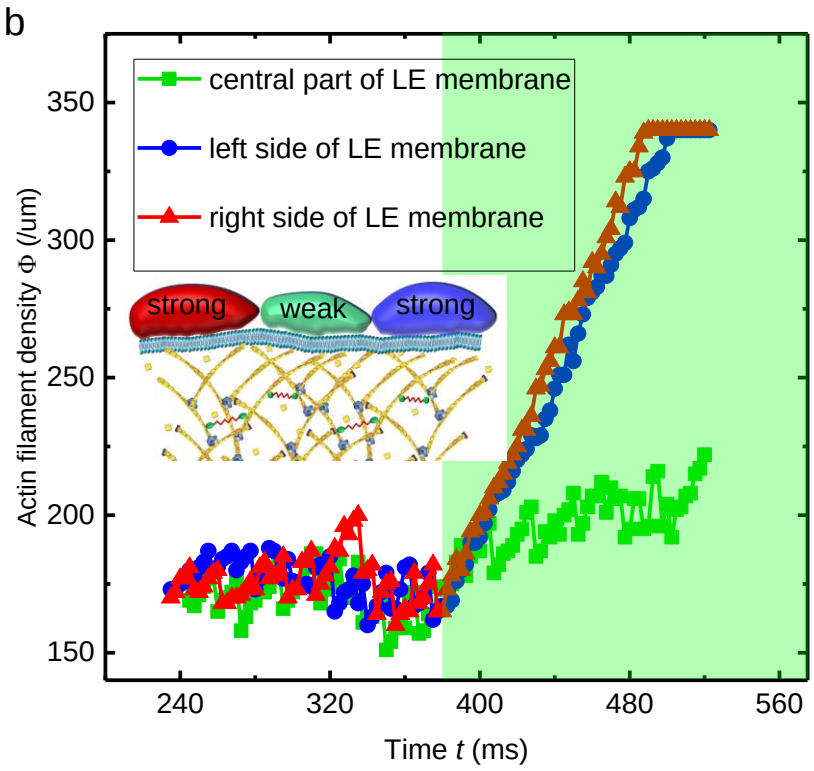
b
central part of LE membrane
left side of LE membrane
right side of LE membrane
strong
weak
strong
Actin filament density Φ (/um)
350
300
250
200
150
240
320
400
480
560
Time t (ms)

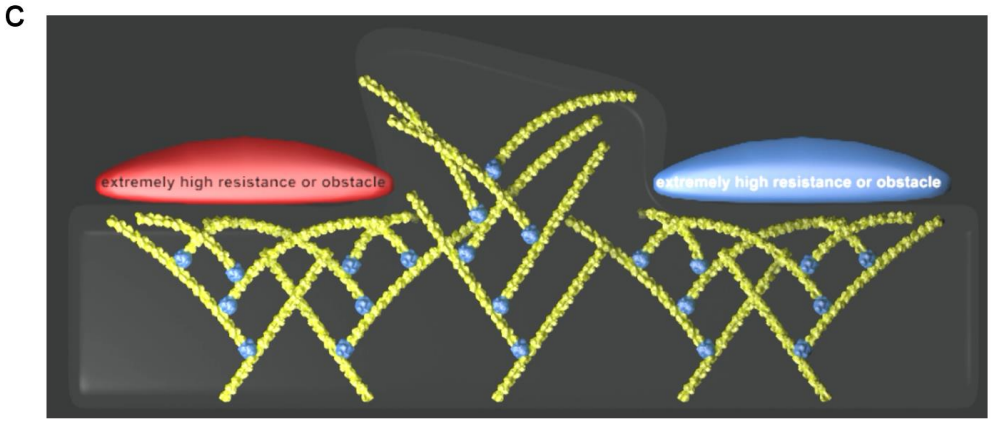

Figure 6.5 The LE of a migrating cell circumnavigates obstacles or very high extracellular resistance regions which it encounters. (a) Protruding distance of the local LE membrane. (b) Polymerizing branched actin filament density. (c) Cartoon demonstration of our simulation result that LE opens a channel form the weak region and circumnavigates obstacles and high resistance regions.

6.2.5 Directional cell migration is steered by the balancing relationship between local extracellular resistance, filament density heterogeneity and local concentration of actin monomers

So far, in order to more straightly capture how the varying extracellular resistance impacts on the LE protrusion behaviours, we have restricted our analysis to the condition that the intracellular concentration of actin monomers is constant (40μM) and sufficient, and thus does not affect actin filament polymerizing rate. Recently, an advanced in vitro experiment shows that the available concentration of actin monomers is affected by the density of branched actin filaments and in turn affects the polymerizing rate of the branched actin filaments and protrusion direction [113]. However, they generated different densities of branched actin filaments by using different concentrations of nucleating-promoting factors in vitro without considering external resistance, which is important for in vivo cell migration. Our study has clearly demonstrated the spatiotemporal architectural evolution process

that different local extracellular mechanical microenvironments lead to different local densities of the branched actin filaments under the LE membrane. Accordingly, the local density of lamellipodial branched actin filaments in migrating cells is coupled with extracellular resistance. Here, we further investigate the complex interplays between the extracellular resistance, density heterogeneity of branched actin filaments, the local concentration of actin monomers and LE protrusion velocity to decipher how they couple together to steer directional cell migration in heterogeneous extracellular microenvironment.

To introduce the effect that the polymerizing rate of the barbed ends of actin filaments is negatively related with actin filament density [113] to our spatiotemporal model, we defined the polymerizing rate V_{fil} under the same concentration of actin monomers is inversely proportional to the polymerizing actin filament density. We hypothesize that the LE leading cell migration is sufficiently wide and has a curvature in the cell migrating plane. Thus, the competition of different directional LE protrusions at different intracellular and extracellular physical microenvironments can be clearly demonstrated (Fig. 6.6). We assume that the fastest LE protruding direction of is the main migrating direction of cells. We test three cases (Case A-C, Table 6.1) of polymerizing branched actin filaments propelling two-directional protrusions on the left and right sides of the LE membrane. In case A (Table 6.1), the extracellular confining resistances on both the left (f_r^{left}) and right (f_r^{right}) sides are controlled as $1nN/um$ (Fig. 6.7c). Therefore, they induce similar densities of branched actin filaments pushing against the LE membrane on the two sides (Φ^{left} and Φ^{right}, Fig. 6.7d). However, the local concentrations of actin monomers on the two sides (C_a^{left} and C_a^{right}) are 20 μM and 40 μM, respectively. Our spatiotemporal simulations show that both the protruding velocity and distance of the LE membrane on the right side are larger than those of the left side (Fig. 6.7a and b). Thus, it is concluded that when extracellular mechanical microenvironments confining cell migration are

homogeneous, lamellipodial LE protrudes more actively on the site where it has a larger local concentration of actin monomers because a high concentration of actin monomers means that sufficient actin monomers can be supplied to the polymerizing barbed ends of branched actin filaments. This emphasizes the determining role of local actin monomer concentration in steering directional cell migration.

In case B (Table 6.1), the left and right sides have the same local concentrations of actin monomers, but their extracellular resistances are different. Our simulations show that the higher resistance on the left side results in denser branched actin filaments on the left side (Fig. 6.8d). However, because the local concentrations of actin monomers on the two sides are the same, denser actin filaments deplete more action monomers, which lead to slower polymerizing rate of their barbed ends. Thus, even though the increased density of actin filament generates a high propulsive force for overcoming the high extracellular resistance, the protruding velocity of the left side LE membrane is slower than that of the right side (Fig. 6.8a and b). Thus, cell mainly migrates toward the right side. Strikingly, we predict the experimental results [134] and reveals their underlying physical mechanism at the LE that when the concentration of actin monomers is homogeneously distributed in lamellipodium, lamellipodium selects the least extracellular resistance path to drive cell migration through because a low resistance induces a sparser density of actin filaments and thus actin monomers can keep them in a higher polymerizing rate. This suggests that the extracellular resistance plays a determining role in directional cell migration. Then, we design Case C (Table 6.1), in which both the local actin monomer concentration and extracellular resistance on the left and right sides are different. According to our prediction, unlike the result of Case B that cell protrudes more faster on the low resistance side, the LE membrane moves forward on the high resistance side with a 2.5 times average speed of that of the low resistance side (Fig. 6.9a and b). Even though the denser actin filaments consume more action monomers on the right side, the local concentration of actin monomers can keep

them in a relative higher polymerizing rate than that of the left side. Thus, the LE membrane protrudes faster on the right side and drives the cell to migrate in this direction.

Collectively, on the basis of our large-scale spatiotemporal simulations of lamellipodial LE driving migrating cell pushing against extracellular confining resistance in Case A-C, we can conclude that directional cell migration is not simply determined by the local actin monomer concentration or extracellular resistance. We reveal its underlying biophysical mechanism that it is the balancing and negotiating consequence of the both. While a high local actin monomer concentration improves the polymerizing rate of actin filaments, a high local extracellular resistance results in denser local branched actin filaments, which in turn reduces the polymerizing rate and slows down the LE membrane protrusion. However, if the local actin monomer concentration is sufficiently high, the locally increased density of branched actin filaments still can propel the local LE protrusion with a high velocity. Note that, unlike the previous research [113] which studies actin-based directional motility without considering the important extracellular confining resistance, here we reveal actin-based directional cell migration in an in vivo context by spatially and temporally simulating the realistic intracellular and extracellular interactive impacts.

Table 6-1 Local concentrations of actin monomers, local extracellular resistances and the induced local densities of branched actin filaments pushing against the local LE membranes in Cases A-C

	C_a^{left}	f_r^{left}	Φ^{left}	C_a^{right}	f_r^{right}	Φ^{right}
Case A	20 μM	1 nN/μm	~ 180 / μm	40 μM	1 nN/μm	~ 180 / μm
Case B	40 μM	3 nN/μm	~ 300 / μm	40 μM	1 nN/μm	~ 180 / μm
Case C	10 μM	0.4 nN/μm	~ 130 / μm	40 μM	3 nN/μm	~ 300 / μm

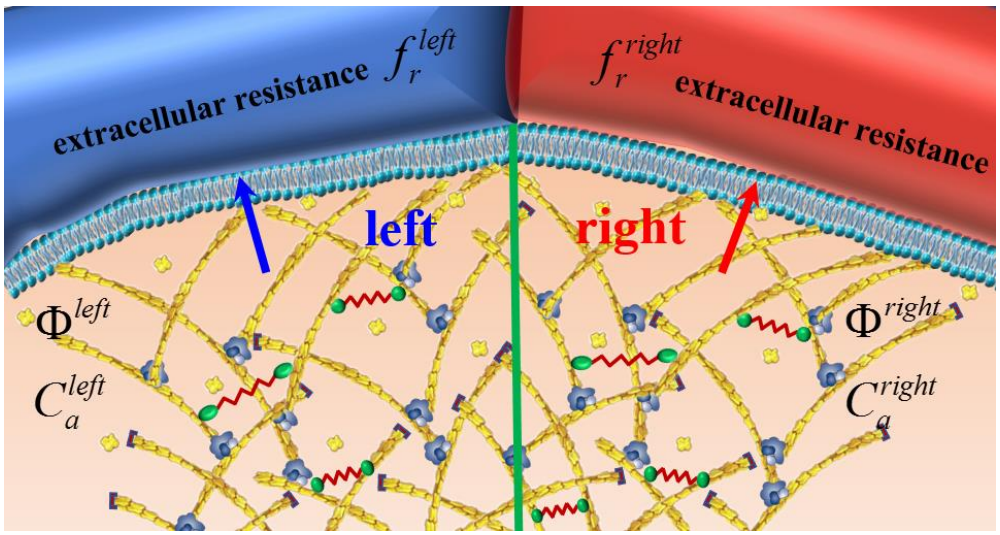

Figure 6.6 Cartoon demonstration of two directional protrusions of a migrating cell.

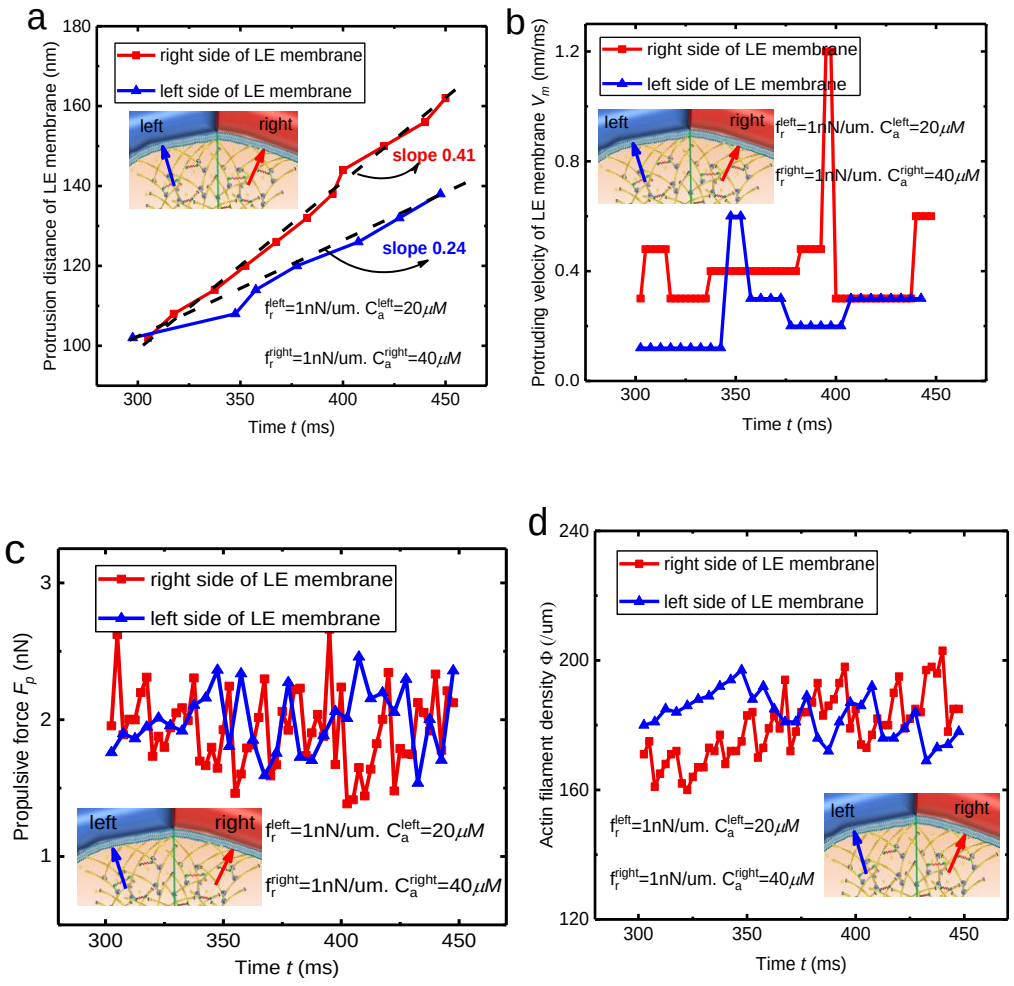

Figure 6.7 Spatial and temporal local protruding behaviours of migration cell and self-assembling of local branched actin filaments in Cases A. (a) Protruding distances of local LE membranes. (b) Protruding velocities of local LE membranes. (c) Local propulsive forces generated by polymerizing actin filaments. (d) Local densities of actin filaments pushing against the local LE membrane.

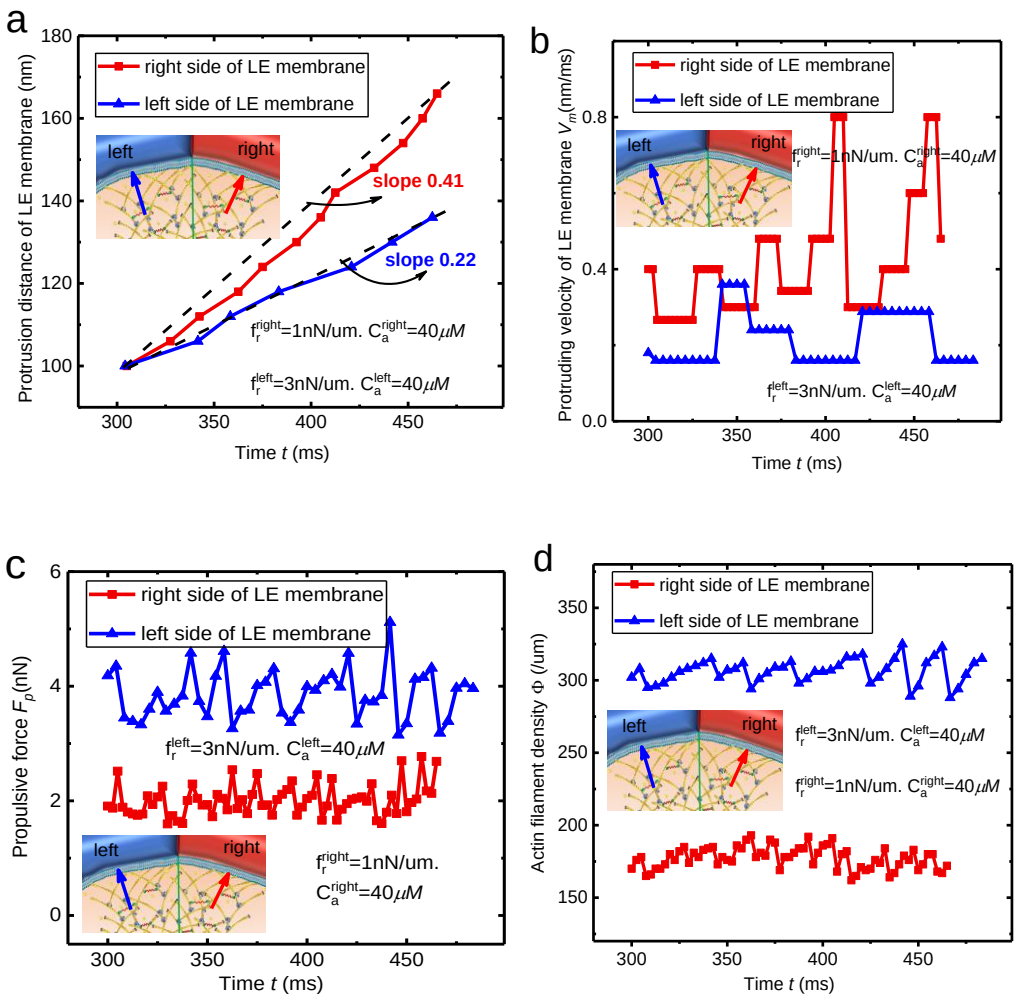

Figure 6.8 Spatial and temporal local protruding behaviours of migration cell and self-assembling of local branched actin filaments in Cases B. (a) Protruding distances of local LE membranes. (b) Protruding velocities of local LE membranes. (c) Local propulsive forces generated by polymerizing actin filaments. (d) Local densities of actin filaments pushing against the local LE membrane.

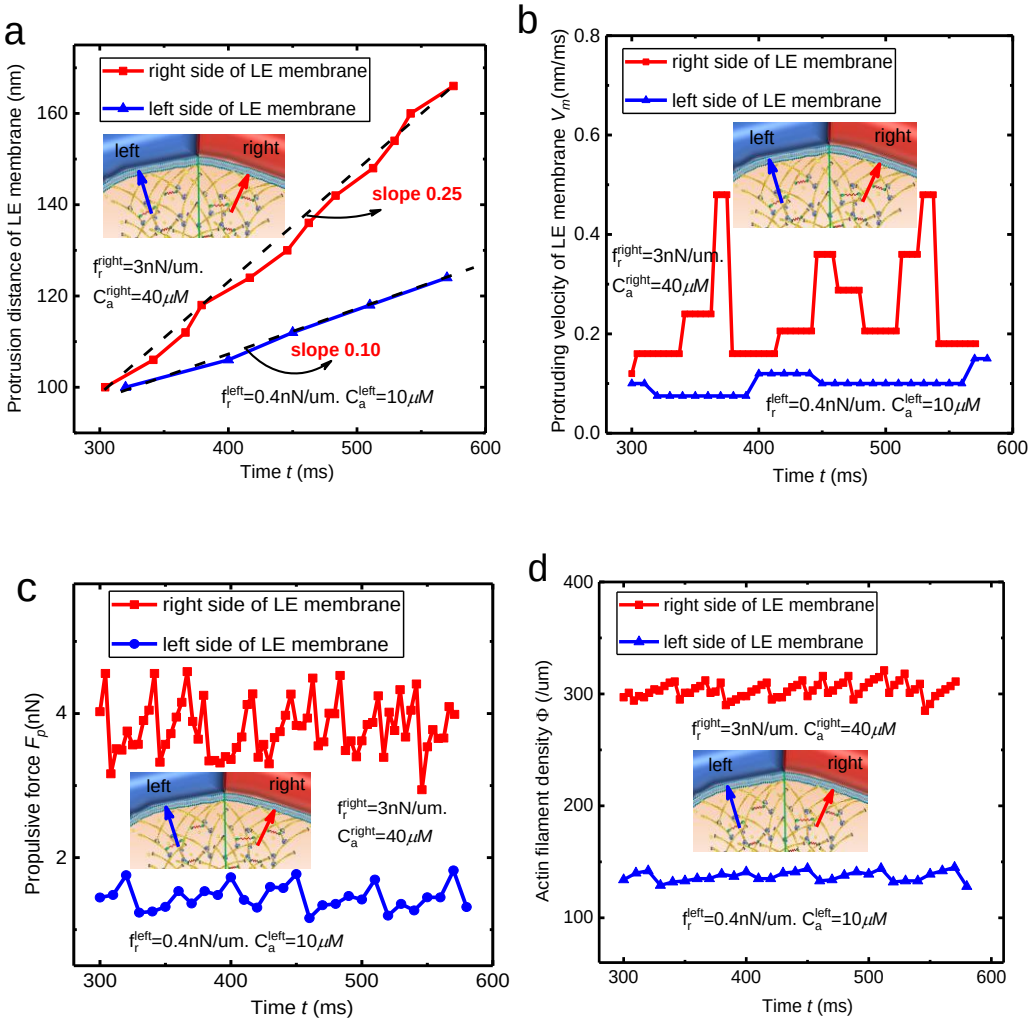

Figure 6.9 Spatial and temporal local protruding behaviours of migration cell and self-assembling of local branched actin filaments in Cases C. (a) Protruding distances of local LE membranes. (b) Protruding velocities of local LE membranes. (c) Local propulsive forces generated by polymerizing actin filaments. (d) Local densities of actin filaments pushing against the local LE membrane.

6.3 Discussion

Since cells are only able to migrate through a channel with sufficient width in vivo [15, 134], the mechanical interaction between the polymerizing lamellipodial

branched actin filaments and the extracellular confining microenvironment essentially determines cell migration [2, 15, 135, 136]. However, at present, none of the existing models can explain all the significant LE protruding behaviours of migrating cells [14]. Published experiments have shown that branched actin filaments pushing against the LE membrane constrained by extracellular resistance experience large scale deformations and even buckle [2, 26, 145]. Accordingly, we proposed a new theoretical actin-based protrusion model (BSER model), which is based on nonlinear geometrical deformation of continuum solid mechanics, to describe the temporal and spatial mechanical evolution between the polymerizing actin filaments and the protruding LE membrane. Importantly, the local curvature of the LE membrane and the mechano-chemical reaction that Arp2/3 complex prefers to bind on the convex side of a bent actin filament and nucleates a new filament [146] are also carefully considered in our theoretical BSER model. Then, we develop the self-assembling spatiotemporal mathematical model of lamellipodium protrusion, which realistically encompass the polymerization of branched actin filaments by adding actin monomers to their barbed ends, Arp2/3 complex binding on pre-existing actin filaments and nucleating new actin filaments, capping protein capping the barbed ends of actin filaments and stopping their polymerizations, curved protruding LE membrane, breaking of the molecular linker between the capped barbed ends and the moving LE membrane and heterogeneous extracellular resisting mechanical microenvironments during in vivo cell migration. Finally, by applying our theoretical BSER model to our spatiotemporal model, we perform large-scale spatial and temporal numerical simulations of polymerizing lamellipodial branched actin filaments in migrating cells driving the LE membrane protrusion in heterogeneous extracellular microenvironment. Our study yields four major contributions.

First, our theoretical BSER model for the first time systematically and quantitatively predicts all the important LE protruding behaviours of actin-base cell migration: (1) lamellipodial branched actin filament density relies on extracellular

resistance; (2) LE protruding velocity depends on loading history; (3) actin-based protrusion is saltatory with time; (4) LE of migrating cells circumnavigate obstacles and directionally migrates in vivo. More importantly, we decipher the physical mechanisms underlying these cell migration behaviours. Specifically, high extracellular resistance results in large bending deformations of actin filaments, which stimulates the more Arp2/3 complexes binding on them and generating more daughter filaments. That's why the increased extracellular resistance induces an increased density of lamellipodial branched actin filaments in the experiments in refs. [2, 13]. Furthermore, we identify that the protruding velocity depending on loading history is because of the hysteresis of high filament density, which is induced by the previous high external load. After the abrupt reduction of the load, the dense polymerizing actin filaments still can generate high propulsive force and hence suddenly push the LE protruding forward with increased speed. Additionally, we also demonstrate the spatial and temporal self-assembling formation process of lamellipodial branched actin filament networks while they interact with extracellular resistance.

Second, extracellular microenvironments are commonly mechanically heterogeneous and in active remodelling states [15, 19]. Here, we reveal the very fundamental microscopic physical mechanism by which migrating cells sense and adapt their propulsive forces to the highly dynamic and complex extracellular microenvironment at their LEs. Through the bending deformation extent of branched actin filaments pushing against the LE membrane, a cell can sense the magnitude and variation of extracellular resistance. If the resistance increases or decreases, the bending curvature of polymerizing actin filaments will simultaneously increase or decrease, which further induces more active or less active Arp2/3 complex binding on these actin filaments and nucleating new actin filaments. Therefore, according to the variation of confining resistance, migrating cells can adapt the density of actin filaments pushing against the LE membrane and hence adapt their propulsive force to overcome the resistance. Through this

mechanism, cells are able to use their intracellular resources with maximum efficiency during migration. Furthermore, this also shows how the heterogeneous density of the lamellipodial branched actin network is produced during cell migration. In addition, cell migration persistence relies on lamellipodial protrusion persistence [132]. Since Arp2/3 complex prefers to bind on the convex side of bent actin filaments, which essentially determines Arp2/3 complex branching direction in the sheet-like lamellipodial space, our theoretical BSER model also reveals why branched actin filaments can be continuously generated and persistently push the LE membrane against the extracellular confining resistance. Moreover, our study hypothesizes that the concentration of Arp2/3 complex is sufficient for nucleating. However, in cells, it might be limited and thus limits the nucleation rate [114]. Published experimental results show that Arp2/3 complex overexpression is tightly associated with cancer cell progression and invasion [44], and more Arp2/3 complex nucleation in lamellipodia can result in more persistent cell migration [95]. Since high Arp2/3 complex concentration means a high nucleation rate to generate more new polymerizing actin filaments in lamellipodia, our proposed biophysical mechanism well explains the above experimental results because more polymerizing actin filaments will produce a larger propulsive force, which can facilitate cancer cells to overcome extracellular resistance more easily and to invade into other tissues and circulating systems.

Third, this study advances our understandings of how the LE of migrating cells directionally navigate in complex and high dynamic in vivo extracellular microenvironment. Through spatial and temporal simulations of LE membrane pushing against different extracellular mechanical microenvironments, we quantitatively identify that directional cell migration is a balancing consequence of local extracellular resistance, the heterogeneous density of polymerizing actin filaments and local concentrations of actin monomers in lamellipodia. To maximize the directional LE protrusion, the local actin monomer concentration should match the local density of actin filaments, which is modulated by extracellular resistance,

and thus make them polymerize at a high rate. If the distribution of actin monomers is roughly homogeneous in lamellipodia, the LE will select the least resistance path to drive cell migration through as the results in ref.[134] because even though the increased propulsive force at the site of high resistance can overcome the resistance, the increased density of actin filaments will, in turn, reduce their polymerizing rate, which will lead to the reduction of the LE protruding velocity at this site. Here, we assume that the concentrations of Arp2/3 complex and its nucleation-promoting proteins, such as WAVE complex, N-WASP and FMNL [118, 197], are sufficient and homogeneous distributed in lamellipodia. However, if some extracellular chemotaxis signals induce the heterogeneous distributions of these intracellular factors, the LE might not lead the cell to migrate along the least resistance path. Even though cell migration in three dimensions is very complicated ranging from LE protrusion, cell-extracellular matrix and cell-cell adhesions, contractility, nuclear deformation and microenvironment condition, our study here provides very fundamental insights into the biophysical interactive mechanism between the LE and the confining extracellular microenvironment, which is extremely important for opening a sufficient wide channel for cell to migrate through in vivo.

Finally, our results highlight that all of the cell migrating behaviours at the LE are closely related to the function of Arp2/3 complex. In cells, except for cell migration, actin-based propulsion related with Arp2/3 complex also plays essential roles in other dynamic physiological activities, such as endocytosis, intracellular pathogen transport and dendritic spine formation in cortical neurons [8, 213]. Similar to the LE protrusion of cell migration, these biological processes also rely on the polymerization of branched actin filaments generated by Arp2/3 complex providing propulsive force to perform their functions [8, 213]. Thus, our theoretical BSER model proposed here is also applicable to explain the underlying physical mechanisms of these biological activities. Furthermore, the discovered principle that through bending deformation of actin filaments, migrating cells sensitively sense the external load, and then through the deformation intrigued mechano-

chemical reaction of Arp2/3 complex, migrating cells make a response and adaptation to the load, can be applied for designing new advanced active materials, such as mechanical sensing artificial skin used on intelligent robotics.

Chapter 7 Elastic Properties of Filopodial/Invadopodial F-actin Bundle and Cell Migration

7.1 Introduction

In this chapter, the three-dimensional regulatable model for simulating the highly dynamic filopodial/invadopodial F-actin bundles is constructed. This model considers undulated actin filaments, α-actinin and fascin. The quantitative relationship between the elastic properties of the filopodial/invadopodial F-actin bundles and the microscopic intracellular factors of actin filament, α-actinin and fascin is investigated with finite element numerical simulations. In addition, the geometrical nonlinearity deformation of the F-actin bundles is studied. The mechanical impacts of the F-actin bundles on cell migration behaviours and how invadopodia and lamellipodia collaboratively regulate cell migration are also analyzed.

7.2 Three-dimensional model simulates the dynamic assembling filopodial/invadopodial F-actin bundle

To construct the regulatable model to mimic the spatial and temporal dynamics architecture of the filopodial/invadopodial F-actin bundles, we firstly develop a mathematical model to simulate the dynamic and stochastic binding process of the F-actin bundles. Briefly, the filopodial/invadopodial F-actin bundle is a finger-like structure. We first create a cylindrical domain, which has a radius of r_b and a length of L_b. The bottom and top surfaces of the cylindrical domain are perpendicular to

the y-axis. A certain number of actin filaments N_b are generated in this domain. Their pointed ends and barbed ends are stochastically produced on the bottom and top surfaces of the cylinder, respectively. However, unlike the lamellipodial actin filament, which has a length about 200 nm, the actin filaments in filopodia and invadopodia can grow to a length of several microns, which is comparable to their persistent length. Consequently, as can be seen from Fig.2.15a in chapter 2, in vivo filopodial and invadopodial actin filaments, which are immersed in the cytosol, undergo thermally induced bending deformations [214]. As a result, the geometric structures of these actin filaments are undulated. To realistically simulate the initial in vivo undulated geometry, each straight actin filament is randomly divided into several segments and then transverse deflections normal to the actin filament are stochastically added to these dividing points. After constructing undulated actin filaments, crosslinking proteins, i.e., α-actinin and fascin, are stochastically generated to bind on and crosslink them. Specifically, the connecting distances of α-actinin and fascin are 24 to 40nm and 5 to 15nm, respectively. Firstly, the shortest distance between each pair of actin filament segments is calculated. If the shortest spatial distance is in the range of connecting distance of α-actinin or fascin, α-actinin or fascin will be stochastically generated along the two actin filament segments until the distance between the two crosslinking points exceeds the connecting lengths of the two proteins. In order to be consistent with in vivo condition [161], the minimal space between two adjacent crosslinking points along an actin filament is controlled as about 36 nm in our model. Note that, in this mathematic model, the spatial and temporal microscopic dynamic architecture remodelling process of the filopodial/invadopodial F-actin bundles induced by actin filaments and crosslinking proteins can be carefully simulated by regulating actin filament polymerizing and the binding and unbinding of α-actinin and fascin, respectively or combinedly.

Actin filaments, α-actinin and fascin are all hypothesized as elastic rods. The stiffness of fascin is likely similar to that of actin filaments [70] and hence the

elastic modulus of fascin is assumed to be 1 GPa. The solid materials properties and cross-section diameters of them (Table 7-1) are all assigned to the mathematical model to further construct continuum mechanics-based three-dimensional regulatable models of the filopodial/invadopodial F-actin bundles. Then, this hybrid F-actin bundle model (Fig. 7.1) is meshed into quadratic interpolated B32 beam elements with circular cross-sections in ABAQUS and the nodes on the bottom surface ($y=0$) are fixed (Eqs. (7.1-4)). The elastic properties of filopodial/invadopodial F-actin bundles can be investigated by applying a displacement to the top surface nodes.

$$u_i^{y=0} = 0 \tag{7.1}$$

$$v_i^{y=0} = 0 \tag{7.2}$$

$$w_i^{y=0} = 0 \tag{7.3}$$

$$\theta_i^{y=0} = 0 \tag{7.4}$$

Where u , v and w denote the displacements in the *x*, *y* and *z* directions, respectively. i is the nodes on the boundary of $y=0$. θ represents the rotational angles around the *x*, *y* and *z* axes.

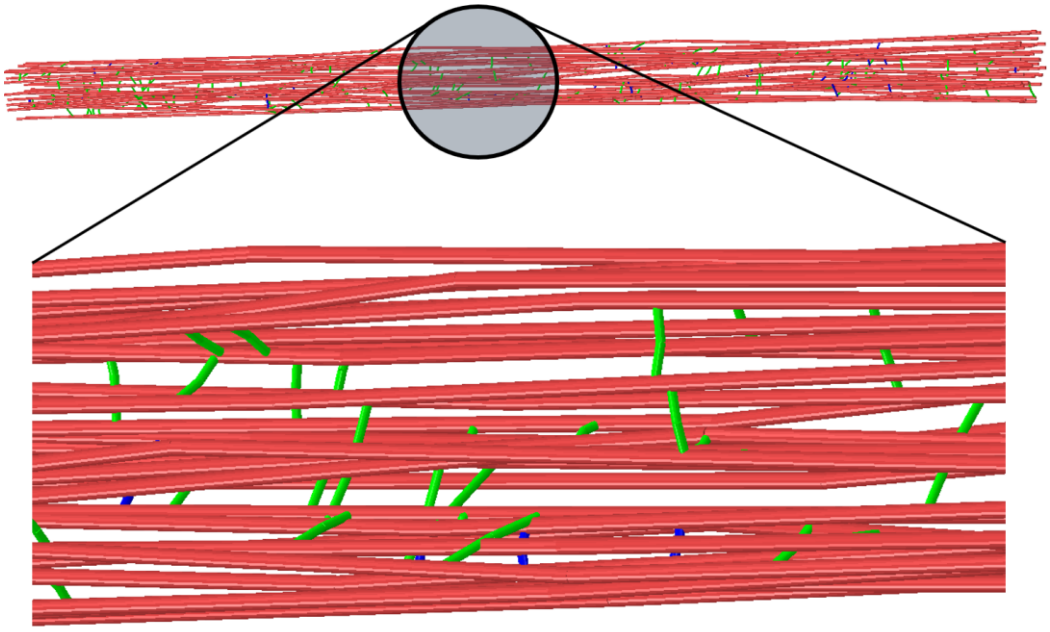

Figure 7.1 Model of the filopodial/invadopodial F-actin bundle. Red, green and blue beams are actin filaments, α-actinin and fascin, respectively.

Table 7-1 Diameters and elastic properties of actin filaments and crosslinking proteins

Types of proteins	Diameter of cross-section	Poisson's ratio	Young's modulus	Refs.
Actin filaments	7 nm	0.3	2 GPa	[23, 31, 184]
α-actinin	4 nm	0.3	60 MPa	[185]
fascin	5 nm	0.3	1 GPa	[70]

7.3 Results

Filopodia and invadopodia are finger-like structures, which mainly generate propulsive force to drive cell migration. Therefore, the most important elastic property of them is the Young's modulus E_2 in their protruding directions. Each

data point in our results is a mean value calculated from about 30 stochastic models with the same set of parameters.

7.2.1 Filament density

The self-assembling number of actin filaments in the filopodia and invadopodia is one of key factors influencing the elastic properties of their F-actin bundles [66]. Here, we define filament density V_f as the volume fraction of actin filaments in the filopodial/invadopodial cylindrical space and it can be expressed as

$$V_f = \frac{\sum_{i=1}^{N^{filament}} l_i d^2}{4 L_b r_b^2} \tag{7.1}$$

where $N^{filament}$ is the number of actin filaments; l_i is the length of the ith actin filament; d is the diameter of an actin filament; L_b and r_a are the length and radius of filopodia/invadopodia, respectively. In this section, we assume that the radius is 75nm.

As can be seen from Fig. 7.2, increased actin filament density V_f significantly improves Young's modulus E_2 of the filopodial/invadopodial F-actin bundles. Specifically, when the number of actin filaments in filopodia/invadopodia increases from 16 to 40, the Young's modulus rapidly increases from 3.3 MPa to 39 MPa. The scale power relationship between the Young's modulus and the actin filament density is about 2.7, i.e., $E_2 \sim V_f^{2.7}$, which is very similar to the scale power 2.5 of isotropic crosslinked actin networks [190]. We further checked the architectures of our models to investigate why the Young's modulus of the filopodial/invadopodial F-actin bundles has such a strong dependent relationship on actin filament density. Here, we introduce a parameter named as the density of crosslinking proteins, which is defined as the average number of crosslinking proteins, namely, actinin

and fascin, binding on every 1 μm actin filament in the F-actin bundle, as expressed by

$$\rho_c = \frac{(N^{actinin} + N^{fascin})}{\sum_i^{N^{filament}} l_i} \tag{7.2}$$

where $N^{actinin}$ and N^{fascin} are the numbers of actinin and fascin in the F-actin bundle, respectively. Interestingly, as shown in Fig. 7.3, we find that when the actin filament density increases, the density of crosslinking proteins also significantly increases because the generation of a crosslinking protein between two actin filaments is based on the length of the crosslinking protein and the spatial distance between the two actin filaments [168]. Thus, denser actin filaments in filopodia or invadopodia mean the spatial distance between each pair of actin filaments is shorter, which will inevitably induce more crosslinking proteins to be generated. Then, we deliberately control the density of crosslinking proteins as a constant value 5 in all models, it is found that the scale power relationship between Young's modulus E_2 and the actin filament density V_f reduces from 2.7 to 1.4 (Figs. 7.2 and 7.4). Consequently, the influence of actin filament density on Young's modulus is strongly coupled with the impact from the density of crosslinking proteins. The dynamic assembling behaviours of actin filaments can regulate the stiffness of the filopodial/invadopodial F-actin bundles in a broad range. Moreover, our results show that Young's modulus of F-actin bundles is in MPa range, which is consistent with that of the in vitro experimental result (20-200 MPa) [66] and is much larger than those of lamellipodial branched actin networks and crosslinked actin networks, which are in kPa and Pa ranges, respectively.

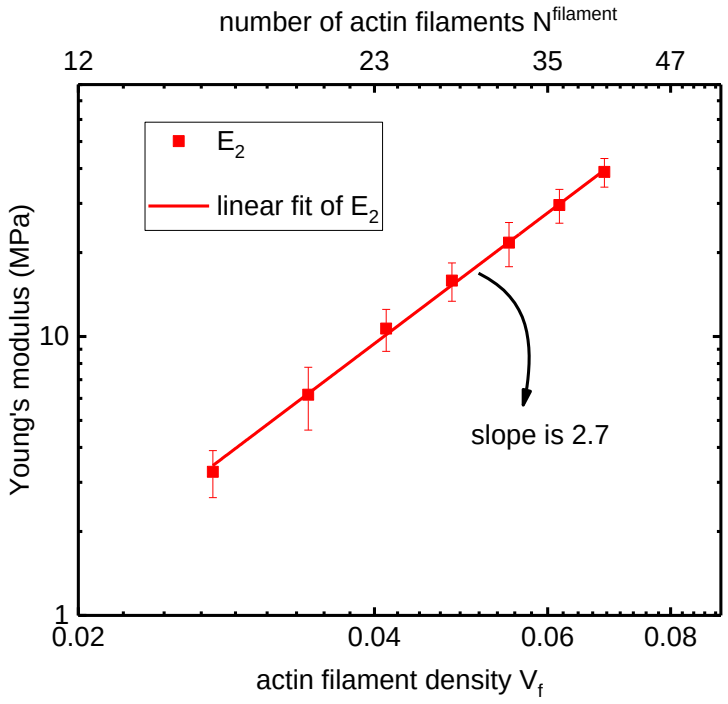

Figure 7.2 The relationship between Young's modulus E_2 and the actin filament density in the filopodial/invadopodial F-actin bundles. However, here the density of actin filaments is coupled with the density of crosslinking proteins because the generation of crosslinking proteins is based on the spatial distance between each pair of actin filaments.

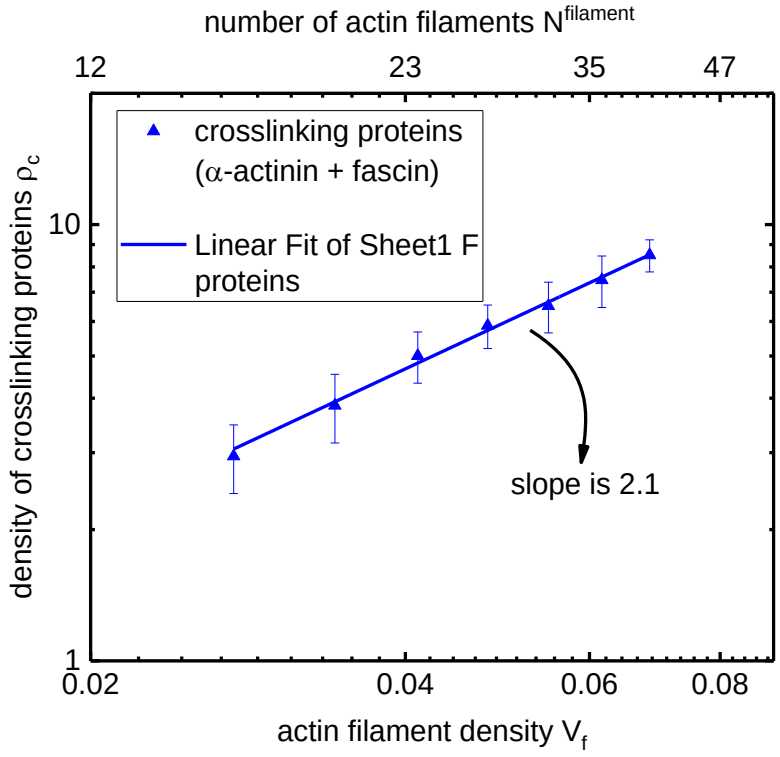

Figure 7.3 The relationship between Young's modulus E_2 and filament density of the filopodial/invadopodial F-actin bundles.

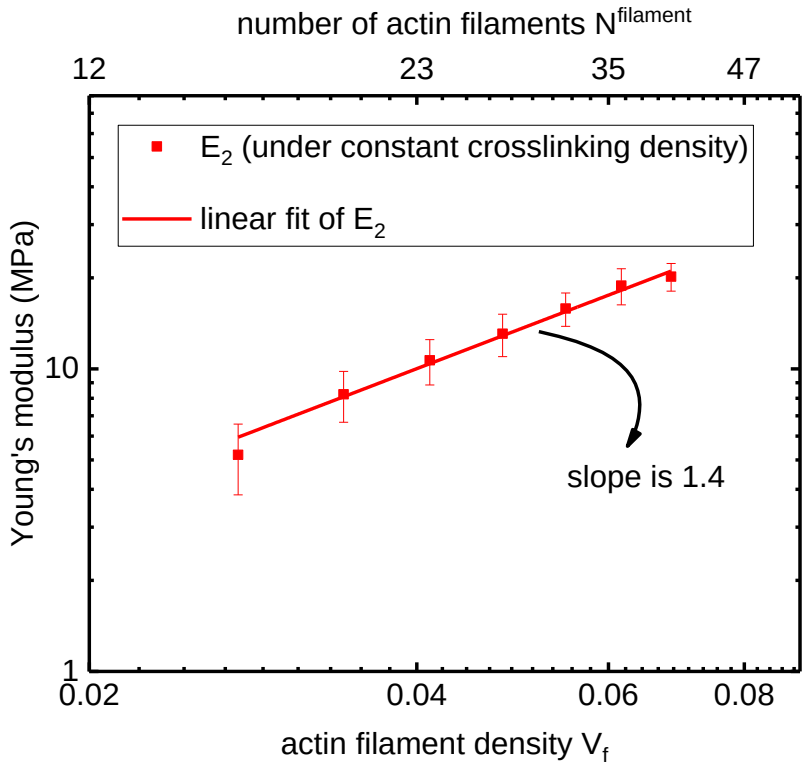

Figure 7.4 The relationship between Young's modulus E_2 and filament density V_f of the filopodial/invadopodial F-actin bundles when the density of crosslinking proteins is kept constant $\rho_c = 5$.

7.2.2 Densities of crosslinking proteins

In this section, we investigate how the highly dynamic binding and unbinding crosslinking proteins, i.e., α-actinin and fascin, modulate the stiffness of the filopodial/invadopodial F-actin bundles. In order to exclude the impact of actin filament density, we keep V_f as a constant 4.8%. As shown in Fig. 7.5, when ρ_c increases from 1.2 to 23.5, E_2 is significantly improved from 2.7 to 52.4 MPa. Thus, increased density of crosslinking proteins ρ_c sensitively improves the protruding direction Young's modulus of the filopodial/invadopodial F-actin bundles. This may explain the experimental findings that fascin and α-actinin are highly

expressed in the invadopodia or filopodia of invasive cancer cells and neurons [152, 153, 158, 215] and inhibiting their activity can block tumour metastasis [216]. Because high expression of crosslinking proteins means stronger F-actin bundles, filopodia/invadopodia with a high density of crosslinking proteins can more easily facilitate cells or neurons to split channels in the confining extracellular microenvironments to migrate through or form neurites.

Furthermore, interestingly, the scale relationship of Young's modulus E_2 to the density of crosslinking proteins can be roughly divided into two stages. In the first stage, the density of crosslinking proteins is less than 11 and Young's modulus E_2 scales with ρ_c as 1.12, i.e., $E_2 \sim \rho_c^{1.12}$. However, when $\rho_c > 11$ (the second stage), $E_2 \sim \rho_c^{0.65}$. They indicate that after the density of crosslinking proteins reaching a certain value, its enhancing sensitivity on the stiffness of filopodial/invadopodial F-actin bundles begins to reduce. To explore the underlying reasons, we further examine the deformation states of these models. Strikingly, as shown in Fig. 7.6, it is found that when the crosslinking density is in the low-value range ($\rho_c = 5$), actin filaments in the filopodial/invadopodial F-actin bundle notably bend individually (Fig. 7.6a) because a low density of crosslinking proteins is unable to resist the shear slip between them and to constrain them to bend away from each other. Thus, in the first stage, increased ρ_c shows a more sensitive enhancing effect on Young's modulus E_2. However, for the condition of high density of crosslinking proteins ($\rho_c = 12$), actin filaments are tightly bound together by crosslinking proteins to prohibit relative slips and thus their deformations are coupled together (Fig. 7.6b). Consequently, compared with that of the first stage, the Young's modulus E_2 of the filopodial/invadopodial F-actin bundles in the second stage has a weaker scaling relationship with the increased density of crosslinking proteins.

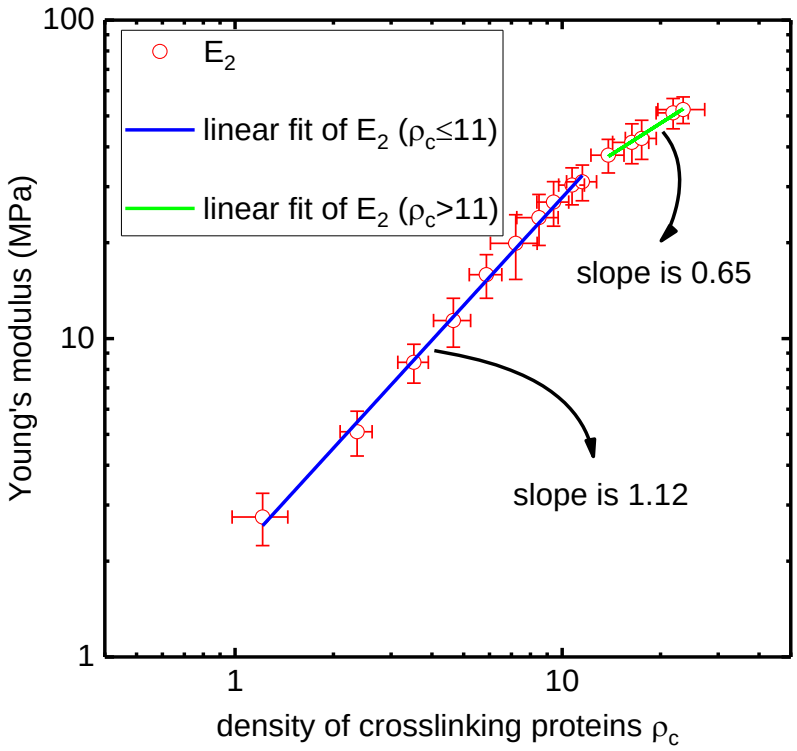

Figure 7.5 The relationship between the Young's modulus E_2 and the binding density of crosslinking proteins ρ_c in the filopodial/invadopodial F-actin bundles.

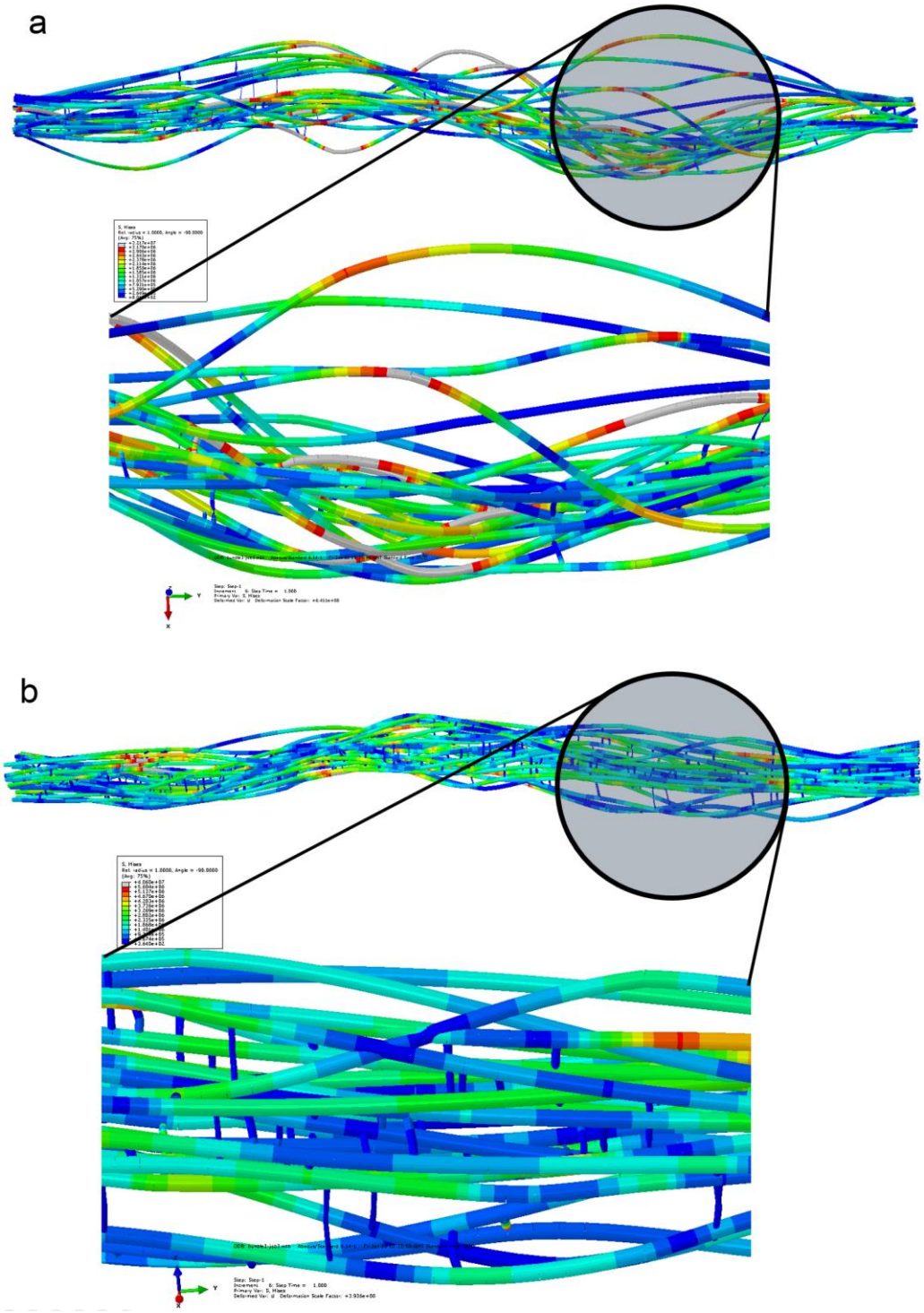

Figure 7.6 Deformation states and Mises stress distributions of the filopodial/invadopodial F-actin bundle after applying a uniaxial compression in the

protruding (longitudinal) direction. (a) The density of crosslinking proteins ρ_c is 5. (b) The density of crosslinking proteins ρ_c is 12.

7.2.3 Nonlinear geometrical deformation of filopodial/invadopodial F-actin bundles

The protrusions of filopodia and invadopodia in extracellular microenvironments are based on the polymerization of actin filaments in their F-actin bundles. Filopodial/invadopodial F-actin bundles are finger-like structures and have large slenderness ratios. Therefore, under the constraint of extracellular resistance, the polymerizing force might induce buckling of them. Thus, here we investigate the nonlinear geometrical deformation behaviours of the filopodial/invadopodial F-actin bundles.

Actin filaments in filopodia and invadopodia usually grow to a length of several to more than 10 micrometers [70, 154], which is comparative to its persistence length. Thus, in vivo thermal fluctuations induce undulations of filopodial/invadopodial actin filaments [23, 26]. To simulate this, as demonstrated in Section 7.2, stochastic transverse deflections (20 nm) are randomly added to each actin filament with average intervals of 300 nm in the filopodial/invadopodial space. We firstly explore the impact of thermal-induced actin filament undulations on the nonlinear geometrical deformation behaviours of the filopodial/invadopodial F-actin bundles. While the densities of actin filaments, α-actinin and fascin and dimensions of filopodia/invadopodia are all kept the same, compared with the straight actin filaments, thermal-induced undulations of actin filaments significantly reduce the initial stiffness of filopodial/invadopodial F-actin bundles (Fig. 7.7). The critical load of the F-actin bundle p_{cr} with undulated actin filaments is 281 pN, which is much smaller than the 745 pN of the F-actin bundle with straight actin filaments (Fig. 7.7). A comparison of their Mises stress distributions shows that severe local stress concentrations are produced in the F-actin bundle with

undulated actin filaments while the Mises stress distributes more homogeneously in the F-actin bundle with straight actin filaments (Fig. 7.8). Consequently, our results demonstrate that thermal-induced actin filament undulations can significantly influence the buckling behaviours of filopodial/invadopodial F-actin bundles. In addition, our results indicate filopodial/invadopodial F-actin bundles buckle at a very low compressive strain (0.1% for the undulated F-actin bundle and 0.03% for the straight F-actin bundle). After buckling, the stiffness of the F-actin bundles steeply decreases. When their strains exceed 1.7%, the impact of thermal-induced actin filament undulations on the F-actin bundle deformation behaviours almost disappears (Fig. 7.7).

Next, we explore how the dynamic self-assembling actin filaments and crosslinking proteins, i.e., α-actinin and fascin, affects the nonlinear geometrical deformation behaviours of the filopodia/invadopodia. As shown in Figs. 7.9, both of the assembling and disassembling of actin filaments and the binding and unbinding of crosslinking proteins can sensitively regulate the buckling properties of the filopodia/invadopodia. To be specific, when the density of actin filaments (6.9%) is reduced by 25%, the critical load decreases from 301 pN to 269 pN. When the density of crosslinking proteins (14.9) is reduced by 25%, the corresponding critical load decrease from 301 pN to 249 pN. These results indicate the bulking of filopodial/invadopodial F-actin bundles is more sensitive to the density of crosslinking proteins. However, when the compressive strain exceeds 2.5%, the variations of the density of actin filaments and the density of crosslinking proteins have similar regulation impacts on the nonlinear geometrical deformations of filopodia/invadopodia.

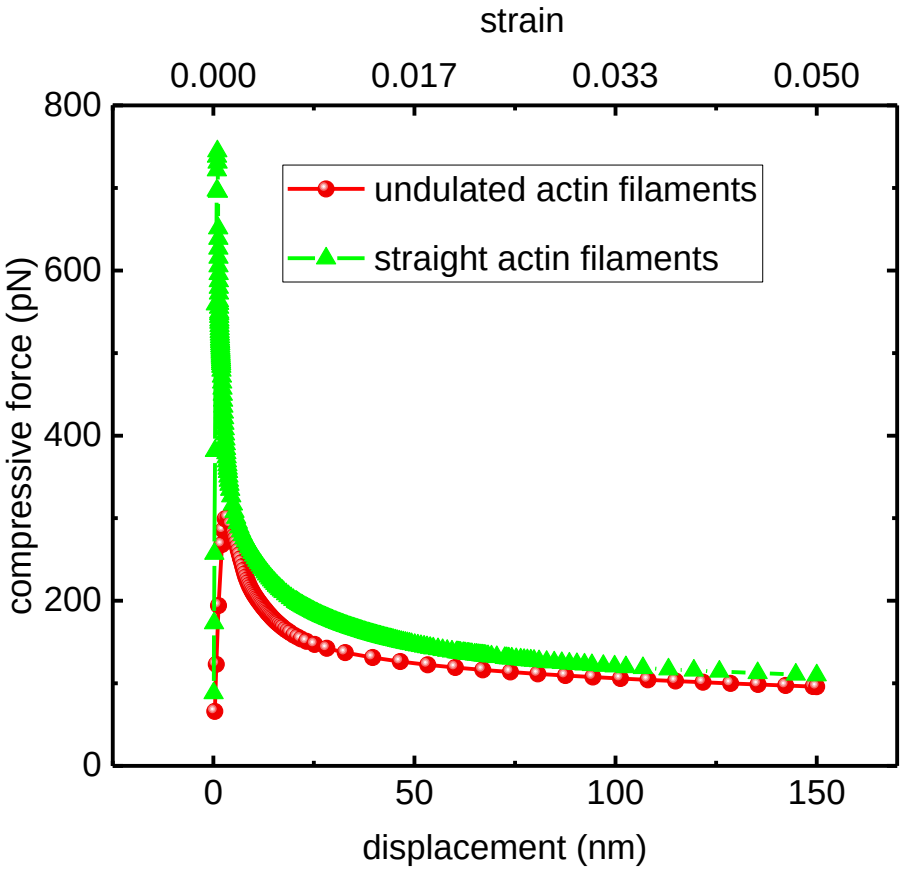

Figure 7.7 Comparison of nonlinear geometrical deformation behaviours of filopodial/invadopodial F-actin bundles with straight and undulated actin filaments. The lengths and radiuses of filopodia/invadopodia are 3um and 80nm. There are 36 actin filaments in the filopodia/invadopodia.

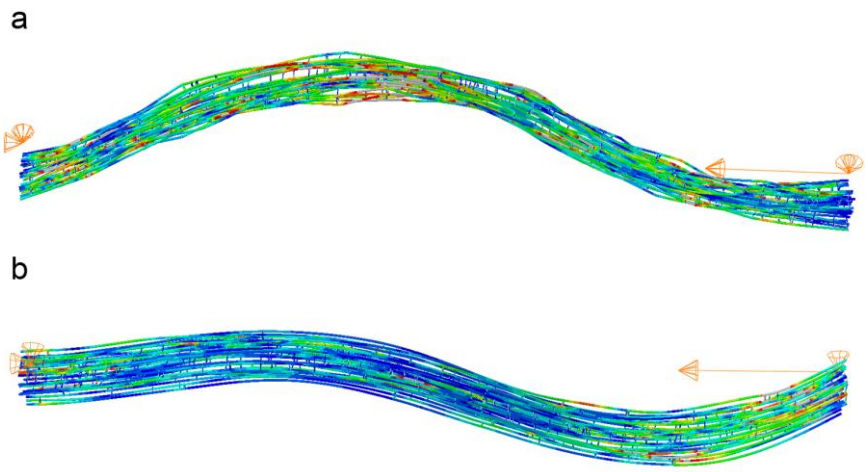

Figure 7.8 Comparison of the deformation states and Mises stress distributions of the filopodial/invadopodial F-actin bundle. (a) Filopodial/invadopodial F-actin bundle with undulated actin filaments. (b) Filopodial/invadopodial F-actin bundle with straight actin filaments.

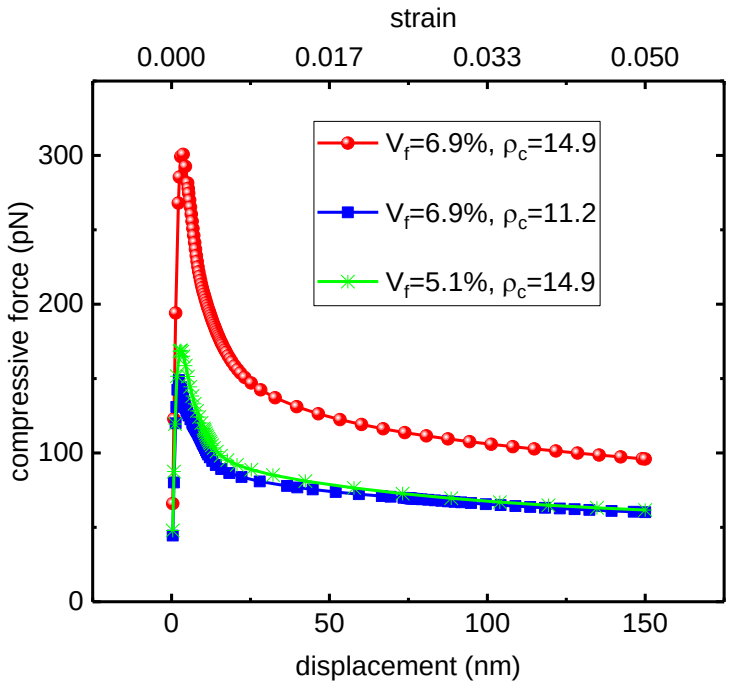

Figure 7.9 Impacts of the densities of actin filament and crosslinking proteins on the nonlinear geometrical deformation behaviours of filopodial/invadopodial F-actin bundles.

7.4 Discussion

Through the three-dimensional regulatable model of filopodial/invadopodial F-actin bundles, we investigate how the highly dynamic assembling and disassembling actin filaments and unbinding and unbinding of crosslinking proteins, namely, α-actinin and fascin, regulate the elastic properties of filopodia/invadopodia, respectively and combinedly. The results show that these intracellular proteins can sensitively modulate Young's modulus of filopodia/invadopodia in a broad range from 2MPa to 80MPa. Using filopodia/invadopodia and lamellipodia, which has Young's moduli in KPa range, cells can sense a wide range of rigidities of extracellular microenvironments for migration. In addition, the stiffness of filopodial/invadopodial F-actin bundles is much larger than those of other cytoskeletons, such as branched actin networks and crosslinked actin networks. This high stiffness is closely related to filopodia and invadopodia functions. Invadopodia with high stiffness can easily protrude in extracellular matrix. Then, they secrete matrix metalloproteinases to degrade surrounding microenvironments [104] and thus enable cancer cells to metastasize into other tissues or circulating systems. Filopodia normally grow out from lamellipodia and they lead the protrusions of lamellipodia. Filopodia first protrude into extracellular matrix to open finger-like channels. However, these finger-like channels have a maximum diameter of about 200nm [70], which is too narrow for cells to migrate through. Then, lamellipodia protrude in this direction to split a wide channel in the extracellular matrix. Thus, filopodia and lamellipodia cooperate to drive cell migration in complex extracellular microenvironments. Furthermore, for neurons, the extension of neurites in different tissues is based on filopodia protrusion [158]. Thus, the high stiffness of filopodia is essentially important for neuritogenesis in different mechanical environments.

Second, it is found that the undulation of actin filaments resulted from in vivo thermal fluctuations significantly reduces the critical load of filopodia/invadopodia.

Increased densities of actin filaments and crosslinking proteins greatly improves their critical loads. In addition, filopodia/invadopodia buckles at very low strains and their stiffness rapidly decreases after buckling. In vivo conditions, however, filopodia/invadopodia are in extracellular matrix and they generate adhesions to bind on extracellular matrix to improve their stability. Hence, the large deformation of filopodia/invadopodia in vivo is constrained by their surrounding extracellular microenvironments. Thus, they can effectively drive cell migration and neural cell neuritogenesis.

Chapter 8 Conclusions and Future Researches

8.1 Conclusions

Cell migration essentially depends on the mechanical interactions between cell leading edges and the confining extracellular microenvironments. This research studies the elastic properties and behaviours of the leading edge lamellipodial branched actin networks and filopodial/invadopodial F-actin bundles, which are high dynamically modulated by various intracellular proteins. More importantly, this research reveals the underlying intracellular biophysical mechanisms of migrating cell sensing and adapting to heterogeneous extracellular microenvironments.

Lamellipodial branched actin network support the leading edge protrusion. The stiffness of lamellipodial branched actin network is sensitive to the concentration of actin filaments. For a migrating cell, the network is highly anisotropic and has a much higher stiffness in the moving direction than that in the transverse and out-plane directions. The physical mechanisms of two experimentally observed architecture transformations in the network induced by different magnitudes of loading are revealed, which indicates that this tuneable network microstructure is important for cell motility under extracellular resistance. Both successive branching generations from a single mother filament and the densities of crosslinking proteins linearly improve the compressive or tensile and shear moduli of the actin network. To effectively support cell motility, there should be at least three successive branching generations from mother filaments. Strikingly, the increase of the density of Arp2/3 complex firstly presents an improving effect and then unexpectedly shows a reducing effect on the stiffness of the network. We identify that the high density of Arp2/3 complex would inevitably induce local heterogeneity in the

global network resulting in the poor mechanical property. Additionally, the in-plane Poisson's ratio ν_{12} is always much larger than the out-of-plane ratio ν_{32} in all models, which can explain why lamellipodium grows into a sheet-like structure.

In addition, under the extracellular resistance load, the deformation mechanism of the network is mainly dominated by the bending deformation of actin filaments. Since Arp2/3 complex prefers to bind on the convex side of a bent actin filament and nucleates a daughter actin filament, this reveals that, on the basis of actin filament deformations, the branched actin network supporting cell migration can mechanically sense the varying stiffness of confining microenvironments and accordingly self-regulate its stiffness by increasing or reducing its filament density and crosslinking proteins' densities to adapt to the varying extracellular resistance. To be specific, when the resistance impeding cell migration increases, actin filaments in the branched actin network will be bent more severely, and thus more Arp2/3 complexes will bind on them and nucleate more daughter filaments. It is found the density of crosslinking proteins is proportional to the filament density, which means that increased density of actin filament improves the self-assembling of crosslinking proteins to strengthen the branched actin network. Hence, the stiffness of the branched actin network becomes larger, which enables the migrating cell to overcome the increased resistance. This resistance-adaptive mechanical mechanism is important for the lamellipodial branched actin network supporting cell migration.

This research also proposes a theoretical 'bending-straightening elastic racket' (BSER) model to explain the propulsive mechanism of cell migration. Through large-scale spatial and temporal simulation of lamellipodium protrusion in highly varying extracellular microenvironments, this model for the first time systematically and quantitatively predicts all the important LE protruding behaviours of actin-base cell migration: (1) lamellipodial branched actin filament density relies on extracellular resistance; (2) LE protruding velocity depends on

loading history; (3) actin-based protrusion is saltatory with time; (4) LE of migrating cells circumnavigate obstacles and directionally migrates in vivo. The underlying microscopic physical mechanisms of these macroscopic cell migration behaviours are also quantitatively deciphered. More importantly, our model reveals the very fundamental microscopic physical mechanism by which migrating cells sense and adapt their propulsive forces to the highly dynamic and complex extracellular microenvironment at their LEs. Through the bending deformation curvature of the polymerizing actin filaments pushing against the LE membrane, a cell can sense the magnitude and variation of extracellular resistance. If the resistance increases or decreases, the bending curvature of polymerizing actin filaments will simultaneously increase or decrease, which further induces more active or less active Arp2/3 complex binding on these actin filaments and nucleating new actin filaments. Therefore, according to the variation of confining extracellular resistance, migrating cells adapt the density of actin filaments pushing against the LE membrane and hence adapt their propulsive force to overcome the resistance. Through this mechanism, cells are able to use their intracellular resources with maximum efficiency to overcome extracellular resistance and to invade into other tissues and circulating systems.

It is quantitatively identified that directional cell migration is a balancing consequence of local extracellular resistance, the heterogeneous density of polymerizing actin filaments and local concentrations of actin monomers in lamellipodia. To maximize the directional LE protrusion, the local actin monomer concentration should match the local density of actin filaments, which is modulated by extracellular resistance, and thus make them polymerize at a high rate. If the distribution of actin monomers is roughly homogeneous in lamellipodia, the LE will select the least resistance path to drive cell migration. In cells, except for cell migration, actin-based propulsion related to Arp2/3 complex also plays essential roles in other dynamic physiological activities, such as endocytosis, intracellular pathogen transport and dendritic spine formation in cortical neurons. Therefore, the

theoretical BSER model proposed here is also applicable to explain the underlying physical mechanisms of these biological activities.

Finally, this research investigates the Young's modulus and buckling behaviours of filopodia/invadopodia F-actin bundles, which is regulated by the highly dynamic assembling and disassembling actin filaments and unbinding and unbinding of crosslinking proteins (α-actinin and fascin), respectively and combinedly. The undulation of actin filaments due to in vivo thermal fluctuation significantly influence on the buckling behaviours of filopodia/invadopodia. The stiffness of filopodial/invadopodial F-actin bundles is much larger than that of lamellipodial branched actin networks. Thus, using filopodia/invadopodia and lamellipodia, migrating cells are able to protrude in a wide rigidity range of heterogeneous extracellular microenvironments. In addition, filopodia normally grow out from lamellipodia and they lead the protrusions of lamellipodia. Filopodia first protrude into extracellular matrix to open thin channels and then lamellipodia protrude in this direction to split a wide channel. Thus, filopodia and lamellipodia cooperate to drive cell migration in complex extracellular microenvironments.

8.2 Future researches

This research only studies the leading edge behaviours of migrating cells. However, cell migration in three dimensions is a very complex and systematic coordinating process of a whole cell body. This systematic coordinating process includes protrusion, contractility, body deformation, adhesions and interactions with extracellular matrix. These behaviours can significantly affect cell migrations. For example, migrating cells can develop larger focal adhesions on stiffer matrices and hence actin stress filaments can exert higher force for cell migration [217]. Thus, with the improvement of computational capability, it is important to construct a multi-scale cell model in future researches to study how these behaviours are coordinated together to determine cell migrations.

References

[1] D.A. Fletcher, R.D. Mullins, Cell mechanics and the cytoskeleton, Nature 463(7280) (2010) 485.

[2] P. Bieling, T.D. Li, J. Weichsel, R. McGorty, P. Jreij, B. Huang, D.A. Fletcher, R.D. Mullins, Force Feedback Controls Motor Activity and Mechanical Properties of Self-Assembling Branched Actin Networks, Cell 164(1-2) (2016) 115-127.

[3] C.C. DuFort, M.J. Paszek, V.M. Weaver, Balancing forces: architectural control of mechanotransduction, Nat. Rev. Mol. Cell Biol. 12(5) (2011) 308.

[4] D.T. Butcher, T. Alliston, V.M. Weaver, A tense situation: forcing tumour progression, Nat. Rev. Cancer 9(2) (2009) 108.

[5] A.J. Engler, S. Sen, H.L. Sweeney, D.E. Discher, Matrix elasticity directs stem cell lineage specification, Cell 126(4) (2006) 677-689.

[6] D.E. Discher, D.J. Mooney, P.W. Zandstra, Growth factors, matrices, and forces combine and control stem cells, Science 324(5935) (2009) 1673-1677.

[7] F.M. Watt, W.T. Huck, Role of the extracellular matrix in regulating stem cell fate, Nat. Rev. Mol. Cell Biol. 14(8) (2013) 467-473.

[8] T.D. Pollard, J.A. Cooper, Actin, a central player in cell shape and movement, Science 326(5957) (2009) 1208-1212.

[9] L. Blanchoin, R. Boujemaa-Paterski, C. Sykes, J. Plastino, Actin dynamics, architecture, and mechanics in cell motility, Physiol. Rev. 94(1) (2014) 235-263.

[10] T.D. Pollard, The cytoskeleton, cellular motility and the reductionist agenda, Nature 422(6933) (2003) 741.

[11] S. van Helvert, C. Storm, P. Friedl, Mechanoreciprocity in cell migration, Nat. Cell Biol. 20(1) (2018) 8.

[12] T.D. Pollard, G.G. Borisy, Cellular motility driven by assembly and disassembly of actin filaments, Cell 112(4) (2003) 453-465.

[13] J. Mueller, G. Szep, M. Nemethova, I. de Vries, A.D. Lieber, C. Winkler, K. Kruse, J.V. Small, C. Schmeiser, K. Keren, Load adaptation of lamellipodial actin networks, Cell 171(1) (2017) 188-200. e16.

[14] A. Mogilner, On the edge: modeling protrusion, Current opinion in cell biology 18(1) (2006) 32-39.

[15] K.M. Wisdom, K. Adebowale, J. Chang, J.Y. Lee, S. Nam, R. Desai, N.S. Rossen, M. Rafat, R.B. West, L. Hodgson, Matrix mechanical plasticity regulates cancer cell migration through confining microenvironments, Nat. Commun. 9(1) (2018) 4144.

[16] M. Krause, A. Gautreau, Steering cell migration: lamellipodium dynamics and the regulation of directional persistence, Nat. Rev. Mol. Cell Biol. 15(9) (2014) 577.

[17] C.D. Paul, P. Mistriotis, K. Konstantopoulos, Cancer cell motility: lessons from migration in confined spaces, Nat. Rev. Cancer 17(2) (2017) 131.

[18] C.H. Stuelten, C.A. Parent, D.J. Montell, Cell motility in cancer invasion and metastasis: insights from simple model organisms, Nat. Rev. Cancer 18(5) (2018) 296.

[19] K.M. Yamada, M. Sixt, Mechanisms of 3D cell migration, Nat. Rev. Mol. Cell Biol. (2019) 1-15.

[20] J. Singla, K.M. McClary, K.L. White, F. Alber, A. Sali, R.C. Stevens, Opportunities and Challenges in Building a Spatiotemporal Multi-scale Model of the Human Pancreatic β Cell, Cell 173(1) (2018) 11-19.

[21] B. Waclaw, I. Bozic, M.E. Pittman, R.H. Hruban, B. Vogelstein, M.A. Nowak, A spatial model predicts that dispersal and cell turnover limit intratumour heterogeneity, Nature 525(7568) (2015) 261.

[22] P.M. Altrock, L.L. Liu, F. Michor, The mathematics of cancer: integrating quantitative models, Nat. Rev. Cancer 15(12) (2015) 730.

[23] C.P. Broedersz, F.C. MacKintosh, Modeling semiflexible polymer networks, Rev. Mod. Phys. 86(3) (2014) 995.

[24] K.C. Holmes, D. Popp, W. Gebhard, W. Kabsch, Atomic model of the actin filament, Nature 347(6288) (1990) 44.

[25] T.D. Pollard, Rate constants for the reactions of ATP-and ADP-actin with the ends of actin filaments, J. Cell Biol. 103(6) (1986) 2747-2754.

[26] O. Chaudhuri, S.H. Parekh, D.A. Fletcher, Reversible stress softening of actin networks, Nature 445(7125) (2007) 295.

[27] T.M. Svitkina, G.G. Borisy, Arp2/3 complex and actin depolymerizing factor/cofilin in dendritic organization and treadmilling of actin filament array in lamellipodia, J. Cell Biol. 145(5) (1999) 1009-1026.

[28] G.A. Holzapfel, R.W. Ogden, Elasticity of biopolymer filaments, Acta biomaterialia 9(7) (2013) 7320-7325.

[29] G. Foffano, N. Levernier, M. Lenz, The dynamics of filament assembly define cytoskeletal network morphology, Nat. Commun. 7 (2016) 13827.

[30] F. Gittes, B. Mickey, J. Nettleton, J. Howard, Flexural rigidity of microtubules and actin filaments measured from thermal fluctuations in shape, J. Cell Biol. 120(4) (1993) 923-934.

[31] H. Kojima, A. Ishijima, T. Yanagida, Direct measurement of stiffness of single actin filaments with and without tropomyosin by in vitro nanomanipulation, Proc. Natl. Acad. Sci. U.S.A. 91(26) (1994) 12962-12966.

[32] C.P. Brangwynne, F.C. MacKintosh, S. Kumar, N.A. Geisse, J. Talbot, L. Mahadevan, K.K. Parker, D.E. Ingber, D.A. Weitz, Microtubules can bear enhanced compressive loads in living cells because of lateral reinforcement, J. Cell Biol. 173(5) (2006) 733-741.

[33] T. Mitchison, M. Kirschner, Dynamic instability of microtubule growth, nature 312(5991) (1984) 237.

[34] M. Kirschner, T. Mitchison, Beyond self-assembly: from microtubules to morphogenesis, Cell 45(3) (1986) 329-342.

[35] S. Etienne-Manneville, Microtubules in cell migration, Annual review of cell and developmental biology 29 (2013) 471-499.

[36] M.B. Omary, P.A. Coulombe, W.I. McLean, Intermediate filament proteins and their associated diseases, New England Journal of Medicine 351(20) (2004) 2087-2100.

[37] G. Wiche, Role of plectin in cytoskeleton organization and dynamics, Journal of cell science 111(17) (1998) 2477-2486.

[38] E.W. Flitney, E.R. Kuczmarski, S.A. Adam, R.D. Goldman, Insights into the mechanical properties of epithelial cells: the effects of shear stress on the assembly and remodeling of keratin intermediate filaments, FASEB J. 23(7) (2009) 2110-2119.

[39] M.-Y. Tsai, S. Wang, J.M. Heidinger, D.K. Shumaker, S.A. Adam, R.D. Goldman, Y. Zheng, A mitotic lamin B matrix induced by RanGTP required for spindle assembly, Science 311(5769) (2006) 1887-1893.

[40] E. Fuchs, D.W. Cleveland, A structural scaffolding of intermediate filaments in health and disease, Science 279(5350) (1998) 514-519.

[41] I. Schwaiger, A. Kardinal, M. Schleicher, A.A. Noegel, M. Rief, A mechanical unfolding intermediate in an actin-crosslinking protein, Nature structural & molecular biology 11(1) (2004) 81.

[42] L.M. Machesky, S.J. Atkinson, C. Ampe, J. Vandekerckhove, T.D. Pollard, Purification of a cortical complex containing two unconventional actins from Acanthamoeba by affinity chromatography on profilin-agarose, J. Cell Biol. 127(1) (1994) 107-115.

[43] J.D. Rotty, C. Wu, J.E. Bear, New insights into the regulation and cellular functions of the ARP2/3 complex, Nat. Rev. Mol. Cell Biol. 14(1) (2013) 7.

[44] N. Molinie, A. Gautreau, The Arp2/3 regulatory system and its deregulation in cancer, Physiol. Rev. 98(1) (2017) 215-238.

[45] K. Rottner, T.E. Stradal, How distinct Arp2/3 complex variants regulate actin filament assembly, Nat. Cell Biol. 18(1) (2016) 1.

[46] E.D. Goley, M.D. Welch, The ARP2/3 complex: an actin nucleator comes of age, Nat. Rev. Mol. Cell Biol. 7(10) (2006) 713.

[47] R.C. Robinson, K. Turbedsky, D.A. Kaiser, J.-B. Marchand, H.N. Higgs, S. Choe, T.D. Pollard, Crystal structure of Arp2/3 complex, Science 294(5547) (2001) 1679-1684.

[48] N. Volkmann, K.J. Amann, S. Stoilova-McPhie, C. Egile, D.C. Winter, L. Hazelwood, J.E. Heuser, R. Li, T.D. Pollard, D. Hanein, Structure of Arp2/3 complex in its activated state and in actin filament branch junctions, science 293(5539) (2001) 2456-2459.

[49] L. Blanchoin, K.J. Amann, H.N. Higgs, J.-B. Marchand, D.A. Kaiser, T.D. Pollard, Direct observation of dendritic actin filament networks nucleated by Arp2/3 complex and WASP/Scar proteins, Nature 404(6781) (2000) 1007.

[50] L.A. Cameron, P.A. Giardini, F.S. Soo, J.A. Theriot, Secrets of actin-based motility revealed by a bacterial pathogen, Nat. Rev. Mol. Cell Biol. 1(2) (2000) 110.

[51] T. Magnuson Osborn, Mechanism of F-actin crosslinking by filamin A and the anti-inflammatory functions of plasma gelsolin in bodily fluids, Inst of Medicine. Dept of Rheumatology and Inflammation Research2007.

[52] C.A. Hartemink, The cross-linking mechanism of filamin A in the actin cytoskeleton, Massachusetts Institute of Technology, 2005.

[53] H.P. Modarres, M. Mofradt, Filamin: a structural and functional biomolecule with important roles in cell biology, signaling and mechanics, Mol Cell Biomech 11(1) (2014) 39-65.

[54] F. Nakamura, T.P. Stossel, J.H. Hartwig, The filamins: organizers of cell structure and function, Cell adhesion & migration 5(2) (2011) 160-169.

[55] J.M. Ferrer, H. Lee, J. Chen, B. Pelz, F. Nakamura, R.D. Kamm, M.J. Lang, Measuring molecular rupture forces between single actin filaments and actin-binding proteins, Proc. Natl. Acad. Sci. U.S.A. 105(27) (2008) 9221-9226.

[56] A.-X. Zhou, J.H. Hartwig, L.M. Akyürek, Filamins in cell signaling, transcription and organ development, Trends in cell biology 20(2) (2010) 113-123.

[57] F. Nakamura, T.M. Osborn, C.A. Hartemink, J.H. Hartwig, T.P. Stossel, Structural basis of filamin A functions, J. Cell Biol. 179(5) (2007) 1011-1025.

[58] B. Sjöblom, A. Salmazo, K. Djinović-Carugo, α-Actinin structure and regulation, Cell. Mol. Life Sci. 65(17) (2008) 2688.

[59] O. Pelletier, E. Pokidysheva, L.S. Hirst, N. Bouxsein, Y. Li, C.R. Safinya, Structure of actin cross-linked with α-actinin: a network of bundles, Phys. Rev. Lett. 91(14) (2003) 148102.

[60] P. Zou, N. Pinotsis, S. Lange, Y.-H. Song, A. Popov, I. Mavridis, O.M. Mayans, M. Gautel, M. Wilmanns, Palindromic assembly of the giant muscle protein titin in the sarcomeric Z-disk, Nature 439(7073) (2006) 229.

[61] K. Djinovic-Carugo, P. Young, M. Gautel, M. Saraste, Structure of the a-actinin rod: molecular basis for cross-linking of actin filaments, Cell 98(4) (1999) 537.

[62] C.M. Hampton, D.W. Taylor, K.A. Taylor, Novel structures for α-actinin: F-actin interactions and their implications for actin–membrane attachment and tension sensing in the cytoskeleton, Journal of molecular biology 368(1) (2007) 92-104.

[63] L. Dupré, R. Houmadi, C. Tang, J. Rey-Barroso, T lymphocyte migration: an action movie starring the actin and associated actors, Frontiers in immunology 6 (2015) 586.

[64] J.D. Winkelman, C. Suarez, G.M. Hocky, A.J. Harker, A.N. Morganthaler, J.R. Christensen, G.A. Voth, J.R. Bartles, D.R. Kovar, Fascin-and α-actinin-bundled networks contain intrinsic structural features that drive protein sorting, Curr. Biol. 26(20) (2016) 2697-2706.

[65] J. Golji, R. Collins, M.R. Mofrad, Molecular mechanics of the α-actinin rod domain: bending, torsional, and extensional behavior, PLoS computational biology 5(5) (2009) e1000389.

[66] M.M. Claessens, M. Bathe, E. Frey, A.R. Bausch, Actin-binding proteins sensitively mediate F-actin bundle stiffness, Nature materials 5(9) (2006) 748.

[67] R.K. Meyer, U. Aebi, Bundling of actin filaments by alpha-actinin depends on its molecular length, J. Cell Biol. 110(6) (1990) 2013-2024.

[68] H. Miyata, R. Yasuda, K. Kinosita Jr, Strength and lifetime of the bond between actin and skeletal muscle α-actinin studied with an optical trapping technique, Biochimica et Biophysica Acta (BBA)-General Subjects 1290(1) (1996) 83-88.

[69] A.J. Ehrlicher, R. Krishnan, M. Guo, C.M. Bidan, D.A. Weitz, M.R. Pollak, Alpha-actinin binding kinetics modulate cellular dynamics and force generation, Proc. Natl. Acad. Sci. U.S.A. 112(21) (2015) 6619-6624.

[70] A. Mogilner, B. Rubinstein, The physics of filopodial protrusion, Biophys. J. 89(2) (2005) 782-795.

[71] K. Baumann, Fascin and 3D nuclear moves, Nature Publishing Group MACMILLAN BUILDING, 4 CRINAN ST, LONDON N1 9XW, ENGLAND, 2016.

[72] A. Jayo, M. Malboubi, S. Antoku, W. Chang, E. Ortiz-Zapater, C. Groen, K. Pfisterer, T. Tootle, G. Charras, G.G. Gundersen, Fascin regulates nuclear movement and deformation in migrating cells, Dev. Cell 38(4) (2016) 371-383.

[73] C. Hug, P.Y. Jay, I. Reddy, J.G. McNally, P.C. Bridgman, E.L. Elson, J.A. Cooper, Capping protein levels influence actin assembly and cell motility in Dictyostelium, Cell 81(4) (1995) 591-600.

[74] M.A. Wear, J.A. Cooper, Capping protein: new insights into mechanism and regulation, Trends in biochemical sciences 29(8) (2004) 418-428.

[75] O. Esue, Y. Tseng, D. Wirtz, α-Actinin and filamin cooperatively enhance the stiffness of actin filament networks, PLoS One 4(2) (2009) e4411.

[76] L.A. Flanagan, J. Chou, H. Falet, R. Neujahr, J.H. Hartwig, T.P. Stossel, Filamin A, the Arp2/3 complex, and the morphology and function of cortical actin filaments in human melanoma cells, J. Cell Biol. 155(4) (2001) 511-518.

[77] M. Vinzenz, M. Nemethova, F. Schur, J. Mueller, A. Narita, E. Urban, C. Winkler, C. Schmeiser, S.A. Koestler, K. Rottner, Actin branching in the initiation and maintenance of lamellipodia, J Cell Sci 125(11) (2012) 2775-2785.

[78] A.J. Koleske, Molecular mechanisms of dendrite stability, Nature Reviews Neuroscience 14(8) (2013) 536-550.

[79] G.J. Doherty, H.T. McMahon, Mechanisms of endocytosis, Annual review of biochemistry 78 (2009) 857-902.

[80] R.J. Petrie, A.D. Doyle, K.M. Yamada, Random versus directionally persistent cell migration, Nat. Rev. Mol. Cell Biol. 10(8) (2009) 538.

[81] M. Abercrombie, J.E. Heaysman, S.M. Pegrum, The locomotion of fibroblasts in culture: IV. Electron microscopy of the leading lamella, Experimental cell research 67(2) (1971) 359-367.

[82] C. Rotsch, K. Jacobson, J. Condeelis, M. Radmacher, EGF-stimulated lamellipod extension in adenocarcinoma cells, Ultramicroscopy 86(1) (2001) 97-106.

[83] V.M. Laurent, S. Kasas, A. Yersin, T.E. Schäffer, S. Catsicas, G. Dietler, A.B. Verkhovsky, J.-J. Meister, Gradient of rigidity in the lamellipodia of migrating cells revealed by atomic force microscopy, Biophys. J. 89(1) (2005) 667-675.

[84] J.V. Small, T. Stradal, E. Vignal, K. Rottner, The lamellipodium: where motility begins, Trends in cell biology 12(3) (2002) 112-120.

[85] A. Giri, S. Bajpai, N. Trenton, H. Jayatilaka, G.D. Longmore, D. Wirtz, The Arp2/3 complex mediates multigeneration dendritic protrusions for efficient 3-dimensional cancer cell migration, FASEB J. 27(10) (2013) 4089-4099.

[86] J. Zimmermann, M. Falcke, Formation of transient lamellipodia, PLoS one 9(2) (2014) e87638.

[87] C. Rotsch, K. Jacobson, M. Radmacher, Dimensional and mechanical dynamics of active and stable edges in motile fibroblasts investigated by using atomic force microscopy, Proc. Natl. Acad. Sci. U.S.A. 96(3) (1999) 921-926.

[88] K.J. Amann, T.D. Pollard, The Arp2/3 complex nucleates actin filament branches from the sides of pre-existing filaments, Nat. Cell Biol. 3(3) (2001) 306.

[89] V.C. Abraham, V. Krishnamurthi, D.L. Taylor, F. Lanni, The actin-based nanomachine at the leading edge of migrating cells, Biophys. J. 77(3) (1999) 1721-1732.

[90] J. Pernier, S. Shekhar, A. Jegou, B. Guichard, M.-F. Carlier, Profilin interaction with actin filament barbed end controls dynamic instability, capping, branching, and motility, Dev. Cell 36(2) (2016) 201-214.

[91] T.M. Svitkina, A.B. Verkhovsky, K.M. McQuade, G.G. Borisy, Analysis of the actin–myosin II system in fish epidermal keratocytes: mechanism of cell body translocation, J. Cell Biol. 139(2) (1997) 397-415.

[92] K. Kasza, C. Broedersz, G. Koenderink, Y. Lin, W. Messner, E. Millman, F. Nakamura, T. Stossel, F. MacKintosh, D. Weitz, Actin filament length tunes elasticity of flexibly cross-linked actin networks, Biophys. J. 99(4) (2010) 1091-1100.

[93] J.L. Podolski, T.L. Steck, Length distribution of F-actin in Dictyostelium discoideum, Journal of Biological Chemistry 265(3) (1990) 1312-1318.

[94] C. Le Clainche, M.-F. Carlier, Regulation of actin assembly associated with protrusion and adhesion in cell migration, Physiol. Rev. 88(2) (2008) 489-513.

[95] J.E. Bear, T.M. Svitkina, M. Krause, D.A. Schafer, J.J. Loureiro, G.A. Strasser, I.V. Maly, O.Y. Chaga, J.A. Cooper, G.G. Borisy, Antagonism between Ena/VASP proteins and actin filament capping regulates fibroblast motility, Cell 109(4) (2002) 509-521.

[96] M. Bailly, F. Macaluso, M. Cammer, A. Chan, J.E. Segall, J.S. Condeelis, Relationship between Arp2/3 complex and the barbed ends of actin filaments at the leading edge of carcinoma cells after epidermal growth factor stimulation, J. Cell Biol. 145(2) (1999) 331-345.

[97] A. Mogilner, Mathematics of cell motility: have we got its number?, J Math Biol 58(1-2) (2009) 105-34.

[98] T. Pujol, O. du Roure, M. Fermigier, J. Heuvingh, Impact of branching on the elasticity of actin networks, Proc. Natl. Acad. Sci. U.S.A. 109(26) (2012) 10364-10369.

[99] J. Weichsel, U.S. Schwarz, Two competing orientation patterns explain experimentally observed anomalies in growing actin networks, Proc. Natl. Acad. Sci. U.S.A. 107(14) (2010) 6304-6309.

[100] R.D. Mullins, J.A. Heuser, T.D. Pollard, The interaction of Arp2/3 complex with actin: nucleation, high affinity pointed end capping, and formation of

branching networks of filaments, Proc. Natl. Acad. Sci. U.S.A. 95(11) (1998) 6181-6186.

[101] T.J. Kirby, J. Lammerding, Emerging views of the nucleus as a cellular mechanosensor, Nat. Cell Biol. 20(4) (2018) 373.

[102] S.A. Koestler, S. Auinger, M. Vinzenz, K. Rottner, J.V. Small, Differentially oriented populations of actin filaments generated in lamellipodia collaborate in pushing and pausing at the cell front, Nat. Cell Biol. 10(3) (2008) 306-313.

[103] M. Prass, K. Jacobson, A. Mogilner, M. Radmacher, Direct measurement of the lamellipodial protrusive force in a migrating cell, J. Cell Biol. 174(6) (2006) 767-72.

[104] M.-C. Kim, Y.R. Silberberg, R. Abeyaratne, R.D. Kamm, H.H. Asada, Computational modeling of three-dimensional ECM-rigidity sensing to guide directed cell migration, Proc. Natl. Acad. Sci. U.S.A. 115(3) (2018) E390-E399.

[105] F. Chemi, D.G. Rothwell, N. McGranahan, S. Gulati, C. Abbosh, S.P. Pearce, C. Zhou, G.A. Wilson, M. Jamal-Hanjani, N. Birkbak, J. Pierce, C.S. Kim, S. Ferdous, D.J. Burt, D. Slane-Tan, F. Gomes, D. Moore, R. Shah, M. Al Bakir, C. Hiley, S. Veeriah, Y. Summers, P. Crosbie, S. Ward, B. Mesquita, M. Dynowski, D. Biswas, J. Tugwood, F. Blackhall, C. Miller, A. Hackshaw, G. Brady, C. Swanton, C. Dive, T.R. Consortium, Pulmonary venous circulating tumor cell dissemination before tumor resection and disease relapse, Nature Medicine 25(10) (2019) 1534-1539.

[106] Q. Zeng, I.P. Michael, P. Zhang, S. Saghafinia, G. Knott, W. Jiao, B.D. McCabe, J.A. Galván, H.P. Robinson, I. Zlobec, Synaptic proximity enables NMDAR signalling to promote brain metastasis, Nature (2019) 1-6.

[107] J. Plastino, L. Blanchoin, Adaptive Actin Networks, Dev. Cell 42(6) (2017) 565-566.

[108] T. Chen, A. Callan-Jones, E. Fedorov, A. Ravasio, A. Brugués, H.T. Ong, Y. Toyama, B.C. Low, X. Trepat, T. Shemesh, Large-scale curvature sensing by directional actin flow drives cellular migration mode switching, Nat. Phys. 15(4) (2019) 393.

[109] O. Medalia, I. Weber, A.S. Frangakis, D. Nicastro, G. Gerisch, W. Baumeister, Macromolecular architecture in eukaryotic cells visualized by cryoelectron tomography, Science 298(5596) (2002) 1209-1213.

[110] A.J. Ridley, M.A. Schwartz, K. Burridge, R.A. Firtel, M.H. Ginsberg, G. Borisy, J.T. Parsons, A.R. Horwitz, Cell migration: integrating signals from front to back, Science 302(5651) (2003) 1704-1709.

[111] M. Tozluoğlu, A.L. Tournier, R.P. Jenkins, S. Hooper, P.A. Bates, E. Sahai, Matrix geometry determines optimal cancer cell migration strategy and modulates response to interventions, Nat. Cell Biol. 15(7) (2013) 751.

[112] Y.L. Han, A.F. Pegoraro, H. Li, K. Li, Y. Yuan, G. Xu, Z. Gu, J. Sun, Y. Hao, S.K. Gupta, Cell swelling, softening and invasion in a three-dimensional breast cancer model, Nat. Phys. (2019) 1-8.

[113] R. Boujemaa-Paterski, C. Suarez, T. Klar, J. Zhu, C. Guérin, A. Mogilner, M. Théry, L. Blanchoin, Network heterogeneity regulates steering in actin-based motility, Nat. Commun. 8(1) (2017) 655.

[114] O. Akin, R.D. Mullins, Capping protein increases the rate of actin-based motility by promoting filament nucleation by the Arp2/3 complex, Cell 133(5) (2008) 841-51.

[115] M.J. Footer, J.W. Kerssemakers, J.A. Theriot, M. Dogterom, Direct measurement of force generation by actin filament polymerization using an optical trap, Proc. Natl. Acad. Sci. U.S.A. 104(7) (2007) 2181-2186.

[116] D. Démoulin, M.-F. Carlier, J. Bibette, J. Baudry, Power transduction of actin filaments ratcheting in vitro against a load, Proc. Natl. Acad. Sci. U.S.A. 111(50) (2014) 17845-17850.

[117] W. Wang, S. Goswami, K. Lapidus, A.L. Wells, J.B. Wyckoff, E. Sahai, R.H. Singer, J.E. Segall, J.S. Condeelis, Identification and testing of a gene expression signature of invasive carcinoma cells within primary mammary tumors, Cancer Res. 64(23) (2004) 8585-8594.

[118] I. Dang, R. Gorelik, C. Sousa-Blin, E. Derivery, C. Guérin, J. Linkner, M. Nemethova, J.G. Dumortier, F.A. Giger, T.A. Chipysheva, Inhibitory signalling to the Arp2/3 complex steers cell migration, Nature 503(7475) (2013) 281.

[119] T. Maritzen, T. Zech, M.R. Schmidt, E. Krause, L.M. Machesky, V. Haucke, Gadkin negatively regulates cell spreading and motility via sequestration of the actin-nucleating ARP2/3 complex, Proc. Natl. Acad. Sci. U.S.A. 109(26) (2012) 10382-10387.

[120] M.-F. Carlier, S. Shekhar, Global treadmilling coordinates actin turnover and controls the size of actin networks, Nat. Rev. Mol. Cell Biol. 18(6) (2017) 389.

[121] M. Mak, M.H. Zaman, R.D. Kamm, T. Kim, Interplay of active processes modulates tension and drives phase transition in self-renewing, motor-driven cytoskeletal networks, Nat. Commun. 7 (2016) 10323.

[122] G. Charras, E. Sahai, Physical influences of the extracellular environment on cell migration, Nat. Rev. Mol. Cell Biol. 15(12) (2014) 813.

[123] I.V. Maly, G.G. Borisy, Self-organization of a propulsive actin network as an evolutionary process, Proc. Natl. Acad. Sci. U.S.A. 98(20) (2001) 11324-11329.

[124] E. Atilgan, D. Wirtz, S.X. Sun, Morphology of the lamellipodium and organization of actin filaments at the leading edge of crawling cells, Biophys. J. 89(5) (2005) 3589-3602.

[125] T.E. Schaus, E.W. Taylor, G.G. Borisy, Self-organization of actin filament orientation in the dendritic-nucleation/array-treadmilling model, Proc. Natl. Acad. Sci. U.S.A. 104(17) (2007) 7086-7091.

[126] J.V. Small, M. Herzog, K. Anderson, Actin filament organization in the fish keratocyte lamellipodium, J. Cell Biol. 129(5) (1995) 1275-1286.

[127] E. Henderson, P. Haydon, D. Sakaguchi, Actin filament dynamics in living glial cells imaged by atomic force microscopy, Science 257(5078) (1992) 1944-1946.

[128] R. Mahaffy, S. Park, E. Gerde, J. Käs, C. Shih, Quantitative analysis of the viscoelastic properties of thin regions of fibroblasts using atomic force microscopy, Biophys. J. 86(3) (2004) 1777-1793.

[129] C. Wu, S.B. Asokan, M.E. Berginski, E.M. Haynes, N.E. Sharpless, J.D. Griffith, S.M. Gomez, J.E. Bear, Arp2/3 is critical for lamellipodia and response to extracellular matrix cues but is dispensable for chemotaxis, Cell 148(5) (2012) 973-987.

[130] J. Condeelis, R.H. Singer, J.E. Segall, The great escape: when cancer cells hijack the genes for chemotaxis and motility, Annu. Rev. Cell Dev. Biol. 21 (2005) 695-718.

[131] A. Kawska, K. Carvalho, J. Manzi, R. Boujemaa-Paterski, L. Blanchoin, J.-L. Martiel, C. Sykes, How actin network dynamics control the onset of actin-based motility, Proc. Natl. Acad. Sci. U.S.A. 109(36) (2012) 14440-14445.

[132] I. Begemann, T. Saha, L. Lamparter, I. Rathmann, D. Grill, L. Golbach, C. Rasch, U. Keller, B. Trappmann, M. Matis, Mechanochemical self-organization determines search pattern in migratory cells, Nat. Phys. (2019) 1.

[133] C. Simon, R. Kusters, V. Caorsi, A. Allard, M. Abou-Ghali, J. Manzi, A. Di Cicco, D. Lévy, M. Lenz, J.-F. Joanny, Actin dynamics drive cell-like membrane deformation, Nat. Phys. (2019) 1.

[134] J. Renkawitz, A. Kopf, J. Stopp, I. de Vries, M.K. Driscoll, J. Merrin, R. Hauschild, E.S. Welf, G. Danuser, R. Fiolka, Nuclear positioning facilitates amoeboid migration along the path of least resistance, Nature 568(7753) (2019) 546.

[135] M. Wang, B. Cheng, Y. Yang, H. Liu, G. Huang, L. Han, F. Li, F. Xu, Microchannel stiffness and confinement jointly induce the mesenchymal-amoeboid transition of cancer cell migration, Nano letters 19(9) (2019) 5949-5958.

[136] A.W. Holle, N. Govindan Kutty Devi, K. Clar, A. Fan, T. Saif, R. Kemkemer, J.P. Spatz, Cancer Cells Invade Confined Microchannels via a Self-Directed Mesenchymal-to-Amoeboid Transition, Nano letters 19(4) (2019) 2280-2290.

[137] D. Mohammed, G. Charras, E. Vercruysse, M. Versaevel, J. Lantoine, L. Alaimo, C. Bruyère, M. Luciano, K. Glinel, G. Delhaye, Substrate area confinement is a key determinant of cell velocity in collective migration, Nat. Phys. (2019) 1.

[138] A. Diz-Muñoz, O.D. Weiner, D.A. Fletcher, In pursuit of the mechanics that shape cell surfaces, Nat. Phys. 14(7) (2018) 648.

[139] C.S. Peskin, G.M. Odell, G.F. Oster, Cellular motions and thermal fluctuations: the Brownian ratchet, Biophys. J. 65(1) (1993) 316-324.

[140] A. Mogilner, G. Oster, Cell motility driven by actin polymerization, Biophys. J. 71(6) (1996) 3030-3045.

[141] C.H. Schreiber, M. Stewart, T. Duke, Simulation of cell motility that reproduces the force–velocity relationship, Proc. Natl. Acad. Sci. U.S.A. 107(20) (2010) 9141-9146.

[142] A. Mogilner, G. Oster, Force generation by actin polymerization II: the elastic ratchet and tethered filaments, Biophys. J. 84(3) (2003) 1591-1605.

[143] J.B. Alberts, G.M. Odell, In silico reconstitution of Listeria propulsion exhibits nano-saltation, PLoS biology 2(12) (2004) e412.

[144] S.H. Parekh, O. Chaudhuri, J.A. Theriot, D.A. Fletcher, Loading history determines the velocity of actin-network growth, Nat. Cell Biol. 7(12) (2005) 1219.

[145] J.V. Small, C. Winkler, M. Vinzenz, C. Schmeiser, Reply: Visualizing branched actin filaments in lamellipodia by electron tomography, Nat. Cell Biol. 13(9) (2011) 1013.

[146] V.I. Risca, E.B. Wang, O. Chaudhuri, J.J. Chia, P.L. Geissler, D.A. Fletcher, Actin filament curvature biases branching direction, Proc. Natl. Acad. Sci. U.S.A. 109(8) (2012) 2913-2918.

[147] J.W. Shaevitz, D.A. Fletcher, Load fluctuations drive actin network growth, Proc. Natl. Acad. Sci. U.S.A. 104(40) (2007) 15688-15692.

[148] D.A. Murphy, S.A. Courtneidge, The'ins' and'outs' of podosomes and invadopodia: characteristics, formation and function, Nat. Rev. Mol. Cell Biol. 12(7) (2011) 413.

[149] M. Schoumacher, R.D. Goldman, D. Louvard, D.M. Vignjevic, Actin, microtubules, and vimentin intermediate filaments cooperate for elongation of invadopodia, J. Cell Biol. 189(3) (2010) 541-556.

[150] N. Akanuma, I. Hoshino, Y. Akutsu, K. Murakami, Y. Isozaki, T. Maruyama, G. Yusup, W. Qin, T. Toyozumi, M. Takahashi, MicroRNA-133a regulates the mRNAs of two invadopodia-related proteins, FSCN1 and MMP14, in esophageal cancer, British journal of cancer 110(1) (2014) 189.

[151] G. Jacquemet, H. Hamidi, J. Ivaska, Filopodia in cell adhesion, 3D migration and cancer cell invasion, Current opinion in cell biology 36 (2015) 23-31.

[152] R.P. Stevenson, D. Veltman, L.M. Machesky, Actin-bundling proteins in cancer progression at a glance, J Cell Sci 125(5) (2012) 1073-1079.

[153] D. Vignjevic, M. Schoumacher, N. Gavert, K.-P. Janssen, G. Jih, M. Laé, D. Louvard, A. Ben-Ze'ev, S. Robine, Fascin, a novel target of β-catenin-TCF signaling, is expressed at the invasive front of human colon cancer, Cancer Res. 67(14) (2007) 6844-6853.

[154] T.A. Sanders, E. Llagostera, M. Barna, Specialized filopodia direct long-range transport of SHH during vertebrate tissue patterning, Nature 497(7451) (2013) 628.

[155] S. Guerrier, J. Coutinho-Budd, T. Sassa, A. Gresset, N.V. Jordan, K. Chen, W.-L. Jin, A. Frost, F. Polleux, The F-BAR domain of srGAP2 induces membrane protrusions required for neuronal migration and morphogenesis, Cell 138(5) (2009) 990-1004.

[156] C. Leterrier, P. Dubey, S. Roy, The nano-architecture of the axonal cytoskeleton, Nature Reviews Neuroscience 18(12) (2017) 713.

[157] H. Witte, F. Bradke, The role of the cytoskeleton during neuronal polarization, Current opinion in neurobiology 18(5) (2008) 479-487.

[158] E.W. Dent, A.V. Kwiatkowski, L.M. Mebane, U. Philippar, M. Barzik, D.A. Rubinson, S. Gupton, J.E. Van Veen, C. Furman, J. Zhang, Filopodia are required for cortical neurite initiation, Nat. Cell Biol. 9(12) (2007) 1347.

[159] P.K. Mattila, P. Lappalainen, Filopodia: molecular architecture and cellular functions, Nat. Rev. Mol. Cell Biol. 9(6) (2008) 446.

[160] D. Bentley, A. Toroian-Raymond, Disoriented pathfinding by pioneer neurone growth cones deprived of filopodia by cytochalasin treatment, Nature 323(6090) (1986) 712.

[161] D. Saczko-Brack, E. Warchol, B. Rogez, M. Kröss, S.M. Heissler, J.R. Sellers, C. Batters, C. Veigel, Self-organization of actin networks by a monomeric myosin, Proc. Natl. Acad. Sci. U.S.A. 113(52) (2016) E8387-E8395.

[162] D. Vignjevic, S.-i. Kojima, Y. Aratyn, O. Danciu, T. Svitkina, G.G. Borisy, Role of fascin in filopodial protrusion, J. Cell Biol. 174(6) (2006) 863-875.

[163] B.M. Baker, B. Trappmann, W.Y. Wang, M.S. Sakar, I.L. Kim, V.B. Shenoy, J.A. Burdick, C.S. Chen, Cell-mediated fibre recruitment drives extracellular matrix mechanosensing in engineered fibrillar microenvironments, Nature materials 14(12) (2015) 1262.

[164] B. Trappmann, J.E. Gautrot, J.T. Connelly, D.G. Strange, Y. Li, M.L. Oyen, M.A.C. Stuart, H. Boehm, B. Li, V. Vogel, Extracellular-matrix tethering regulates stem-cell fate, Nature materials 11(7) (2012) 642.

[165] A. Parekh, N.S. Ruppender, K.M. Branch, M. Sewell-Loftin, J. Lin, P.D. Boyer, J.E. Candiello, W.D. Merryman, S.A. Guelcher, A.M. Weaver, Sensing and modulation of invadopodia across a wide range of rigidities, Biophys. J. 100(3) (2011) 573-582.

[166] S.W. Moore, P. Roca-Cusachs, M.P. Sheetz, Stretchy proteins on stretchy substrates: the important elements of integrin-mediated rigidity sensing, Dev. Cell 19(2) (2010) 194-206.

[167] H.E. Johnson, S.J. King, S.B. Asokan, J.D. Rotty, J.E. Bear, J.M. Haugh, F-actin bundles direct the initiation and orientation of lamellipodia through adhesion-based signaling, J. Cell Biol. 208(4) (2015) 443-455.

[168] P. Chugh, A.G. Clark, M.B. Smith, D.A. Cassani, K. Dierkes, A. Ragab, P.P. Roux, G. Charras, G. Salbreux, E.K. Paluch, Actin cortex architecture regulates cell surface tension, Nat. Cell Biol. 19(6) (2017) 689.

[169] W.R. Legant, A. Pathak, M.T. Yang, V.S. Deshpande, R.M. McMeeking, C.S. Chen, Microfabricated tissue gauges to measure and manipulate forces from 3D microtissues, Proc. Natl. Acad. Sci. U.S.A. 106(25) (2009) 10097-10102.

[170] Y. Ma, H. Zhu, B. Su, G. Hu, R. Perks, The elasto-plastic behaviour of three-dimensional stochastic fibre networks with cross-linkers, J. Mech. Phys. Solids 110 (2018) 155-172.

[171] F. Beroz, L.M. Jawerth, S. Münster, D.A. Weitz, C.P. Broedersz, N.S. Wingreen, Physical limits to biomechanical sensing in disordered fibre networks, Nat. Commun. 8 (2017) 16096.

[172] H. Zhu, J. Hobdell, A. Windle, Effects of cell irregularity on the elastic properties of open-cell foams, Acta Mater. 48(20) (2000) 4893-4900.

[173] H. Zhu, T. Fan, Q. Peng, D. Zhang, Giant Thermal Expansion in 2D and 3D Cellular Materials, Advanced Materials (2018) 1705048.

[174] H.X. Zhu, N. Mills, The in-plane non-linear compression of regular honeycombs, International Journal of Solids and Structures 37(13) (2000) 1931-1949.

[175] H. Zhu, J. Knott, N. Mills, Analysis of the elastic properties of open-cell foams with tetrakaidecahedral cells, J. Mech. Phys. Solids 45(3) (1997) 319-343.

[176] H. Zhu, J. Hobdell, A. Windle, Effects of cell irregularity on the elastic properties of 2D Voronoi honeycombs, J. Mech. Phys. Solids 49(4) (2001) 857-870.

[177] L. Cardamone, A. Laio, V. Torre, R. Shahapure, A. DeSimone, Cytoskeletal actin networks in motile cells are critically self-organized systems synchronized by mechanical interactions, Proc. Natl. Acad. Sci. U.S.A. 108(34) (2011) 13978-13983.

[178] E. Urban, S. Jacob, M. Nemethova, G.P. Resch, J.V. Small, Electron tomography reveals unbranched networks of actin filaments in lamellipodia, Nat. Cell Biol. 12(5) (2010) 429.

[179] D.R.-B. Aroush, N. Ofer, E. Abu-Shah, J. Allard, O. Krichevsky, A. Mogilner, K. Keren, Actin Turnover in Lamellipodial Fragments, Curr. Biol. 27(19) (2017) 2963-2973. e14.

[180] L.A. Cameron, T.M. Svitkina, D. Vignjevic, J.A. Theriot, G.G. Borisy, Dendritic organization of actin comet tails, Curr. Biol. 11(2) (2001) 130-135.

[181] F. Nakamura, T.M. Osborn, C.A. Hartemink, J.H. Hartwig, T.P. Stossel, Structural basis of filamin A functions, J. Cell Biol. 179(5) (2007) 1011-25.

[182] O. Pelletier, E. Pokidysheva, L.S. Hirst, N. Bouxsein, Y. Li, C.R. Safinya, Structure of actin cross-linked with alpha-actinin: a network of bundles, Phys Rev Lett 91(14) (2003) 148102.

[183] H. López-Menéndez, J.F. Rodríguez, Microstructural model for cyclic hardening in F-actin networks crosslinked by α-actinin, J. Mech. Phys. Solids 91 (2016) 28-39.

[184] T. Van Dillen, P. Onck, E. Van der Giessen, Models for stiffening in cross-linked biopolymer networks: A comparative study, J. Mech. Phys. Solids 56(6) (2008) 2240-2264.

[185] X. Wei, Q. Zhu, J. Qian, Y. Lin, V. Shenoy, Response of biopolymer networks governed by the physical properties of cross-linking molecules, Soft Matter 12(9) (2016) 2537-2541.

[186] Z. Zhang, H. Zhu, R. Yuan, S. Wang, T. Fan, Y. Rezgui, D. Zhang, Auxetic interpenetrating composites: A new approach to non-porous materials with a negative or zero Poisson's ratio, Composite Structures (2020) 112195.

[187] T.M. Svitkina, Actin bends over backward for directional branching, Proc. Natl. Acad. Sci. U.S.A. 109(8) (2012) 2693-2694.

[188] S.A. Koestler, K. Rottner, F. Lai, J. Block, M. Vinzenz, J.V. Small, F- and G-actin concentrations in lamellipodia of moving cells, PLoS One 4(3) (2009) e4810.

[189] T.D. Pollard, L. Blanchoin, R.D. Mullins, Molecular mechanisms controlling actin filament dynamics in nonmuscle cells, Annu. Rev. Biophys. Biomol. Struct. 29(1) (2000) 545-576.

[190] F. MacKintosh, J. Käs, P. Janmey, Elasticity of semiflexible biopolymer networks, Phys. Rev. Lett. 75(24) (1995) 4425.

[191] D. Raz-Ben Aroush, N. Ofer, E. Abu-Shah, J. Allard, O. Krichevsky, A. Mogilner, K. Keren, Actin Turnover in Lamellipodial Fragments, Curr Biol 27(19) (2017) 2963-2973 e14.

[192] M. Gardel, F. Nakamura, J. Hartwig, J. Crocker, T. Stossel, D. Weitz, Prestressed F-actin networks cross-linked by hinged filamins replicate mechanical properties of cells, Proc. Natl. Acad. Sci. U.S.A. 103(6) (2006) 1762-1767.

[193] L.C. Kelley, Q. Chi, R. Cáceres, E. Hastie, A.J. Schindler, Y. Jiang, D.Q. Matus, J. Plastino, D.R. Sherwood, Adaptive F-actin polymerization and localized ATP production drive basement membrane invasion in the absence of MMPs, Dev. Cell 48(3) (2019) 313-328. e8.

[194] J. van der Gucht, E. Paluch, J. Plastino, C. Sykes, Stress release drives symmetry breaking for actin-based movement, Proc. Natl. Acad. Sci. U.S.A. 102(22) (2005) 7847-7852.

[195] W.W. Ahmed, T. Betz, Dynamic cross-links tune the solid–fluid behavior of living cells, Proc. Natl. Acad. Sci. U.S.A. 112(21) (2015) 6527-6528.

[196] K. Rottner, F. Kage, Actin Networks: Adapting to Load through Geometry, Curr. Biol. 27(23) (2017) R1274-R1277.

[197] F. Kage, M. Winterhoff, V. Dimchev, J. Mueller, T. Thalheim, A. Freise, S. Brühmann, J. Kollasser, J. Block, G. Dimchev, FMNL formins boost lamellipodial force generation, Nat. Commun. 8 (2017) 14832.

[198] N. Molinie, S.N. Rubtsova, A. Fokin, S.P. Visweshwaran, N. Rocques, A. Polesskaya, A. Schnitzler, S. Vacher, E.V. Denisov, L.A. Tashireva, Cortical branched actin determines cell cycle progression, Cell research (2019) 1.

[199] M. Gardel, J. Shin, F. MacKintosh, L. Mahadevan, P. Matsudaira, D. Weitz, Elastic behavior of cross-linked and bundled actin networks, Science 304(5675) (2004) 1301-1305.

[200] D.A. Head, A.J. Levine, F. MacKintosh, Deformation of cross-linked semiflexible polymer networks, Phys. Rev. Lett. 91(10) (2003) 108102.

[201] N. Alieva, A. Efremov, S. Hu, D. Oh, Z. Chen, M. Natarajan, H. Ong, A. Jégou, G. Romet-Lemonne, J. Groves, Myosin IIA and formin dependent mechanosensitivity of filopodia adhesion, Nat. Commun. 10(1) (2019) 1-14.

[202] D. Wirtz, K. Konstantopoulos, P.C. Searson, The physics of cancer: the role of physical interactions and mechanical forces in metastasis, Nat. Rev. Cancer 11(7) (2011) 512.

[203] K. Kessenbrock, V. Plaks, Z. Werb, Matrix metalloproteinases: regulators of the tumor microenvironment, Cell 141(1) (2010) 52-67.

[204] L.B. Case, C.M. Waterman, Integration of actin dynamics and cell adhesion by a three-dimensional, mechanosensitive molecular clutch, Nat. Cell Biol. 17(8) (2015) 955.

[205] D. Pantaloni, C. Le Clainche, M.-F. Carlier, Mechanism of actin-based motility, Science 292(5521) (2001) 1502-1506.

[206] C. Co, D.T. Wong, S. Gierke, V. Chang, J. Taunton, Mechanism of actin network attachment to moving membranes: barbed end capture by N-WASP WH2 domains, Cell 128(5) (2007) 901-913.

[207] A.D. Lieber, Y. Schweitzer, M.M. Kozlov, K. Keren, Front-to-rear membrane tension gradient in rapidly moving cells, Biophys. J. 108(7) (2015) 1599-1603.

[208] S.C. Kuo, J.L. McGrath, Steps and fluctuations of Listeria monocytogenes during actin-based motility, Nature 407(6807) (2000) 1026.

[209] O. Chaudhuri, L. Gu, M. Darnell, D. Klumpers, S.A. Bencherif, J.C. Weaver, N. Huebsch, D.J. Mooney, Substrate stress relaxation regulates cell spreading, Nat. Commun. 6 (2015) 6365.

[210] J.T. Parsons, A.R. Horwitz, M.A. Schwartz, Cell adhesion: integrating cytoskeletal dynamics and cellular tension, Nat. Rev. Mol. Cell Biol. 11(9) (2010) 633.

[211] J.-P. Kaiser, A. Reinmann, A. Bruinink, The effect of topographic characteristics on cell migration velocity, Biomaterials 27(30) (2006) 5230-5241.

[212] J. Renkawitz, K. Schumann, M. Weber, T. Lämmermann, H. Pflicke, M. Piel, J. Polleux, J.P. Spatz, M. Sixt, Adaptive force transmission in amoeboid cell migration, Nat. Cell Biol. 11(12) (2009) 1438.

[213] I.H. Kim, M.A. Rossi, D.K. Aryal, B. Racz, N. Kim, A. Uezu, F. Wang, W.C. Wetsel, R.J. Weinberg, H. Yin, Spine pruning drives antipsychotic-sensitive locomotion via circuit control of striatal dopamine, Nature neuroscience 18(6) (2015) 883.

[214] E.M. Huisman, T. van Dillen, P.R. Onck, E. Van der Giessen, Three-dimensional cross-linked F-actin networks: relation between network architecture and mechanical behavior, Phys. Rev. Lett. 99(20) (2007) 208103.

[215] L.M. Machesky, A. Li, Fascin: Invasive filopodia promoting metastasis, Communicative & integrative biology 3(3) (2010) 263-270.

[216] L. Chen, S. Yang, J. Jakoncic, J.J. Zhang, X.-Y. Huang, Migrastatin analogues target fascin to block tumour metastasis, Nature 464(7291) (2010) 1062.

[217] J.D. Humphrey, E.R. Dufresne, M.A. Schwartz, Mechanotransduction and extracellular matrix homeostasis, Nat. Rev. Mol. Cell Biol. 15(12) (2014) 802-812.